Manufacturing Three-dimensional Carbon-fibre Preforms for Aerospace Composites

by

Thanos Drivas

Thesis submitted to the
Faculty of Graduate and Postdoctoral Studies
In partial fulfillment of the requirements
For the M.A.Sc. degree in
Mechanical Engineering

Department of Mechanical Engineering
Faculty of Engineering
University of Ottawa

Abstract

Carbon fibre reinforced polymer matrix composites (CF PMCs) are increasingly used in state-of-the-art aerospace applications. Aerospace manufacturers favour components made of CF PMCs over those made of traditional metallic alloys because of their light weight and corrosion resistance, which lead to significant improvements in fuel consumption, increased payload capability, and reduced maintenance and inspection costs. However, manufacturing of CF PMC components is performed differently than traditional material in all stages – design, prototyping and production – and therefore, many commercial manufacturers have only recently begun producing components with CF PMCs.

The first half of this thesis was written as a contribution to the CRIAQ COMP-501 project, which focusses on investigating the cost-effective procurement of airframe components that are manufactured from final-thickness, net-shaped, and through-thickness reinforced CF preforms. Reinforcement preforms were assembled from commercial 2D woven fabric using stacks of various configurations of structural through-thickness CF stitch. The contribution herein provides the results obtained from investigations into the mechanical behaviour of the relevant reinforcements, when subjected to pre-infusion operations typical to RTM VARTM; mechanical behaviour in compaction, shear (draping) and bending (forming).

The second half of this thesis presents the major developments which were made to an alternative process for producing thick 3D preforms with great versatility, a process originally proposed as a candidate for supplying preforms to the COMP-501 project. This process interfaces a proprietary kinematic drape optimization (CAD) software with proprietary automated dry fibre placement assembly (CAM) machinery to produce variable or final-thickness reinforcements which are highly-drapable and can lay steered tow yarns.

Keywords: Mechanical testing; Compaction; Draping; Bending; Dry fibre placement; Fibre steering; Tow deposition

Dedication

This is presented as a work of factual observation and dedicated to nobody.

"Not all those who wonder are lost."

Acknowledgements

Neil deGrasse Tyson once proclaimed "Science is a cooperative enterprise, spanning the generations. It's the passing of a torch, from teacher to student; a community of minds reaching backward to antiquity, and forward to the stars."

I would like thank my thesis supervisor, Dr. F. Robitaille for passing much of his invaluable knowledge to me. His guidance, support, trust, and motivation drove my achievements to extend beyond what I previously recognized as possible. His patience and guidance was critical in developing this thesis, the contents of which would have otherwise become forgotten notes scattered within logbooks, binders, and files.

A huge thank you to my parents. They persisted to help me realize my potential, even though I made every step a futile struggle, which pushed them ever closer to the brink of insanity. They have been there for me through thick and thin and their deeds will never be forgotten. My appreciation is endless.

To my colleagues & friends from within the walls of Colonel By Hall, these days were unforgettable; from 24h final exams, high-speed camera nights, machine-shop chatter, DUSTEDs, and pub nights, all of it was legendary. Stay true to yourself and the elements of success: fluorine, uranium, carbon, potassium, bismuth, technetium, helium, sulfur, germanium, thulium, oxygen, neon, and yttrium.

My friends from the YB, you've shown me that true friendship isn't about being inseparable, but about being separated and having nothing change. You've put up with a lot over the course of the thesis writing process and it's not without thanks.

Lastly, I would like to extend a special thank you to Jimi Hendrix, whose rhythmic blues kept me going during many late nights and early mornings.

Contents

List of Tables

List of Figures

Nomenclature

$\Delta\gamma$	Bend angle
ϵ	Connecting rod angle WRT horizontal
γ	In-plane shear angle
γ_i	Instantaneous internal bending rig angle
γ_o	Initial internal bending rig angle
ρ_c	Density of carbon fibre
θ_s	Trellising acute internal angle from vertical
A_p	Platen compaction area
F_s	Shear force
F_T	Force in bend apparatus connecting rod
$F_{i,d}$	Instantaneous force measured in dry bending apparatus
$F_{i,w}$	Instantaneous force measured with bend sample present
$F_{normalized}$	Normalized shear force
h_c	Corrected platen height
h_i	Instantaneous Instron displacement
k_c	Carbon sample spring constant
k_p	Platen spring constant

k_t	Normalized torsional spring coefficient
k_{eq}	Equivalent spring constant
L_{fabric}	Length of the fabric reinforcement specimen
L_{frame}	Length of the members that make up the trellising shear testing frame
m_c	Mass of carbon fibre
M_O	Moment within bending rig – Point 'O'
$M_{normalized}$	Normalized bending moment
s_c	Compressive displacement of carbon sample
s_p	Compressive displacement of platen
V_f	Fibre volume
v_f	Fibre volume fraction
V_p	Volume between compaction platens
w_s	Bending sample width

Chapter 1

Introduction

1.1 Background

Carbon fibre polymer matrix composites (CF PMCs) are increasingly used in state-of-the-art aerospace applications as they offer significant advantages over other common structural materials, namely metallic alloys. In the aerospace industry CF PMCs are highly sought after as their extremely high specific mechanical properties (specific tensile modulus and specific strength) enable the design of lightweight airframes, which provide significant improvements in fuel consumption and/or increased payloads. Recently, major aerospace manufactures such as Boeing® and Airbus® drastically accelerated the integration of CF PMC primary and secondary load bearing structures for civil aviation. This shift has facilitated the development of three of the most environmentally friendly, spacious and inexpensive civil aircraft to operate, namely the *Boeing® 787 Dreamliner, Airbus® A380 and A350*.

Structural CF PMC components manufactured to meet strict tolerances and airworthiness requirements are typically manufactured using autoclave-cured prepreg. Prepreg, short for pre-impregnated carbon fibre, is a form of carbon semi-product where collimated or woven fibres are wetted with a thermoplastic or most commonly, a partially-cured (B-stage) thermoset resin prior to layup. Manufacturing components from prepreg requires large capital investment towards acquiring the processing equipment. Furthermore, storage and handling of unprocessed prepreg contributes to added cost. As a result of economic and practical inconveniences involved with manufacturing CF PMC

components from prepreg, airframe manufacturers recently begun exploring the use of out-of-autoclave and liquid moulding processes such as resin transfer moulding (RTM), RTM-light, vacuum infusion (VI) and resin film infusion (RFI) for making primary and secondary load-bearing aircraft structures and skins [1–6]. Unfortunately, liquid moulding processes also present challenges; they require that dry preforms be manufactured by cutting, positioning and draping superimposed patches of dry textile material cut from roll-stock. The manufacturing of each preform is typically carried out manually and individually. This process is inherently time-consuming and introduces concerns over manufacturing consistency. Automating the production of dry preforms from roll-stock has been demonstrated to be possible [7, 8], however there are severe limitations in the geometries that may be produced [9–11].

As a result, a production method for dry preforms as textiles requiring little or no further assembly or trimming work and close to final shape is, highly sought after. Preforms produced with such characteristics are typically referred to as 3D and net-shape respectively and their production has been investigated previously [12–24]. In an ideal scenario, such preforms would be suitable for a large array of PMC part geometries, be manufactured using largely automated processes [25–28], exhibit high part-to-part consistency, and feature fibre orientations optimized for processing [29] and structural performance.

Textile preforms for more complex or realistic parts often feature thick sections, integral ribs or flanges and/or assemblies of intersecting shells or other similar features. Designing and manufacturing such preforms as self-contained textiles demands thorough planning and understanding of limitations in preform construction. Often, compromises must be made to the component geometry in order to ensure manufacturability.

Typically, self-contained 3D textile preforms are produced by 3D weaving, 3D braiding, knitting or embroidery [30]. 3D weaving extends on the conventional weaving process by integrating superimposed layers of 2D fabrics with diverse degrees of Z-binder and yarn interlacing [31–40]. The reinforcements are mostly woven as thick, flat slivers or wider sheets where machinery capability is available; however, specific geometries such as domes are also possible [41–44]. Preforms made for specifically complex component geometries may be manufactured by assembling a small number of generic 3D textile pieces using a mechanical assembly process such as stitching. Such preforms are manufactured with increased use of automated technologies, which replace layup and as such, yield the advantage of increased preform consistency and reduced labour need. However

the jointing techniques used for assembling these preforms must be capable of withstanding later manufacturing operations such as handling and processing. Similarly, joining techniques must be sufficiently robust to meet the desired structural requirements of the processed component [45].

The CRIAQ COMP-501 project is a joint research effort involving three Canadian universities, namely the University of Ottawa (UO), École de Technologie Supérieure (ETS) and Université Laval (UL) as well as industrial partners Bell Helicopter (BH), Bombardier Aéronautique (BA), Delastek, Hutchinson Aerospace (HA) and JB Martin (JB). The effort was initiated in 2012. The COMP-501 project focuses on investigating and assessing the feasibility of manufacturing and processing final-thickness, net-shaped preforms into airframe components. Aimed at the procurement of a cost-effective method for producing said components it was decided that reinforcements for the project would be primarily manufactured by assembling stacks of internally sourced fabric with a structural carbon fibre lock stitch rather than seeking 3D woven, braided, or embroidered reinforcements from suppliers external to the project. The manufactured preforms would be assembled using the same structural stitch, and likely feature stitch in areas not requiring assembly in an effort to provide some degree of through-thickness reinforcement. In tune with the theme of cost effective production, preforms will be geared toward processing using vacuum assisted resin transfer moulding. (VARTM), a process described in detail in Section 2.3.2.2.

This thesis is presented as a contribution towards the CRIAQ COMP-501 project and contains information regarding the effects of the proposed assembly techniques the on reinforcements' mechanical properties, in terms of behaviour in compaction, shear (draping) and bending (forming). It also presents the major developments made to an alternative process for producing thick 3D preforms with great versatility, a process originally proposed as a candidate for supplying preforms to the COMP-501 project.

1.2 Objectives

This first objective of this thesis is to address the work done to investigate the mechanical and forming characteristics of CRIAQ COMP-501 reinforcements and shed light on how these characteristics are altered by the presence of a one-sided structural lock stitch in various configurations. The second major objective is to summarize the development of

a new and novel process for producing highly drapable final-thickness, near-net-shaped preforms with featuring steered yarns.

The following is a summary of the specific objectives completed towards the first and second major objectives:

- Determine the average maximum attainable fibre volume fraction,v_f, at 1 bar final compaction pressure for each sample type.
- Obtain the fibre volume fraction, v_f, to compaction pressure relationship for samples without stitching, with single stitching and with superimposed stitching patterns.
- Determine the in-plane shear characteristics for each type of sample.
- Obtain the in-plane shear angle, γ, to normalized shear force, $F_{normalized}$, relationship for samples tested in shear.
- Determine the bending coefficient, k_b, of the COMP-501 samples in single curvature forming (bending).

- Develop the overall process and implement automated manufacturing equipment suited to the automated production of net-shaped final-thickness steered yarn preforms.
- Develop an electromechanical actuation system capable of interfacing directly with an instructing computer.
- Develop software post-processor that is capable of translating outputs from the drape optimization software developed at the University of Ottawa into an ordered set of instructions codified in a machine-language. This post-processor will serve as the primary means for generating and programming the aforementioned automated machinery with operational instructions.

Chapter 2

Literature Review

2.1 Introduction to composite materials

Composite materials are a subset of engineered materials resulting from the organized integration of two or more distinct engineering materials. These distinct materials are not put into solution, instead they remain distinct with each material bringing a contribution to the physical properties of the composite. As such, the properties of the composite can be approximated as a volumetric average, or some other function of the properties of the constituent materials. However, it is important to note that as the materials remain distinct, composites featuring oriented fibres as their reinforcement often display some form of orthotropy. Hence, volumetric approximations will only be valid for some material properties.

Composite materials are commonly referred to as composites. In aerospace engineering, the term composites largely refers to materials that are constructed from a high stiffness and high strength fibrous reinforcing material encapsulated in a polymer matrix. In other industries, other types of composites are prevalent. For example, reinforced concrete is a composite material that features a concrete-matrix reinforced with fibrous aggregate and steel rebar.

Composite materials are by no means a new concept. Straw reinforced mud bricks were used as a building material thousands of years ago. Reinforced concrete was implemented as early as 1871. Cotton-reinforced rubber was implemented in the construction of pneumatic tires in the early 1900's by the Goodyear Rubber Company [46]. Com-

posite materials continue to evolve using new constituent materials and manufacturing techniques being researched and developed every day, worldwide.

Composite materials are required to feature a minimum of two distinct constituent materials by definition; at least one type of reinforcement and matrix. This can be seen in Figure 2.1. The matrix in composites typically is a material capable of transitioning from a liquid-state to a rigid, solid-state during processing. Matrix materials are most commonly thermosetting or thermoplastic polymers; metal and ceramic matrix materials are also used [47]. Reinforcement materials of many kinds are available, ranging from metallic wire, natural fibres, glass fibres, polymer fibres, aramid fibres such as Kevlar™, and various grades of carbon fibres. Furthermore, reinforcing fibres are available in many textile configurations including classic weaves such as plain, twill and satin weaves, as well as non-crimp unidirectional configurations. Composites can be manufactured using more than one type of reinforcement [48]. For advanced structures, combining various reinforcement types enables designers to impart different properties to different areas of a structure, whether for functional or sometimes aesthetic purposes. For example, Kevlar™ is sometimes integrated within the reinforcement to enhance the ballistic protection properties of the composite. This technique is commonly seen in applications such as the front body panels of modern-day racing vehicles. In aerospace construction, certification issues do limit design freedom.

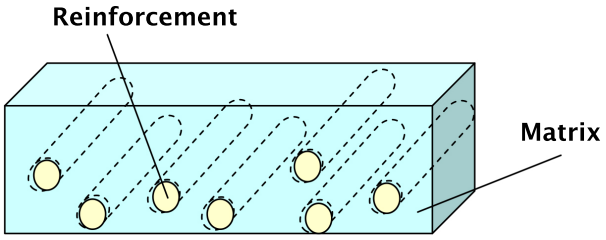

Figure 2.1: Schematic view of a composite material [49].

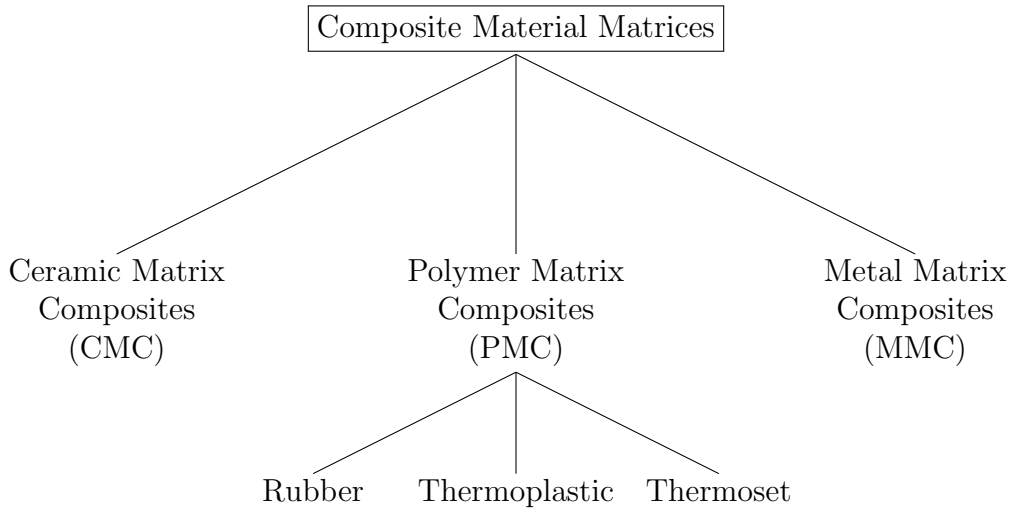

Figure 2.2: Partial breakdown of composite matrix materials by type.

2.2 Origin of carbon composites

In 1960 Curry Ford and Charles Mitchell filed a patent [50] for a process which could manufacture carbon fibre plies by heating rayon cloth to nearly 3000^{o}C. By 1963 Ford and Mitchell's process was producing a material that became recognized as an advanced composite. In similar times the material began to appear in gaskets and rubberized packing materials. While at this time carbon fibres lacked the high moduli sought for reinforcing materials, the advanced composite market was dominated by stiff, strong, yet heavy and expensive tungsten-boron fibres [51]. By late 1969 Roger Bacon and Wesley Schalamon [52] manufactured carbon fibres from rayon filament using a 'hot-stretching' process. Bacon and Schalamon discovered that stretching the precursors while heating them, rather than at final temperature would result in layers of graphite within the filaments becoming aligned along the filament axis. This discovery produced fibres marketed under the name *Thornel 25*, with a ten-fold increase in Young's modulus over existing fibres [51]. The Thornel line would continually expand through products with superior mechanical properties for the next ten years.

The U.S. Air Force was amongst the first adopters of Thornel fibres, implementing them in a new generation of high performance rocket nozzles, missile nose-cones and aircraft structures. In space applications the fibres were used for reinforcing phenolic resins and played a vital role in keeping the resin heat-shields intact during vehicle re-entry. Over time carbon fibre technology has trickled down from strictly military

applications toward various consumer markets. Thin shell polymer reinforced laminates have been used in the construction of specialty marine craft for more than sixty years, in aircraft for more than forty years, and over thirty years in civil infrastructure and high-performance automotive applications [1].

Carbon composites are increasingly integrated into consumer products with the intent of gaining an advantage over similar products whether said advantage is to be technical, visual or a combination thereof. It has become common to see carbon fibre reinforcements used in a variety of consumer and prosumer applications including sporting goods (bicycles, helmets, hockey sticks, rackets, skis, sleds), after-market & high performance automotive components and photography equipment such as tripods. Similarly, CF PMCs have appeared in applications where structural makeup is of minimal concern, where they are used purely for aesthetic reasons.

2.3 Manufacturing fibre composites

PMCs are manufactured by arranging a fibre reinforcement into a desired pattern in or on a closed or an open single-sided surface mould that replicates the shape of the final component to be made. Next, the fibre reinforcement is infused, most often with a liquid thermosetting resin and transformed into a permanent, rigid component by curing the polymer matrix that surrounds the fibres.

Two distinct manufacturing philosophies divide the manufacturing of PMCs into two main process streams. The two process streams are differentiated by the time at which the introduction of the polymer resin into the fibre reinforcement occurs before layup, where the combination results in a partially cured semi-product in the form of pre-impregnated tape – prepreg, which is laid onto the mould in a later, distinct operation; or following the layup of the dry fibrous reinforcement onto the mould, resulting in a group of processes identified as liquid composite moulding –LCM, Figure 2.3.

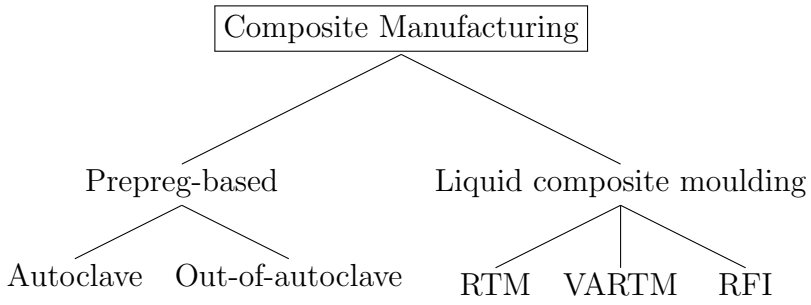

Figure 2.3: Breakdown of various manufacturing processes used for creating PMCs.

2.3.1 Prepreg

Prepreg, short for pre-impregnated tape or fabric, designates a group of semi-products where carbon fibres are pre-impregnated with resin during the manufacture of the semi-product. The pre-impregnated resin is allowed to cure partially to an intermediate B-stage, at which the reaction is halted and the material is cooled and packaged for delivery to third-party component manufacturers. As a result, prepreg reinforcements require uninterrupted cold-storage to impede the cure of the B-stage resin from resuming. The reaction continues to progress albeit at a very slow rate, and so the shelf life of a B-stage prepreg is finite, regardless of the level of care displayed in controlling its storage environment.

Upon part manufacturing, prior to prepreg layup the semi-product is removed from cold storage and allowed to thaw under seal to avoid condensation forming on the material. Following the completion of ply-by-ply layup the prepreg is sealed on the mould under a plastic membrane and loaded into an autoclave. It is then subjected to a precise cure cycle, which follows prescribed variations in temperature and pressure. As the semi-product is fully pre-impregnated, no additional resin in needed during processing. Instead, a vacuum is drawn on the component to further compress the prepreg stack and remove any trapped volatiles, air bubbles and excess resin. While out-of-autoclave prepreg-based manufacturing processes do exist, these typically do not produce components equivalent to those produced using autoclave manufacturing, especially in terms of equivalent v_f and void content [53, 54].

Due to requirements for cold storage and advanced processing equipment, manufacturing PMC components from prepreg is costly, often prohibitively so. Furthermore, large-scale production both in terms of production volume and physical component size

entails the use of more material, increased storage and larger processing equipment, further adding to the often prohibitive cost associated with prepreg manufacturing. As such the material is often unsuitable for high volume mass manufacturing applications.

However, prepreg does offer processing and performance advantages. For instance, as the partially-cured resin in the prepreg material reaches layup temperatures it becomes inherently tacky, which aids in handling and maintaining prepreg position during layup, increasing manufacturing consistency between different components. The addition of resin to the material prior to layup ensures greater uniformity and distribution of the matrix within the composite, and it reduces the number of voids and inclusions in the final PMC component. Autoclave processing enables greater pressures to be applied during processing, leading to higher v_f and superior mechanical properties. Hence, the use of prepreg is often justified for low- to medium-volume production when strict control over mechanical properties, high v_f and low void content is required along with high manufacturing consistency. Aerospace applications generally rely on prepreg for manufacturing any primary load-bearing component. High-performance sport equipment manufacturers generally implement prepreg in high-end equipment [55, 56].

2.3.2 Liquid composite moulding

The alternative to manufacturing with prepreg semi-products is a family of processes generally known as liquid composite moulding (LCM). As shown in Figure 2.3, LCM refers to a family of processes that feature specific manufacturing techniques. Manufacturing with LCM is favoured because of its relative simplicity, accessibility, flexibility and contained cost. Liquid composite moulding processes are more economical than prepreg-based manufacturing at any production volume. Secondly, they offer a viable option for manufacturing small to midsize components relatively quickly without major compromises over component quality.

Only the two most relevant LCM processes, resin transfer moulding (RTM) and vacuum assisted resin transfer moulding. (VARTM) are discussed in detail below.

2.3.2.1 Resin transfer moulding (RTM)

Resin transfer moulding (RTM) is performed by enclosing a stack of fibre-based reinforcement, or preform, within two or more sections that fit together to form an essentially

rigid and entirely sealed closed mould, Figure 2.4. As the mould sections are closed, the preform within is subjected to compaction which, in turn, rearranges the preform's fibres and brings them closer together. This compacting action confines the same volume of fibre reinforcement into a reduced volume, reducing the free space within the mould cavity to be filled by the resin in a subsequent step.

As the reinforcement's contribution to the mechanical properties of the final PMC component increases with the volumetric fraction, v_f, of reinforcement within, this compacting action is desirable.

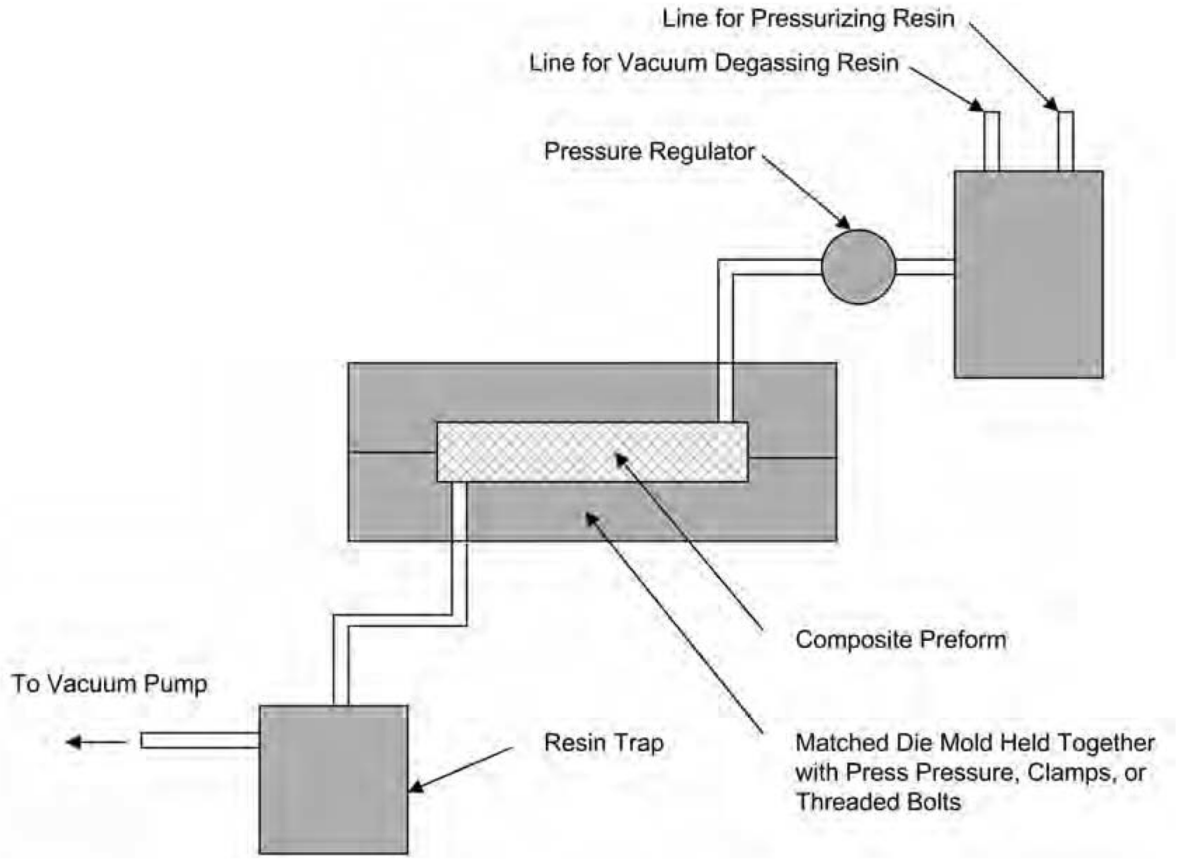

Figure 2.4: Diagram of the RTM process [57].

Prior to resin injection, a vacuum is sometimes drawn within the closed mould. This has two purposes. First, removing the majority of atmospheric gas from within the

mould results in fewer bubbles forming in the resin leading to fewer voids within the cured matrix. Second, it increases the pressure gradient within the mould, allowing resin to flow into the preform under lower positive gauge pressure. As an additional advantage, mould surfaces continue to apply compacting pressure to the preform rather than containing the pressure of the resin, reducing the risk of the mould opening during injection.

Liquid resin is injected into the mould so that it completely impregnates the volume between individual fibres, and it is let to cure within the cavity. The rate of matrix cure slows markedly as the reaction progresses past the halfway mark, hence it is common for components to be removed from the mould as soon as the resin is cured sufficiently to withstand demoulding. By demoulding early the tooling becomes available for the next production run thereby increasing the production rate by reducing manufacturing downtime. Prematurely demoulded, partially-reticulated components are post-cured in a controlled environment to complete the curing process. By monitoring and controlling the post-cure environment, components may be prematurely demoulded without affecting their quality adversely. However, PMC components that are demoulded too early may suffer distortions and loss of in dimensional accuracy that is often incompatible with aerospace requirements [58].

RTM is most often performed using moulds made from metal, composites, or metal-composite combinations. Such moulds are capable of withstanding large internal pressures, allowing resin to be injected at significantly high pressure, up to 500 psi [57]. By injecting resin using high pressure gradients large flow rates can be achieved, reducing the time required to impregnate the preform fully, lowering overall process cycle times. Similarly, resin under high pressure gradients is capable of deeper penetration and better flow through preforms with low porosity, allowing production of PMCs with thicker sections and higher v_f [59]. However, resin pressure gradients cannot be so great as to displace the preform within the mould [18]. Similarly, resin pressures cannot be so great as to open the mould during injection.

Resin cure is an exothermic chemical reaction, for which the rate of heat release at any given time is dependent on the temperature of the curing resin at that time. As composites have low thermal conductivity the possibility of excessive heat accumulation within a curing component is present. As a result, the temperature and rate of resin cure must be considered in order to avoid heat accumulation that may lead the reaction rate to increase beyond safe limits. If this is allowed, the reaction will induce thermal

degradation within the composite [60], potential damage to tooling and/or environmental hazards such as fire and toxic gas emission. As a result, RTM moulds are often fitted with integrated heating/cooling systems to control the temperature over areas of the composite, or the part as a whole. In such cases, RTM enables the production of composites with thicker sections.

2.3.2.2 Vacuum-assisted resin-transfer moulding (VARTM)

VARTM is the most flexible method for processing preforms into PMC components. In similarity to RTM, VARTM uses a rigid half-mould to impart a shape to the component. VARTM differs from RTM as the other mould-half is not rigid. Instead, VARTM moulds are sealed using a flexible sheet membrane or 'vacuum bag'. This affects the resulting PMC components in several ways. Surface finish on the side of the component in contact with the vacuum bag is inferior to the surface finish created through contact with the solid mould, and so the membrane is generally positioned on the side of the part usually hidden in operation or for which accurate dimensions are not required.

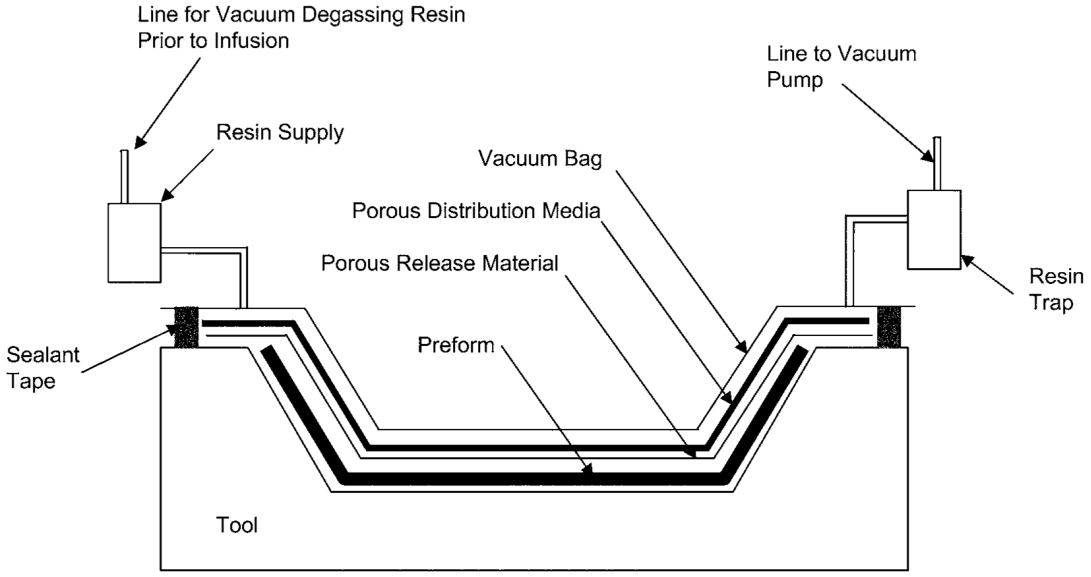

Figure 2.5: Diagram of the VARTM process [57].

Following the sealing of the membrane, a vacuum is drawn. This allows atmospheric

pressure to bear down on the preform, causing it to compact prior to infusion. Vacuum is maintained throughout the process by drawing on the resin outlet ports as seen in Figure 2.5. After checking for leaks, resin inlet plumbing is submerged into a pot of resin at atmospheric pressure. The inlets are opened and resin is drawn into the preform under a pressure gradient equivalent to the difference between atmospheric and the vacuum induced at the outlet. Once the resin has impregnated the preform thoroughly, resin inlets are closed while vacuum is continually drawn at the outlets in an effort to keep compressing the preform and remove any lingering voids.

As VARTM setups are typically not used in conjunction with autoclaves, the sum of compaction pressure on the preform and resin infusion pressure is limited to atmospheric pressure. As a result, the placement of resin inlets and outlets must be considered carefully to ensure that the preform will be impregnated fully upon infusion. Similarly, limited compaction pressure induces limits in the fibre volume fraction that may be achieved within the component. It is generally agreed that the fibre volume fraction of PMC components produced by VARTM will have a v_f in the 50% - 55% range; fibre volume fractions approaching 60% have been achieved in laboratory settings [61].

Given the limitations of VARTM stated above, it is important to note that VARTM also offers many advantages. VARTM is especially suitable to low volume production runs. Its low tooling costs make it possible to produce PMC components economically as single component runs to low volume production. Similarly, VARTM's tooling simplicity makes it possible to produce large components such as radar domes, wind turbine blades and yacht hulls.

2.4 Limitations to current PMC manufacturing technology

Lightweight and structural materials are sought by aerospace manufacturers as weight reduction is intimately tied to incentives such as fuel savings and larger payload capacity. A study published in 1975 by J.G. Williams and M.M. Mikulas compared the weight efficiency of aluminum compression panels with their composite counterparts. Analytical models concluded that airframe weight reductions as high as 50% are possible by replacing aluminum airframe components with CF PMCs. Findings were validated experimentally

to demonstrate weight reductions spanning from 32% to 42% [62].

The successful implementation of PMCs into aerospace structures requires that high manufacturing standards be fulfilled toward airworthyness certification. Composites that are manufactured towards aerospace applications must exhibit high v_f and low void content, characteristics that are typically not attained using conventional dry fabrics and VARTM manufacturing. As such, PMCs destined to aerospace applications are predominantly manufactured using prepreg-based technologies.

High production costs remain a significant barrier plaguing the mass production of PMCs. PMC manufacturing requires significant development by specially qualified engineers to ensure that the resulting components will meet design specifications. Each preform must be engineered individually with due regard to unique geometry and processing challenges, as well as performance requirements. Extensive testing on prototype components is required to ensure that design specifications are met and may be relied upon in future production runs. Furthermore, the process of transforming raw materials into PMC components is extensively labour intensive and must be tended to by skilled workers. Raw materials including carbon fabrics and polymer reinforcements are expensive and the industrial equipment required for cutting, moulding and infusing the raw materials into fully manufactured components demands large capital investment.

The involvement required for manufacturing a PMC component rises rapidly with every increase in component complexity. Any increased complexity in the manufacturing process is often coupled with increased labour need and with increased cost. Components featuring complex curves or double curvatures often involve complex layup sequences, fabric darting, and/or post-infusion joining operations such as secondary bonding [63].

High volume production brings further limitations, notably the inability to meet required production rates generally regarded as commonplace. Production at one minute per part is generally regarded as a standard manufacturing rate by the mass-production automotive industry, and this standard has been as longstanding as the domination of metal-stamping manufacturing operations used in that industry. While processing times for composites continue to improve, the in-mould time required for producing a single component of moderate size such as a automobile trunk-floor pan currently averages around 5 minutes [64]. In short, the one-minute composite is still far from a reality. A refreshing truth balancing the above unwelcome reality is that composite tooling costs amount to a fraction of those of metal-forming dies. Hence, the composite industry puts forward the opinion that the low manufacturing rates plaguing composite production can

be offset by implementing a larger array of tooling operating in a parallel manufacturing arrangement [64].

Regardless of the available tooling array, speed of impregnation and cure time, each liquid moulded composite component is manufactured from a precursory preform. Preforms are manufactured individually through a sometimes tedious and time-consuming process called preform layup. Layup is often performed by layering reinforcement plies directly onto the same mould that will later be used for infusing the preform. During layup tooling is disconnected from infusion equipment so that preform layup may occur, contributing to non-operational tooling time and total tooling time required by a facility.

To enable a shift toward a mass-production paradigm, it would be ideal for preform manufacturing to occur using automated preforming processes that would not require the removal of moulding tools from the infusion line. This would reduce the time and manual labour required for production, and reduce tooling capacity lost to non-operation time while boosting preform consistency and component reproducibility. Furthermore, these benefits towards preform consistency and component reproducibility would be sustained in low production volume applications.

Unfortunately, a remarkable degree of manual dexterity as well as a thorough capacity to understand and interpret what must be visual feedback upon draping is required for performing the majority of conventional fabric layup procedures, putting conventional layup out of the scope of today's robotic equipment. As such, composites manufacturers have turned to semi-automated manufacturing using implementations such as CNC-fabric cutting and laser guided ply placement to aid, but not replace, skilled manual labour. Similarly, careful planning and tuning of aspects such as plant arrangement and batch size allow manufacturers to optimize production thus recovering margins of lost efficiency. Such manufacturing aids increase feasibility, but do not pave direct routes toward mass producibility. Semi-automated preform manufacturing is not sufficient for supplying preforms at rates required for mass production. Fully-automated preforming techniques are required, and a reliable method for their construction is highly sought-after.

2.5 3D Preforms

2.5.1 Woven 3D reinforcements

Weaving is an age-old practice by which individual yarns are transformed into a planar fabric by interlacing these yarns at perpendicular angles. These perpendicular yarns are referred to as warp and weft yarns. Conventional 2D woven fabrics have been used as reinforcement in PMCs for more than half a century.

Three-dimensional weaving is an extrapolation of conventional 2D weaving where thick, multilayered fabrics are produced essentially by binding layers similar to conventional woven fabrics with an additional, third set of yarns spanning in the through-thickness direction of the fabric [65]. These yarns, referred to as binder or Z-binder yarns, are typically continuous filaments with a weight in the 50-500 tex (g/km) range and they are woven into the fabric.

Binder yarns often run orthogonal to the layers of warp and weft yarns, but not always [18]. Variations exist where binder yarns pass through the layers of planar fabric at an oblique angle, as seen in Figure 2.6.

Two main types of 3D woven fabrics exist, known as 3D interlock and 3D orthogonal non-crimp. In the former – 3D interlock weaves – warp, weft and binder yarns interlace to produce a fully interlocked fibre structure [18,65]. The resulting fabric is analogous to a stack of conventional crimped fabrics bound together by yarns interwoven through the thickness of the preform in alternating directions [65]. In the latter type – 3D orthogonal non-crimp fabrics – warp and weft yarns are stacked as discrete layers similar to multiple stacked plies of unidirectional reinforcements. No interlacing exists between the structural warp and weft yarns. As a result, orthogonal non-crimp fabrics are capable of producing composites with higher in-plane stiffness than those produced with interlocked 3D weaves [18].

Binder yarns are typically used for holding multiple plies of the warp and weft structures as one [66], or as structural yarns in warp-interlock woven reinforcements, providing through-thickness reinforcement [37]. Whilst binder yarns are woven into the fabric at volume fractions ranging roughly 0.5% to 10% [65], and most often represent less than 10% of total fibre mass, their presence causes inter-laminar shear strength (ILSS) and impact properties to be superior to those of traditional laminates, at the expense of

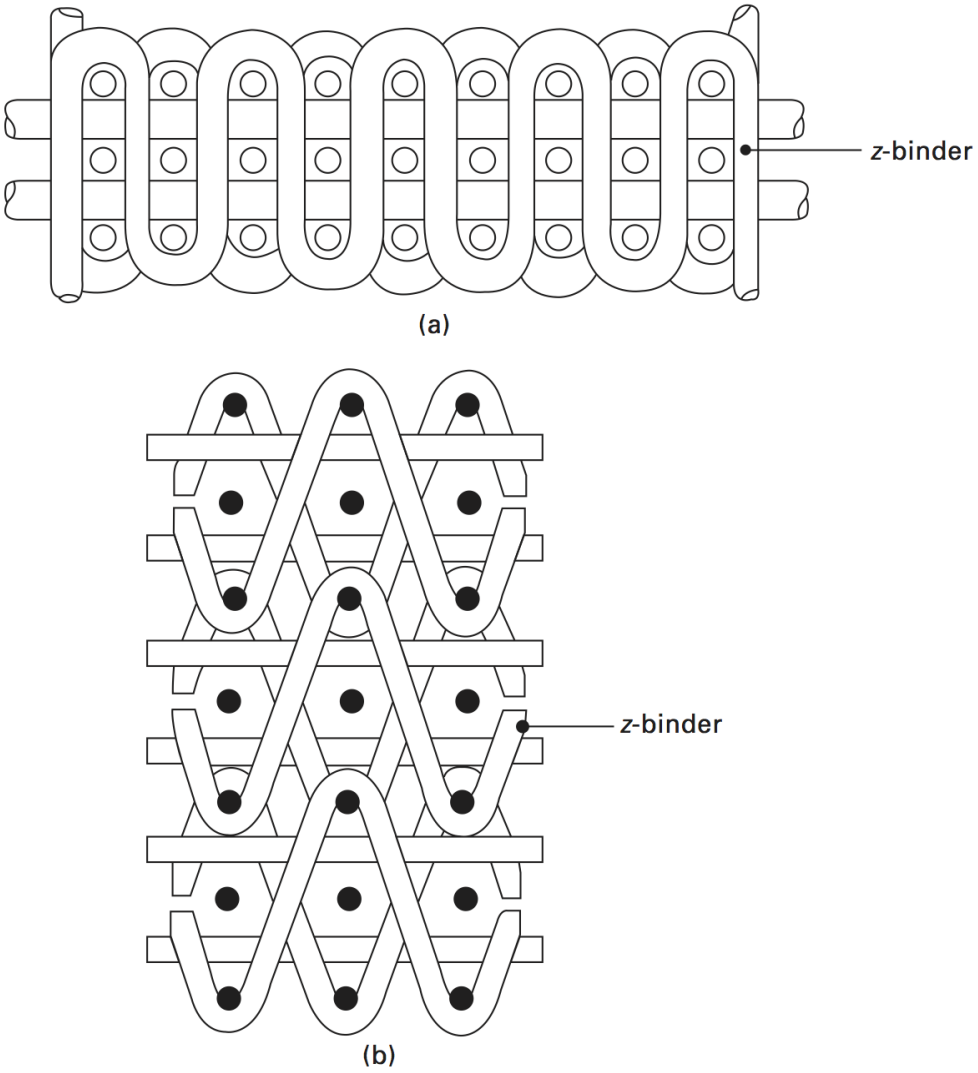

Figure 2.6: Z-binder reinforcement patterns in (a) 3D orthogonal and (b) 3D interlock woven fabrics [65].

in-plane strength [1]. This makes woven 3D composites well suited to applications that demand high levels of damage tolerance, such as military airframes [1, 67].

Woven 3D reinforcements are produced using looms that are similar to conventional 2D weaving machines. Given the added mechanical complexity involved in producing fabrics that include a binder yarn, 3D weaving equipment is inherently more complex, and as a result it is more limited in terms of the diversity of fabric types that may be produced. Currently one such limitation is the ability to produce fabrics with in-plane

yarn orientated at angles other than $0^o/90^o$ [1, 18]. Hence, composites produced with woven 3D fabrics tend to have inferior performance compared to stacked multidirectional 2D weaves when subjected to shear and torsional loading [1]. As such, 3D weaves are deemed generally unsuitable for application in aerospace structures where materials well suited to resisting torsional and in-plane shear loading are required [1].

2.5.2 Stitched 3D reinforcements

Three-dimensional fabrics can be produced by introducing an element of through-thickness reinforcement via stitching operations. High strength thread is inserted into stacks of unidirectional or woven fabric stacks such that it acts as a Z-binder and to lesser extent, structural reinforcement [1].

Stitching is achieved using equipment as simple as single needle machines, similar to those found in households, or more complex setups that are capable of performing single sided stitching operations. Such single sided stitching equipment is extremely complex and often utilizes multiple computer-controlled needles that are housed in units mounted to articulated robotic arms.

Stitching can be performed using various types of high strength threads of thermoplastic, glass, aramid or carbon fibre, depending on the application and amount of through-thickness reinforcement sought. Similar to various types of thread materials, various thread weights are available, the most commonly used in the range of 100-2000 tex (g/km) [65].

Various stitch angles (orthogonal and inclined) and patterns can be achieved using computer controlled equipment. The three most common locked-stitch patterns used are the 'lock stitch', 'chain stitch' and 'modified lock stitch', the most popular type being the modified lock stitch as it imparts the least degree of crimp on the reinforcement's in-plane fibres [18].

Stitch can be inserted into fabrics at varying stitch density, usually in grid patterns. Surface stitch densities of 1 to 25 stitches/cm^2 are common, equating to stitch volume fractions of roughly 0.1% to 10%, similar to those observed in woven 3D fabrics [65].

Stitching is performed on fabrics after weaving or following some degree of preform layup, hence stitching can be used for introducing an element of through-thickness reinforcement without restriction on preform fibre directionality. This allows the production

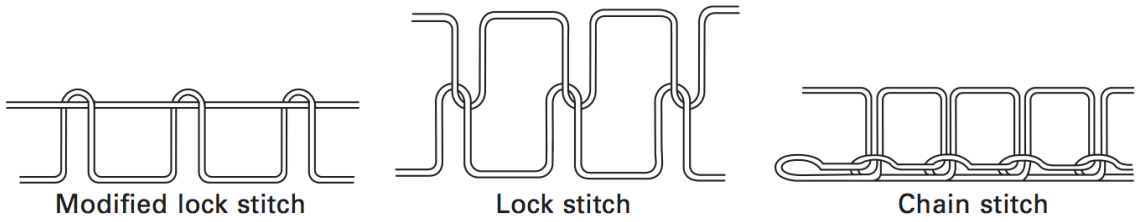

Figure 2.7: Common stitching patterns [65].

of through-thickness reinforced multidirectional laminates, and allows designers to introduce increased damage tolerance associated with the presence of Z-binders to laminates with in-plane mechanical properties that resemble those of conventional 2D fabrics. Additionally, restrictions in terms of the maximum preform thickness that may be stitched, approximately 40mm [68], rarely surface as a design concern.

2.5.3 Z-pinned 3D reinforcements

Z-pinning is a process which involves inserting pin-like reinforcing structures through the thickness of an existing preform or stack of fabric plies. Pins are usually made from extruded metal wire, or pultruded fibre composite, with pin diameters ranging from 0.15mm to 1mm [18]. Z-pinning can be performed on both prepreg and dry reinforcements though it is most commonly used with prepreg, as it currently is the only method by which through-thickness reinforcement can be applied to prepreg materials [65].

Many methods for inserting Z-pins exist. One of the popular methods for performing Z-pinning on prepreg materials is the UAZ® process, which uses ultrasonic compressive stress-waves to drive pins into the reinforcement. The ultrasonic waves agitate the partially cured resin in the surrounding area and cause local heating. This action softens the resin and eases the insertion of the pin [18]. Once all pins are successfully inserted any excess, protruding pin material is shaven off and the composite is processed either in an autoclave or in the case of dry reinforcements, through one of the available LCM processes.

Similar to stitching and tufting, Z-pinning can be performed off-loom on preassembled multidirectional reinforcements. This allows the production of composites with shear and torsional properties better than those obtained using 3D woven reinforcements, while

maintaing the elements of damage tolerance provided by the presence of a through-thickness reinforcement.

2.5.4 Tufted 3D reinforcements

Tufting is a process comparable to one-sided stitching, but performed using a single needle and thread. Structural thread is inserted in the through-thickness direction using a hollow needle that punches through the reinforcement. After the needle penetrates the entire thickness of the reinforcement it is withdrawn along the same path though which it was inserted, with tension removed from the thread. Friction between the inserted thread and the reinforcement fibres grips the thread, leaving it embedded in the material. The result is a non-locked stitch, similar in structure to that produced by a conventional sewing machine with a malfunctioning or empty bobbin, Figure 2.8. Turfing leaves excess, looped Z-binders on the underside of the reinforcement. The excess binder thread is either kept or shaved off prior to preform processing.

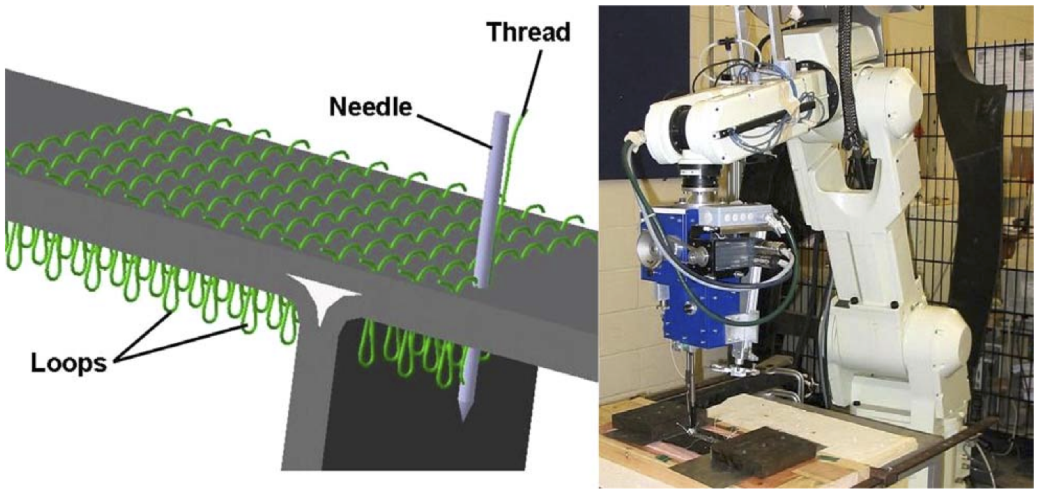

Figure 2.8: Tufted Z-direction reinforcement inserted into a T-section (left), robotic arm-mounted KSL KL150 tufting head (right) [69].

Tufting is a simple process, making it common and popular. It can be performed using relatively simple equipment. Minimal restrictions apply to possible reinforcement thickness, geometry or spatial orientation in which tufting can be performed.

Tufting typically uses high-strength yet highly flexible thread such as aramid or other organic-based filaments [65]. Brittle filaments made of carbon or glass are prone to micro-cracking failure when tightly bent around the needle, producing Z-binders with variable degrees of reinforcement and hence composites with unpredictable mechanical properties.

2.6 Automated composite layup

2.6.1 Tape laying

Tape laying is an automated process that was developed for fabricating components that are too large for manual tape layup or filament winding. Tape laying is performed using prepreg material in the form of thin tape, which is fed into processing machinery as a roll where each layer is separated with a paper backing. The efficiency of the process generally increases as component size grows and the prescribed lay-up sequences are simplified, Figure 2.9. As such, tape laying is typically well suited to the layup of large semi-flat panels such as aircraft aerodynamic surfaces, wing skins and fuselage bulkheads [57].

Tape is deposited using a robotic head that ejects the material while actively pressing it onto a substrate, which will later be used as the mould that will impart a shape to the component during processing. Tape laying heads are mounted to multi-axis, gantry-mounted articulated robotic arms [57]. Commercially available tape laying heads that are configured to lay flat components and are mounted to fixed-bed machines or open-bay gantries are known as flat tape-laying machines (FTLMs), typically exhibiting four degrees of motion. Commercial tape laying heads that are capable of laying components with mild contours that rise and fall at angles up to roughly 18^o are called contour tape-laying machines (CTLMs) [57].

Typically, component size and complexity are limited by the ranges of motion and articulation built into the gantry to which the tape laying head is coupled. Installations geared for production of aerospace components are usually quite large, with the ability to deposit tape within envelopes typically on the order of 40 ft $\times$ 20ft [71] and greater. However, once installed most gantry machines offer little to no possibility for expansion.

Tape laying machines are controlled using numerical control (NC) programming lan-

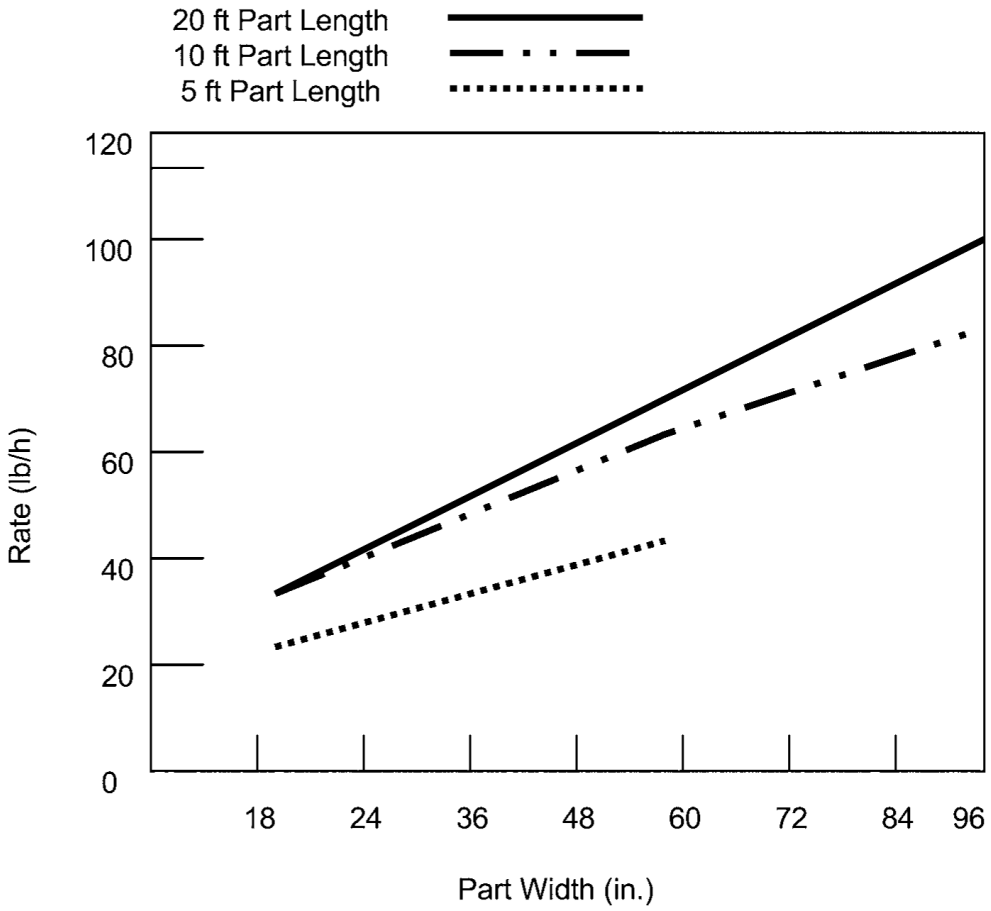

Figure 2.9: Tape-laying efficiency vs. part size [70]

guages, which consist of an ordered set of commands that directly instruct and coordinate the motion of each machine axis independently. Each NC program is specific to a given part geometry and must be compiled prior to beginning the tape laying process. Tape laying heads and gantry tracking equipment are usually constructed for precise motion, with positional certainty of the order of a few tenths of a millimetre (fractional-thousandths of an inch). Given this available precision, tape-laying equipment can be programmed for producing net-shaped components requiring no post-lay trimming.

Gantry NC machinery is capable of very rapid motion, but tape-laying heads are susceptible to problems such as jamming when pushed to high speeds, limiting the speed at which tape can be deposited, and increasing layup time. As such, deposition rates are low while the cost of automated tape-laying equipment remains high [71]. While

deposition rates can be increased by depositing tape of larger width, this is achieved at the expense of coarser deposition resolution. Simply put, by depositing tape as wide as 305 mm significant deposition speeds can be achieved; however, PMCs with greater geometric complexity and/or more complex lamination sequences often require the resolution provided by depositing much narrower tape, limiting layup speed [57, 71]. This is the case with both FTLMs and CTLMs as both types of devices are compatible with a variety of tape widths [57]. Figure 2.9 quantifies tape deposition rate in lb/h as a function of component size.

Tape-laying heads are extremely complex components. Modern commercial tape laying equipment often features a multitude of auxiliary feedback sensors and operator aids such as optical sensors that are capable of detecting process flaws in real-time and notifying the operator, as well as laser-projected boundary traces that allow the operator to verify correct placement of tape plies in real-time [57]. Furthermore, each head exhibits many axes of mechanical input to drive and control the functions necessary to make the process possible. For example, inputs are required to control the payout of tape from the supply reel. Similarly, tape is loaded into the tape-laying head on a paper backing that must be collected during deposition. As the thickness of the tape reduces after the reinforcement is ejected onto the tool surface, the take-up reel must revolve at a different speed than that of the supply reel, hence requiring input and control that is independent of the supply reel. Typically, mechanical input is provided to the head using stepper or servo motors and in some instances pneumatic actuators.

Prepreg tape is wound on a supply reel seen in Figure 2.10, that remains in the same frame of reference as the tape-laying head. As the prepreg tape is fed off the supply reel it passes through a cutter and then through a tape heater. Throughout this time the prepreg tape remains adhered to the paper backing. The cutter is configured so that it can separate the prepreg tape from the remainder of the supply stock while keeping the paper backing intact. Tape pre-heating elements are implemented on modern tape-laying machinery to raise the tape's temperature to around 25^oC - 45^oC. By preheating the tape, it becomes tacky and exhibits better tape-to-tool and tape-to-tape adhesion [57]. Tape pre-heating is accomplished using infrared radiation or solenoid valve-controlled forced-air heating, with sensors in place to monitor and control the tape's temperature [57]. Tape pre-heating is not said to effect the geometry of tape reinforcement noticeably, hence this can be accomplished after the tape is cut. This allows cuts to be made while the prepreg is still cold and hard, allowing an easier cut and reducing the accumulation

of tacky material on the cutting components.

As the tape-laying head moves on the surface of the tool, tape is fed from the supply reel through a tape guiding channel and to the tool's surface where it is actively pressed onto the manufacturing substrate or previously deposited tape. This pressure combined with the tackiness of the tape causes the tape to adhere to the substrate surface and plays a vital role in maintaining the position of the freshly deposited tape, reducing manufacturing flaws. As seen in Figure 2.10, the tape cutter is mounted at some distance from the tool surface. As a result the tape cutter is activated as the tape-laying head nears the end of a tape-laying sweep rather at the end of the path. Following the cut, the feed head must continue to traverse in order to clear the remaining tape that is separated from the supply stock, yet still within the feed-head. After the robotic head has finished depositing a strip of tape the head is repositioned for the next laying sweep.

After all tape-laying passes are completed, the tape is left on the substrate on which it was laid, which doubles as the tooling/mould used for processing the PMC component. Processing options are identical to those used with conventional hand-laid prepreg; in-autoclave processing or out-of-autoclave processing when component size or budget prohibits the use of an autoclave.

As tape laying is performed using prepreg it is well suited to the aerospace industry, which readily favours the semi-product. However tape laying can only be performed using prepreg, introducing need for storage, handling and processing equipment associated with the material, at a cost that is often prohibitive for smaller manufacturers.

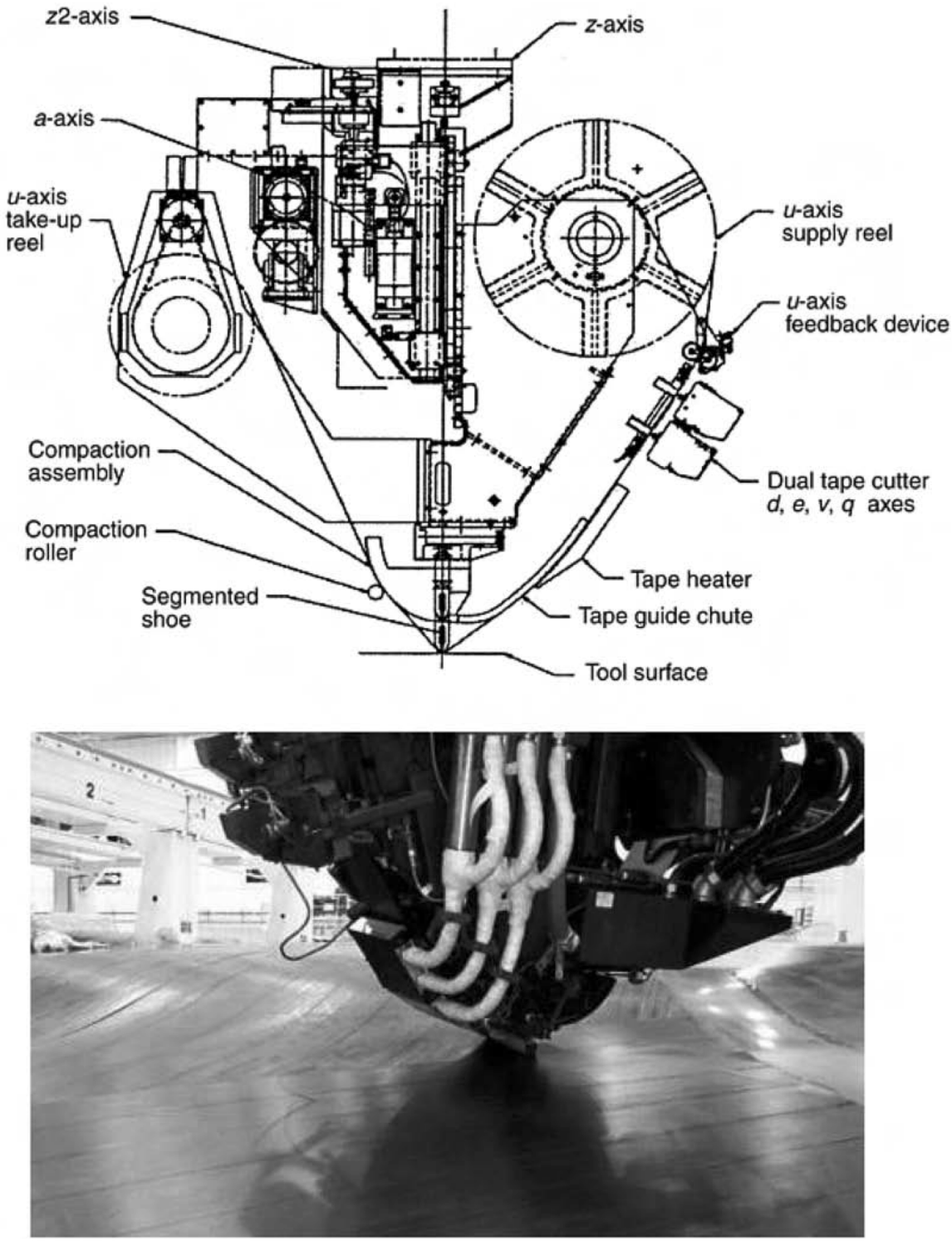

Figure 2.10: Tape laying head typical of flat tape-laying machines and contour tape-laying machines; top: schematic, bottom: image [57].

2.6.2 Advanced fibre placement (AFP)

Fibre placement can be described as a cross between tape laying and filament winding processes as it is often, but not always, performed by depositing material onto a substrate mounted on a spinning mandrel as seen in Figure 2.11.

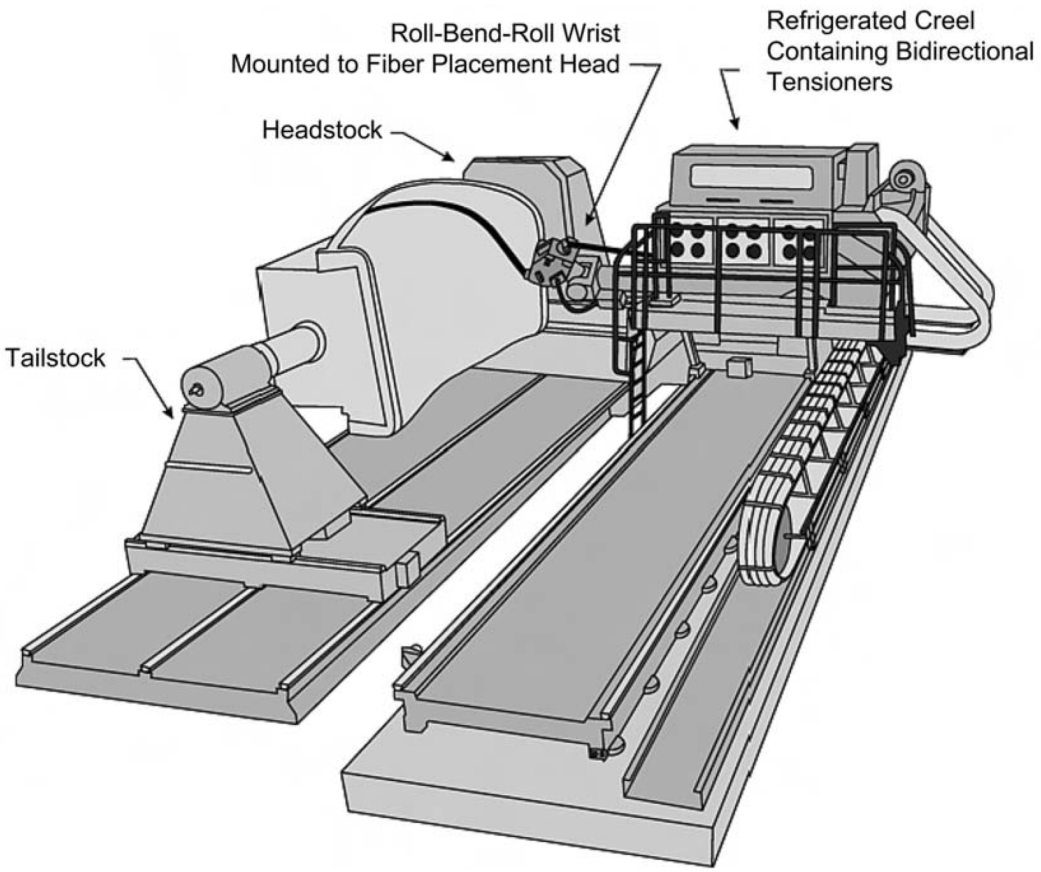

Figure 2.11: Towpreg fibre placement machine [72].

Fibre placement uses a material laying head similar to that used in tape laying, however instead of being loaded with a single wide strip of prepreg tape it is fed by 12, 24 or 32 thin strips of prepreg tow each approximately 3.175mm – 4.623mm in width (0.125" – 0.182") referred to as towpreg [57].

Tows can be controlled individually, allowing individual tows to be cut and added back. As such, AFP machines are capable of achieving the high deposition resolution

provided by the use of single strand tows, while remaining capable of rapid layup using simultaneous tow deposition. Furthermore, capability to disengage and reengage independent tows as they are needed contributes to significant reduction in material waste. Advanced fibre placement is commonly performed with scrap rates as low as two to five percent.

Fibre placement is capable of producing components with complex geometries and contours, including many geometries which are usually aimed at hand layup. Quintessential applications include C-channel spars, fuselage sections, engine cowls, inlet ducts, fan blades and nozzle cones [73]. The concavity that can be manufactured using fibre placement is limited by the diameter of the compaction roller which, similar to tape-laying, is used to force the tows onto the surface of the mould substrate, tacking them into place. In some instances large forces can be applied (up to 400 lbs) by the compaction roller to debulk the preform prior to processing [57].

Components manufactured by fibre placement are generally constrained to be greater than 10.2 cm (4") in length and no less than 5.1 cm (2") in concave radius by the geometry of the placement head [57]. Maximum component size is limited by the machine's overall size and tracking travel. Fibre placement machines are large. Setups capable of handling components up to 20ft in diameter and 70 ft in length are available, however, such equipment weighs well over 80,000 lb [57]. Fibre placement also caries the limitations associated with prepreg processing and storage, discussed in Section 2.3.1.

Overall, the largest disadvantages plaguing fibre placement operations are machine complexity, expense and low fibre deposition rates in contrast to conventional filament winding operations [57].

2.6.3 Dry fibre placement

The possibility of depositing reinforcing carbon fibres while in their dry configuration offers intriguing advantages. Similar to tape-laying and AFP operations, in despite of large capital equipment costs there are potential cost savings exist from reduced material waste and elimination of the preform tailoring process [73].

Dry fibre placement offers several unique advantages over tape-laying and AFP. The use of dry fibres eliminates difficulties associated with the use of prepreg, primarily in regard to storage and processing. Further, dry fibres show consistent behaviour in sub-

jection to temperature change, eliminating the need for pre-heating or chilling operations that increase prepreg tack and aid in cutting respectively [57]. Eliminating the systems responsible for such operations would reduce the overall complexity and cost of dry fibre placement equipment.

Dry fibres do not possess ability to adhere or tack like fibres pre-impregnated with a partially cured resin. As such, dry fibre placement is usually performed by depositing fibres onto a flat substrate, rather than on a mould of geometry similar to that of the finished component. The completed dry preform is subsequently formed into its contoured, three-dimensional shape during LCM-type processing, which imparts the intended geometry to the final component. As such, flat tow placement reduces tooling and set-up costs, simplifies preform handling and enables processing to be performed off site and/or at later time [73].

Dry fibre placement technology is generally viewed as proprietary; few if any commercial units are available for procurement [73].

2.7 Mechanical testing

2.7.1 Compaction

The behaviour of fabric reinforcements subjected to compaction normal to their plane is very important to many aspects of the processing of fibre reinforcements into PMC components. Compaction controls reinforcement permeability which largely dictates how resin flows through the reinforcement during processing [74]. It also controls the fibre volume fraction, which influences the mechanical properties of the PMC and it affects void content, which is important to certification of PMC components for aerospace applications [55, 75].

Numerous investigations into the behaviour of a fibrous material subjected to compaction have been published [76]. In 1946, C. Van Wyk published a study focused on the relationship between compaction pressure and fibre density [77]. Since then, much work has been published regarding the compaction behaviour of single and multilayered fabrics.

The compaction behaviour of a fabric material may be documented using a standard

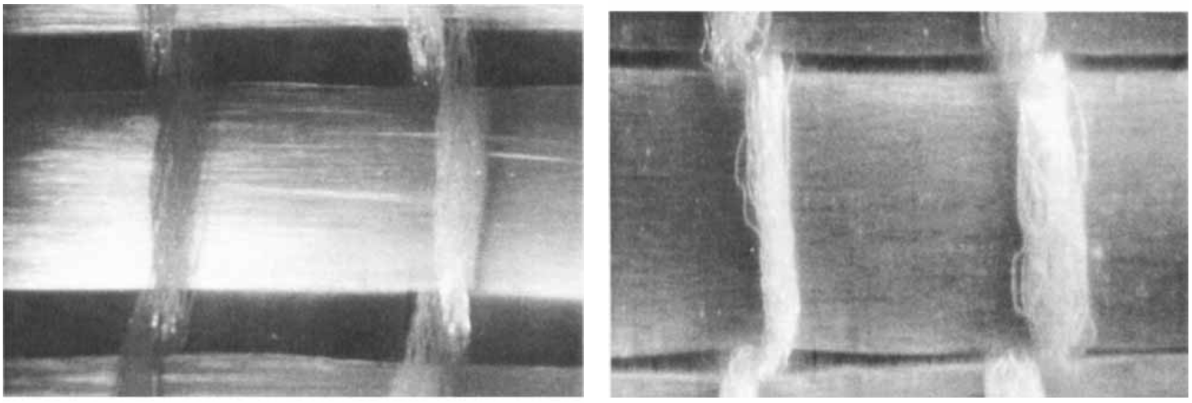

Figure 2.12: JB Martin 81 053 A fibre reinforcement at 22× magnification; (a) left: initial state; (b) right: after 51 compaction cycles at 1.0 MPa max pressure [75].

load cell coupled to rigid compaction platens with a known footprint area [74]. Generally, testing is performed by moving the platen onto the fabric at a constant displacement rate and recording the reaction force applied by the compacted fabric on the platen. Recorded values can be processed to display the fibre volume fraction to compaction pressure relationship after correcting for rig deflection. The compaction curve for a single fabric layer or for a stack thereof is non-linear and may be represented in three independent stages as displayed in Figure 2.13(b). The first linear section is attributed to intra-yarn fibre reorganization where the majority of gaps within yarns are reduced with relative ease. In the second non-linear region, fibre reorganization continues but the progressive reduction of gaps leads to a progressive increase in the compressive stiffness of the fabric. In the third region (said to begin at point $(2h_y, p_0)$ in Figure 2.13(b)) gaps within the fabric are much reduced and fibre reorganization is no longer possible [78]. Fibres can no longer be displaced and compressive stiffness grows rapidly and asymptotically [65].

Quantifying of the compaction behaviour of single-layer and multi-layer woven reinforcements is performed using identical test equipment and methods, and the same general behaviour is observed in both cases. However, the behaviour of woven multi-layer reinforcements is typically less consistent [65]. This is often attributed to nesting, a phenomenon where yarns within adjacent fabric layers reorganize to fit next to each other as illustrated in Figure 2.14.

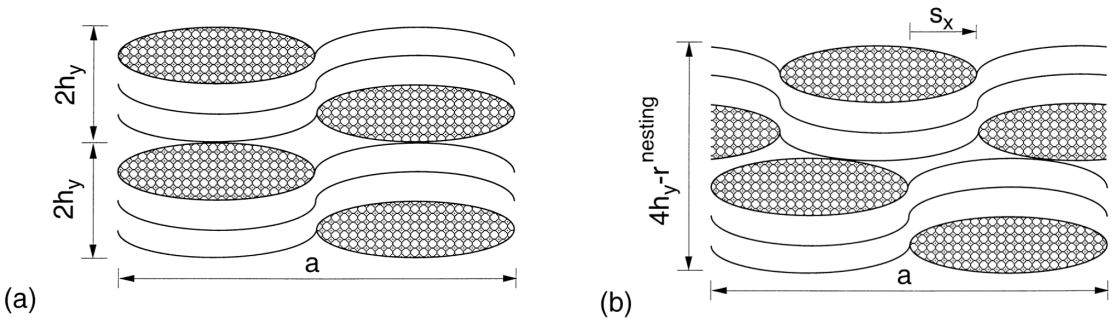

Figure 2.14: Unit-cell cross-section of two-layer woven fabric reinforcements showing stacking: (a) without nesting, (b) with nesting occurring [78].

Nesting does not modify the general behaviour of multi-layer reinforcements during compaction but it does influence quantitative results; initial reinforcement thickness and v_f values display much sensitivity to nesting [78] as shown in Figure 2.13(a). Nesting is dependent on the relative initial positioning and orientation of adjacent fabric layers within a stack of woven reinforcements. As such, nesting is difficult to control regardless of any efforts aimed at inducing or reducing it, and it remains a source of variation in quantitative observations made during compaction testing.

Successive compaction cycles can further reduce void content within the final component [75]. Generally, large gains in fibre volume fraction are made through a first few compaction cycles and gains diminish with each successive compaction cycle as seen in Figure 2.15. As the number of compaction cycles grows, gains from each successive cycle become negligible and a stable hysteresis loop is formed, which essentially repeats as a single stabilized compaction curve [65].

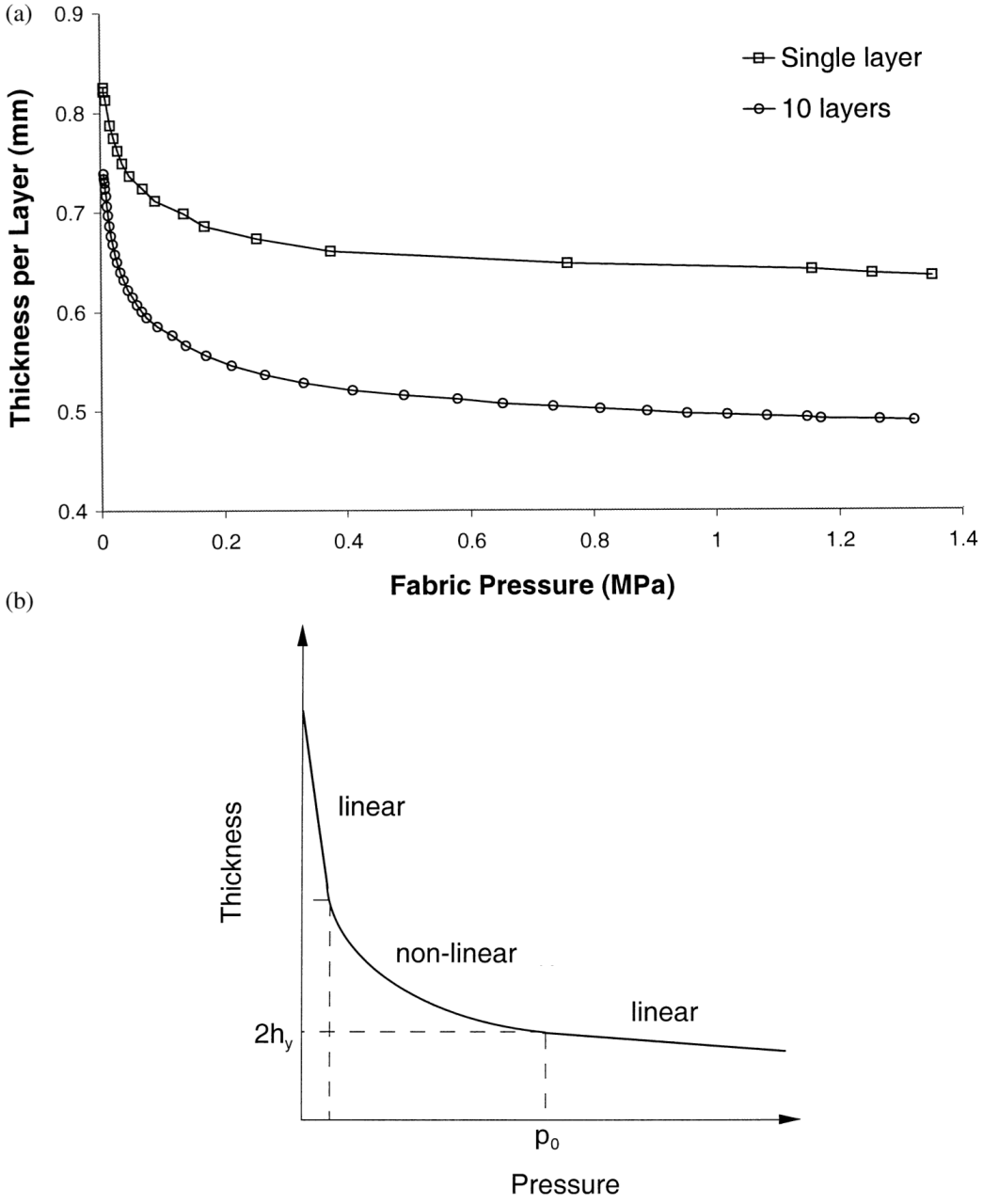

Figure 2.13: (a) Typical pressure–thickness curves of single and multilayer plain weave fabrics under compaction; (b) stages within a typical pressure–thickness compaction curve [79].

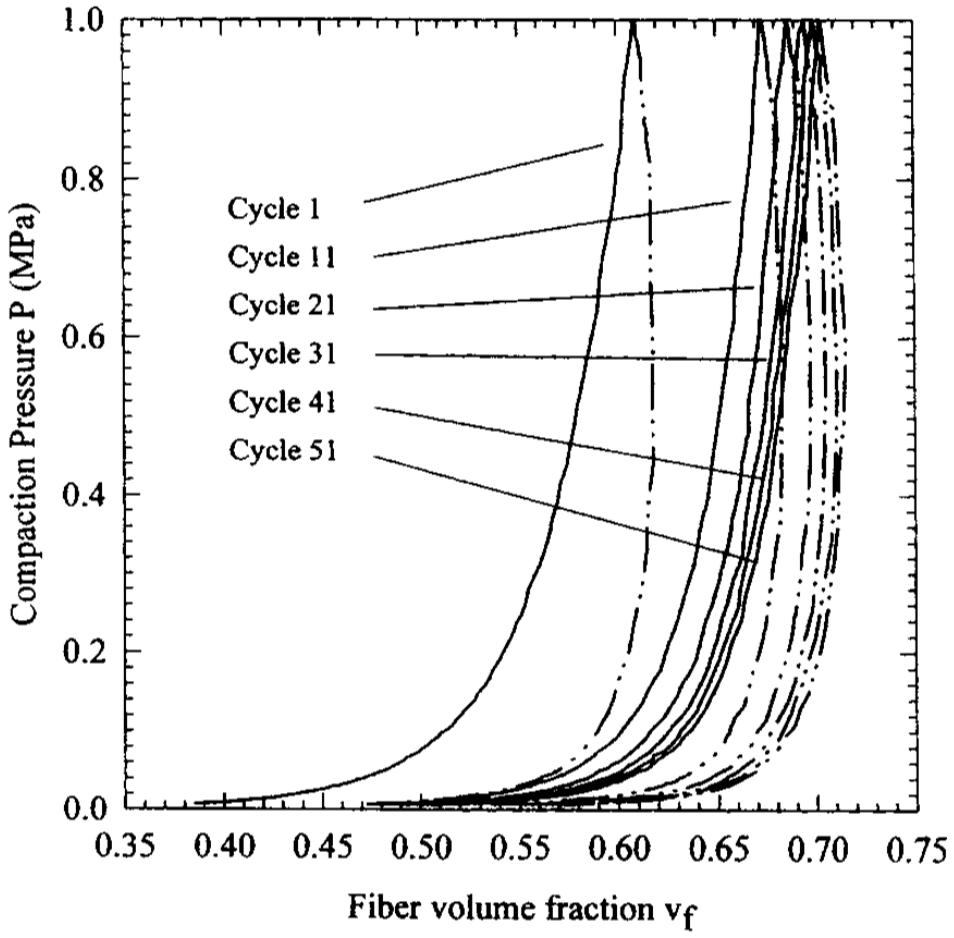

Figure 2.15: Typical compaction curve displaying cycles number: 1, 11, 21, 31, 41, 51 for a Owens Corning 24 oz Plain Weave compacted to 1.0 MPa [80]

2.7.2 In-plane Shear

Forming flat fibre reinforcements into PMC components that incorporate any degree of curvature will produce localized changes in fibre orientation, v_f and permeability. These variations will alter resin infiltration properties and induce non-homogenous mechanical properties within the PMC [81]. Forming reinforcements over more complex geometries, for example draping over surfaces featuring double curvature, will induce more significant changes within the reinforcement. The dominant deformation mode is inter-fibre in-plane shear [73, 81], though some degree of lateral fibre shift (inter-tow spacing) has also been observed [73].

Inter-fibre in-plane shear is defined as the rotation that may occur at yarn crossovers, between yarns that once intersected perpendicularly along their axes. It is measured and expressed as an angle which quantifies the angular displacement of the fibres from their perpendicular configuration [73].

Generally, if inter-fibre shear is allowed to progress beyond some limit known as the shear locking angle, yarns in the reinforcement will respond by locking, disallowing any further shear deformation to occur. At this point, any further shear deformation will result in yarn buckling, causing the reinforcement to wrinkle and eventually leading to the production of a defective component [73].

In laboratory testing, fabrics are deformed in in-plane shear using a load cell device to measure the force required for the deformation. Plotted results of such tests reveal a general response curve referred to as a classical non-linear shear curve, Figure 2.16. The classical non-linear shear curve can be subdivided into three phases: the first corresponds to small shear angles typically up to 30^o where yarn rotation occurs with relative ease and the majority of force required to shear the fabric is due to overcoming frictional forces between yarns. In this phase the shear force required is minimal. The onset of the second phase takes place when gaps between yarns begin to close and lateral contact between yarns begins to occur locally. In subsequent deformation yarns continue rotating, but their progressive displacement results in further closing of the gaps within the fabric and generates more extensive lateral contact between yarns. The progressively growing number of yarns in lateral contact with one another is met with a progressive increase in the force required to perpetuate shear. Hence, the second part of the classical non-linear shear curve is said to be a transitionary phase between the quasi-linear first phase and the highly non-linear third phase. The third phase of the non-linear shear curve is initiated

at the shear locking angle, which is the angle at which most gaps within the fabric have been eliminated and lateral contact between yarns has progressed to a state of lateral compression [65]. Any further shear deformation will cause the fabric to wrinkle.

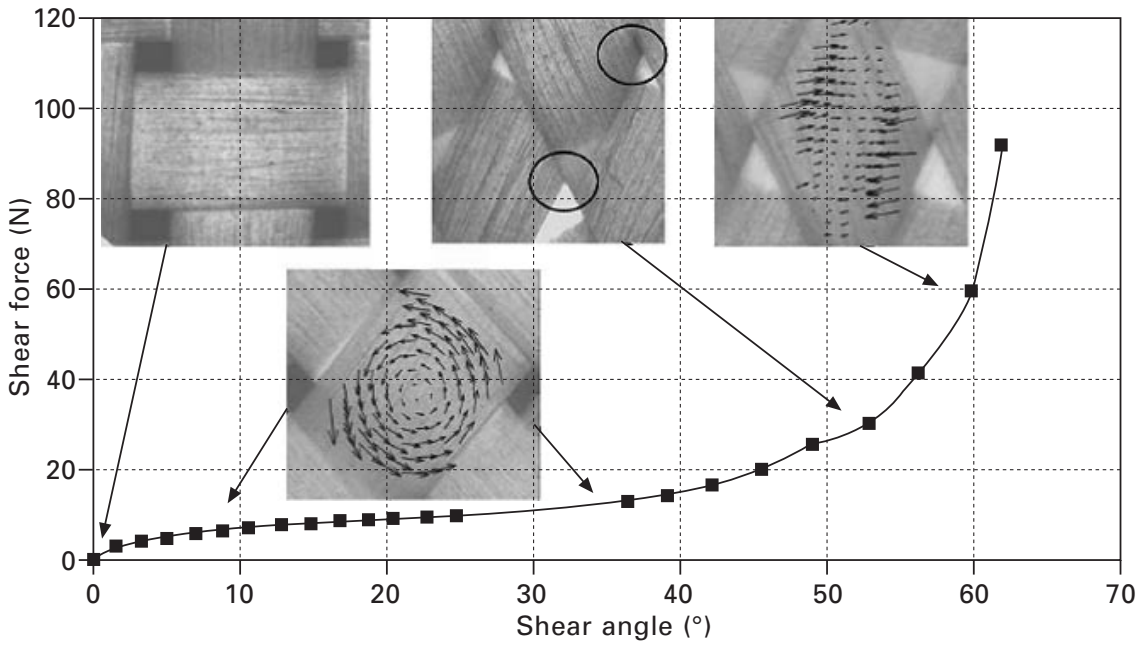

Figure 2.16: Classical non-linear shear curve; the top three images correspond to optical observations made within the three subdivided phases within [65].

Bidirectional fibre reinforcements can tolerate relatively high levels of in-plane shear, typically 10^o - 60^o [81] prior to the onset of wrinkling, with limits varying with fabric construction and characteristics. Generally, loosely woven reinforcements and satin weaves with higher harness numbers can withstand greater in-plane shear prior to the onset of lockup [81]. Figure 2.17 presents a set of images depicting various types of woven fabrics in their unsheared state and at their lock angle.

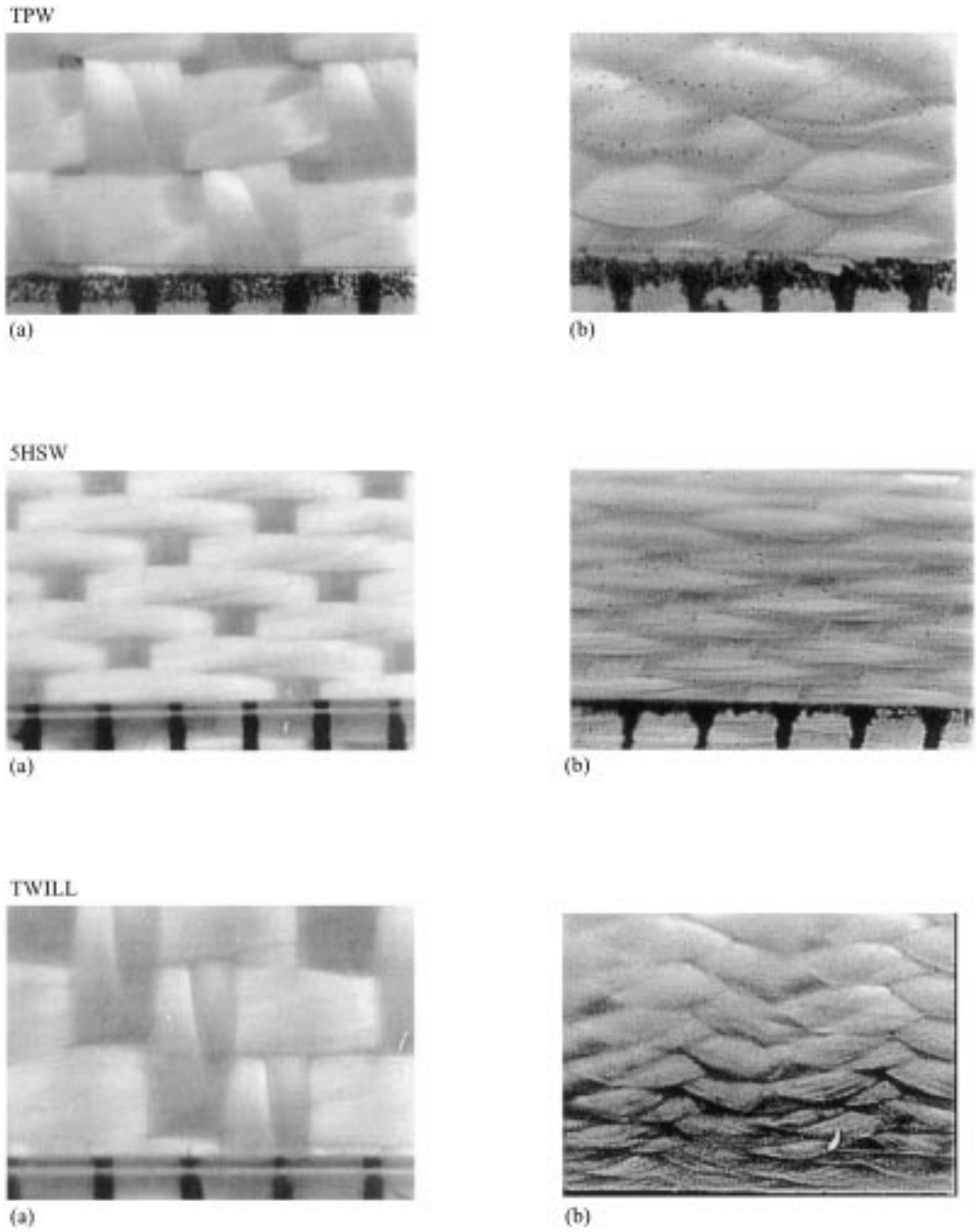

Figure 2.17: Change in microstructure from (a) unsheared state to (b) shear locking angle for various types of Fothergill woven fabrics: 'TPW'–Y0212 tight plain weave at 61^o; '5HSW'–Y0227 5 harness satin weave at 26^o; and 'TWILL'–Y0185 twill weave at 25^o [81].

2.7.3 Bending of textile preforms

Consideration of the bending behaviour is important for assessing preform drapability, and so it has a major effect on part manufacturability and part design, especially for thick textiles. The bending behaviour dictates much about how a fabric can be shaped from its initial flat state into a complex shell geometry.

Classical material and mechanical theories can be used for modelling the bending of isotropic materials. This is common practice when designing components to be manufactured using sheet-metal forming operations. On the other hand, textiles are highly anisotropic in nature and more importantly they are discontinuous, with fibres subjected to compressive stresses and strains at risk of buckling under relatively light loading; hence classical continuum mechanics cannot be used for modelling those materials in similar forming operations without making major assumptions and oversimplifications. A study by Yu et al. compared values for textile bending stiffnesses obtained experimentally and numerically. Numerical values were generated using only in-plane mechanical properties of the textile. The comparison revealed that values obtained numerically were unrealistically high, and that the bending stiffness cannot be derived solely from in-plane mechanical properties [82].

The textile bending behaviour can be evaluated at the macroscopic scale using testing apparatus and standards developed specifically for fibrous materials, namely the cantilever bending test (ASTM D1388), the Kawabata bending test (KES-FB2) and the new cantilever test proposed recently by de Bilbao et al. which uses a digital camera to better record the deflection of a cantilevered textile mounted in jig similar to that used in the aforementioned ASTM method [83]. The ASTM cantilever bending test uses the linear elastic theory to determine an equivalent bending stiffness at various bend radii [65]. The Kawabata pure bending test enables non-elastic behaviour to be accounted for, aiming at measuring the bending moment produced directly as the sample is deformed continuously to progressively smaller bend radii [84]. A diagram showing the mounting and path of a sample within a Kawabata testing machine can be seen in Figure 2.18.

Adopters of Kawabata pure bending equipment have reported problems with the apparatus which include lacking precision at small bend radii, variations stemming from sample loading and general variation within identical samples [84]. Furthermore, the Kawabata pure bending apparatus is incapable of testing samples to bend radii less than

2.5 cm^{-1} in magnitude [65].

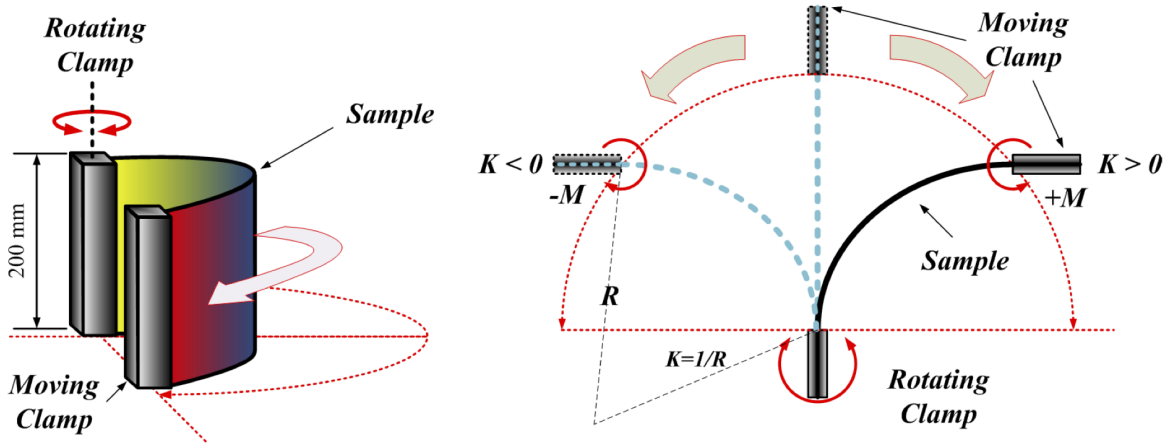

Figure 2.18: Kawabata (KES-FB2) pure bending testing method. [84]

2.8 Automation

2.8.1 The 'G' programming language

The 'G' programming language, which is simply referred to as g-code, is a popular and widely used programming language implemented in automated numerical control (NC) systems. The language allows humans to communicate and instruct machinery on necessary actions that must be carried out in order to complete a task. Instructions are broken down into ordered and structured sets of commands, for the machinery to follow step-by-step.

G-code and NC have military and aerospace roots, originating in a time similar to carbon fibre composites, the early 1960s. After punch-card computers were used for demonstrating numerical path interpolation, the technology was implemented into NC equipment and used in production of accurate and precise airfoil patterns. In present day,

elements of early computing such as program demarcates and program-end/tape-rewind instruction cues remain nested within modern G-code language.

G-code is regarded as the standard language in present day automated manufacturing. It is deeply nested within computer-aided design (CAD)/computer-aided manufacturing (CAM) manufacturing. It is found in all types of automated manufacturing, appearing in CNC machining centres, automated water-jet/plasma/oxyacetylene cutting equipment, robotic welders, 3D printers as well as large industry assembly plant equipment.

2.8.2 NC-code & G-code generation

Contemporary G-code is written in the form of electronic plain text. A typical program can contain as few as 10 lines of code in very simple operations or many hundreds of thousands of lines in more complex operations. Program size is typically limited by writing time and storage medium memory.

Simple code can be generated manually. However, it is often performed with assistance from a computer utility (wizard). This is adequate for NC equipment purposed to perform simple repetitive tasks, typical of custom assembly-line machinery which is rarely reprogrammed.

3D printers and machining centres are capable of manufacturing components with significant geometric diversity at high turnover rates, requiring frequent, lengthy and complex NC code generation. As such, semi-autonomous code writing utilities ('post-processors') were created. Post-processors are programs written to interface with a CAD software package and translate the physical and geometric information into a complete NC program for manufacturing the physical component. Post-processors have limitations; they are highly machine specific, they still require a high-level of manual involvement and typically they are only readily available for brand-name commercial NC machinery. Additionally, generated code must be verified before it is run, ensuring that it will not prescribe a motion that may damage the machine. Hence the development of customized automated NC machinery which aims at manufacturing components with large geometric part-to-part diversity is met with challenges that extend well beyond the design of the physical machinery.

2.8.3 Elements within the G-code language

G-code language[1] is based on discrete lines of code where each line is referred to as a block and a program is a complete collection of blocks. Each block may contain one or more instructions; however each block may contain only one instruction from each discrete modal group, Table 2.1.

A complete instruction is made of a word, sometimes followed by axis designations and corresponding numbers. A word is any letter other than N, A, B, C, D, V, U, W, X, Y, Z which denote line numbers and axes labels, concatenated with a real integer value between 00 and 99 [85]. A number is any positive of negative real value. An example of a complete instruction is:

N04 G00 X0.5 Y10.5

where N04 denotes the 4th block in the code, the word G00 requests a rapid motion to a position 0.5 along the X axis and 10.5 along the Y axis.

Possible words are sorted within modal groups such that each block may contain only one word from each modal group. A key summary of modal groups relevant to this thesis is presented in Table 2.1. Similarly Table 2.2 displays a summary of various key G-code words and examples of their use in blocks.

[1] G-code discussed and implemented within this thesis follows the National Institute of Standards and Technology RS274NGC Interpreter - Version 3 specification.

Table 2.1: Summary of key G-code modal groups [85].

Group	Words	Description
	G words	
1	G0, G1, G2, G3, G38.2, G80, G81, G82, G83, G84, G85, G86, G87, G88, G89	Motion
2	G17, G18, G19	Working plane selc.
3	G90, G91	INC./ABS. coordinate sys.
5	G93, G94	Feed rate mode
6	G20, G21	Units
7	G40, G41, G42	Cutter radius comp.
8	G43, G49	Tool length offset
10	G98, G99	Canned cycle return mode
12	G54, G55, G56, G57, G58, G59, G59.1, G59.2, G59.3	Coord. system selc.
13	G61, G61.1, G64	Path cntrl. mode
	M words	
4	M0, M1, M2, M30, M60	Stop/halt/pause
6	M6	Tool change
7	M3, M4, M5	Spindle Speed/Dir
8	M7, M8, M9	Coolant
9	M48, M49	Feed speed override
	Non-modal words	
0	G4, G10, G28, G30, G53, G92, G92.1, G92.2, G92.3	

Table 2.2: Summary of the key elements of the G programming language.

Code	Translation	Example	Description
G00	Rapid motion	G00 X1.25 Y2.375	Rapid linear motion at traverse feed rate. To only occur at the safe height.
G01	Linear feed	G01 X1.25 Y3.75 F100.0	Linear feed at the prescribed feed rate 'F'.
G02/G03	Arc feed (CW/CCW)	G02 X2.0 Y0.0 R2.0	CW arc feed - radius 2.0 at centre (2,0).
G17/G18/G19	XY/XZ/YZ-plane selc.	G17	Select XY plane
G20/G21	Inch/mm selc.	G20	Select inches
G90/G91	Abs./inc position	G90	Select Abs. coord. sys.
F	Set feed rate	F20.0	Feed rate = 20"/min

2.8.4 Motors

NC systems typically rely on electric motors for rotary actuation. The two most common electric motors used are stepper motors and servomotors.

Stepper motors, simply referred to as steppers, are capable of providing mechanical input with good positional accuracy without the use of a position feedback sensor. As such, their ability to operate in open-loop configuration allows for their inexpensive implementation, at the expense of absolute positional certainty. Once initial position is registered a stepper motor can be instructed to move to a new relative position by transmitting a number of pulses to the motor; each pulse is called a step and corresponds to a discrete angular distance. The speed of the motor is directly controlled by the pulse frequency sent to the stepper. The machine control unit (MCU) computes the new position of the stepper by adding the motion requested to the previous known position, but without the presence of a feedback sensor the MCU cannot verify and must assume that every pulse sent to the motor was successfully translated into a corresponding motion. In situations where the torque provided by the stepper surpasses that required for motion this assumption is valid and capable of maintaining good positional accuracy within the system. However, if the available torque is overcome by that required (for example a large acceleration of a sizeable inertial load) the stepper motor will skip, leading to a discrepancy between the position recorded by the MCU and the actual position of the stepper. Repeated occurrences of this will compound to large positional errors and may damage the machinery by causing motions beyond physical machine limits or stationary machine elements, called a crash, if left uncorrected.

Hence, stepper motors are most suited for use in applications where the available torque continuously surpasses the required torque; however one cannot guarantee that this is always the case and hence various actions may be taken to ensure safe implementation of steppers. For example, if the total actuation distance is minimal, limited opportunity exists for positional errors to become large. Similarly, stepper-driven systems may be returned ('homed') to a known parking position, where the absolute position may be verified and corrected. Homing provides reliable position error correction, but it requires commandeering the erred system, often leading to interruption of machine operations. Systems that provide intermittent service to NC machines have expendable blocks of non-operation time during which homing correction can be performed without interrupting the whole of machine operation.

Servomotors, simply referred to as servos, are essentially open-loop electric motors coupled with a position feedback sensor. Their closed-loop design allows for rotary actuation with precise velocity and acceleration control, at the expense of greater cost and complexity. As servos are more expensive, their implementation is generally reserved for applications requiring continuous and absolute positional certainty or applications where the required torque may intermittently spike or exceed the capacity of stepper motors.

2.8.5 Microstepping

Microstepping is a technique that is implemented in an effort to increase the resolution of a stepper motor, often far beyond the natural ($\approx$ full-step $\sim$ 200 step/rev) resolution. Microstepping is typically performed by splitting a full motor step into halves, quarters, eights or sixteenths to increase the stepper resolution two-fold, four-fold, eight-fold, or sixteen-fold. This is respectively referred to as half-, quarter-, eighth- and sixteenth-step microstepping.

Microstepping is accomplished by controlling the electric current flowing through each phase within the motor at a finer resolution; doing so increases the quantity of discrete electric current levels possible within each phase and enables simultaneous excitation of multiple phases. By exciting multiple stator phases simultaneously the rotor's poles are able to find equilibrium at positions between full steps, increasing the number of steps and detent positions within the motor [86].

While microstepping increases the resolution of a stepper motor, it carries at a major drawback: a severe resolution–accuracy tradeoff. As the number of microsteps per full step grows, the motor's positional accuracy becomes increasingly problematic. Table 2.3 shows the positional resolution and corresponding accuracy of a 200 steps/rev motor with a full step accuracy of $\pm$ 0.05^o/step operating at various levels of microstepping.

Table 2.3: Positional accuracy of the microstepping technique given a stepper motor with 200 step/rev. and an accuracy of $\pm 0.05^o$.

Micro-stepping	Resolution (deg/step)	Accuracy (±%)
Full	1.8	2.8
Half	0.9	5.6
Quarter	0.2250	22.25
Eighth	2.8125E-2	177.8
Sixteenth	1.7578E-3	2844.4
32^{nd}	5.4931E-5	91022.2
64^{th}	8.5830E-7	5825422.2
128^{th}	6.7055E-9	745654044.4
256^{th}	2.6193E-11	190887435377.7

Chapter 3

Mechanical Testing of Stitched Carbon Preforms

3.1 Context: The CRIAQ COMP-501 project

As part of the CRIAQ COMP-501 project, several industry parties and members from educational institutions gathered to assess the feasibility of producing aerospace secondary structures with through-thickness reinforced preforms and VARTM processing, a method discussed in Section 2.3.2.2. A structural member with a T-shaped cross-sectional profile was proposed by industrial partners and later decided upon. Figure 3.1 displays the cross-sectional geometry and dimensions of the T-section demonstrator.

Several lamination sequences were put forth for reinforcements to be used in the project. These are outlined in a document titled 'Def_laminates.pdf' by ETS MASc candidate C. Leduc, found on page C.1, Appendix C. It was proposed that these reinforcements would be assembled and reinforced using a structural carbon stitch, inserted using a Keilman® one-sided stitching machine operated by Centre des Technologies Textiles (CTT), St-Hyacinthe, QC. Manufacturing specifics regarding assembly sequence as well as stitch position, density and direction that would yield the most efficient assembly process remained to be discussed, at the time of writing, as the project is ongoing.

An investigation into at the effect of stitching on the properties and forming behaviour of the selected reinforcement was launched prior to instituting an assembly procedure for the demonstrator. This investigation aimed at answering questions regarding the effect of stitch density and pattern on local fibre volume fraction as well as, the effect of multiple compaction cycles on the reinforcement and stitch. This was investigated

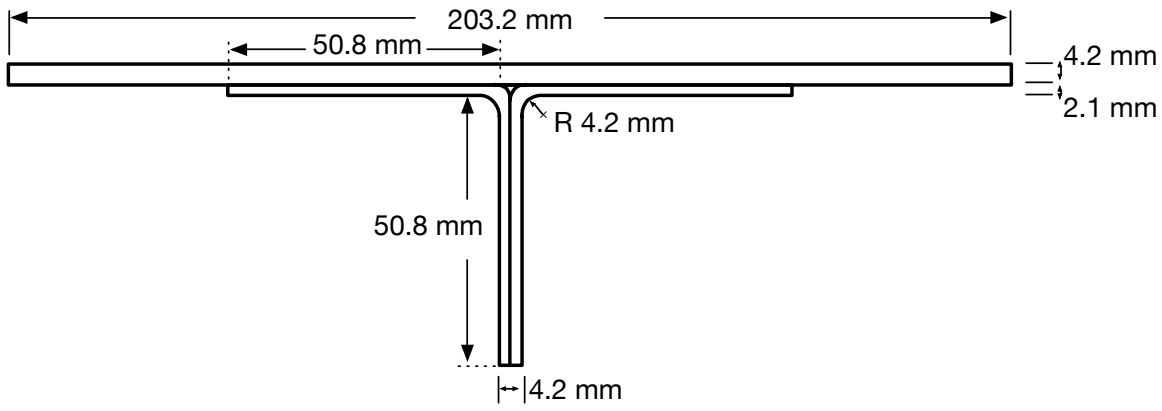

Figure 3.1: Cross-sectional geometry of the T-section demonstrator part.

in a series of compaction tests, outlined in Section 3.3. Questions about the ability of the stitched reinforcement to be formed in shear and about a bend arose and similar investigations were carried out to asses those characteristics. Those investigations are outlined in Sections 3.5 and 3.4 respectively.

3.2 Materials and apparatus common to compaction, shear and bending experiments

All mechanical testing was performed using a Instron 4482 100 kN universal testing frame. In all instances an Instron Series 2525-806 - 1 kN load cell was used for measuring rig loading. This cell is capable of measuring loads up to $\pm 1kN$ with an accuracy better than the larger of $0.25N$ or 0.25% of the measured load [87].

Extensive photographic evidence was captured to document the samples prior to and following the tests. In instances where the view of the sample was not obscured during testing, video recordings or time-lapse photo series were constructed. The photographic equipment used for documenting is listed in Table 3.1.

Unless otherwise noted, preforms used in the following tests were constructed using the *'Quasi'* 20 layer lamination sequence defined as $[((\pm 45)/(0/90))_5]_S$ by C. Leduc's document titled 'Def_laminates.pdf, found on page C.1, Appendix C. All preforms were constructed with TC-06-T 6.2oz/yd^2 carbon weave provided by JB Martin. The preforms were stitched using a Keilmann® RS 530 two-needle stitching head and two 67 tex (g/km)

Table 3.1: Summary of photographic equipment used during testing.

Quantity	Item
1	Nikon D600 FX camera
1	Nikon D5100 DX camera
1	Nikon 60mm f/2.8 AF-S G Micro-Nikkor lens
1	Nikon 24-85mm f3.5-5.6 AF-S G lens
1	Nikon SB-700 iTTL flash
1	Manfrotto 055XPROB horizontal tripod
1	Manfrotto 454 micro positioning plate
1	Helicon Focus Optical CT Software

structural carbon fibre thread. Samples were stitched with a 25.4 mm stitch width and 4mm or 8mm stitch pitch, Figure 3.2.

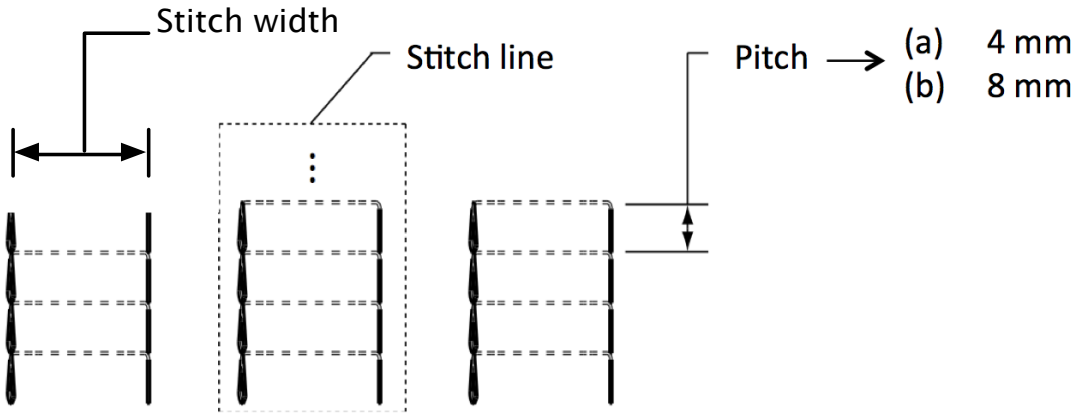

Figure 3.2: Intra-stitch geometry; dotted stitch line represents the stitch axis [88].

3.3 Effect of compaction on CRIAQ COMP-501 preforms

3.3.1 Justification

The ability of a preform to be compacted in the through-thickness direction is of crucial importance to several aspects of PMC manufacturing. Compacting a fibrous preform causes gaps within the fabric to close, and the fibres within to reorganize in a more orderly structure. This reorganization results in increased v_f, which in turn can yield a component with superior structural properties. However, as a consequence, compaction decreases the permeability of a preform and leads to increased challenges in processing stages of manufacturing[1].

The CRIAQ COMP-501 project implements thick preforms which are reinforced in the through-thickness direction by a structural, heavy carbon stitch, discussed in Section 3.1. These preforms are processed using VARTM, hence prior to infusion they are compacted to a pressure equivalent to the atmospheric ambient. As such, compaction testing was performed to 1 bar final pressure.

Compaction tests were performed to uncover the maximum v_f achievable with the COMP-501 fabrics, and to asses the effect of the reinforcing stitch on local v_f.

3.3.2 Apparatus

The apparatus used to perform compaction testing is summarized in Table 3.2 and includes the apparatus discussed in Section 3.2.

Table 3.2: Summary of apparatus used in compaction testing

Item	Quantity
Compaction platens	2
Sample support table	1
Assorted 0.127 mm (0.005”) and 0.025 mm (0.001”) shims	-

Samples were manufactured from JB Martin carbon style TC-06-T. A data sheet as

[1]The importance and effect of compaction is discussed in Section 2.7.1

produced by JB Martin is included in Appendix C. A summary of properties is provided in Table 3.3 and an diagram of sample geometry is shown in Figure 3.3. Larger samples featuring stitches in different configurations were subjected to compaction tests at a number of locations sufficient for quantifying variability.

Table 3.3: Compaction sample details.

Parameter	Value	Unit	Symbol
Weave	2×2	Twill	-
Warp/weft ratio	50/50	% by mass	-
Surface weight	205	g/m^2	-
Fibre density	1760	kg/m^3	ρ_c
Ends count	13.0	in^{-1}	-
No. of plies	20	plies	-

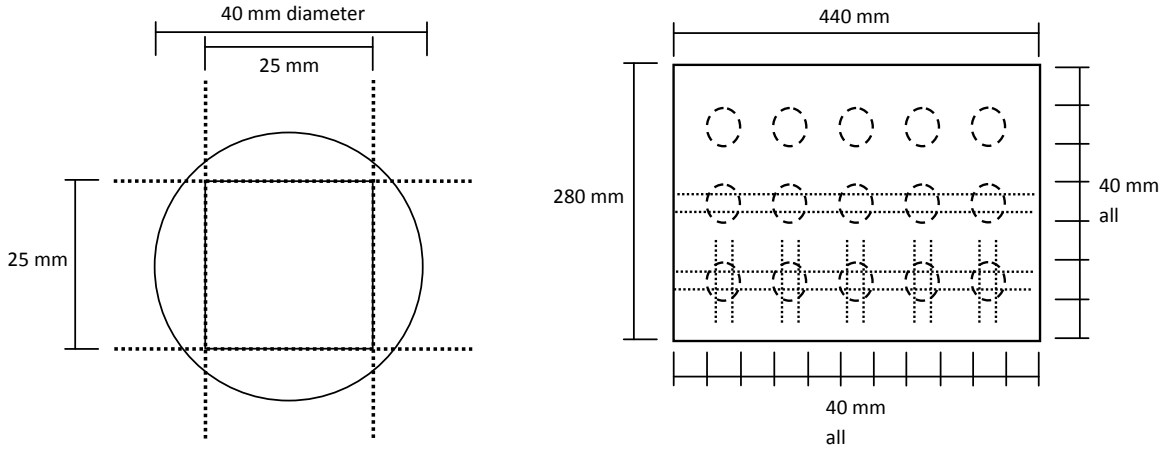

Figure 3.3: Left: Platen Footprint. Solid and dotted lines represent stitch lines. Right: Compaction sample geometry. Circles represent platen footprint and lines are representative of stitch lines.

3.3.3 Procedure

Each sample was divided into several graphic areas centred about each test site. Prior to testing, each plot was photographed at different focal lengths for 3D CT reconstruction, and 2D focus stacked image generation with Helicon® Focus software. The position of the test patch and the area captured by each frame was then documented in a wide view image of each sample. Figures 3.4 and 3.5 show the respective frontside and backside of each test plot site; for example, areas 'A2' and 'B2' are respectively the front and back of the same test site. The white boxes that enclose each sample label outline the area and frame limits of the photo-documentation captured prior to testing. The arrow printed within each plot area is used for showing the orientation of the camera during capture; a similar arrow exists on a keyframe captured for each plot and can be used to ensure the alignment of images before and after. All plot overview images can be found in larger size and detail in Appendix A.1.

In an effort to minimize any defects that may be introduced by handling of the sample preforms, the face that was visible upon reception was photographed first and designated to be the frontside. The samples were then flipped gently and the backside was photographed, after which they were left backside up. It was decided prior to testing that samples need not be flipped frontside up in order to perform testing, hence any data, imaging and results generated after testing bear a name corresponding to the face of the sample visible during testing.

Prior to testing, the load cell and compaction platens were loaded into the Instron testing machine. A sample support level with the lower compaction platen allowed testing to be performed without separating each sample test site from the sample stock, which reduced handling-induced defects and stitch unravelling caused by cutting. The Instron testing frame fully configured for testing is shown in Figure 3.6.

Figure 3.6: Instron testing frame configured for compaction testing. Left: sample support table fitted ∼2.5mm below bottom compaction platen. Right: Sample stock loaded in testing frame prior to test.

A feeler gauge was used for checking the uniformity of the gap between the top and bottom compaction platen. Shims were inserted under the bottom platen until the top and bottom platens were parallel. Full compaction load was applied to the platens before they were checked again with the feeler gauge. Following setup, a set of four dry tests (no sample inserted) were performed to obtain the stiffness of the platen setup, later to be used for removing apparatus deformation from raw sample compaction data. Testing was performed using the parameters summarized in Table 3.4.

Table 3.4: Compaction test parameters.

Parameter	Value	Unit
Compaction rate	5	mm/min
Final compaction pressure	1	bar
Platen diameter	40	mm
Platen area	1.2566×10^{-3}	m^2
Final compaction force	125.66	N
DAQ Frequency	10	Hz
Hold time	60	s
Cycles per sample	5	-

Testing begun with inserting the sample between the platens and running the compaction sequence, whereby the sample was compacted at a rate of 5 mm/min to a final

pressure of one bar. When final pressure was reached, compaction was halted for 60 seconds at the current displacement, after which the platen was retracted and data was saved as a '.CSV' file. The test was repeated four more times for a total of five cycles per test area. Following each completed set of cycles the sample was removed, examined and the footprint caused by the platens was marked using a labeled leaflet. Images were captured in order to document defects incurred or arising anomalies. The process was repeated for each of the 23 sample area summarized in Table 3.5.

A summary of the plot areas used in testing is shown in Table 3.5.

Table 3.5: Summary of samples tested in compaction.

Backside	Frontside	Preform	Stitch pitch (mm/stitch)	Stitch Pattern
B1	A1	700-0005-P4	0	CAMERA TEST AREA
B2	A2	700-0005-P4	4	Superimposed
B3	A3	700-0005-P4	4	Superimposed
B4	A4	700-0005-P4	4	Superimposed
B5	A5	700-0005-P4	4	Superimposed
B6	A6	700-0005-P4	4	Superimposed
B7	A7	700-0005-P4	4	Single
B8	A8	700-0005-P4	4	Single
B9	A9	700-0005-P4	4	Single
B10	A11	700-0005-P4	4	Single
B11	A11	700-0005-P4	4	Single
D1	C1	720-0006-P8	8	Superimposed
D2	C2	720-0006-P8	8	Superimposed
D3	C3	720-0006-P8	8	Superimposed
D4	C4	720-0006-P8	8	Superimposed
D5	C5	720-0006-P8	8	Superimposed
D6	C6	720-0006-P8	8	Single
D7	C7	720-0006-P8	8	Single
D8	C8	720-0006-P8	8	Single
D9	C9	720-0006-P8	8	Single
D10	C10	720-0006-P8	8	Single
E1	-	720-0006-P8	-	Sans
E2	-	720-0006-P8	-	Sans
E3	-	720-0006-P8	-	Sans

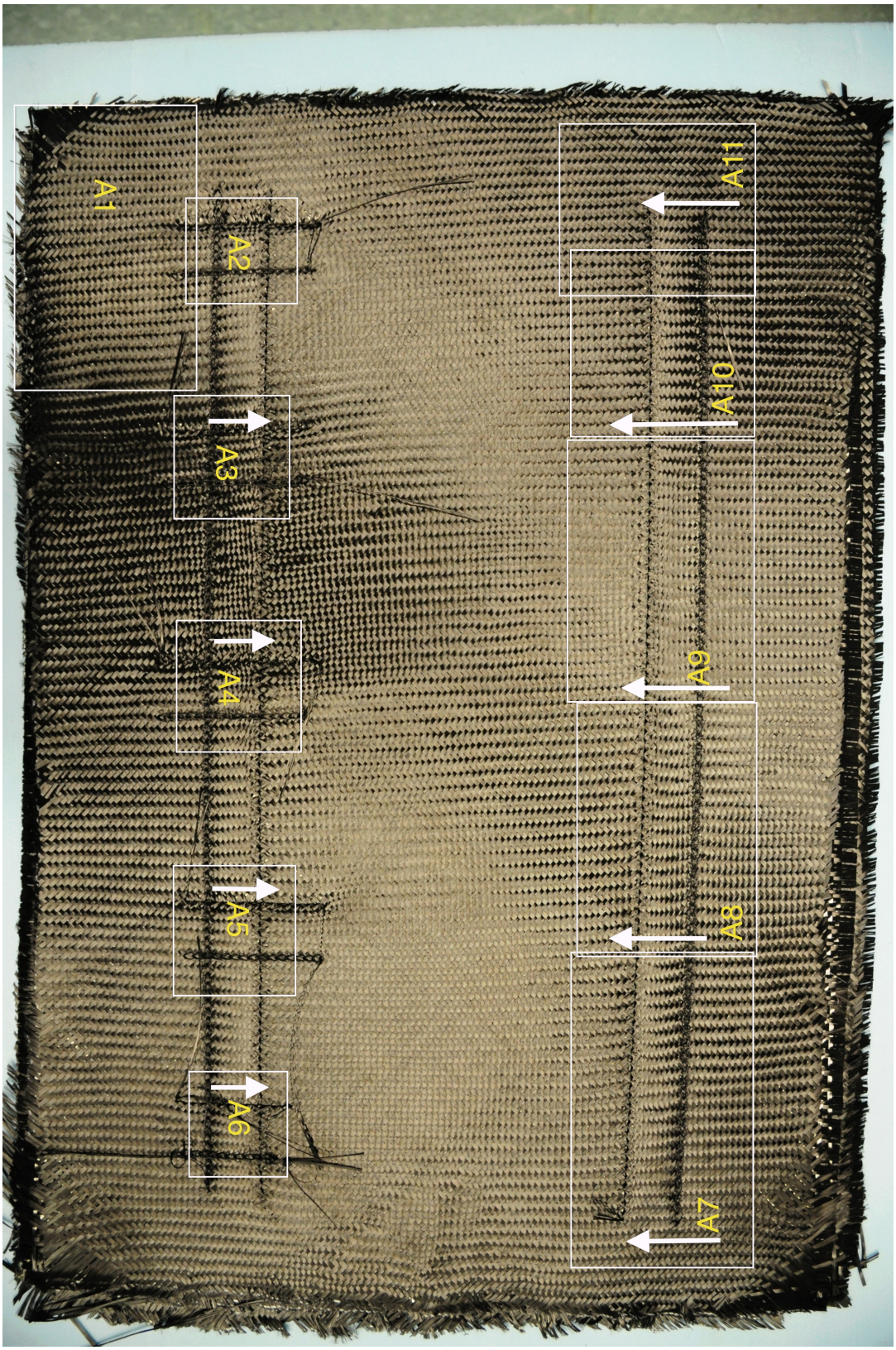

Figure 3.4: Frontside overview of the '700-0005-p4' (4mm stitch) test preform, showing frontside test sample designations and photo frame areas.

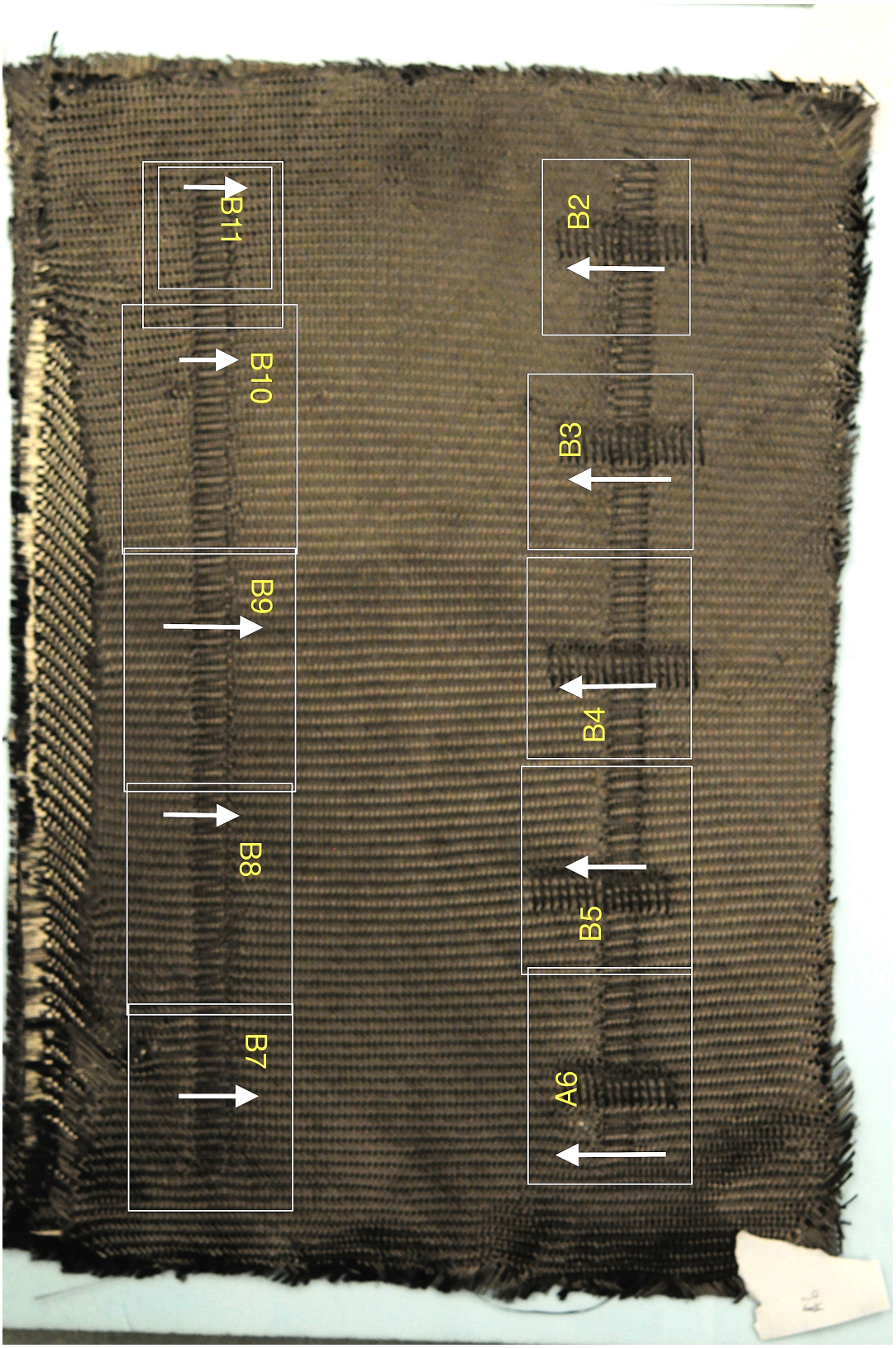

Figure 3.5: Backside overview of the '700-0005-p4' (4mm stitch) test preform, showing backside test sample designations and photo frame areas.

3.3.4 Analysis

The fibre volume fraction of the preform between the compaction platens, v_f, is defined as the ratio of the volume occupied by fibres, V_f, to the volume existing between the platens, V_p:

$$v_f = \frac{V_f}{V_p} \tag{3.1}$$

where the volume of fibres was found using the theoretical mass of carbon between the platens, m_c (the product of the surface weight of the fabric, surface area of the platen and number of fabric plies between platens) and the density of the carbon fibres, ρ_c:

$$V_f = \frac{m_c}{\rho_c} \tag{3.2}$$

and the volume existing between platen surfaces, V_p, is the product of the platen area, A_p, by the corrected distance between the platen faces, h_c. Platen distance was corrected by applying a correction factor, s_p, which removed the deflection of the platen assembly from the displacement measured within the apparatus. The corrected platen distance is given by:

$$h_c = h - s_p(F) \tag{3.3}$$

where the correction factor s_p was expressed as a function of the force applied on the preform, F. It was reasonably assumed that the compaction platen assembly could be modelled using a linear spring constant. Using data obtained from running a test without a sample in place, the spring constant of the compaction platens, k_p, was obtained with Hooke's law, as follows:

$$k_p = F/x \tag{3.4}$$

After a sample was introduced between the platens the model was adapted to account

for the presence of the sample, which acted as a second spring with nonlinear behaviour. This can be seen in Figure 3.7.

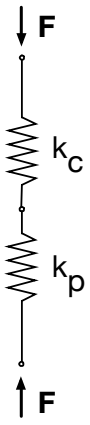

Figure 3.7: Mechanical model of platens and carbon sample

The equivalent spring constant, k_{eq}, can be found by combining the following equations:

$$s_{tot} = s_c + s_p \tag{3.5}$$

$$\frac{1}{k_{eq}} = \frac{1}{k_p} + \frac{1}{k_c} \tag{3.6}$$

$$k_{eq} = \frac{F}{s_{tot}} \tag{3.7}$$

$$\frac{s_c}{s_p} = \frac{k_p}{k_c} \tag{3.8}$$

By combining Equations 3.6 and 3.7 the spring constant of the carbon sample k_c can be obtained as a function of the compaction force F as displayed in Equation 3.9.

$$k_c(F) = \frac{F k_p}{k_p s_{tot} - F} \tag{3.9}$$

Combining Equations 3.5 and 3.8 the displacement of the platens s_p as a function of the compaction force is obtained:

$$s_p(F) = \frac{s_{tot}}{1 + \frac{k_p}{k_c(F)}} \tag{3.10}$$

Lastly, the instantaneous fibre volume fraction throughout the test is given by:

$$v_f = \frac{m_c \rho_c^{-1}}{A_p h_c} \tag{3.11}$$

3.3.5 Results and observations

All compaction experiments displayed good repeatability. Figure 3.8 displays the fifth and final compaction cycle for the first, third and fifth test sample in each case, where the largest variance in final v_f is roughly 1.25 % in the 8mm superimposed stitch case. Larger variability was observed within superimposed stitch samples than in single stitch samples, which exhibited variation remaining well within one percent.

The sans stitch cases were observed to attain the highest fibre volume fraction, roughly 57.5% at the final pressure of one bar. Final fibre volume fraction was observed to decrease with the addition of more reinforcing stitch. Samples with the single stitch were observed to display higher volume fraction than samples with the superimposed stitch regardless of stitch pitch. The addition of the superimposed stitch was observed to decrease the maximum volume fraction by roughly 1.5% in samples with 8mm stitch pitch and 2% in samples with 4mm stitch pitch.

It is interesting to compare samples of 4mm single stitch and 8mm superimposed stitch because both stitch geometries theoretically possess equal surface through-thickness reinforcement density, Table 3.6. Comparing the results of these two sample groups revealed noticeably lower v_f in the superimposed stitch configuration. This may be simply due to stitch threads passing directly over one another, or to other factors at play. Figure 3.9 reveals that tension within the stitch actively pulls yarns within the fabric together creating a localized area of higher fibre density in the actual reinforcement. Such an area would likely require larger pressure to be compacted to the same thickness as the surrounding area, decreasing v_f measured beneath the area of the rigid compaction platens. Logically, the addition of a second stitch in the perpendicular direction causes fabric

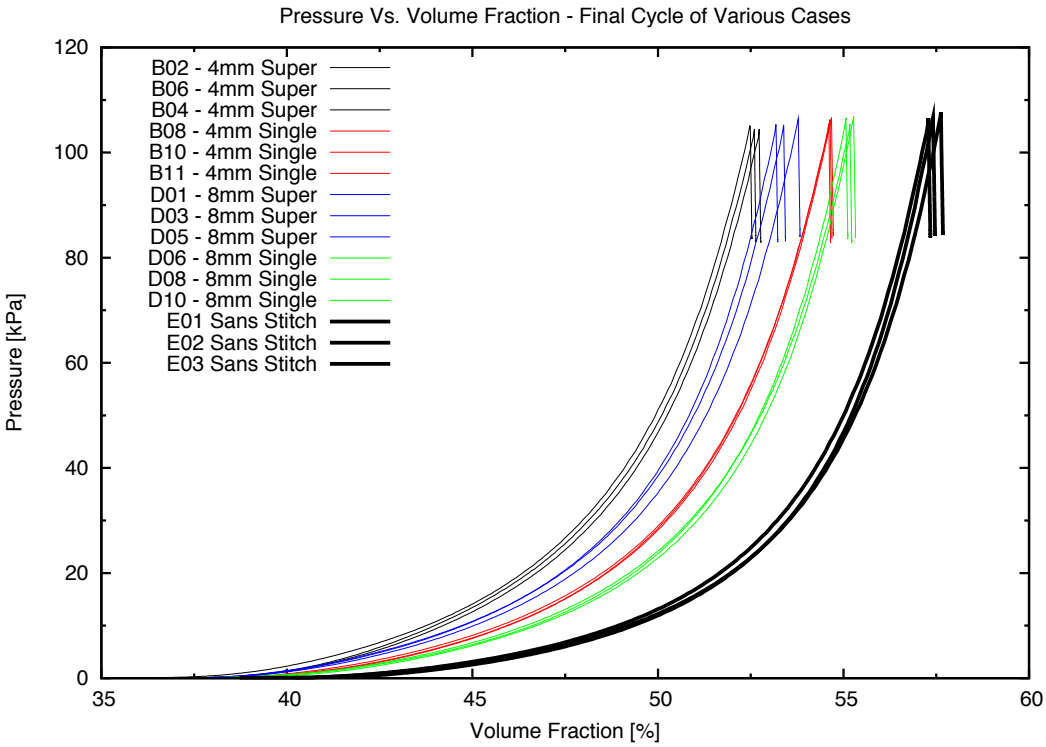

Figure 3.8: Final compaction cycle of first, third and fifth test samples.

yarns to also gather along this second direction, as seen in Figure 3.10, further lowering v_f.

While the data presented is not sufficiently extensive to allow confirmation of this theory, it is an interesting possibility. Further investigation of the area within single and superimposed stitch lines may be performed to test this theory, perhaps by using small-diameter platens that compact the area within the stitch without making physical contact with the visible overlaying thread.

It was not feasable to make any visual observations during testing as samples were obscured by the compaction platens. Samples were inspected after the final compaction cycle and any areas of interest were photographed at high magnification. Minimal fibre reorganization was observed in the outermost ply after compaction. Gaps existing between fibres, yarns and within openings created by the stitching needle appeared essen-

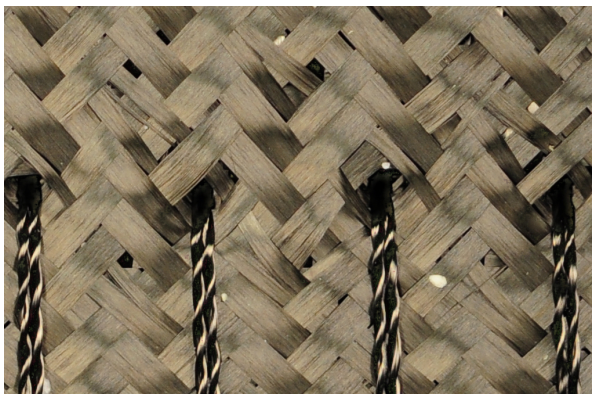

Pre-Compaction

Post-compaction

Figure 3.9: Close-up stitch area of 8mm single stitch sample D8 before and after compaction.

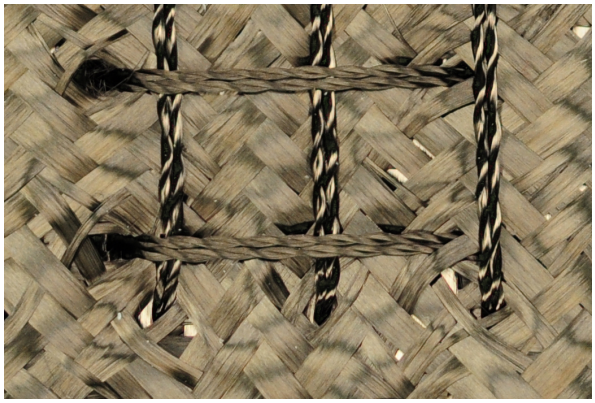

Pre-Compaction

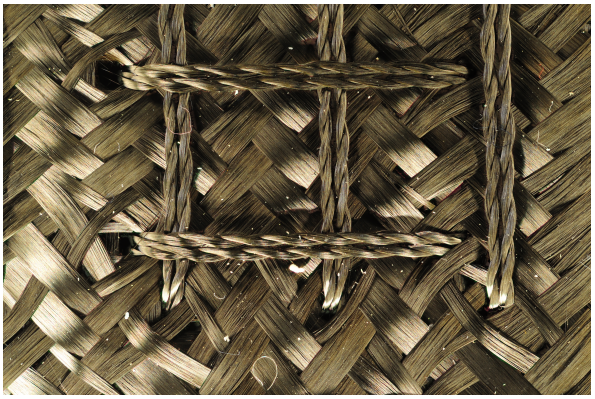

Post-compaction

Figure 3.10: Close-up stitch area of superimposed stitch sample D1 before and after compaction.

tially unchanged by compaction as seen in Figures 3.9 and 3.10. This was so, irrespective of stitch pitch and configuration. No increase in fibre breakage was observed comparing the fabrics before compaction and after compaction.

Table 3.6: Average fibre volume fraction reached at the end of each compaction and hold cycle, shown in percent.

Sample	v_f at cycle [%]				
	1	2	3	4	5
4mm Super	50.73	51.83	52.08	52.39	52.64
4mm Single	52.85	53.71	54.22	54.61	54.88
8mm Single	53.11	53.99	54.53	54.90	55.22
8mm Super	51.44	52.27	52.79	53.18	53.83
Sans Stitch	55.50	56.29	56.81	57.22	57.50

3.4 Effect of shear on CRIAQ COMP-501 preforms

3.4.1 Justification

Composites manufactured from multidirectional reinforcements display better performance when subjected to in-plane shear loading. As a result, multi-directional lamination sequences are often implemented in aerospace components, many of which must display some level of resilience to failure when sheared in-plane [1]. Fundamentally, this resilience is attributed to fibres running in a third, non-principal direction, which is analogous to adding a reinforcing cross-member to a rectangular frame structure.

Similar to their processed counterparts, unprocessed dry multidirectional preforms do not respond well when deformed in shear. Multidirectionals display fibre lock-up and reinforcement wrinkling at very low angles of inter-fibre shear. As such, multidirectional reinforcements are essentially undrapable onto double curvature surfaces, and they cannot be tested in shear.

This becomes a problem for designers wishing to incorporate the mechanical behaviour made possible by multidirectional lamination sequences into curved components such as wing skins, radar domes and T-section airframe formers.

This limitation extends to preforms relevant to the COMP-501 project, defined by the lamination sequences displayed in C. Leduc's document Def_laminates.pdf, (Appendix C, page C.1), and as a result renders a direct inquiry into the shear properties of COMP-501 preforms impractical. However, multidirectionals can be assembled by layering bidirectional preforms that have already been formed to near final shape.

In a similar fashion, thick bidirectional preforms featuring a through-thickness rein-

forcement such as lock stitch that runs along the preform's principal axes can be used in similar cases, and draped. In doing so, it is possible to manufacture multidirectional preforms that exhibit properties associated with 3D reinforcements, such as high damage tolerance, with little restriction to geometric complexity.

This procedure could be used for manufacturing composites with multidirectional lamination sequences similar or comparable to those sought by the COMP-501 project (soft or hard1 sequences shown in Appendix C, page C.1), and this prospect is sufficiently valuable in justifying a limited number of in-plane shear trials aimed at informing on the shear behaviour of stitched bidirectionals.

3.4.2 Apparatus

The apparatus used for performing shear testing is summarized in Table 3.7 and includes the apparatus discussed in Section 3.2.

Table 3.7: Summary of apparatus used in shear testing

Quantity	Item
1	Trellising articulated testing frame
1	Sample cutting template

The specimens tested in shear were manufactured from JB Martin carbon weave style 'TC-06-T'. A data sheet is included in Appendix C. Table 3.8 displays details about the each specimen's lamination sequence and stitching configuration.

Table 3.8: Summary of specimens tested in shear.

Quantity	Sample Code	Lamination sequence	Stitch pitch (mm/stitch)	Stitch Pattern
3	N/A	$[0/90]_4$	-	No stitch
3	720-0010-P4	$[0/90]_4$	4mm	Single stitch
3	720-0009-P4	$[0/90]_4$	4mm	Double stitch

3.4.3 Procedure

Prior to testing any samples, testing was performed on the shear frame with no fabric sample present in order to obtain a baseline measurement, later used in removing the effect of the frame's inertial and frictional forces from experimental data.

Samples were cut from pre-stitched reinforcement stacks with a $140mm \times 140mm$ testing area and $20mm$ extensions hanging off each end to hold the sample within the testing frame, Figures 3.11 and 3.12.

To ease preparation and standardize the size of each test sample, a wooden template with dimensions shown in Figure 3.12 was clamped over uncut stock material. Cuts were made by depressing a sharp blade along the perimeter of the template, until the surrounding material could be lifted away freely.

Samples were loaded into the trellising test frame such that tows ran parallel with the frame, Figure 3.11. During loading a cross-brace was installed on the test frame to maintain rig at 90^o, or 0^o shear. Samples were fixed along all four sides of the testing frame by tightening a total of 16 socket-head cap screws onto plates which, in-turn, applied a strong bearing force along the entire span of the sample's four extensions. It was assumed that tows held under the clamps remained fixed within the frame of reference of each frame element, and that a single shear angle was induced at all points of the sample within the test frame throughout testing, an assumption with good validity [89].

The rig was reinserted into the Instron testing frame and the centre of the test sample

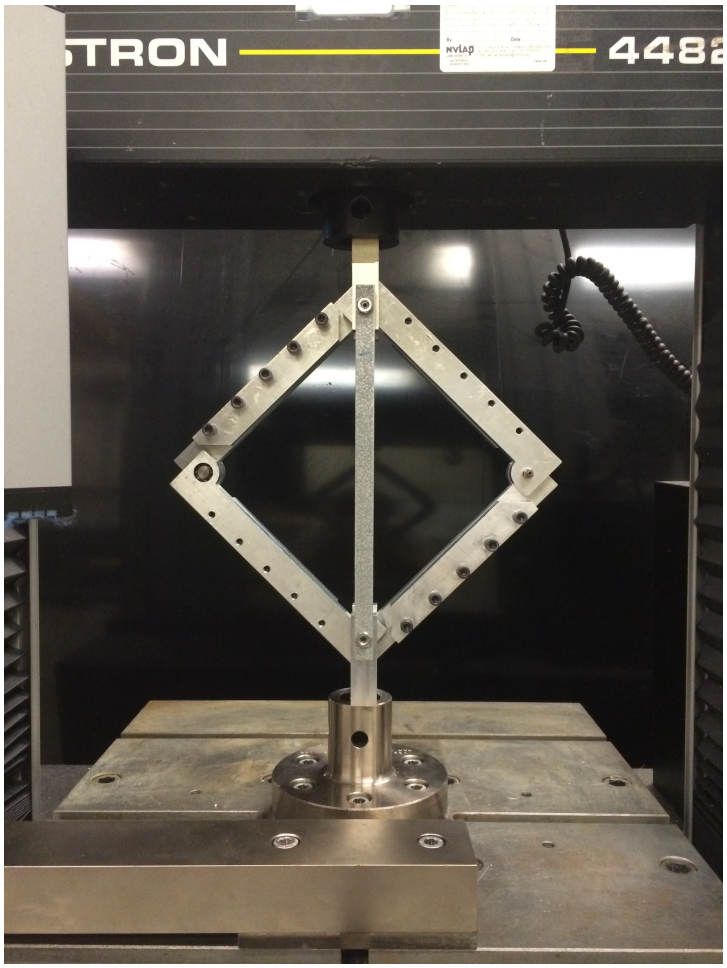

Figure 3.11: Trellising shear testing rig.

was marked by inserting a conventional sewing pin in the through-thickness direction of the sample. Doing so provided a visual reference in photographic evidence. The cross-brace was removed from the testing frame and the load cell was zeroed.

Each test begun by instructing the Instron testing frame traverse to move upward at a prescribed, constant rate. At the same instant, tripod-mounted photographic equipment was cued to record the test and a computer began to record frame extension (mm) and load cell force (N) to a '.CSV' file . A summary of the Instron testing parameters can be found in Table 3.9.

The testing procedure was identical and repeated for all nine specimens (Table 3.8), which were each tested on a single cycle. After all specimens were tested, numerical data was analyzed using the method described in Section 3.4.4.

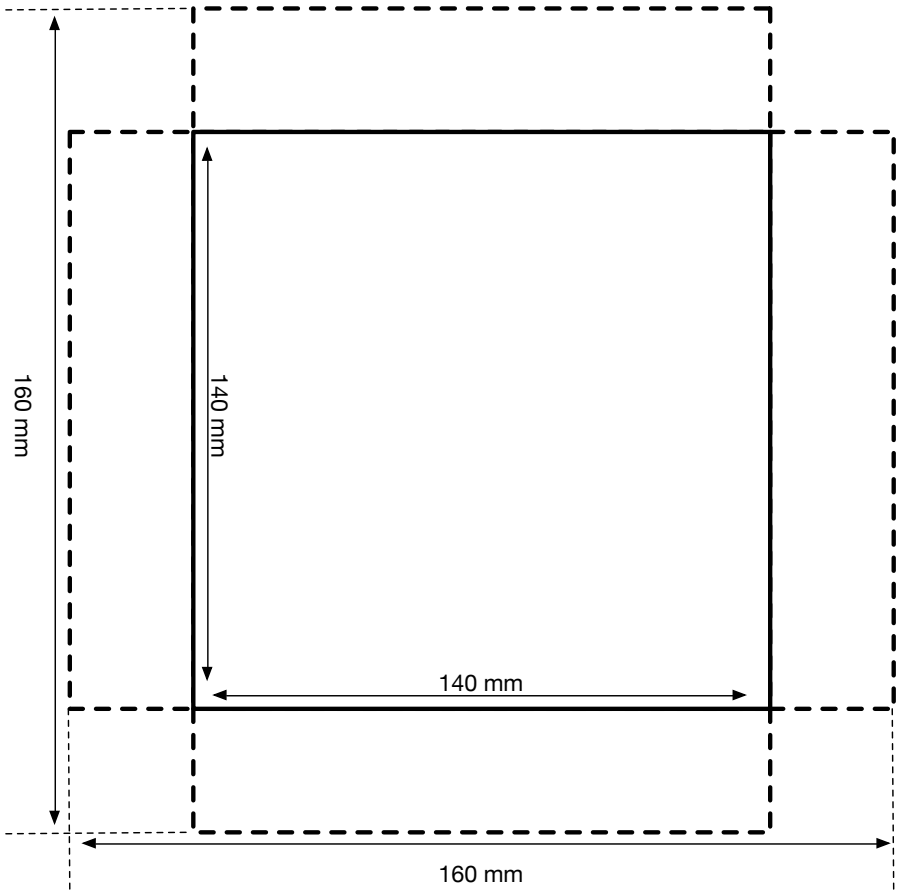

Figure 3.12: Cutting pattern for shear test sample.

Images collected during testing were compiled into two versions of time-lapse video. The first was a raw time-lapse, compiled using images as captured by the camera. In a second time-lapse, raw camera images were converted into an 8-bit greyscale layered stack using the ImageJ software package. Layers were aligned using the pinhead that was inserted into each specimen prior to the onset of testing. Alignment was carried out by translating the image in plane with any image alignment by rotation disallowed.

Table 3.9: Shear test parameters.

Parameter	Value	Unit
Test and Data Parameters		
Extension rate	5	mm/min
Maximum extension	95	mm
DAQ Frequency	1	Hz
Photographic Parameters		
Frame rate	1	fps
Shutter speed	1/5	s
Aperture	$f/3.2$	
Film speed	250	iso

3.4.4 Analysis

The shear angle, γ, relates to the angle defined between warp and weft yarns as determined using Equation 3.12:

$$\gamma = 90^o - 2\theta \tag{3.12}$$

where θ represents the half angle within the test frame and is given by Equation 3.13 [89]:

$$cos(\theta) = \frac{\sqrt{2}L_{frame} + \Delta l}{2L_{frame}} \tag{3.13}$$

The force required to shear the specimen, F, is obtained by removing the force required to actuate the test frame with no sample inserted, F', from the data recorded while testing a specimen, F'' as seen in Equation 3.14 [89]:

$$F = F''(\Delta l) - F'(\Delta l) \tag{3.14}$$

The shear force required to shear the specimen, F_s, is determined as a function of F and θ and given by the relation shown in Equation 3.15 [89]:

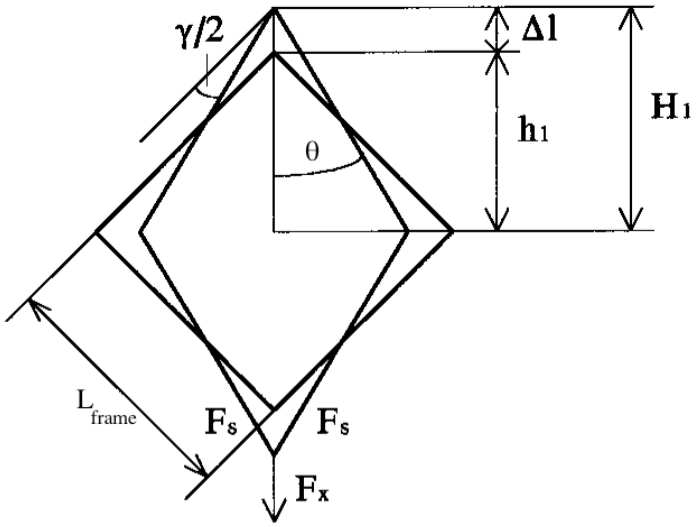

Figure 3.13: Geometric representation of shear frame analysis [81].

$$F_s = \frac{F}{2cos(\theta)} = \frac{F''(\Delta l) - F'(\Delta l)}{2cos(\theta)} \tag{3.15}$$

Lastly, the normalized shear force (with respect to the length of the fabric), $F_{normalized}$, is computed using the shear force as seen in Equation 3.16 [89]:

$$F_{normalized} = F_s \frac{L_{frame}}{L_{fabric}^2} \tag{3.16}$$

Constants used in the above analysis are summarized in Table 3.10.

Table 3.10: Summary of constants used in analyzing shear data displayed in this section.

Symbol	Description	Value	Unit
L_{frame}	Length of frame member	175	mm
L_{fabric}	Length of sample edge	140	mm

3.4.5 Results and observations

This section discusses the results and observations obtained by completing the procedures and analysis outlined in Sections 3.4.3 and 3.4.4. Localized stitch lockup was said to have occurred when a local set of three adjacent yarns were observed to be in a state of lateral compression. Total stitch lockup was defined to have occurred when 15 (for outside stitch area) and 5 (for inside stitch area) adjacent yarns were observed in a state of lateral compression.

Overall, good repeatability was observed within each specimen group. Only two outliers were observed in nine trials, one in the sans-stitch group and one in the single stitch group.

Due to the lack of through-thickness reinforcement in the sans-stitch specimens loading the specimens into the testing frame proved to be more difficult and tedious than loading the stitched specimens. During sample loading, extra care was taken with sans-stitch specimens in an effort to maintain the alignment between individual fabric plies. Regardless of best efforts, during the early portion of the first sans-stitch test, a noticeable amount of slack was observed in the first specimen, most likely originating during specimen loading. It was decided that the test had progressed past the point of no return and the test was allowed to continue. As seen in Figure 3.14, the curve corresponding to test one displays a slight, early dissimilarity from the following two curves; later portions of the curves show greater similarity. This is presumably attributed to imperfect loading of the first specimen.

Sans-stitch specimens two and three returned similar results with good repeatability between the tests. In these two tests the onset of fibre lockup was observed to occur in localized areas at shear angles as low as 27^o. Total fibre lockup was observed to occur around 35^o of shear, with reinforcement wrinkling beginning beyond that point.

In contrary to what was hypothesized, specimen number two was observed to a display larger normalized shear force at the onset of localized fibre lockup than at the point at which fibre lockup occurred over the total sample area. While originally surprising, Figure 3.14 shows that in all tests conducted the normalized shear force increased steadily until roughly 20^o of shear, where it then began to decrease slightly until roughly 35^o of shear, after which it began to rise exponentially. The brief period of decreasing normalized shear force may be attributed to tows located in areas where fibre lockup was observed to occur prior to full reinforcement fibre lockup, slipping toward areas with less

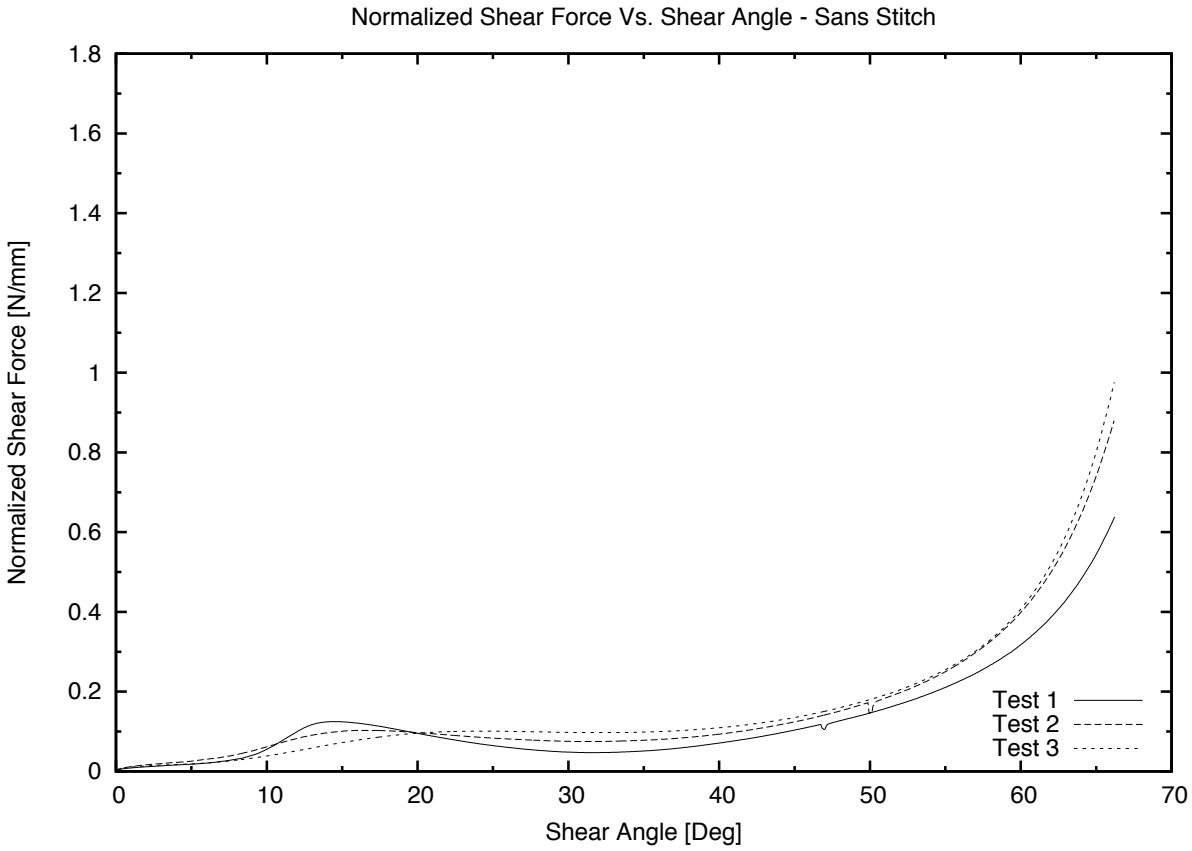

Figure 3.14: Normalized shear force vs. shear angle for sans-stitch specimens.

fibre crowding.

Stitched specimen were monitored for fibre lockup in two locations, the area bound within the stitch lines and areas outside the stitch lines. In the case of superimposed stitch, the area said to be inside the stitch was the area within the intersection of the stitch lines, located about the centre of the reinforcement. Figure 3.15 illustrates each area of observation.

The analysis of data collected while testing the single stitch specimens displayed behaviour closer to what was expected, with the exception of one outlier, test two. This specimen displayed a curve similar in that of sans-stitch specimens with normalized shear dipping before growing again, and it exhibited stronger variation in magnitude when contrasted to test specimens one and three. The curves corresponding to test specimens one and three displayed behaviour typical of a classical non-linear shear curve [65].

Fibre lockup outside of the single stitch was first observed to develop locally at 29.5^o.

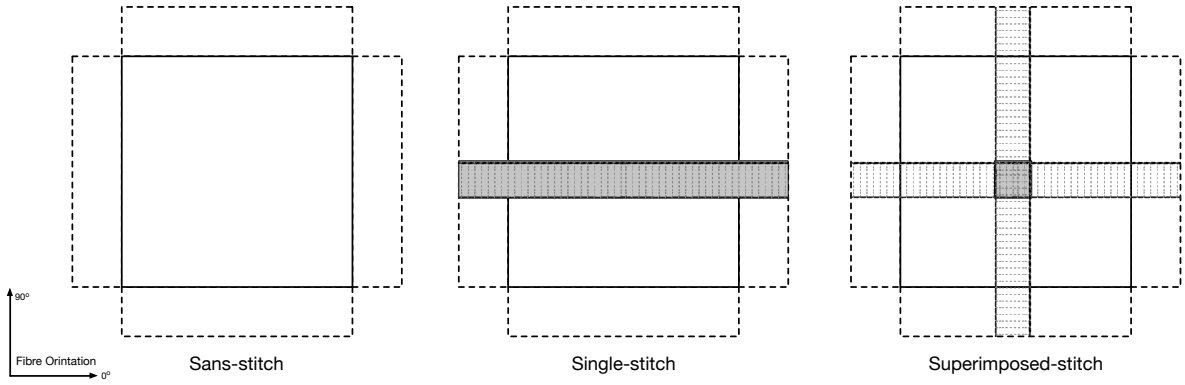

Figure 3.15: Diagram depicting the placement of stitch and on each specimen type. The area bound by the solid white lines is referred to as 'outside stitch' area. The area shaded in grey is referred to as the 'inside stitch' area.

Total fibre lockup was first observed to occur at 35^o. Both phenomena occurred at very similar angles to those observed in sans-stitch tests. Total and localized fibre lockup were observed to occur at lower shear angles within the area bound by the stitch lines, with the earliest localized and total onset of lockup observed at 18^o and 21^o respectively.

The results of tests performed on specimens with superimposed stitch are displayed in Figure 3.17. All curves generated by the superimposed stitch specimens displayed the same general trend seen in the classical non-linear shear curves. Test specimen three exhibits a significant departure in magnitude of normalized shear force when contrasted with other similar specimens of the same type, however retains similar to other tests.

Fibre lockup outside of the stitch was observed first observed to develop locally at 20^o. Total fibre lockup was first observed to occur at 36^o. Total fibre lockup occurred at angles very similar to those observed in both sans-stitch and single stitch tests.

Total and localized fibre lockup within superimposed stitch samples were observed to occur even earlier than in the single stitch case. Earliest localized and total onsets were observed at 16^o and 20^o respectively.

With the exception of the second single stitch test specimen which can be seen in Figure 3.18, all tests samples displayed reasonably similar behaviour when subjected to shear. Noticeable differences in magnitude of normalized shear force were seen from variations in stitch configurations at angles of shear well beyond the onset of fibre lockup and reinforcement wrinkling.

Tables 3.11 and 3.12 present a summary of the shear angle and normalized shear

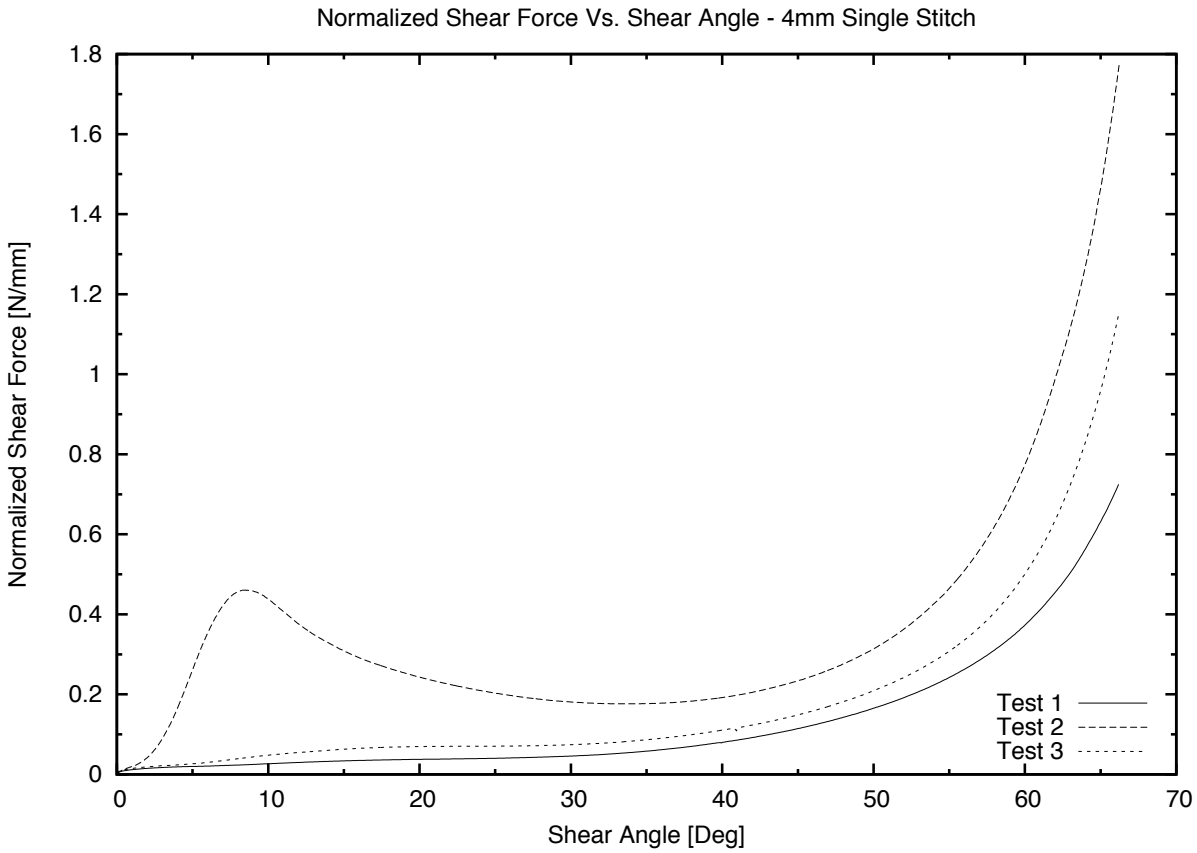

Figure 3.16: Normalized shear force vs. shear angle for single stitch specimens.

force that correspond with the point at which fibre lockup was first observed in localized areas, noted in the columns labeled 'Localized onset'. Similarly, the same tables display identical information relating to the point at which fibre lockup was first observed across the entirety of the reinforcement. This information is presented as two columns, 'outside stitch lockup' and 'inside stitch lockup' which correspond to observations made across the unstitched area and with the area bound by structural reinforcing stitch. These areas are defined pictorially in Figure 3.15.

The '-' character is used to denote a value that could not be obtained with reasonable certainty and hence was omitted. Cells fitted with 'N/A' denote that a value can not be applied to this measurement.

It was observed that the presence of stitching does not affect the maximum shear angles of entire fibre reinforcements. It was also observed that fibre lockup across a stitched reinforcement occurs in stages rather than all at once; however, not enough data

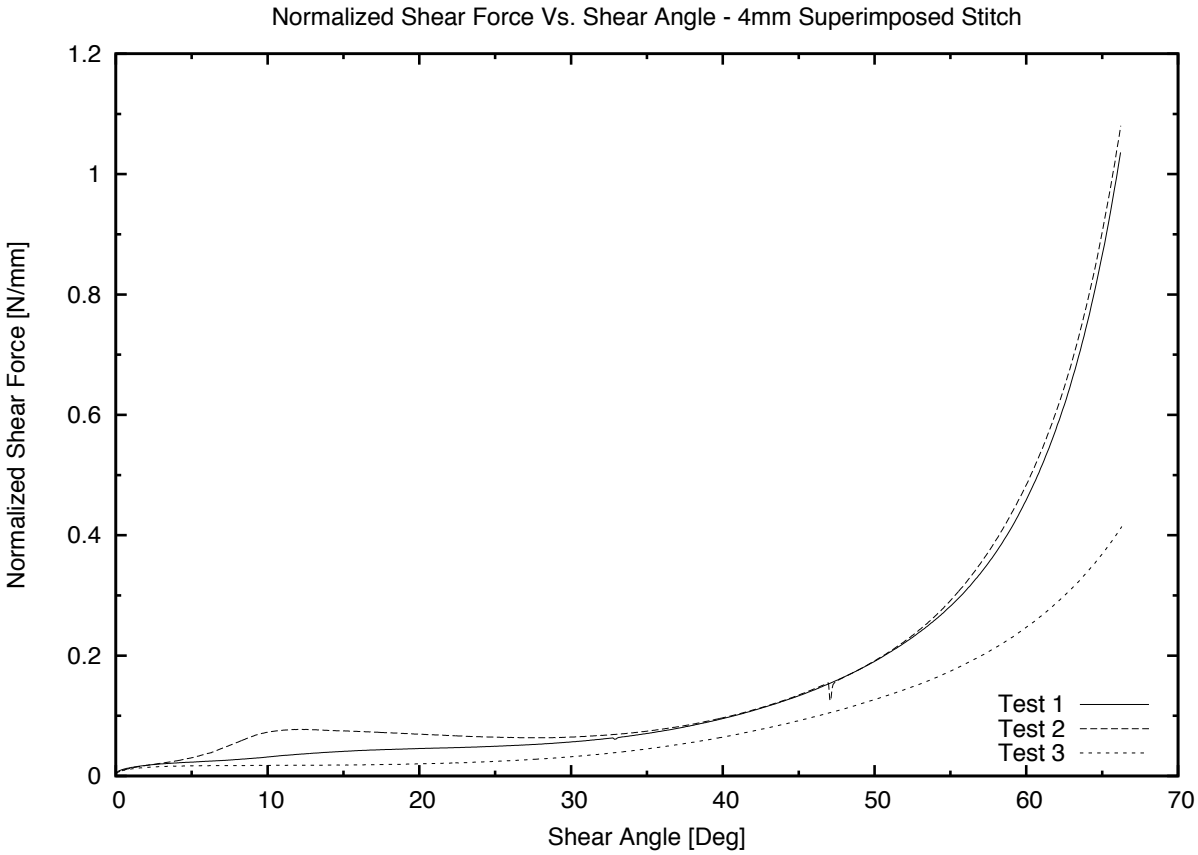

Figure 3.17: Normalized shear force vs. shear angle for superimposed stitch specimens.

was available to isolate any pattern of how stitch configuration influences the lockup propagation.

It was noticed prior to testing that tows directly underneath the path of the stitches had been pulled together by stitching tension. This reduced the spacing of tows in the across-stitch direction, while leaving tows running in the along-stitch direction unaffected, as seen in Figure 3.19.

Fibre lockup is defined as the angle at which gaps within the fabric close and neighbouring tows contact one another, in a state of lateral compression. Hence, it is logical that inside stitch tows, which are already confined by the presence of stitch, lock earlier than those surrounding.

Little variation in maximum shear angle was observed between sans-stitch, single stitch and superimposed stitch tests in respect to total reinforcement lockup. Variation in locking angle in inside stitch areas were observed between different specimen groups.

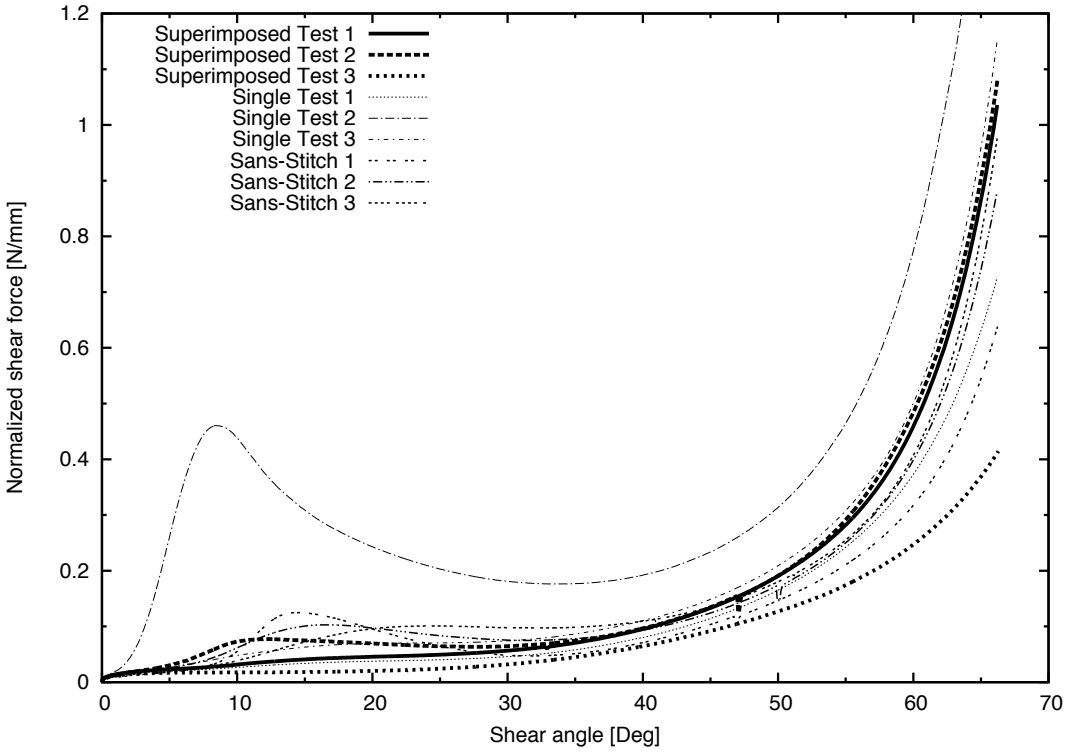

Figure 3.18: Normalized shear force vs. shear angle for all specimen types and test tests.

The locking angle decreased from a maximum of 34.5^o to 20.0^o with the addition of a superimposed stitch. Overall, data displayed greater variability between specimen groups than variation within.

Table 3.11: Summary of shear angle at which fibre lockup was observed in reinforcement specimens.

Specimen type	Test number	Outside stitch lockup onset Localized $[deg]$	Outside stitch lockup onset Total $[deg]$	Inside stitch lockup onset Localized $[deg]$	Inside stitch lockup onset Total $[deg]$
Sans-stitch	1	-	-	N/A	N/A
Sans-stitch	2	27.0	35.0	N/A	N/A
Sans-stitch	3	-	-	N/A	N/A
Single stitch	1	29.5	35.0	18.0	21.0
Single stitch	2	35.0	40.0	19.0	34.5
Single stitch	3	-	-	-	-
Superimposed stitch	1	-	-	-	-
Superimposed stitch	2	20.0	36.0	16.0	20.0
Superimposed stitch	3	-	-	-	-

Table 3.12: Summary of the normalized shear force which fibre lockup was first observed in reinforcement specimens.

Specimen type	Test number	Outside stitch lockup onset Localized $[N/mm]$	Outside stitch lockup onset Total $[N/mm]$	Inside stitch lockup onset Localized $[N/mm]$	Inside stitch lockup onset Total $[N/mm]$
Sans-stitch	1	-	-	N/A	N/A
Sans-stitch	2	0.0793	0.0782	N/A	N/A
Sans-stitch	3	-	-	N/A	N/A
Single stitch	1	0.0451	0.0584	0.0366	0.0381
Single stitch	2	0.1770	0.1937	0.2562	0.1765
Single stitch	3	-	-	-	-
Superimposed stitch	1	-	-	-	-
Superimposed stitch	2	0.0695	0.0787	0.0739	0.0695
Superimposed stitch	3	-	-	-	-

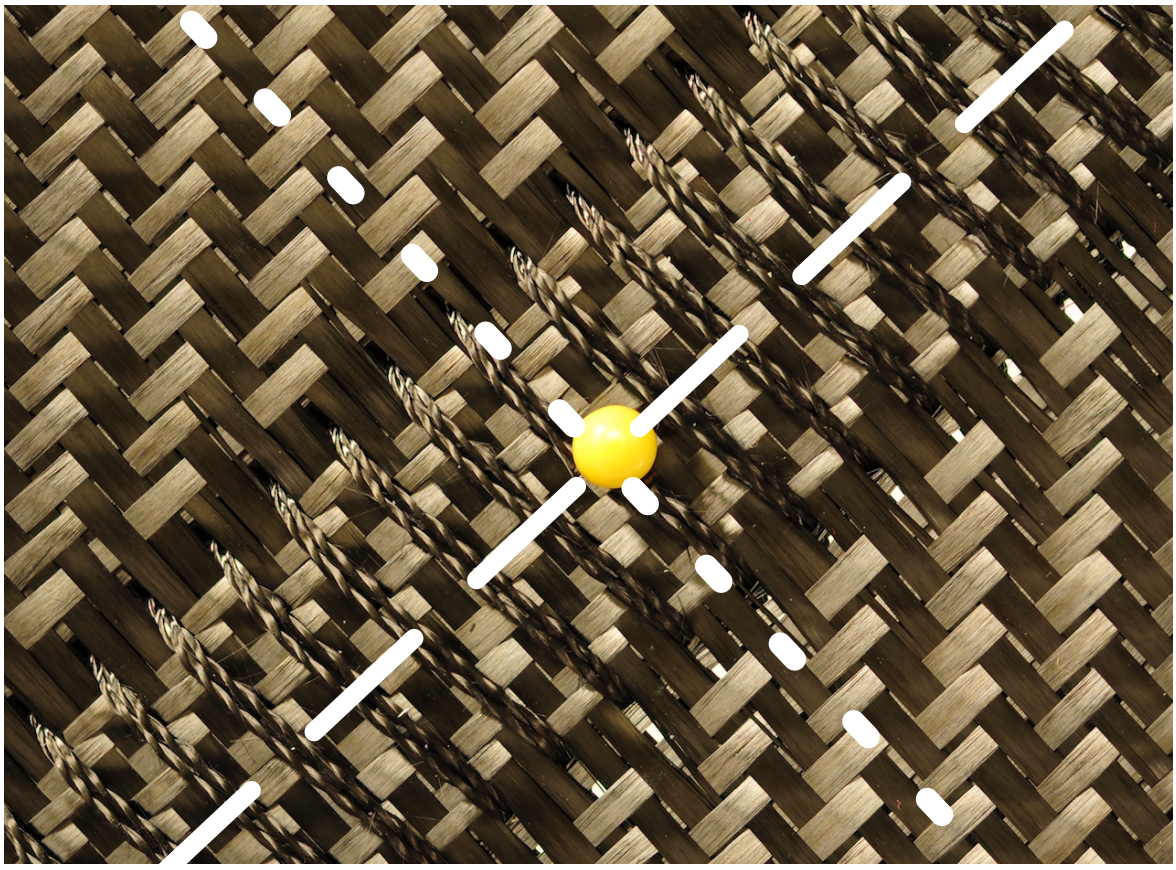

Figure 3.19: Stitching within single stitch specimen number two, before testing. Lateral compaction of tows in the across-stitch direction is evident. Specimen from CRIAQ COMP-501 preform: 720-0010-P4. – **Along-stitch direction: long-dotted line. Across-stitch direction: short-dotted line.**

3.5 Evaluation of bending behaviour of COMP-501 preforms

3.5.1 Justification

The demonstrator T-section outlined in Section 3.1 exhibits 90^o bends with 4.2 mm inner bend radii performed on 4.2 mm thick reinforcements. Due to the significant thickness (4.9 mm prior to processing) of the preforms it is suspected that complications such as dry fibre buckling will arise during this operation. Furthermore, any stitch inserted before bending may alter the behaviour of preform during bending, or in more extreme cases, impart defects to the preform or stitch itself.

In light of the above, the behaviour of preform samples assembled using the CRIAQ COMP-501 'quasi' lamination sequence was probed in bending. Trials were conducted on preforms of 4 mm and 8 mm stitch pitch. Tests on these preforms were conducted with the stitch oriented in directions parallel and perpendicular to the bending axes. These configurations are discussed below.

3.5.2 Apparatus

The apparatus used for assessing bending behaviour is summarized in Table 3.13 and includes apparatus discussed in Section 3.2.

Table 3.13: Summary of apparatus used in bending tests.

Item	Quantity
Bend test rig	1
Cutting pad	1
Cutting wheel	1

The samples tested in bending were manufactured from JB Martin carbon fibre woven fabric style 'TC-06-T'. A data sheet is included in Appendix C. Preforms were assembled using the CRIAQ COMP-501 'quasi' lamination sequence defined as $[((\pm 45)/(0/90))_5]_S$ by C. Leduc, page C.1, Appendix C. Stitched fabric stacks were requested and received

in the configuration shown in Figure 3.20. Individual samples were cut from the received stock along the dashed lines.

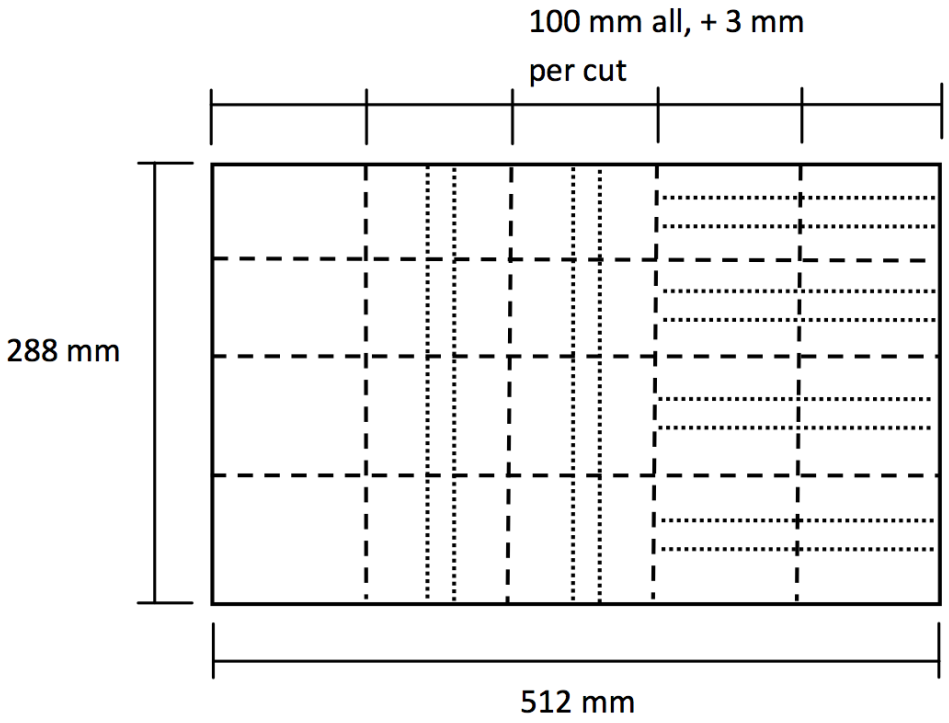

Figure 3.20: Geometry of the stock sample received for testing. Short dotted lines represent stitch lines, long dotted lines represent cutting lines along sample boundaries.

As per the CRIAQ COMP-501 project demonstrator, an internal bend radius of 4.2 mm shown in Figure 3.1 was to be used. Such a radius was outside the capability of testing equipment available at the University of Ottawa. Commercially available solutions were investigated, some of which discussed in Section 2.7.3; however, they were deemed outside of budget.

In order to measure the bending behaviour of fabric samples in a configuration relevant to the CIRAQ COMP-501 project, a custom testing rig was designed and manufactured. Prior to designing the rig, the nominal thickness of test samples was measured. This measurement was required in order to design the rig so that samples would fit snuggly within it, while allowing enough clearance for samples to be loaded without requiring major disassembly of the rig. The latter was extremely important because excessive

disassembly and reassembly of the rig between samples could induce variability within results. Table 3.14 lists average measured sample thicknesses.

Table 3.14: Average measured thickness of bending samples.

Sample	Average thickness
Sans stitch	4.902 mm
Single Stitch	5.410 mm

The complete testing rig mounted in the Instron testing frame appears in Figure 3.21a.

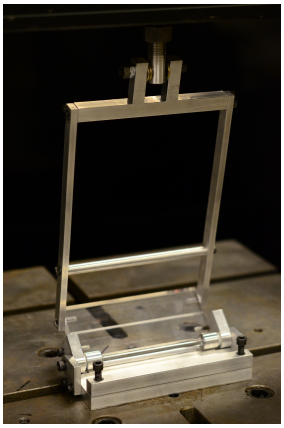

(a) Bending test rig mounted within the Instron testing frame.

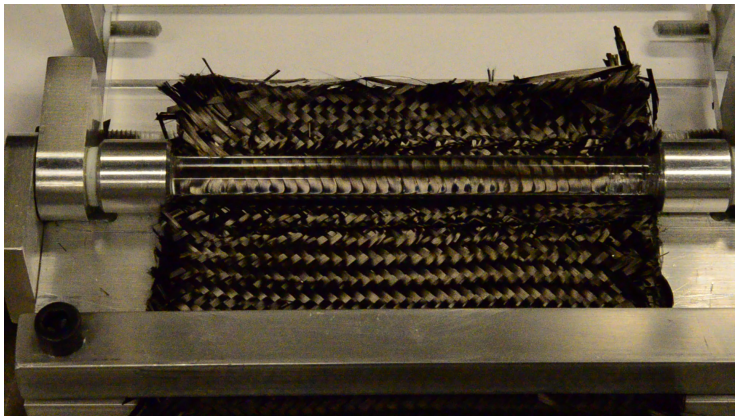

(b) Loaded sample prior to bending test as viewed from the perspective of the video recording device.

Figure 3.21

The rig was manufactured with a perspex rotating hinge and bend radius, allowing observation of the inner and outer bend radii during testing. Samples were loaded into the rig as shown in Figure 3.21b and clamped at one end using a plate secured with two socket-head cap screws as shown in Figure 3.21.

3.5.3 Procedure

The bending rig was loaded into the Instron testing frame and five dry runs were performed with no sample loaded. The dry run data was plotted and it was confirmed that

data variations between dry runs was less than 0.15 N; well within an acceptable range. Using the same plots, it was the concluded that the rig was free any measurable stiction, producing no data spikes when actuated. Before loading each sample, another dry test was performed in order to measure the baseline corresponding to frictional and inertial forces present in the apparatus prior to testing that sample. Samples were cut from the preform stock as outlined in Figure 3.20, and loaded into the the testing rig as shown in Figure 3.21b.

The video-recording device was cued to begin capturing right before the Instron testing frame was instructed to begin the test. Data acquisition was cued automatically by the Instron testing frame's systems. Data recording began at the same time the Instron testing frame began to extend the testing frame. Testing parameters are displayed in Table 3.15.

Table 3.15: Bending test parameters.

Parameter	Value	Unit
Extension rate	20	mm/min
Maximum extension	70	mm
DAQ Frequency	5	Hz

Testing was performed twice for each of the three orientations shown in Figure 3.22. However, one bending cycle was performed per sample. Samples were tested with the upper side of the stitch on the inside of the bending radius, where the upper side of the stitch is defined in Figure 3.23b. One test was performed in the underside-in configuration, and is later referred to as 'underside'. This test was performed using a sample with a 8 mm stitch pitch; a sample which had been left over after the planned tests were completed.

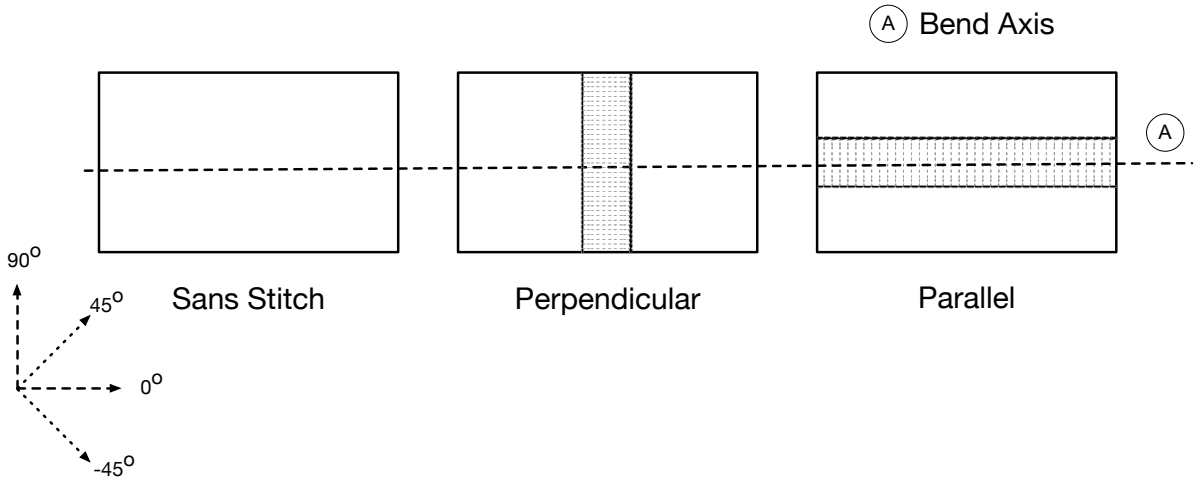

Figure 3.22: Sample orientations for bending tests and their respective naming schemes.

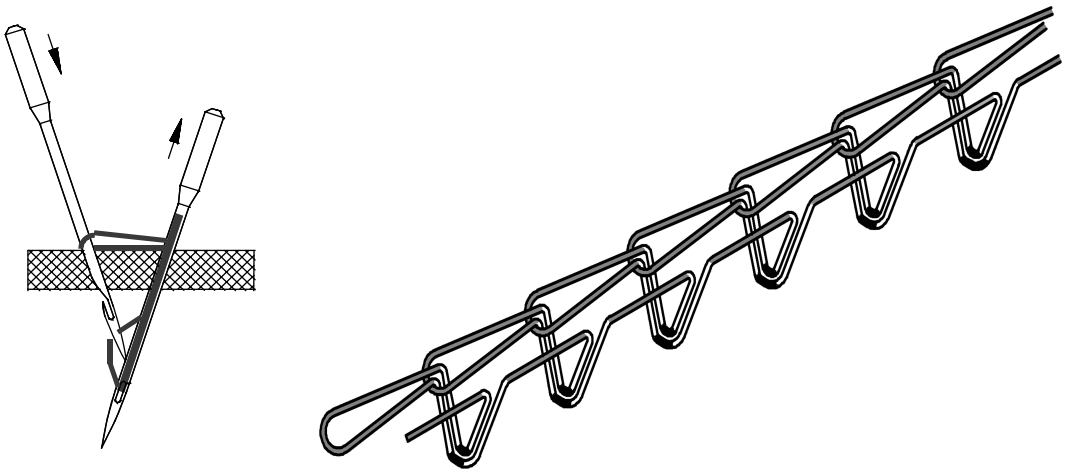

(a) One sided stitching process [90].

(b) Stitch pattern used for all samples in compaction, shear and bending tests. Stitch visible from the upper side is shaded grey, from the underside shaded black and stitch obscured within the thickness of the reinforcement is shaded white [90].

Figure 3.23

3.5.4 Analysis

Similar to the two preceding analyses, a series of dry tests were performed prior to loading a sample in order to check the rig for any stiction. Dry tests data was used to normalize the data obtained from actual tests, where samples were loaded in-place. Raw force

data was normalized using Equation 3.17, where $F_{i,w}$ represents the instantaneous force measured at position i with a sample present, and $F_{i,d}$ is the force measured at the same position without a sample present.

$$F_i = F_{i,w} - F_{i,d} \tag{3.17}$$

Geometric analysis of the bending rig was approached using the theory governing planar crank-slider linkages, Figure 3.24. Angles within the linkage were determined using the trigonometric relations outlined in Equations 3.18, 3.19 and 3.20 where h_i is the vertical displacement measured. A summary of linkage member lengths at a bending angle of 0^o is presented in Table 3.16. In this table, the length of a linkage member along a coordinate system axis is denoted with a subscript.

$$\gamma_i = \arccos\left(\frac{a^2 + (b_o + h_i)^2 - c^2}{2a(b_o + h_i)}\right) \tag{3.18}$$

$$\alpha = \arcsin\left(\frac{a\sin\gamma}{c}\right) \tag{3.19}$$

$$\beta = 90 - \alpha - \gamma_i \tag{3.20}$$

$$\epsilon = 90 - \alpha \tag{3.21}$$

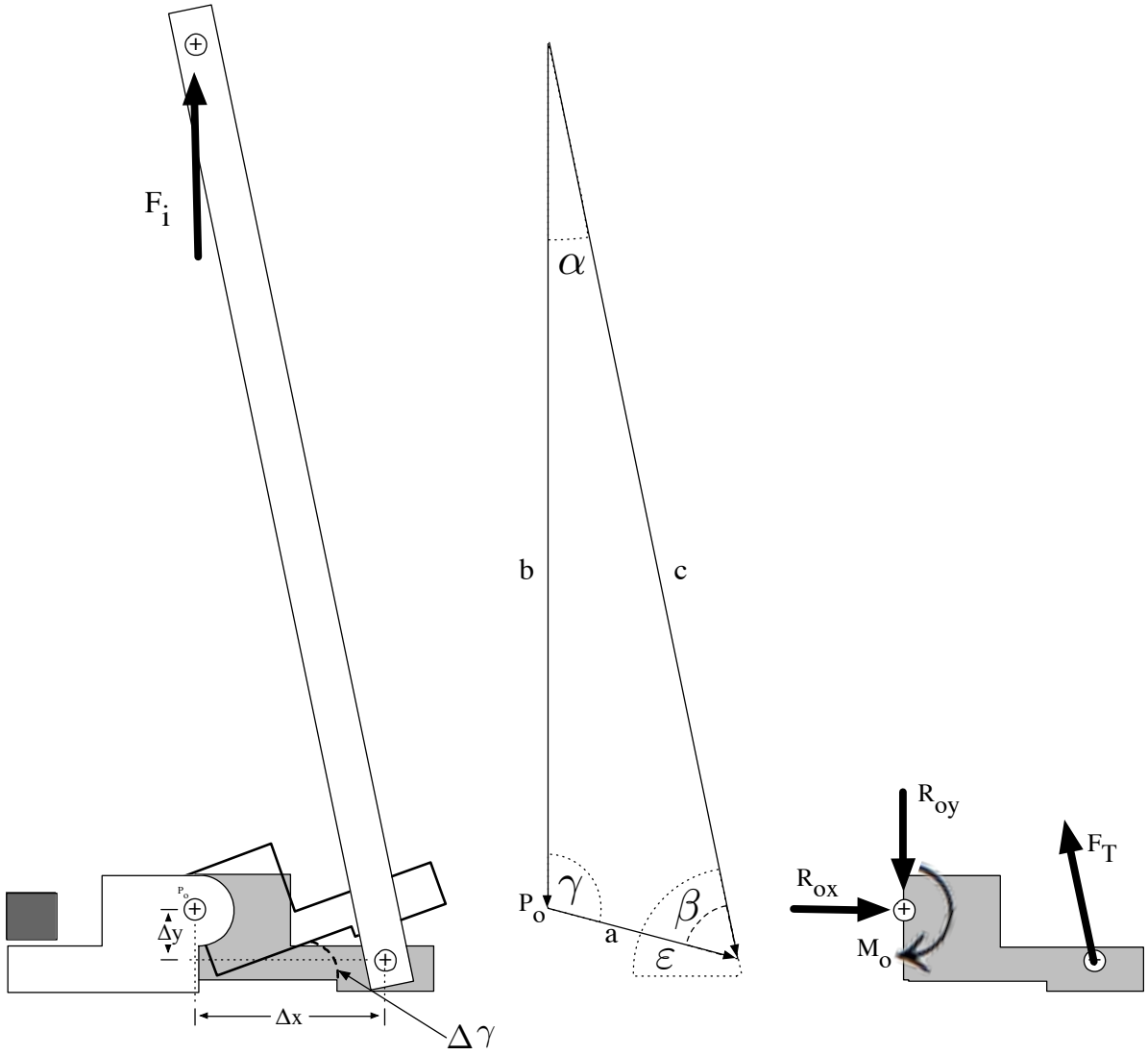

Figure 3.24: Side view and free body diagram of bending test apparatus.

The bend angle, $\Delta\gamma$, was then calculated as outlined in Equation 3.22 where γ_i is the angle γ at the instantaneous position i and γ_o is the value of angle γ at a bending angle of nil, or the value of angle γ before the onset of testing. The value of γ_o for the bending rig is presented in Table 3.16.

$$\Delta\gamma = \gamma_i - \gamma_o \tag{3.22}$$

Table 3.16: Summary of constants used in bending analysis. Various values correspond with lengths shown in Figure 3.24

Symbol	Value	Unit
a	52.66	mm
a_x	50.89	mm
a_y	13.54	mm
b_o	232.07	mm
c	250.83	mm
γ_o	104.90	Deg

Analysis was carried out by considering the sample as a torsion spring mounted about the bending axis of the rig. As the sample bends, it introduces reactionary moment on the rig, about point P_o. This moment is calculated as a function of the bending angle. Similar to experiments carried out towards quantifying the shear behaviour, a slow extension rate was used in the bending tests. This allowed the use of static analysis.The force transferred through the linking arm which connects the load cell to the bending rig's base, F_T, is given by Equation 3.23 where ϵ is the angle between the link and the horizontal plane as shown in Figure 3.24.

$$F_T = \frac{F_i}{\sin(\epsilon)} \tag{3.23}$$

The summations of forces and moments about point O is given by:

$$\rightarrow_+ \sum_{F_y} \vdots \qquad 0 = R_{ox} + F_T \sin(\alpha) \tag{3.24}$$

$$\uparrow_+ \sum_{F_y} \vdots \qquad 0 = R_{oy} + F_T \cos(\alpha) \tag{3.25}$$

$$\curvearrowleft_+ \sum_{O} M \vdots \qquad 0 = \Delta x \cdot F_T \cos(\alpha) - \Delta y \cdot F_T \sin(\alpha) - M_O \tag{3.26}$$

where Δx and Δy are the instantaneous distance from point P_o to the linkage pin and are respectively expressed as:

$$\Delta x = a_x \cos(\Delta\gamma) + a_y \sin(\Delta\gamma) \tag{3.27}$$
$$\Delta y = a_y \cos(\Delta\gamma) - a_x \sin(\Delta\gamma) \tag{3.28}$$

Hence the moment M_O, required to bend the preform at an angle $\Delta\gamma$ was calculated using Equation 3.29:

$$M_O = \Delta x \cdot F_T \cos(\alpha) - \Delta y \cdot F_T \sin(\alpha) \tag{3.29}$$

The bending moment was then normalized relative to the width of the sample w_s, Equation 3.30.Widths of all samples are listed in Table 3.17.

$$M_{normalized} = \frac{M_O}{w_s} \tag{3.30}$$

Table 3.17: Bending sample dimensions and measured mass prior to testing

Test case	Test number	Stitch pitch [mm]	Sample Width (w_s) [mm]	Sample length [mm]	Sample Mass [g]	ASTM D3776 Linear density [kg/m]
Sans Stitch	1	-	100	72.5	26.0	1.033
	2	-	100	72.5	26.0	1.033
Perpendicular Stitch	1	4	100	100	39.3	1.132
	2	4	100	100	38.8	1.117
	1	8	100	72.5	30.0	1.192
	2	8	100	72.5	31.0	1.231
Parallel Stitch	1	4	100	100	40.0	1.152
	2	4	100	100	40.5	1.166
	1	8	100	72.5	30.0	1.192
	2	8	100	72.5	30.0	1.192
Underside	-	8	100	72.5	-	-

3.5.5 Results and observations

Analyzed data from bending tests appears in Figure 3.25. In this figure all trials are superimposed for comparison; specific plots are listed for the various cases in Appendix A.5.

Sans stitch samples produced the smallest bending moments at any angle. Samples with a stitching pitch of 4 mm that were bent in the parallel configuration (along stitch lines) showed greater resistance to bending than those bent in the perpendicular configuration. Test samples with a stitching pitch of 8 mm bent in the perpendicular bend configuration were observed to fluctuate above and below the minimum values recorded with parallel bend samples with the same stitching pitch. Overall, samples with 8 mm stitching pitch displayed minimal levels of variability in behaviour and magnitude regardless of bending configuration and stitching density; however, bending coefficients varied more significantly. This is reflected in Table 3.18 which reports the linear slope of best fit for all samples; equating to the torsional coefficient in 'N-mm/ mm Deg'.

Table 3.18: Torsional coefficients of obtained from a linear curve-fit.

Test case	Test number	Stitch pitch [mm]	Torsional Coefficient (k_b) $[\frac{N-mm}{Deg} \cdot mm^{-1}]$
Sans Stitch	1	-	0.0005
	2	-	0.0003
Perpendicular Stitch	1	4	0.0042
	2	4	0.0038
	1	8	0.0034
	2	8	0.0031
Parallel Stitch	1	4	0.0144
	2	4	0.0120
	1	8	0.0046
	2	8	0.0039
Underside	-	8	0.0040

Bending the 4 mm stitching pitch samples in the parallel configuration lead to the largest bending moment. Notable, visual observations were made during testing, including potential fibre buckling on the inside radius during 4 mm parallel bend and stitch

unravelling propagating from cut lines in the 8 mm parallel bend in test number two. However, these notable events do not clearly appear in the data. Overall, the bending moment required to form the reinforcement to the bend increases as the stitching density grows. The greatest bending moment is required when the reinforcement in bent in a direction parallel to the stitch.

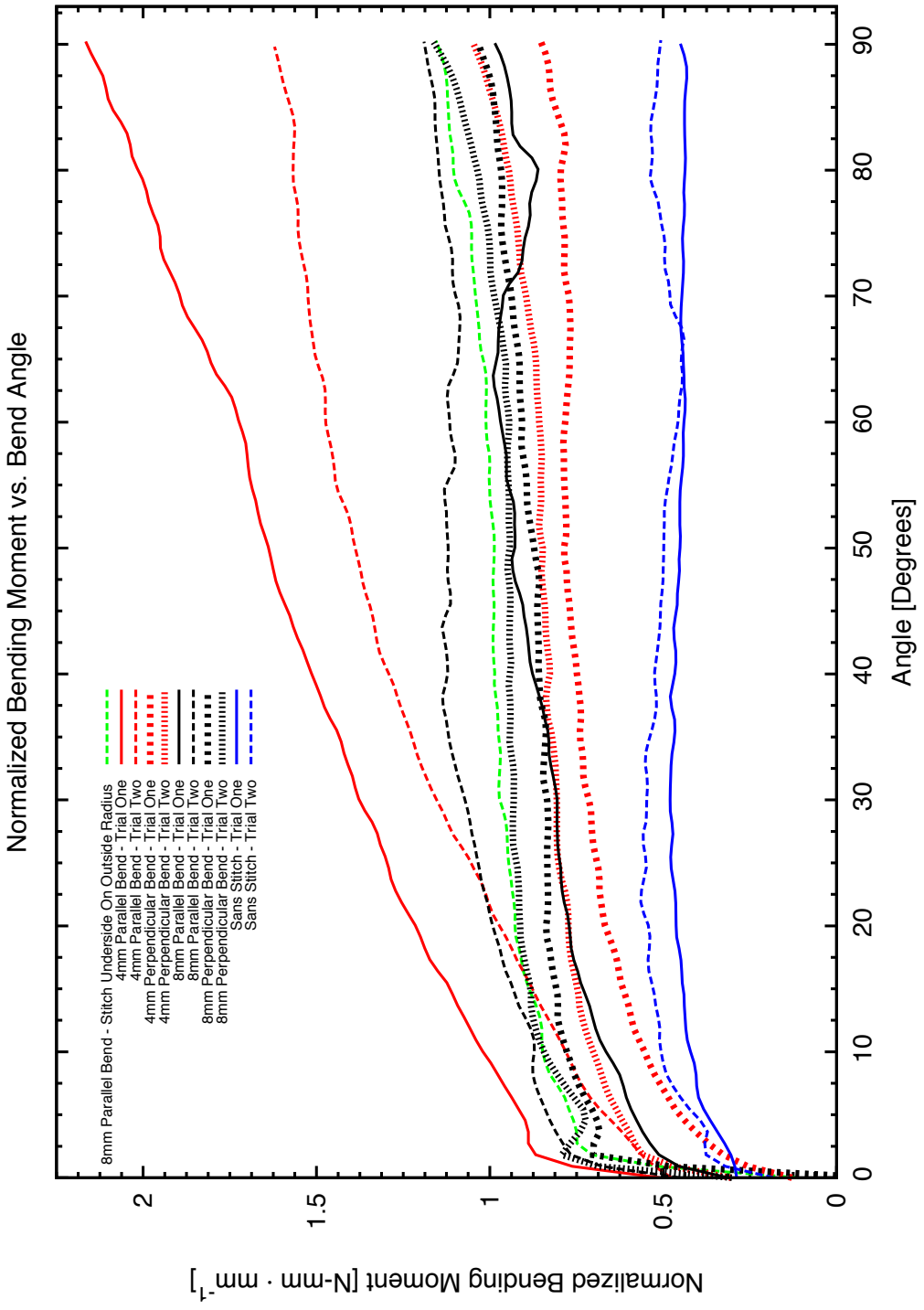

Figure 3.25: Curves obtained from bending experiments.

Chapter 4

Manufacturing Process

Fibre reinforcements for PMC components can be manufactured a wide variety of available processes, some of which are discussed in depth in Chapter 2. Each process have unique advantages over others, each excels at producing reinforcements for PMC components with distinct geometric features, mechanical properties and production volumes. Conversely, each process has limitations that leave significant room for improvement in terms of the reproducibility and efficiency of manufacturing 3D preforms that exhibit variable thicknesses, net-shape outlines, high drapability and formability.

In previous work by N. Burnford [91], a method for overcoming many challenges facing the production of reinforcement for manufacturing PMC components was developed and validated. This work constitutes the foundation of a pre-production reinforcement manufacturing process developed at and proprietary to the University of Ottawa. This pre-production process enables the design and manufacturing of textile reinforcements with variable spacings between adjacent tow yarns, allowing them to be steered. Local alterations in the tow spacings allow localized adjustments to be made to the forming behaviour and mechanical properties of the reinforcement. Therefore, by strategically tailoring the tow spacings within a reinforcement, it is possible to produce a final-thickness textile reinforcement that is uniquely suited to easily form to an otherwise complex and challenging manufacturing geometry.

The process begins with the selection of the desired component geometry. A virtual model of the component is produced from design dimensions or, in the case of a pre-existing physical model, imported using digital CMM or 3D laser scanner. The model is then converted into a shell geometry by discretizing it as a continuous mesh of

three-noded triangular elements. The mesh is loaded into proprietary kinematic draping software named uO-Drape [91]. The software is used for simulating the draping of a bidirectional fabric with constant tow spacings over the mesh surface, enabling the identification of areas featuring excessive in-plane shear where draping may become problematic, as well as the maximum fabric coverage. The operator is then prompted to define a parameter to be maximized or minimized; parameters include v_f, in-plane shear, fibre orientation and area covered by the draped reinforcement. Similarly, the operator must provide the software with information regarding the nominal tow spacings (for areas where spacings will remain constant), along with and the maximum & minimum spacings constraints, to maintain tow spacings within a manufacturable bounds.

An iterative algorithm which is embedded within the software is used to alter tow spacings by shifting node positions, where node positions corresponds to the unique intersection point of a warp and weft tow. The algorithm uses process shown in Figure 4.1 and computation continues until convergence occurs. (Information regarding the uO-Drape algorithms and software can be found in within [91]).

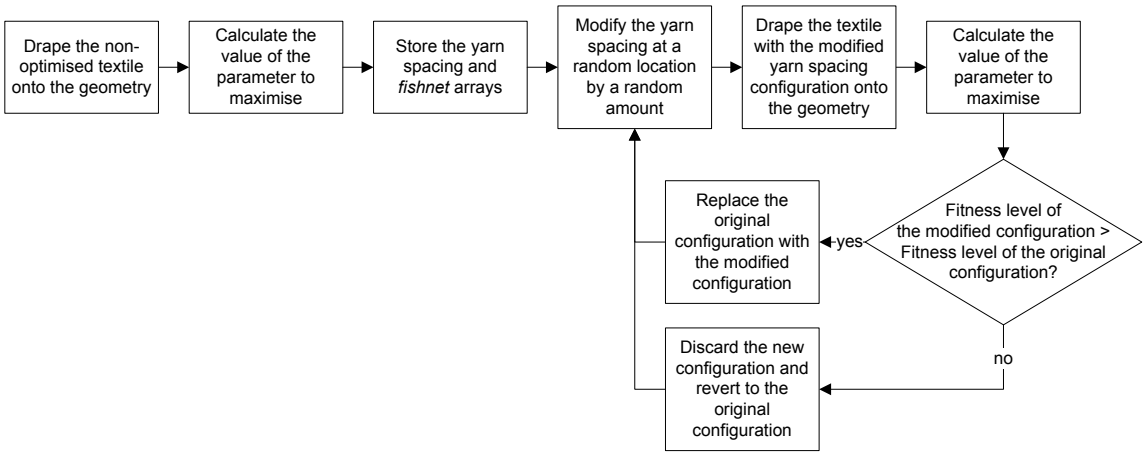

Figure 4.1: Variable spacing fabric optimization algorithm [91].

The optimized design is displayed as a virtual fabric draped over the surface mesh where tow paths and intersection points are highlighted. The operator has the ability to inspect the design and map the node spacings and tow paths from their draped configuration identified in the reference frame of the surface mesh to a flat configuration in a planar reference frame. This numerical transformation is referred to as undraping

and it is critical to the process; to be clear, undraping is only ever done in software as a part of the preform design process. The physical preform is manufactured flat, and undraped as the first step in PMC manufacturing. Undraping transforms the designed preform from its shell configuration (draped) into a flat configuration that is used for preform manufacturing. After manufacturing, the flat reinforcement may be immediately processed or stored and transported to an offsite facility for further processing into a PMC component at a later time. As the reinforcement is manufactured using dry fibres and without using tackifiers, it does not require cold-storage and it has an open-ended shelf-life.

Upon intent to process a flat reinforcement into the shell geometry for which it was designed, the reinforcement is removed from storage and placed on or within an LCM mould, typically requiring no further layup. As the reinforcement is draped into its geometry, in-plane shear built into the flat preform upon undraping is reversed, allowing the reinforcement to fit its intended shape with ease.

Variable tow spacing reinforcements were manufactured manually in prototype quantities (at the University of Ottawa), which were used to validate the process experimentally. However, manual manufacturing is not a viable process in terms of production efficiency and reproducibility; neither is manual manufacturing capable of producing preforms in quantities required for large-scale production.

The keystone for implementation of the UO manufacturing process, hereon referred to as the uO-Tow process, is an efficient and reproducible method for producing the reinforcements. By mechanizing the manufacturing processes a high degree of component-to-component repeatability can be achieved. Automating the manufacturing process removes a significant degree of human involvement, furthering manufacturing repeatability and efficiency.

Towpreg laying appears ideal for producing variable tow-spacing reinforcements, though towpreg laying's use on the use of prepreg semi-products limits its practicality and viability due to two key factors; namely, reduced ease in storage and processing of the semi-product and most importantly, the inherent tackiness of prepreg limits the ability of the tow to bend in-plane – a mechanism vital to the process. Similarly, production of variable tow-spacing reinforcements is beyond the capability of current fabric weaving machinery.

Implementation of the uO-Tow process is reliant on the availability of a manufacturing process tailored to its specificity while addressing the issues of efficiency and

reproducibility facing current 3D preform manufacturing. The remainder of this chapter is devoted toward outlining the design, manufacturing and development of the proprietary pre-production machinery used for automating preform manufacturing, designed to be compatible with the aforementioned tailoring process. Mechanical, electrical and electromechanical systems and interfacing thereof will be discussed in detail.

4.1 Overview of the manufacturing process

Physical preform manufacturing occurs in two distinct operations, implemented in two distinct machines: the laydown machine (LM) and the contour stitching machine (CSM).

Manufacturing begins on the LM, a CNC-device with four axes of motion and two service axes. The LM tracks above a part-specific manufacturing substrate while depositing individual tows. Deposition continues until the specified preform geometry and thickness are reached. The deposited tows are then transferred to the second machine, CSM, where a thermoplastic or semi-structural stitch is inserted to assemble the tows into a preform. The stitch secures the tows into final position; when sewn with a semi-structural thread it can provide limited through-thickness reinforcement.

4.2 Laydown machine

4.2.1 Introduction to the laydown machine (LM)

The laydown machine (LM) was developed to automate the tow placement operation, Figure 4.2. The machine operates on principles similar to those of tape or towpreg laying systems, however the development of the LM is centred around deposition of dry carbon tows, most commonly using 12k tows.

Carbon tows are deposited via a specially developed deposition head that is able to track above a large aluminum base using electromechanical actuators.

The tracking system incorporates a total of four positional actuators, three linear (X,Y,Z) and one rotational (A), providing precise open-loop control of the deposition head's position, velocity and acceleration in four degrees of freedom (DOF). Additionally,

the LM has two service axis (V,C); the V axis is used to control the tow payout system and the C axis is used to control the cutting system. Tows are deposited by tracking the deposition head along the intended trajectory and coordinating tow-payout with tracking velocity.

By coordinating motion along linear axes X and Y with rotation around the A axis, curved tow paths can be deposited in the X–Y plane, allowing production of reinforcements with local variations in tow spacing. Similarly, tow paths may be curved to better orient fibres along principal loading axes or to navigate around cutouts and other structural or assembly features.

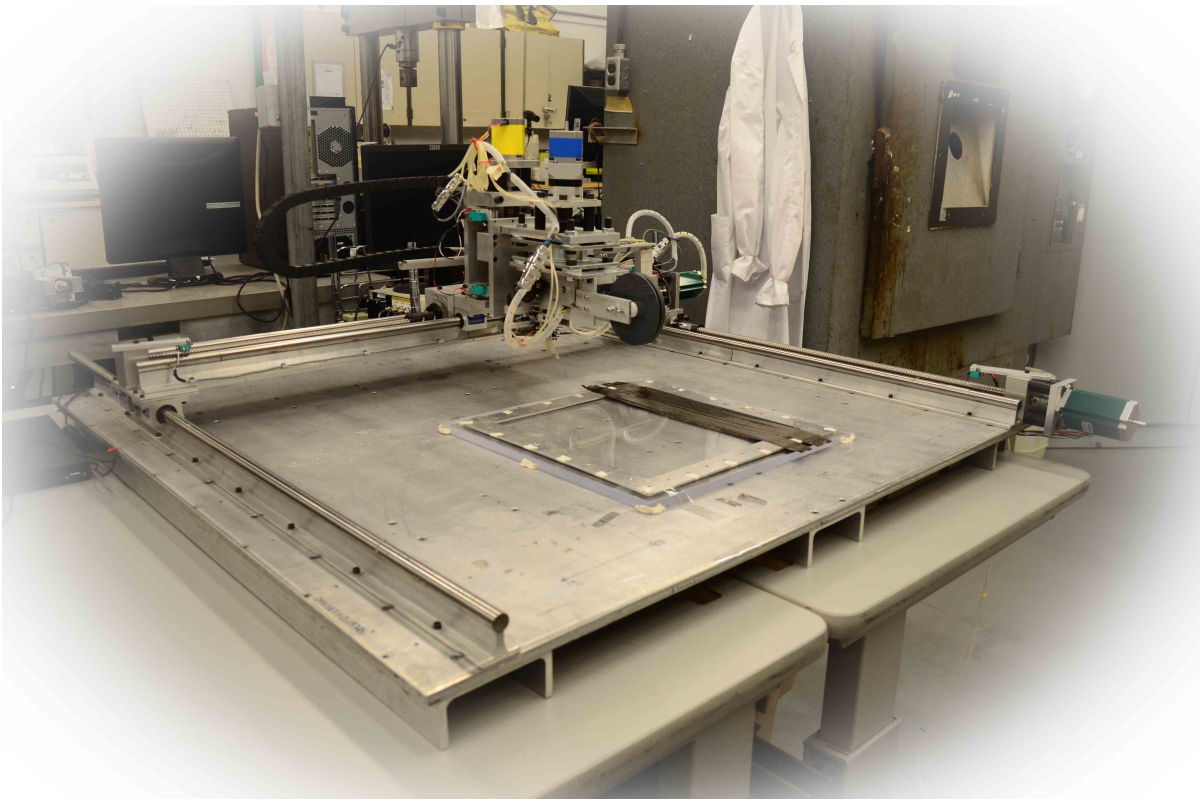

Figure 4.2: The laydown machine.

Laydown begins by positioning and levelling of the substrate designed for the intended reinforcement geometry, Section 4.3.3.4. The deposition head is brought in contact with the substrate reference point and the head position is registered. A continuous carbon tow is loaded into the deposition head and final pre-operation checks are performed. The

LM is programmed by loading a specific NC program and a cue for machine start is given, beginning tow laydown.

4.3 Laydown machine systems and components

The LM features various systems, namely the machine control unit (MCU), tracking, tow payout and manufacturing substrate systems. These systems and their main constituents are summarized in Table 4.1 and discussed in respective sections.

Table 4.1: Systems of the laydown machine and their main constituents.

System	Constituents
MCU	PC, main board, motor drivers, sensors and PSU
Tracking	Stepper motors, ball screws and ball nuts, linear bearings and rails and gantry platforms
Tow-Payout	Tow spool, feed & cut mechanisms and feed nozzle
Manufacturing substrate	Substrate and transport frames

4.3.1 Laydown machine Machine control unit (MCU)

The MCU is the system responsible for receiving human instructions as NC-code or direct input, logging machine position, performing kinematic and trajectory calculations and providing electrical input/output connections necessary to drive stepper motors, monitor sensors and interface with peripheral devices, Figures 4.3 and 4.4. It is the system which provides power, control and regulates all electrical systems. The MCU features various subcomponents including a PC, logic controller, break-out boards, motor-drivers (power-electronic amplifiers), power supply units (PSUs), limit switches, heat sinks and peripheral connections. Table 4.2 presents a summary of the components and quantities found within the MCU. The internal layout and main component relationships within the MCU are depicted in Figure 4.5.

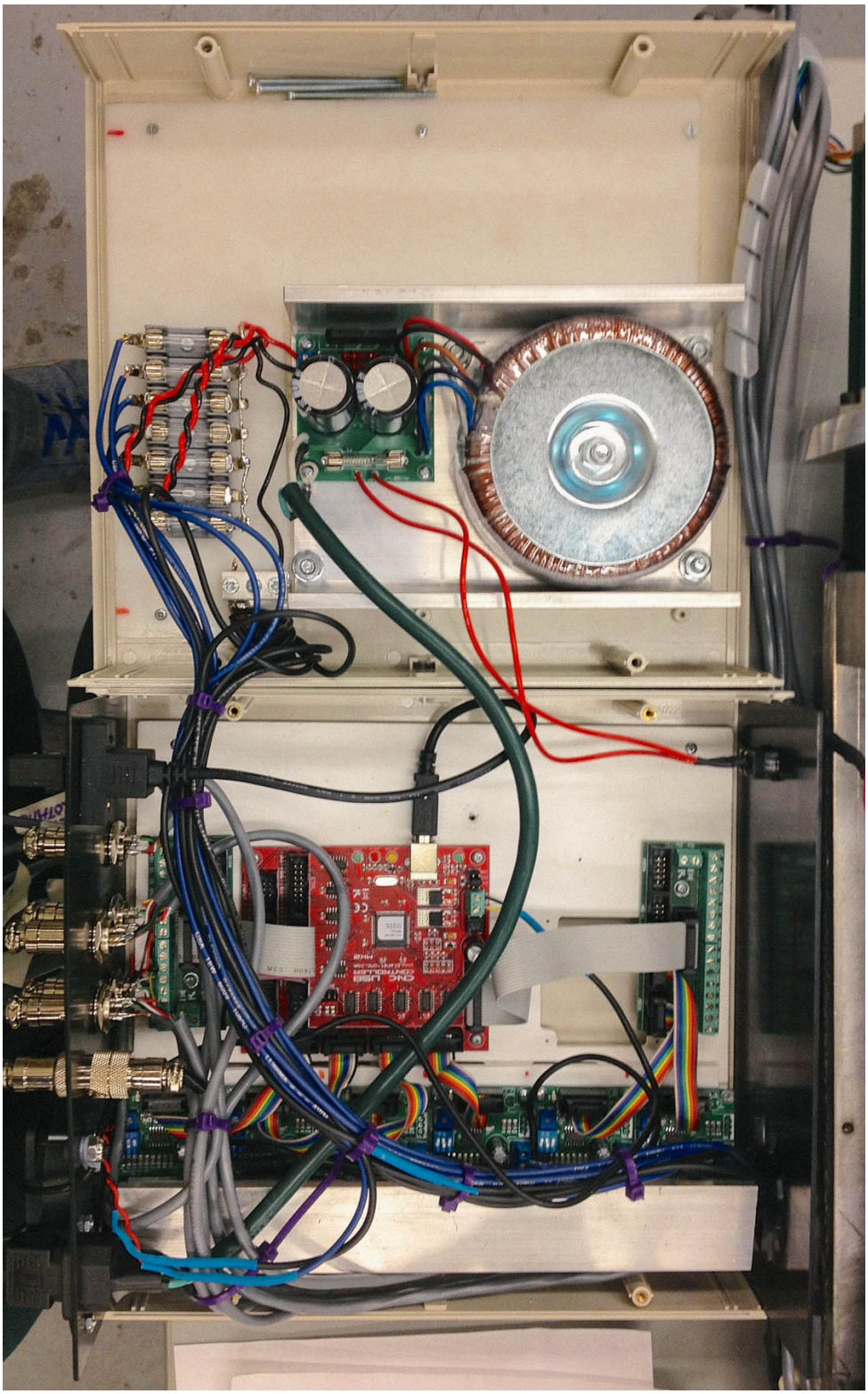

Figure 4.3: The MCU's internal components.

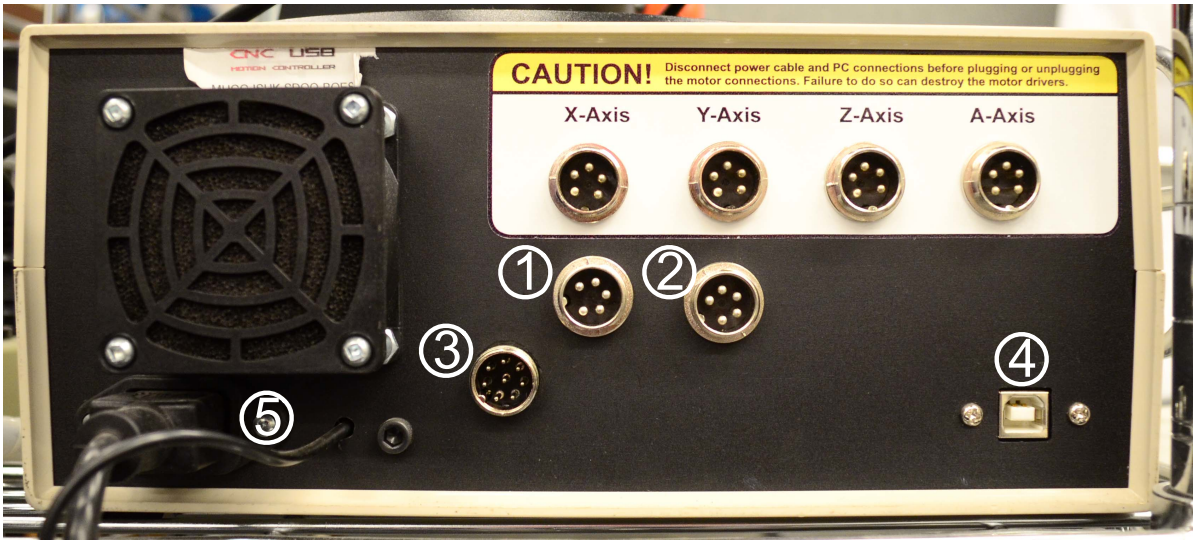

Figure 4.4: Rear of the MCU housing and its peripheral connections. ① V axis connector (tow payout), ② C axis connector (cutting), ③ limit switch connector, ④ USB in, ⑤ AC/DC in .

Table 4.2: Major components housed within the machine control unit (MCU).

Function	Component	Quantity
Human interface device (HID)	PC	1
Main logic control board	Mk2	1
Breakout board	-	2
Motor driver	Unipolar Stepper Motor Chopper Driver	6
Power supply unit (PSU)	40VDC - 10A Linear PSU	1
Power supply unit (PSU)	9VDC PSU	1
Fuse	3A - 250V AGC slow blow fuse	7
Cooling/heat management	9VDC - 0.25A 60 mm x 60 mm fan	1
Peripheral connectors	5 pin DIN connector	6
Peripheral connectors	8 pin DIN connector	1

The MCU controller housing is fitted with several receptacles intended for specific input and output connections, Figure 4.4. Six 5-pin and one 8-pin threaded DIN connectors were installed to attach the six stepper motors and limit switches respectively, Figure 4.4. One IEC 60320-1-C14 connection was fitted to provide 120VAC line voltage

to the linear PSU which services the stepper motor drivers. A usb 2.0 type B receptacle was fitted to the housing to provide direct interface with the main board. Not pictured in Figure 4.4 is the 9VDC PSU, which has no connection port, but instead is attached directly to the MCU housing. The 9VDC PSU services the main board and cooling fan.

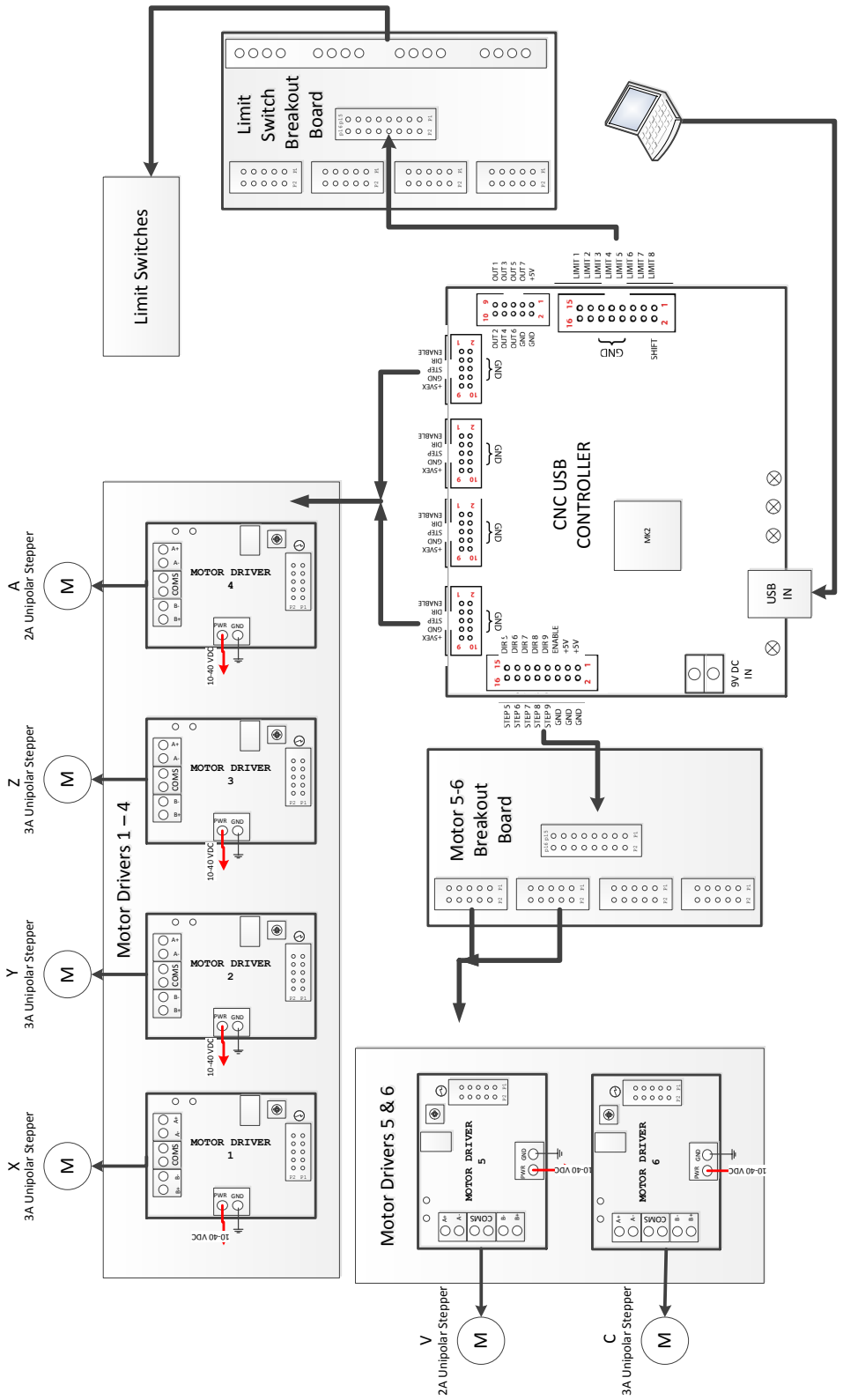

Figure 4.5: Diagram showing the controller system

4.3.1.1 Mk2 main control board

The main board housed within the MCU is a model Mk2 manufactured by Planet-CNC, Figure 4.6a. The main board interfaces via USB 2.0 with a PC running Planet-CNC software, namely CNC-USB. CNC-USB provides a machine-operator interface, allowing the MCU to be programmed with previously written G-code[1] file used in manufacturing, and manual control of the machine's motion ('jogging') which aids in machine setup. G-code programs are processed in sequential block-by-block order by the CNC-USB software and transmitted to the Mk2 board via the USB connection; each instruction block is processed and transmitted after complete execution of the previous. Position data is stored within the Mk2 board and transmitted back to the computer in real-time, allowing it to be monitored by the machine operator. Kinematic calculation are performed by the Mk2 board using the stored current position, active coordinate system and desired motion commands.

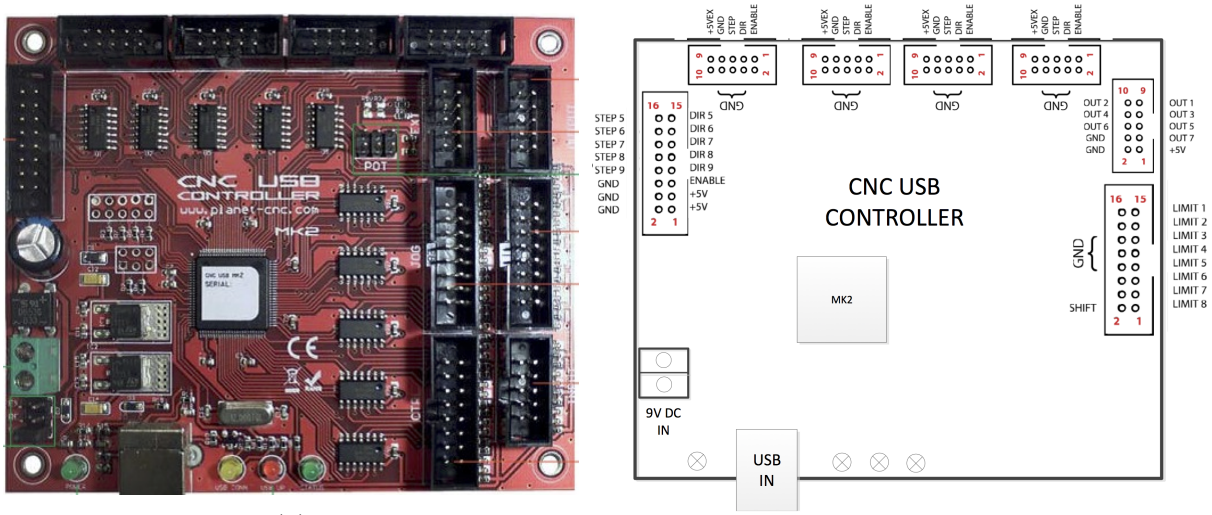

(a) (b)

Figure 4.6: (a) Mk2 CNC controller board [85] (b) relevant connection busses on the Mk2 controller.

The MCU main board communicates using digital logic signals at $\sim$ +5VDC. When motion of a given axis is requested the main board transmits the corresponding digital

[1]For more information on G-code see Section 2.8.1.

instruction signal to the axis' corresponding motor driver. The motor driver translates the instructions signal from the format used by the main board into that understood by the stepper motor. Then, the motor driver amplifies the signal to deliver it at the intensity required to drive the stepper.

Table 4.3: Features of the Mk2 board [85].

Features
• 100 kHz maximum step frequency • 7 digital outputs • 12 μs minimum pulse width • manual jog input keys for all axes • limit keys for all axes • 5 general inputs • 8 control inputs for pendant or similar device • SD card support for running G-code without computer • control external devices with I2C protocol

4.3.1.2 Motor drivers

Instruction signals sent from the Mk2 main board are incapable of interfacing directly with a stepper motor; signals from the Mk2 differ in format from those expected by a stepper and lack the required power required to drive a motor. As a result, intermediate motor driver circuits which boost and translate the low power signals sent by the Mk2 are installed between the Mk2 and each stepper motor. The motor driver circuit boards selected for the application are ProboStep unipolar motor drivers manufactured by Probotix® , built around the Sanken® SLA7078MPR power management integrated circuit (PMIC) with built-in control system and translator. Each driver board is capable of servicing one 8-wire unipolar stepper motor rated to an operational maximum of 44V and 3A. Six unipolar motor drivers are housed within the MCU.

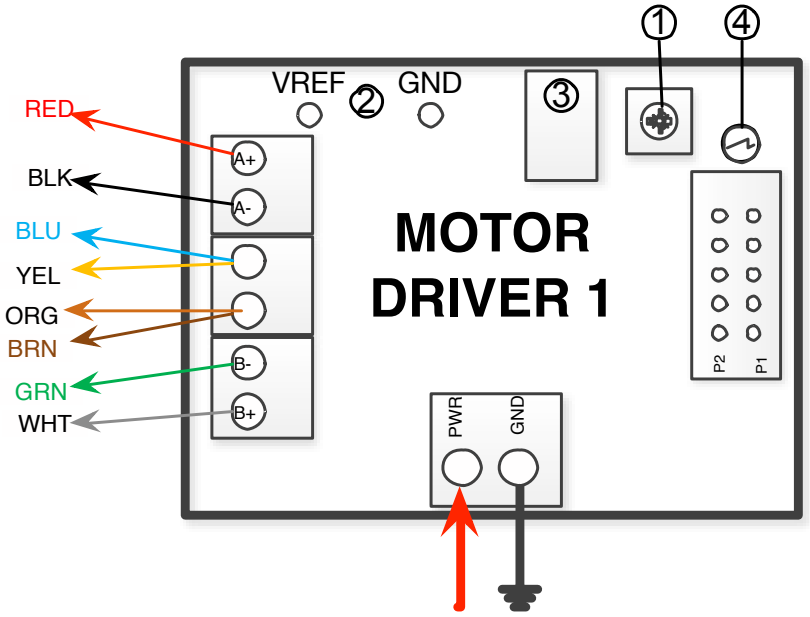

Figure 4.7: Diagram of one of the six identical motor drivers. Labelled items are: ① V_{ref} trimmer, ② V_{ref} & GND test points, ③ mode switches, ④ power LED.

Aside from providing the signals necessary to drive stepper motors, motor drivers provide a failsafe mechanism within the MCU system. The driver boards are the only circuits within the MCU that are connected to the high-voltage PSU. Their isolation (physical and electrical) from the remainder of MCU circuitry provides a barrier, impeding the spread of damage that may be caused by an electrical malfunction or spike.

Each motor driver board also contains an electrical current regulator to limit the maximum electrical current supplied to each phase within a connected stepper motor; this is vital for preventing motor damage and damage to the motor driver itself. The regulator may be adjusted to any value of current less than or equal to the motor driver's maximum current (3A); all motor drivers installed within this project were adjusted to provide their respective motor with its maximum safe-working current, Table 4.7. This enabled each motor to provide its maximum rated output torque.

The motor driver's current regulation setting was verified by reading the voltage across the V_{ref} test points (Figure 4.7) while the motor driver is fully powered but not

connected to a motor[2,3]. The current limit value is obtained by comparing the voltage read with the specifications shown in Table 4.4. The current limit is adjusted[4] via the V_{ref} trimmer (Figure 4.7), by matching the read V_{ref} to that prescribed within Table 4.4.

Table 4.4: Table of V_{ref} for setting desired motor current limits.

Current per phase [Amps]	V_{ref} [Volts]
0.5	0.07
1.0	0.15
1.5	0.22
2.0	0.29
2.5	0.36
3.0	0.44

4.3.1.2.1 Heat management

A heat sink is required to cool the PMIC of any motor driver that provides more than 1A per phase. Every motor driver used within this project is set to provide a minimum of 2.0A and requires a heat sink. The heat sink installed complies with manufactures recommendations: a $25.4mm \times 25.4mm \times 3.175mm$ $(1'' \times 1'' \times 1/8'')$ aluminum T-section attached to the PMIC with thermally conductive paste and #4-40 machine screws.

MCU housings were shipped from the retailer with three motor drivers installed, which were all attached one long T-section heat sink in no particular order. While retrofitting the MCUs to support six motors, motor drivers were mounted on a similar but larger heat sink in order of descending current-limit setting. The cooling fan was retrofitted for installation nearest to motor drivers providing the largest output current, to direct cooling on the most stress-ridden circuitry.

Following retrofit of the LM's MCU more torque was sought from the (2.0A – 180 oz-in) C axis motor which serves to actuate the tow cutting mechanism. The torque provided

[2]Motors connected while making adjustments may experience excessive heating. Temperatures in excess of 100^oC are harmful to most stepper motors; internal melting and seizing may occur.

[3]Motor drivers with an output in excess of one amp per phase are required to have a heat sink. Extreme care must be taken when providing power to any motor driver without a heat sink.

[4]For more information see Appendix C, Page C.3

by the motor was already at its maximum, hence a stronger 3A- 280 oz-in motor was installed and the current regulator within the C axis motor driver was raised to 3A. Periodic monitoring of heat sink temperature was performed following the upgrade in an effort to ensure that the C axis motor driver was being cooled properly by the distant fan. C axis heat sink temperatures remained stable under high-load operation and relocation of the motor driver in closer proximity to the cooling fan was deemed unnecessary. The final order of the motor drivers within the MCU is summarized in Table 4.5.

Table 4.5: Table showing the order of the motor drivers as mounted within the laydown machine MCU housing.

Position from fan	1	2	3	4	5	6
Axis	X	Y	Z	A	V	C
Current (A)	3	3	3	2	2	3
Designation	lin.	lin.	lin.	rot.	payout	cut

4.3.1.2.2 Driving Modes

The Probostep motor driver supports five drive stepping modes, namely full-, half-, quarter-, eighth- and sixteenth-step, with two variations of the full-step and half-step drive modes which are named mode F and mode 8. The drive mode is selected via the setting the mode selector switches shown as ③ in Figure 4.7 to one of the configurations shown in Figure 4.8.

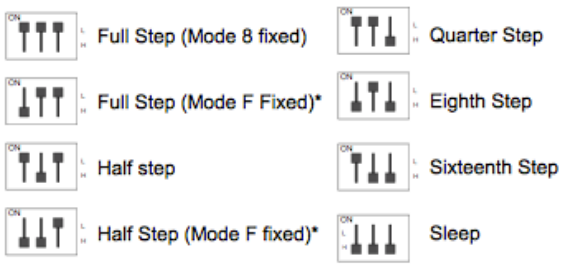

Figure 4.8: Diagram of driver operational mode switches [92].

In single-phase operation the motor driver provides power to a one phase ($A/\bar{A}$ or $B/\bar{B}$) within the motor at any given time, and torque is induced on the rotor is the

sole contribution of the single energized phase. In mode F and mode 8 the motor driver operates in a two-phase configuration, simultaneously providing current to two perpendicular stepper phases ($A/\bar{A}$ and $B/\bar{B}$), Figure 4.9. In this case both energized phases induce torque on the rotor; the total torque is equivalent to the vector sum of the phase contributions. Mode F delivers the maximum rated current-per-phase to both phases (100% current ratio between phases) and provides maximum torque output, Figure 4.9a. Mode 8 delivers 70% of the maximum rated current-per-phase to both phases (70% current ratio between phases), resulting in reduced torque output, Figure 4.9b. In mode F and mode 8 perpendicular motor phases are energized equally causing a 45^o shift in the detent (rest) positions, Figure 4.9 and Equation 4.4.

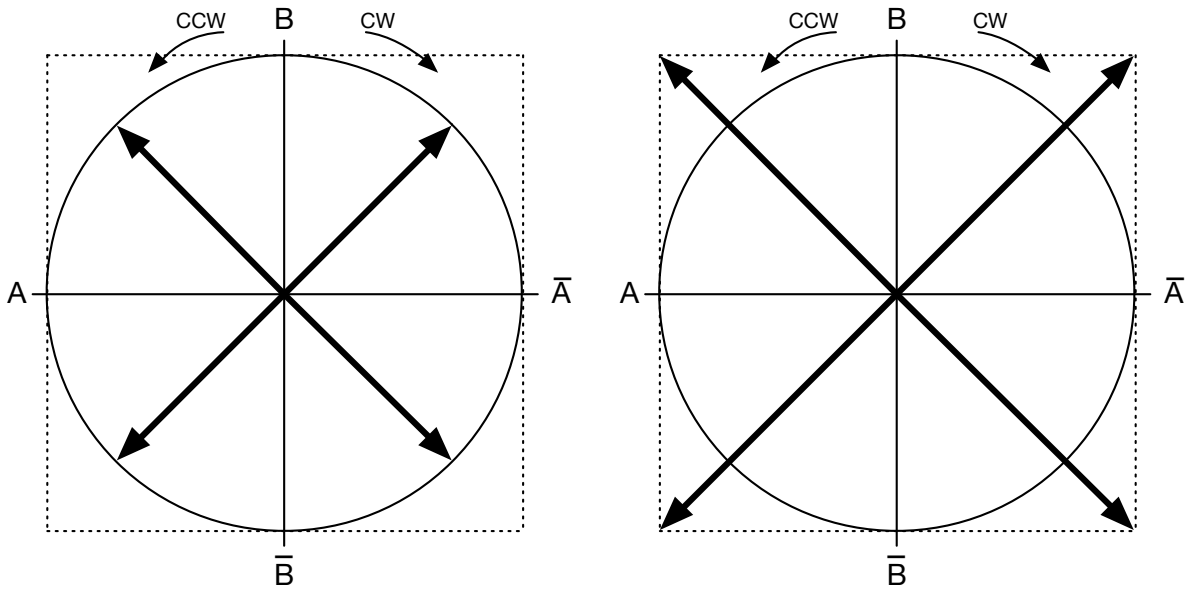

(a) (b)

Figure 4.9: Full-step phasor diagram in (a) mode 8 and (b) mode F.

Figure 4.9a shows the operation of full-step mode F where coils A and B are both energized at a 100% current ratio. This results in a torque that is greater than the motor's rating in single-phase operation; the resulting torque produced is proportional to the magnitude of the vector summation of orthogonal current ratio vectors I_A and I_B, Equation 4.1. The shift in detent positions is equal to the shift in phasor angle θ and is given by the trigonometric relation in Equation 4.3.

$$\text{Phasor length} = \sqrt{I_A^2 + I_B^2} \tag{4.1}$$
$$= \sqrt{100\%^2 + 100\%^2} \tag{4.2}$$
$$= 141.42\% \text{ torque}$$

Mode 8 operates by clipping all current ratios delivered to each phase ($I_A, I_{\bar{A}}, I_B, I_{\bar{B}}$) to $100\%(\sin 45^o) \approx 70.7\%$. This results in a phasor length of 100%, where the motor produces 100% of its single-phase rated torque – providing marginally smoother operation, Figure 4.9b.

$$\text{Phasor angle} = \arctan\left(I_B / I_A\right) \tag{4.3}$$
$$= \arctan\left(100\%/100\%\right) \tag{4.4}$$
$$= 45^o$$

Half-step operation is enabled by superimposing single-phase and two-phase operating configurations. Like full-step operation, it is available in both Mode F and Mode 8 configurations, Figures 4.10a and 4.10b respectively. Half-stepping has eight detent positions and provides smoother operation than any full-step driving mode. Half-step mode F allows the motor to alternate between 100% and 141% of the rated torque output, at times providing greater torque than half-step mode 8 at the expense of smooth operation.

All motors and motor drivers used in developing the LM and CSM were set to operate in full-step mode F.

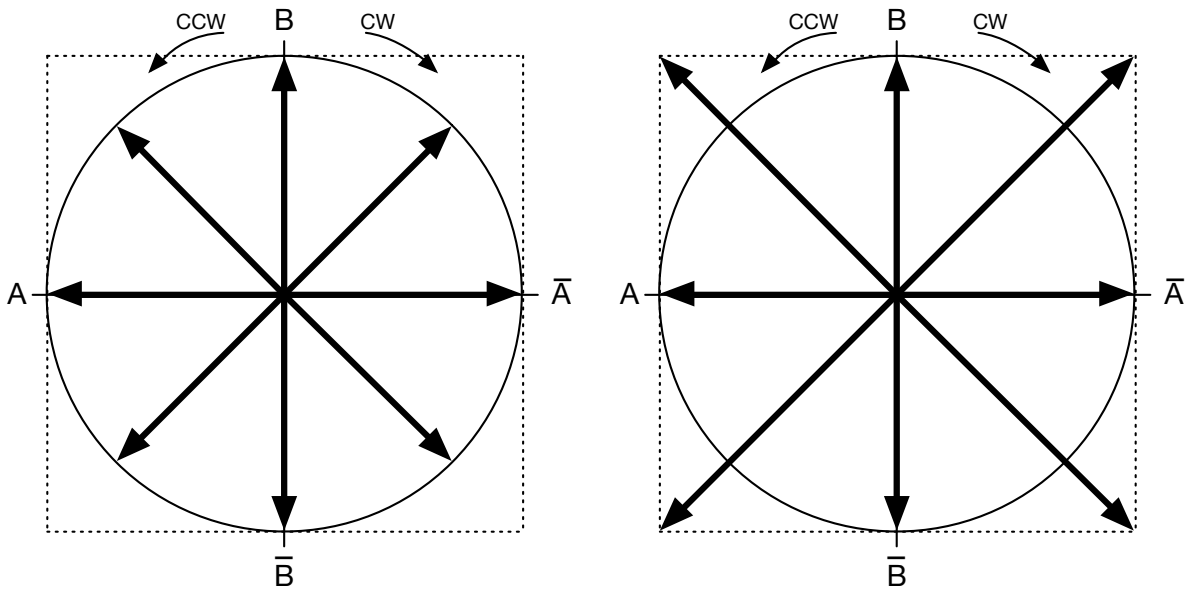

(a) (b)

Figure 4.10: Half-step phasor diagram in (a) mode 8 and (b) mode F.

Table 4.6: Warnings and cautions for motor driver operation.

Warnings and cautions
• Turn off box and wait one minute before disconnecting any motor or inductive loads. Failure to do so will result in destruction of the motor driver.
• Ensure that cooling fan always provides substantial flow over the motor driver heat sinks when they are powered.
• A heat sink and fan is required by any motor driver that is operating a motor rated at more than 1A.
• Never remove a connection to the stepper motor with power applied. There is a possibility that the SLA7078 IC will be damaged. The SLA7078 is rated for 46VDC max. The PSU voltage should be limited to 42VDC to allow for back electromotive force (EMF) generated by the stepper.

4.3.2 Tracking system

The tracking system features of components that allow machine elements to move and hold a precise position. These components consist of stepper motors which provide mechanical input, and various machine elements for converting the stepper motors' rotational motion into linear motion. These components include various bearings, rails,

gears, ball screws, ball-nuts and carriages. Carriages are stable platforms that serve as a mounting base for components that are intended to move via an electromechanical actuator. Carriages can be manufactured to allow motion in a linear or rotational path.

4.3.2.1 Linear motion

Three linear axes of motion exist on the LM, namely axes X, Y and Z. The X, Y and Z axes have a maximum travel of 83.8 cm (33”), 81.3 cm (32”) and 5.1 cm (2”) respectively, Figure 4.11. Linear axes have displayed reliable motion at rates in excess of 508 cm/min (200 in/min) and accelerations of 2.54 mm/^{2} (1 in/s^2), however while depositing a tow absolute feed rate was capped to a maximum of 323 cm/min (127 in/min), the maximum reliable deposition rate attainable by the deposition head, Section 4.3.3.

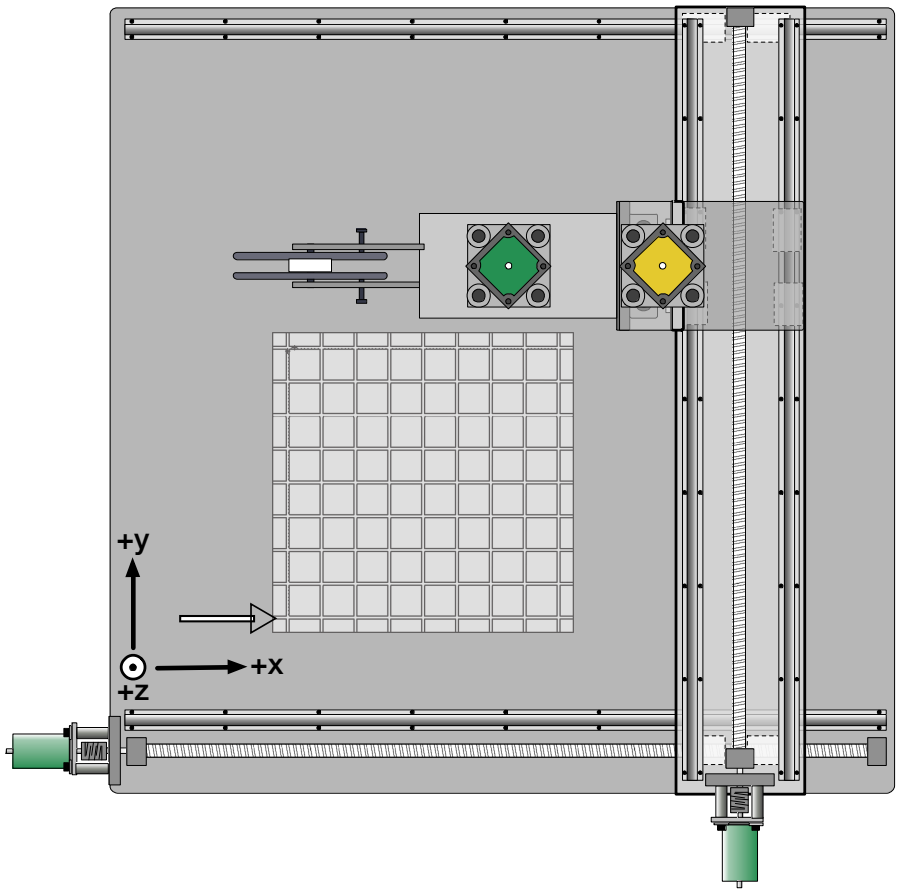

Figure 4.11: Laydown machine top view: solid arrows are machine’s coordinate system; hollow arrow is substrate’s first pin (Section 4.3.3.4.8).

For linear motion, components are mounted upon a carriage supported by linear bearings and rails such that a single degree of freedom exists along the rails' axis. Each carriage is coupled with a ball nut which is fixed within the reference frame of the carriage and a ball screw that runs parallel to the rails' axis, and is fixed within the stationary reference frame, Figure 4.12. Rotating the ball screw about its axis causes the respective carriage to translate along its linear bearings. Conversely, when no rotation is induced on the ball screw the carriage remains fixed within its current position and little to no holding torque is required on the shaft to prevent back drive.

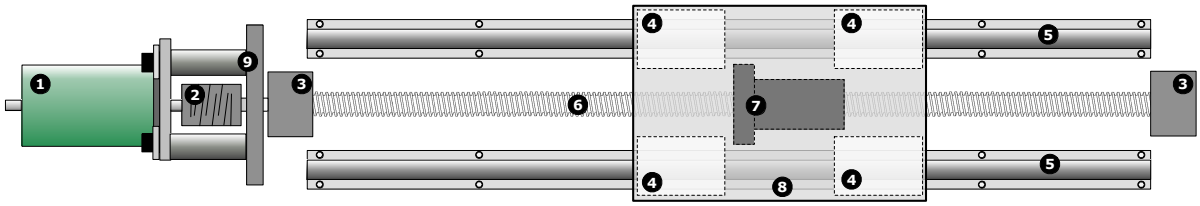

Figure 4.12: Linear motion actuator, top view: ① stepper motor, ② flexible shaft-coupler, ③ ball screw bearing-blocks, ④ linear bearings, ⑤ linear rails, ⑥ ball screw, ⑦ ball nut, ⑧ carriage, ⑨ stepper motor mount.

4.3.2.2 Rotational motion

The A axis is the only rotational DOF on the LM. The A axis allows the deposition head to rotate within a range of $\pm 135^o$

Original plans called for the A axis stepper to couple directly with the deposition head, allowing it to be rotated. It was originally hypothesized that the 1.8 degree full step resolution provided by the stepper motor would provide adequate control. However, upon testing several problems were encountered. The first was brought by nozzle offset, the distance between the axis of rotation and the deposition nozzle end, Figure D.1, which amplifies small discrepancies in angular position to unacceptably large deviations on in-plane position. The second problem stemmed from the large rotational inertia of the deposition head, which the motor struggled to accelerate or decelerate via a direct drive. The third and most significant problem of this initial design surfaced while attempting to maintain steady position of the deposition head: the directly coupled motor was incapable of suppling sufficient holding torque. While coming to a stop, the motor

allowed the deposition head to oscillate at significant amplitude and for a significant time before coming to rest near the motor's detent position. Once at rest, it was noticed that minimal disturbances caused by interaction of the deposition head with the manufacturing substrate would induce further oscillation. This underdamped behaviour had a detrimental effect to laydown performance, frequently causing the machine to deposit misplaced tows, hence a solution was sought.

The first solution considered involved configuring the A axis stepper to operate in the half-step mode F microstepping mode. Half-stepping the motor would double the number of detent positions to one detent every 0.9^o. It was originally proposed that increasing the number of detent positions would reduce the amplitude of oscillation, reducing the overall settling time. This was confirmed, however it was also noticed that disturbances acting on deposition head caused increased interference and position errors.

Half-step mode F operates in a one-two phase mode, switching between single-phase and two-phase operation every step. Hence, the holding torque at detent positions excited by two-phase operation located along phasor angles of 45, 135, 225, 315 degrees is equivalent to the holding torque in the previously used full-step mode F. However, holding torque at detent positions excited in single-phase operation along phasor angles of 0, 90, 180, 270 degrees is significantly reduced, leading to problems. In light of the aforementioned a solution involving the use of a reduction gearbox was probed.

4.3.2.2.3 Gearbox

A reduction gearbox placed between the stepper motor and the rotating deposition head would increase the holding torque well beyond the level sought, eliminating any measurable oscillations of the deposition head. Secondly, implementing a gearbox would largely increase the precision of the rotational axis. In view of these advantages, a reduction gearbox was installed.

The gearbox sourced for the application was a Carson 23SP010 10:1 single stage planetary gearset with specified maximum backlash of six arc-minutes. This gearbox was selected because of its inline profile where input and output shafts remain coaxial, and standard NEMA-23 input and output dimensions; the gearbox is designed to be compatible with and to mimic the motor geometry, requiring no modification to the existing motor mount. Figure 4.14, item ⑧ shows the gearbox and its installation configuration.

After installation of the gearbox, concerns about the linearity of axis response arose, spawning an investigation. The deposition head was rotated to eight positions interpreted as nondimensional values by the MCU and a machinists' protractor was used for measuring the resulting angle. The data was plotted and a curve fit displaying the head angle to MCU position transfer function was created, Figure 4.13. The response of rotational A axis displayed satisfactory high linearity.

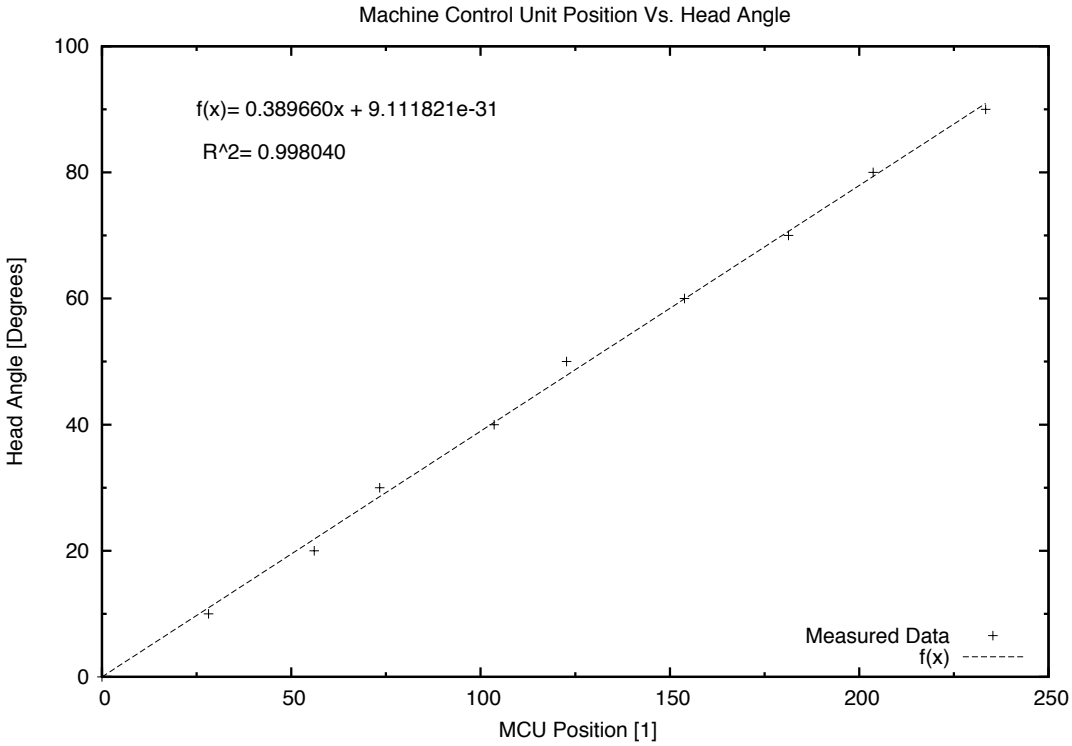

Figure 4.13: A axis (deposition Head) MCU position vs. actual position

4.3.2.3 Motors

The stepper motors used in the LM are eight-wire NEMA-23 frame motors supplied by Probotix® . Each motor has a full-step resolution of 200 steps/rev or 1.8^o/step and is

wired in a six-wire unipolar configuration. Motors were selected with consideration to dimensional constraints and torque requirements. Table 4.7 provides a summary of the motors selected for each axis and application.

Table 4.7: Summary of stepper motors used in the laydown machine.

Axis	Current [A/Phase]	Actuation	Role	Model # HT23-×	Max torque [N-m (oz-in)]
X	3	Linear	Drive X carriage	400-8	2.82 (400)
Y	3	Linear	Drive Y carriage	400-8	2.82 (400)
Z	3	Linear	Drive Z carriage	280-8	1.98 (280)
A	2	Rotational	Rotate deposition head	180-8	1.27 (180)
V	2	-	Tow payout	180-8	1.27 (180)
C	3	-	Tow cutting	280-8	1.98 (280)

Motors must be installed with due regard to shaft alignment. Misalignment in coupled rotating shafts is problematic not only during assembly, but also during operation. Misalignment is a source of vibrations and contributes to premature wear/failure of bearings and shaft components. In an effort to minimize such problems, components supporting and mating with other rotating bodies such as ball-screw bearing blocks were manufactured to tight tolerances on a CNC work centre. Shims were used for making minor adjustments in alignment while installing these components. Flexible shaft-couplings were used as a final defence in joining rotating components; bearing-blocks and motor mounts were designed to incorporate flexible couplings. Such couplings have intrinsic dampening effects and aid in reducing vibrations that are generated within the stepper motors during normal operation.

Table 4.8: Warnings and cautions for motor operation.

Warnings and cautions
• Motor connectors on the MCU do not provide identical power output. Be aware of the current supplied by each connector before plugging in a peripheral. For more information on the power provided to each axis see Figure 4.5.

4.3.3 Tow payout system

The deposition system is the part of the deposition head that is responsible for physically placing tows in sequence to construct a preform. It consists of various components including a tow reservoir spool, various tow feeding and guiding components, a tow cutting mechanism and manufacturing substrate.

4.3.3.1 Tow payout subsystem

The tow payout subsystem features components that facilitate the payout of tows onto the manufacturing substrate, Section 4.3.3.4. The tow payout subsystem assembly is often referred to as the deposition head. This subsystem features components such as the tow reservoir spool, inbound tow tensioner, routing rollers, tension roller, payout roller, feed nozzle, compressed-air pressure regulator and pneumatic distribution subsystem, Figure 4.14.

Carbon tow is stored within the reservoir spool, which is mounted on bearings that allow the spool to rotate freely and expel stored stock, Figure 4.14 ①. The inbound tow tensioner ② contacts the reservoir's outside walls and can be adjusted to apply variable pressure; friction created by the contact induces a drag force on the spool, allowing the tow to be tensioned. As the tow leaves the reservoir spool it passes over the routing roller ③, guiding the tow in a 90 degree bend and positioning it in between the traction rollers ④ and ⑤.

One driven ⑤ and one idle ④ traction roller are used to unwind the tow from the reservoir spool. The idle roller is mounted on an adjustable spring-loaded swing-arm, which applies a contact pressure onto the driven roller via the tow sandwiched between. The compressive pressure increases the friction between the driven roller and tow, eliminating slip from occurring and ensuring that an accurate length of tow is deposited at a rate matching that of the deposition head.

The driven traction roller is connected to the V axis stepper motor via a 1:1 timing-belt drive, hence the length and rate of tow payout is calculated with Equations 4.5 and 4.6 respectively. Figure 4.14 shows the path of the carbon tow as it unwinds from the tow reservoir travels over the routing roller ④, between the drive roller tensioner and drive roller ④ and ⑤ respectively, and through the feed nozzle ⑥. The tow is shown as a thick solid line when it is externally visible and as a dotted line when it is obscured by the feed head components.

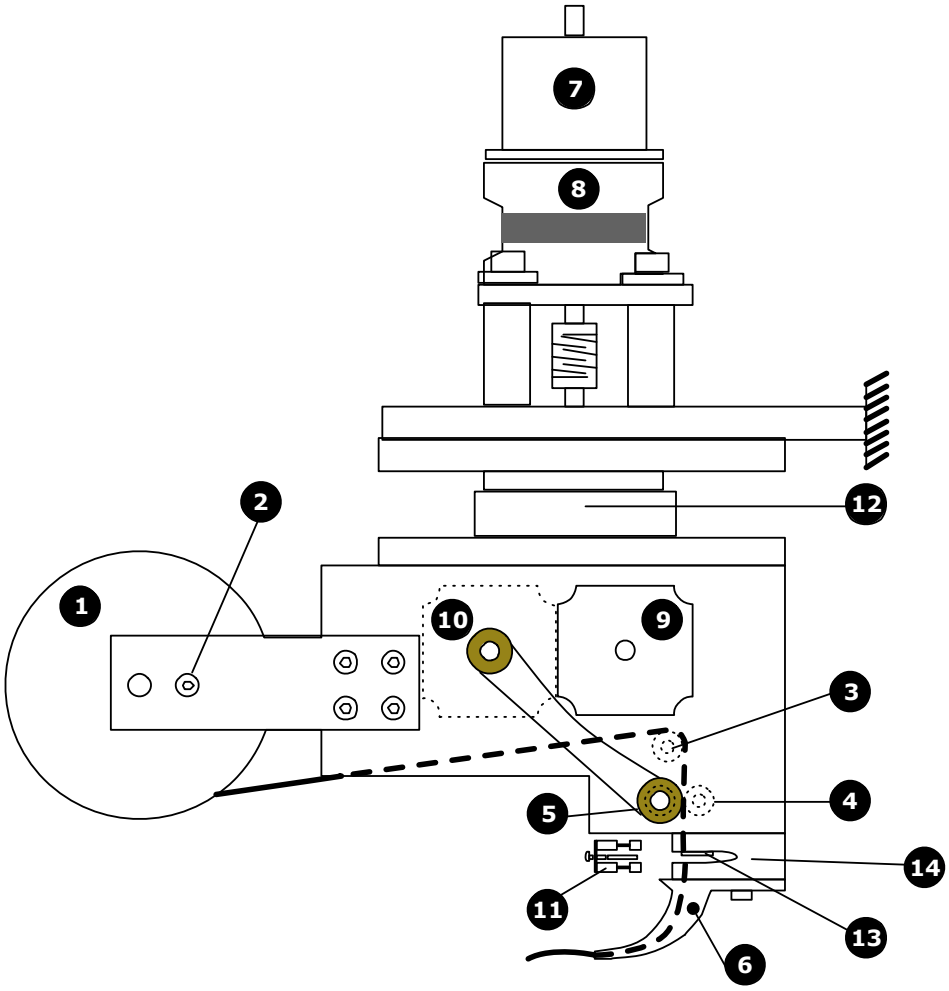

Figure 4.14: Components of the payout system: ① tow reservoir, ② inbound tow tensioner, ③ routing roller (idle), ④ traction tension roller (idle), ⑤ driven traction roller, ⑥ feed nozzle, ⑦ A axis stepper motor ⑧ planetary gearbox, ⑨ C axis (cutting) stepper motor, ⑩ V axis (payout) stepper motor, ⑪ cutting carriage, ⑫ head-rotation bearing, ⑬ fixed blade, ⑭ cutting block.

$$L_{tow} = \theta_v r_{dr} \tag{4.5}$$

$$\dot{L}_{tow} = \omega_v r_{dr} \tag{4.6}$$

4.3.3.2 Tow cutting system

The tow cutting system is actuated at the end of a tow laying cycle to separate the deposited tow segment from the remaining stock within the deposition head and its reservoir spool. The components of the tow cutting system are shown and listed in Figures 4.15 and 4.16.

Cutting is achieved by shearing the tow between two sharp blades. One blade is fixed in the frame of reference of the deposition head. The other blade is mounted on an arm which allows rotation. This arm is called the cutting carriage, Figure 4.14 (11). The cutting carriage is powered by the C axis stepper motor via a straight bevel-gear drivetrain, Figure 4.15 (2).

The cutting carriage also supports two spring-loaded pressure pads and a mechanism for adjusting their position relative to the moving blade, Figure 4.15 (8). During the cutting cycle, the pressure pads apply pressure to the tow via contact on both sides of the blade, fixing it into place and preventing the blade from uprooting the deposited portion of tow. The pressure pads also keep the tow taut during the cutting cycle, improving the reliability of the cutting mechanism and reducing the amount of tow fraying arising at the cut, which is important to reliable operation of the deposition nozzle.

4.3.3.2.4 Cutting cycle

The cutting cycle is initiated at the end of every tow laydown cycle by activating the C axis stepper motor. Tow payout is stopped and the carriage-arm pressure pads and moving blade move toward the cutting block and tow, Figure 4.16. Pressure pads make first contact with tow, above and below the blades. The carriage-arm continues to rotate toward the tow (7), compressing the pressure-pad springs (6) and exposing the tow to the moving blade (3), Figure 4.16. After the moving blade makes full contact with the tow, a high-frequency vibration is induced into the moving blade, as this was noticed to improve cutting reliability. Then, the carriage-arm is retracted, marking the end of the cutting cycle. In order to ensure that a complete cut is made, the cutting cycle may be programmed to repeat several times after each tow is deposited, Section 5.2.2.

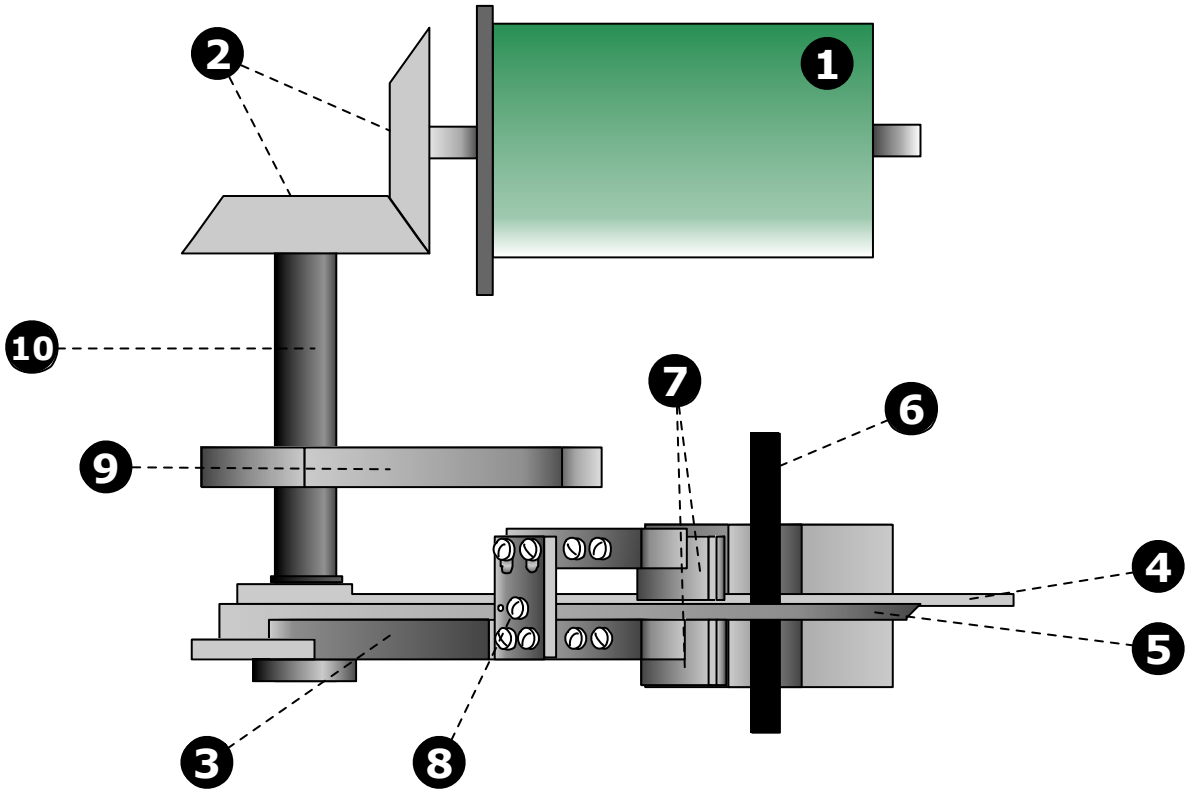

Figure 4.15: Front view of tow cutting mechanism: ① C axis stepper motor, ② bevel gears, ③ cutting carriage arm, ④ fixed blade, ⑤ moving blade, ⑥ tow, ⑦ top and bottom pressure pads, ⑧ pressure pad position adjustment screw, ⑨ cutting shaft bushing lower mount, ⑩ cutting shaft.

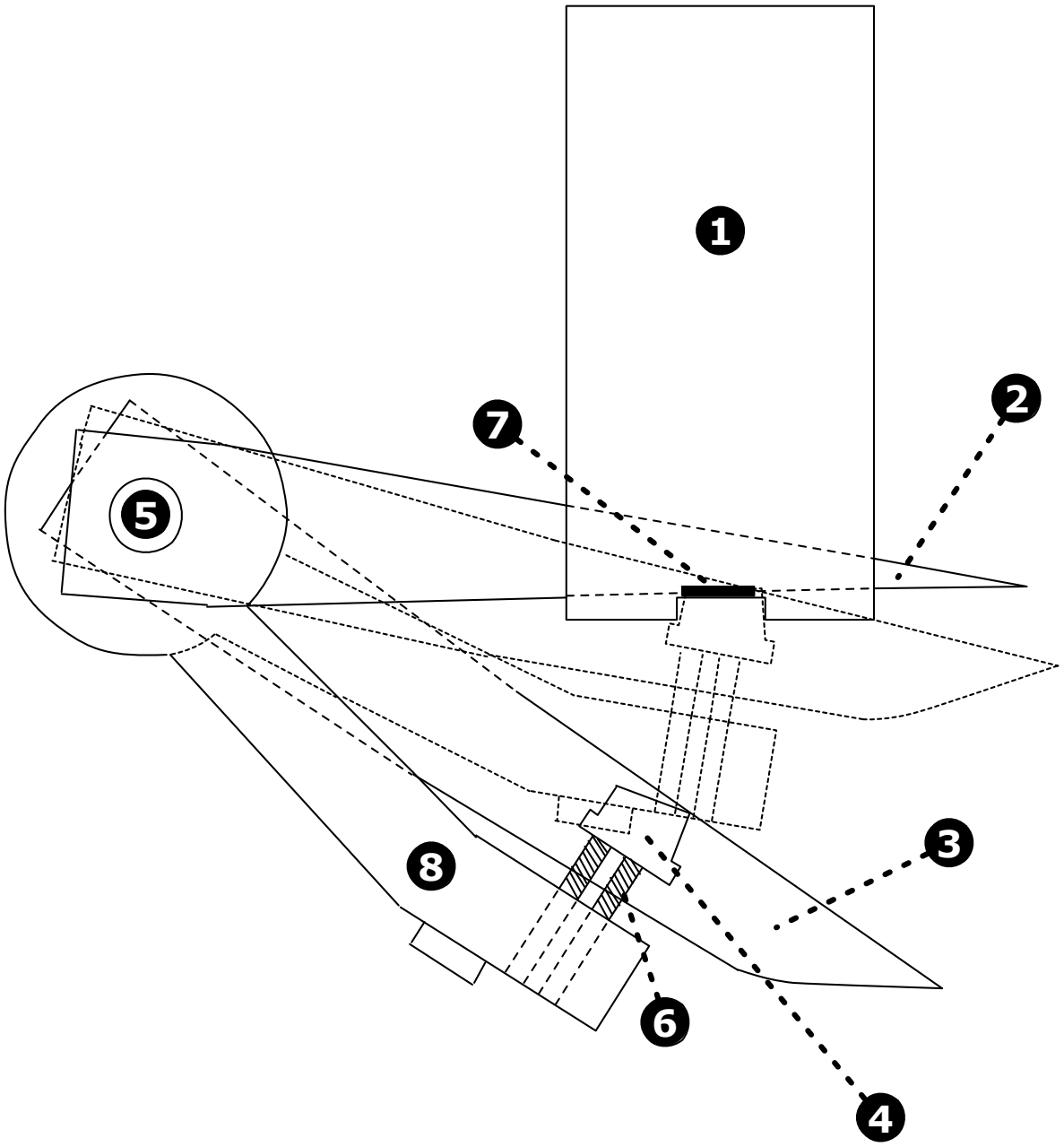

Figure 4.16: Top view of tow cutting mechanism; thick lines in payout position, thin lines in cutting position. Parts: ① cutting block, ② fixed blade , ③ moving blade, ④ top pressure pad, ⑤ drive shaft, ⑥ pressure pad springs, ⑦ tow, ⑧ cutting carriage arm.

4.3.3.3 Feed nozzle

The feed nozzle plays an extremely important role that consists in precisely placing the tows into their final position on the manufacturing substrate. Its proper operation is critical to the success of the manufacturing process; in its development, multiple design iterations were required prior to arriving at a reliably working prototype.

4.3.3.3.5 Design requirements and challenges

The use of dry fibres in the uO-Tow process introduces specific challenges not typically faced by towpreg and tape-laying manufacturing processes. Prepreg tape and tows are received on large spools, where each layer of material is separated with a paper backing that prevents adjacent layers from adhering to each other. In towpreg and tape laying this paper backing typically travels with the material until the material meets the tool surface, where the fibres adhere to the surface and the paper backing is peeled away, traveling back into the placement head and collected onto a spool, Figure 2.10. Following a cutting cycle, the paper backing, which remains intact, behaves like a heaving line and provides a reliable method for guiding the next piece of prepreg material through the guiding channel and onto the tool surface, Figure 2.10. Dry tows are not adhesive and they are supplied without a paper backing. Hence a system that is capable depositing dry tows requires a different technique to enable tow feeding to resume after a cut is made. This required the development of a nozzle through which a cantilevered and sometimes frayed tow-end could be fed reliably by a drive roller that is mounted upstream. This posed a challenge analogous to pushing a thread through the eye of a needle that is essentially equal in diameter to that of the thread, as there is a strict practical limit to nozzle width, which is discussed in this Section and Section 4.3.3.4. In addition the nozzle is a relatively long tube which contains a significantly sharp bend.

Towpreg and tape laying processes utilize the tack of prepreg materials by pressing them onto the tool surface during deposition, so that the materials adhere to and maintain their position on the surface. This is not possible with dry tow fibres. Hence, the uO-Tow process requires the use of a unique substrate to maintain the position of tows, and the feed nozzle had to be designed so that it would be compatible with said substrate. This substrate is discussed in Section 4.3.3.4.

In summary the deposition system required a feed nozzle design capable of:

- positioning tows accurately.

- positioning tows such that they remain in position throughout the remainder of the process.
- reliable operation after a cutting cycle (rethreading the fibre though the nozzle without jamming).
- reliable operation during a laydown cycle (no jamming during fibre payout).

4.3.3.3.6 Design iterations

The first nozzle design was a simple guide channel, Figure 4.17. It was manufactured from aluminium and attached under the cutting block. This nozzle design consisted of a single static open channel which was intended to guide the tow through a 90^o bend and onto the manufacturing substrate. In testing, the design operated unreliably. Tows often became jammed within the nozzle's sharp bend which caused them to buckle. This resulted in tows derailing out of the channel's guiding walls and deviating from their intended trajectory.

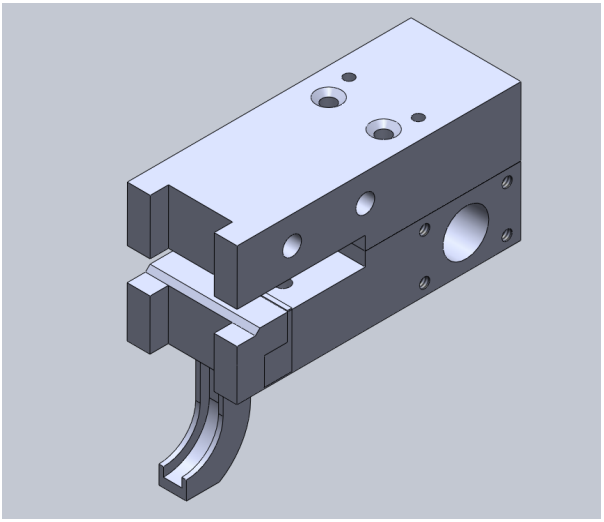

Figure 4.17: First nozzle design attached to the deposition head's cutting block.

Following a lack of success with the static nozzle design it was conjectured that a tow which passed through a nozzle in a state of tension would be less prone to buckling and jamming, leading to more reliable operation. Several designs of an active feed nozzle were

considered. These designs incorporated stepper motor driven rollers and/or conveyor belts which were mounted downstream from the cutting mechanism, in an effort to guide the tow to the substrate's surface while maintaining tension within the fibres. The driven components were positioned as close as possible to the nozzle's end in an effort to impart tension along the entire length of tow passing through it, Figure 4.18.

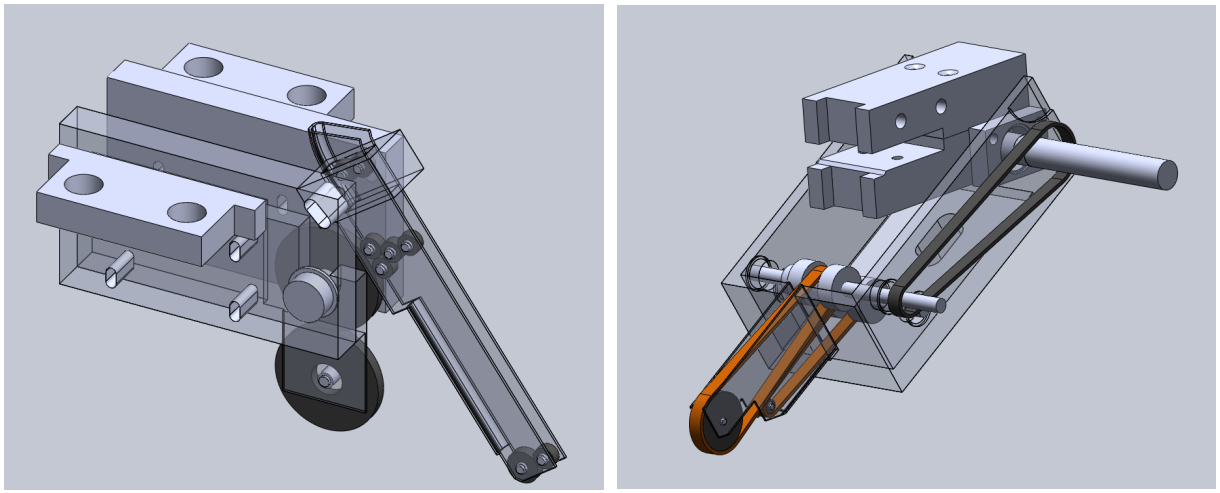

(a) (b)

Figure 4.18: (a) First active feed nozzle, shown without belts installed. (b) Second active feed nozzle design.

The first active feed nozzle design, Figure 4.18a, was tentatively approved prior to beginning the design of the manufacturing substrate. The feed nozzle used a large compaction roller and guide channel which were driven by externally arranged belt pulleys, Figure 4.18a. When it was realized that a substrate featuring guiding needles was required as described further in this chapter, unavoidable geometric interferences between the drive mechanism and substrate pins surfaced. The feed nozzle design was revised extensively to relocate the driving mechanisms within the feeding channel. Revisions were extensive and so the modified design was referred to as the second active feed nozzle design.

The second active nozzle design used two rear-driven conveyor belts to deliver the tow to the substrate's surface, Figure 4.19. One conveyor was positioned above the tow and the other below it, sandwiching the tow moving toward the substrate. The width of the final guiding channel was required to be no more than 6.0 mm to ensure compatibility

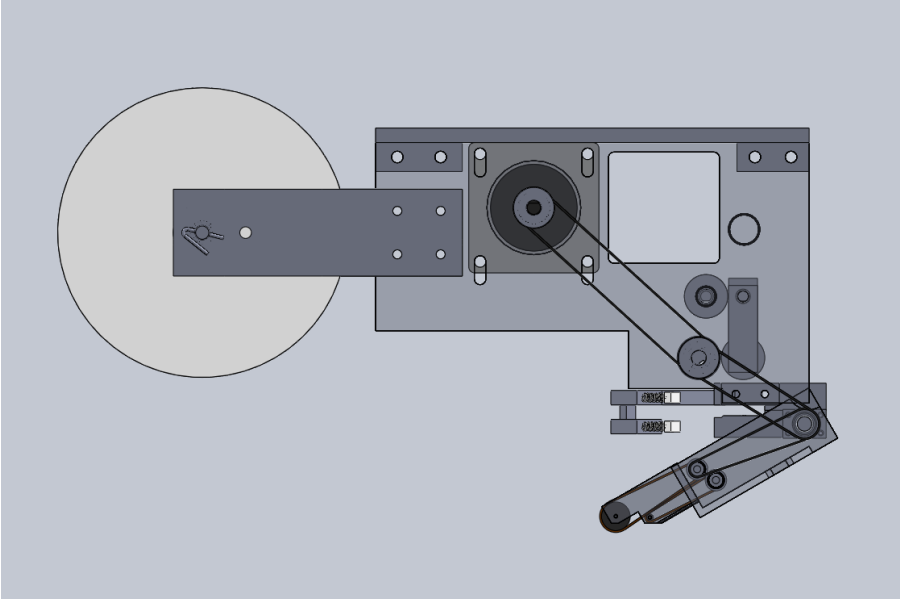

Figure 4.19: Second active feed nozzle installed within the deposition head.

with the pin-board type substrate. However, the width of belts and their respective pulleys had to be greater than or equal to the nominal width of 12K tows ($\geq$4 mm) in order to prevent fibres from becoming caught around pulley shafts or between belts and the channel's walls. As such, this spared less than 2 mm for the channel structure, pulley shafts and bearings. Nonetheless, the active nozzle design was completed and sent to the UO machine shop to be manufactured. Most of components were manufactured without complications; however, making the final channel structure proved more complicated. Attempts at machining the component's thin cantilevered sections failed due to excess cutting chatter, which ultimately caused the bit to bite into the thin material and destroy it. When manufacturing was attempted using sheet metal forming operations, required tolerances could not be achieved.

Problems extended beyond manufacturing and into the versatility of the nozzle, which was extremely limited. If a reinforcement design was to require wider tows, this nozzle would be incompatible. The whole nozzle up to the cutting block would have to be changed to a scaled-up version, requiring further manufacturing. High cost, lack of versatility, potential lack of reliability and challenges in manufacturing lead to abandonment of this design.

Problems encountered while manufacturing the thin geometry found in the active

feed nozzle design brought about the notion that of a type static feed nozzle could be manufactured using a one-step additive manufacturing process. Such a nozzle design would be exempt from many of the constraints imposed when designing a component for manufacture by conventional CNC machining. Additionally, production of a feed nozzle using additive manufacturing is significantly quicker than machining. As such, the time between nozzle prototype design and testing is greatly reduced, allowing more tuning of a design within a given time. A fleet of feed nozzles with various widths and geometries may be produced quickly, allowing a range of tow sizes. Inquiries into the cost associated with 3D printing a polymer feed nozzle revealed that outsourcing to a printshop was orders of magnitude less expensive than machining. On this notion, the green light was given to produce a first nozzle using additive manufacturing.

The first additive design sported a geometry largely similar to the initial static nozzle design, with a variable curvature and fully enclosed channel, Figure 4.20a. This was done in an effort minimize tow jamming and stop tows from escaping the guiding walls of the nozzle. The nozzle was manufactured by ShapeWays® using a which Multijet Modeling process which produces components from a UV curable acrylic plastic resin, Appendix B, Page B.2. The process produces high resolution components with a smooth surface finish and is capable of wall thicknesses as small as 0.3 mm. The cured plastic is translucent, allowing the tow to be viewed as it passes through it. Testing was performed with the component mounted on the deposition head; this revealed that the tight curvature near the end of the nozzle lead to frequent jamming.

The nozzle was removed from the deposition head and its end was trimmed using a bench mill. This removed the tight bend near the nozzle's end, slightly increasing the minimum radius of curvature of the nozzle. The modified nozzle underwent successive cycles of testing and material milling until a profile that performed well was found. This eventually lead to destruction of the first nozzle, but provided extremely insightful information that was used in designing following versions of the feed nozzle: versions two, three and four.

Feed nozzle version two exhibited a gentle curve sweeping to a final angle of 25 degrees with the substrate, Figure 4.21a. This nozzle operated with greater reliability than the first design. The frequency of tow jamming was greatly reduced. However, jamming still occurred approximately once every five laydown cycles, requiring improvement. The design also showed occasional problems in terms of interaction with substrate pins, specifically with pins that had been bent previously. Pins sometimes would deflect towards

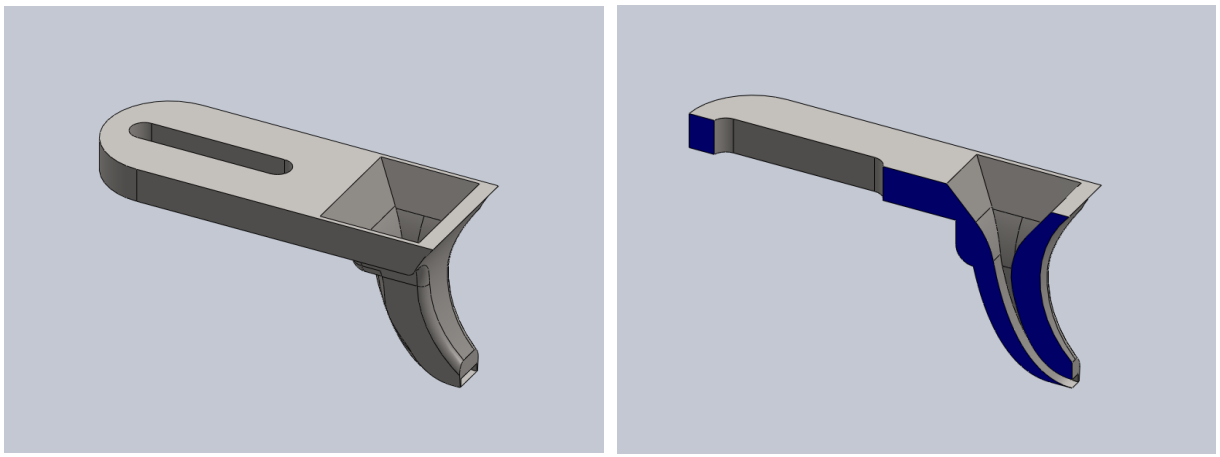

(a) (b)

Figure 4.20: Additive manufacturing feed nozzle version one; (a)full view (b) section view.

the wrong side of the nozzle, damaging them further while placing the tow incorrectly.

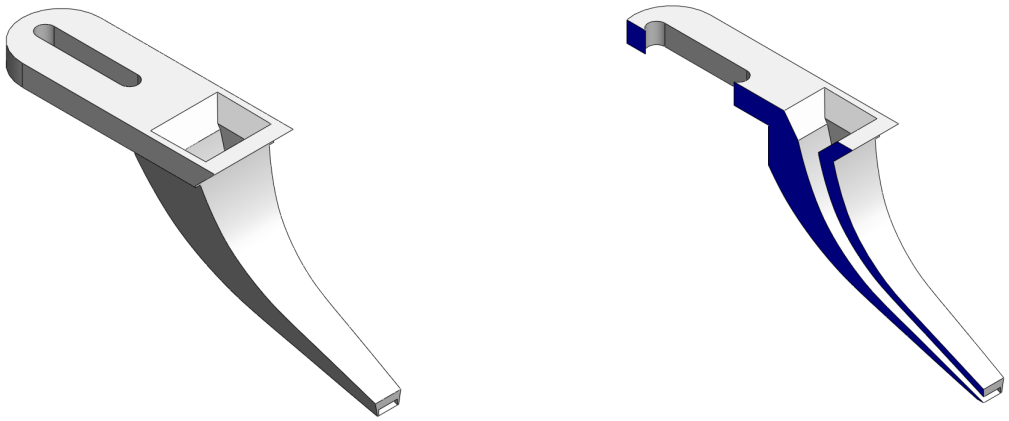

(a) (b)

Figure 4.21: Additive manufacturing feed nozzle version two; (a)full view (b) section view.

The third version of the additive feed nozzle featured two improvements over version two. The channel inlet was widened and large radii fillets were added to usher tows back into the correct path should the become astray, Figure 4.22b. The outside profile on the nozzle's leading face was altered from a pure parabolic profile to be slightly more

pointed in an attempt to better guide the nozzle through the manufacturing substrate. The change in the leading face profile resolved the issue where pins were deflected to the wrong side of the nozzle.

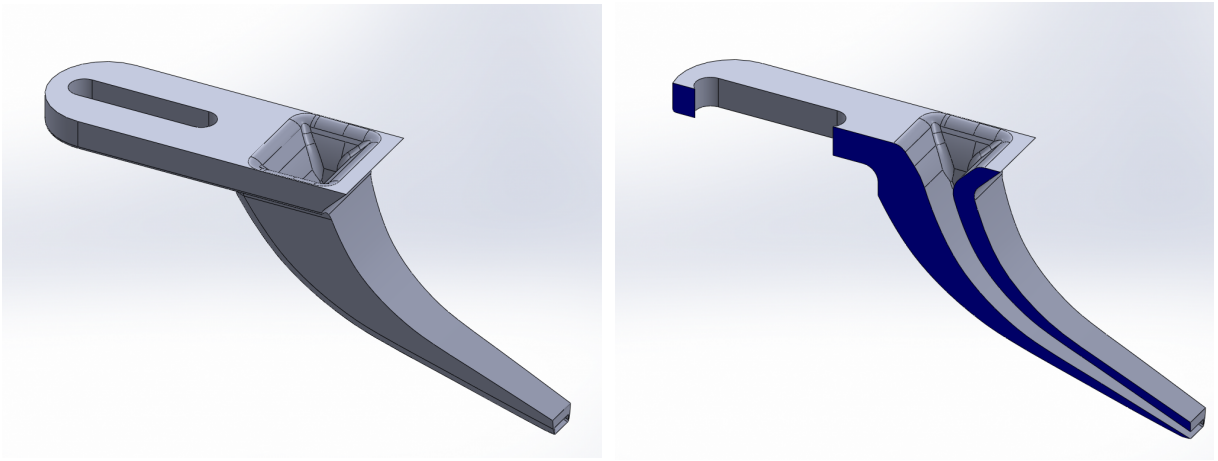

(a) (b)

Figure 4.22: Additive manufacturing feed nozzle version three; (a)full view (b) section view.

The fourth version of the additive feed nozzle is the final design to date, Figure 4.23a. Though the internal and external profiles are identical to those of the third design, this nozzle is drastically different from it predecessor. The nozzle contains two additional channels above and below the tow channel, Figure 4.23b. Compressed air is flowed though these channels to induce an area of low pressure at the tow channel inlet and provide a virtually frictionless cushion of air for the tow to ride on while traveling through the nozzle. The incorporation of this pneumatic conveyor further improved the overall reliability of the nozzle and largely eliminated tow jamming. Much improvement was noticed during tow clearing performed following a cutting cycle to remove the remaining portion of tow from the feed nozzle, whereas before the tow would occasionally remain stuck in the nozzle.

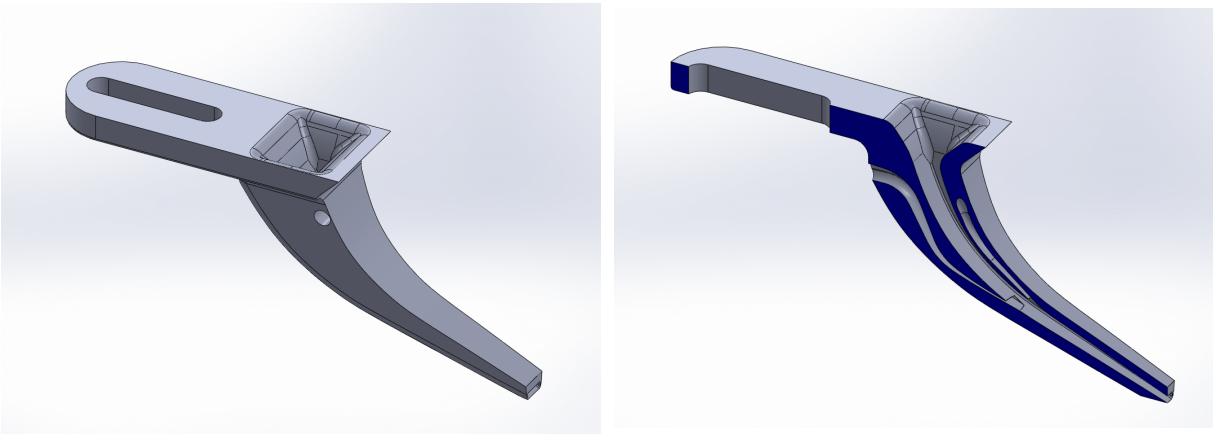

(a) (b)

Figure 4.23: Additive manufacturing feed nozzle version four; (a) full view, showing top air channel inlet (b) section view, showing top and bottom air channels.

4.3.3.4 Manufacturing substrate

The manufacturing substrate is the flat surface onto which steered tows are deposited. Dry tows are non-adhesive and non-tacky; as such, they are easily displaced from their position after they are deposited. Preforms that featured steered tows and variable tow spacings pose a greater challenge: variations in tow spacings requires the tows to bend. Carbon tows, which are made of extremely stiff, linear elastic filaments are resistant to bending and store significant amounts of strain energy as they are bent. Following such a deformation tows are unstable, and if left unconstrained they will distort into a configuration of lower strain energy. The type of distortion that may occur is influenced by the orientation in which the original deformation was incurred and by the presence of fixities acting upon the tow. If a tow is deformed in-plane and left unconstrained, it will naturally straighten itself while remaining in-plane, thus reaching a state of lesser strain energy.

Tows that are constrained with absolute fixities at both ends and are not able to straighten may still distort to achieve states of lesser strain energy. Consider the tow shown in Figure 4.24, which exhibits a 90^o in-plane bend where both tow ends are fixed. The bend occurs about neutral axis A–A; in this configuration the second moment of area is large and so is the stored strain energy. However, in accommodating constant fibre lengths the tow may twist about its longitudinal axis, resulting in bending occurring about the neutral axis B–B, Figure 4.25, which exhibits a lesser second moment of area,

and hence lower strain energy.

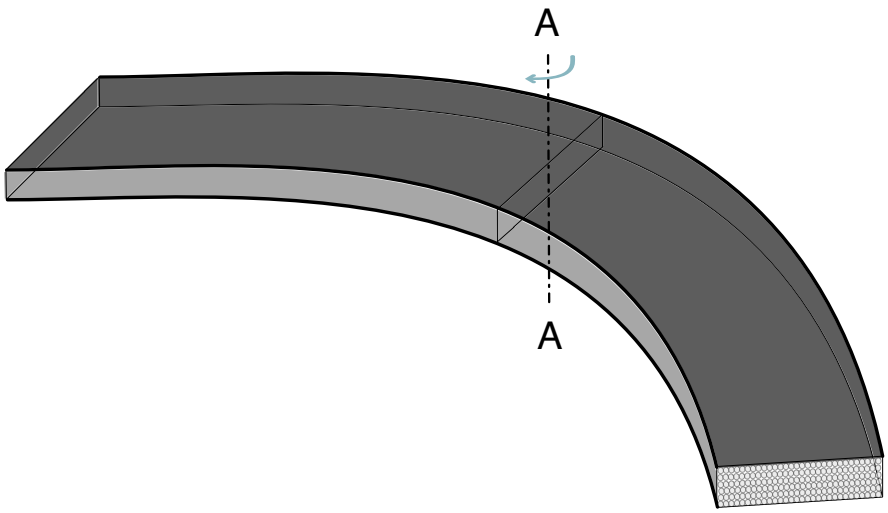

Figure 4.24: Tow bent in-plane without distortion.

In the context of the deposition system a substrate design that is capable of maintaining tow position (prohibiting tows from straightening) and orientation (prohibiting tows from twisting) is required. Several substrate design concepts were considered; the first was inspired by *Tow placement studies for liquid composite moulding, by CD Rudd et al. [73]*, which discusses a dry fibre placement technique that relies on a manually applied polymer/latex tackifier and porous suction bed to maintain fibre position.

A porous bed suction type substrate offers many advantages, including design simplicity, ease of manufacture and ability to function for a wide range of preform geometries. However, the use of a porous bed type substrate is also riddled with problems. Firstly, the large volume of air which is drawn continuously toward and through the preform is saturated with environmental pollutants, leading to preform contamination during manufacturing which may disqualify preforms from use in manufacturing high-quality components. Furthermore, as preforms are manufactured layer–by–layer contaminants would accumulate between each layer, worsening the problem. While a clean room environment could be utilized to solve contamination issues, clean rooms require large capital investment and continuous operational costs which would be prohibitive for many manufactures. Secondly, while suction provides a strong hold on the first layer of deposited tows, the holding force acting on layers deposited subsequently is minimal, requiring

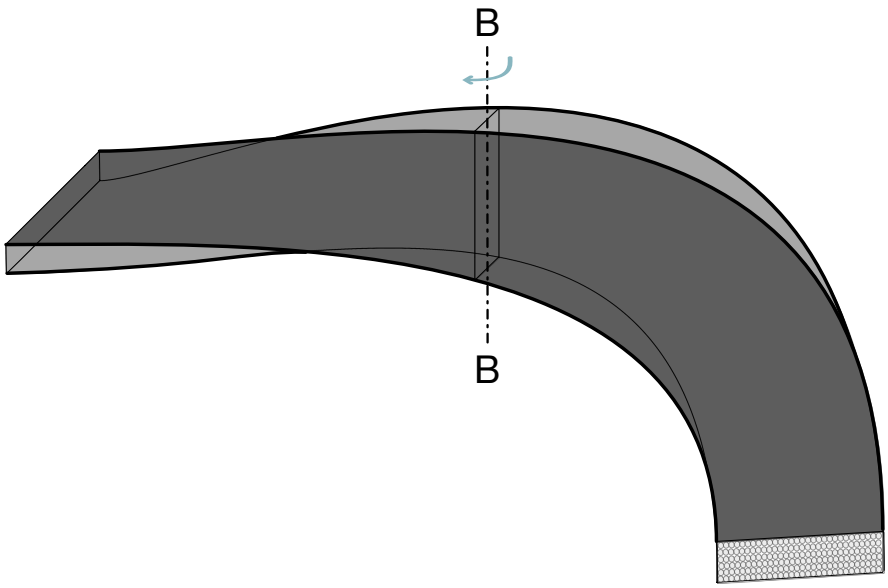

Figure 4.25: Tow bent in-plane with distortion.

tackifiers to hold these layers. As the uO-Tow manufacturing process is to avoid the use of tackifiers, a substrate design incorporating porous suction was ruled out.

A substrate which uses induced electrostatic charges to attract and hold fibres was considered. Electrostatic forces can act though previously deposited tow layers and apply a holding force on tows that are currently being deposited. Similarly to suction type substrates, electrostatic substrates display large part–to–part versatility and operate irrespective of preform geometry, subject to the preform fitting within the substrate's active area.

Electroadhesive systems have been demonstrated in machine-assisted preform layup where electrostatic attraction provides a mechanism for gripping fabric plies in performing pick-and-place layup operations. Such operations use manually-assisted ergonomic cranes or automated robotic arms [93–95]. Attraction forces are induced by a charge that is accumulated between one or more parallel-plate capacitors. In one-sided electrostatic gripping devices an alternating series of positive and negative electrodes are mounted within the gripper substrate and are charged using a voltage on the order of several kilovolts [94], Figure 4.26. A smooth surfaced dielectric material is used for separating the electrode from the fabric.

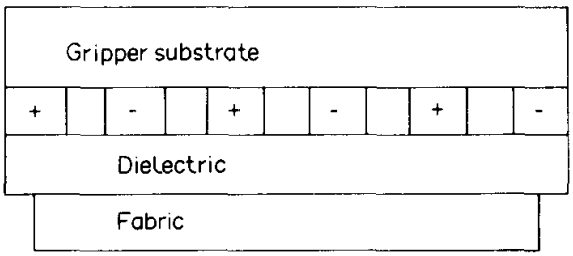

Figure 4.26: Dual-pole electrostatic gripper [94].

An electrostatic substrate for dry tow deposition is subject to the same contamination problem which plagues suction bed substrates. The forces that attract tows to the substrate also attract dust and other pollutants, contaminating the preform; the level of contamination is typically proportional to the electrostatic charge within the substrate and to the time duration which the preform rests on the active substrate.

Electrostatic charge is a hazard to the machine's electric systems and operator. A substrate of a practical size typically stores significant electric charges while operating. As such, failure of the substrate's electrical insulation may cause a discharge into the LM, easily destroying all electric components and systems therein. Similarly, if the substrate was to discharge accidentally into the machine's operator it could result in a fatality. Due to potential risks of such a system and limited design experience with high-voltage electrical systems, this type of substrate design was abandoned.

4.3.3.4.7 Final design

The final manufacturing substrate prototype was inspired by the apparatus used for maintaining tows in position when variable tow spacing preforms were manufactured manually as a proof of concept to the uO-Drape theory. This original apparatus, referred to as a pin-board, consisted of hundreds of stiff steel pins embedded into a thick polymethyl methacrylate – a transparent thermoplastic (PMMA) plate, Figure 4.27. Pins were placed into drilled holes located at 4.0 mm nominal intervals to support tows on both sides of each tow path. The placement of the pins ultimately dictated the preform geometry and the paths of tows running therein, hence a given pin-board corresponds to a specific preform and part geometry.

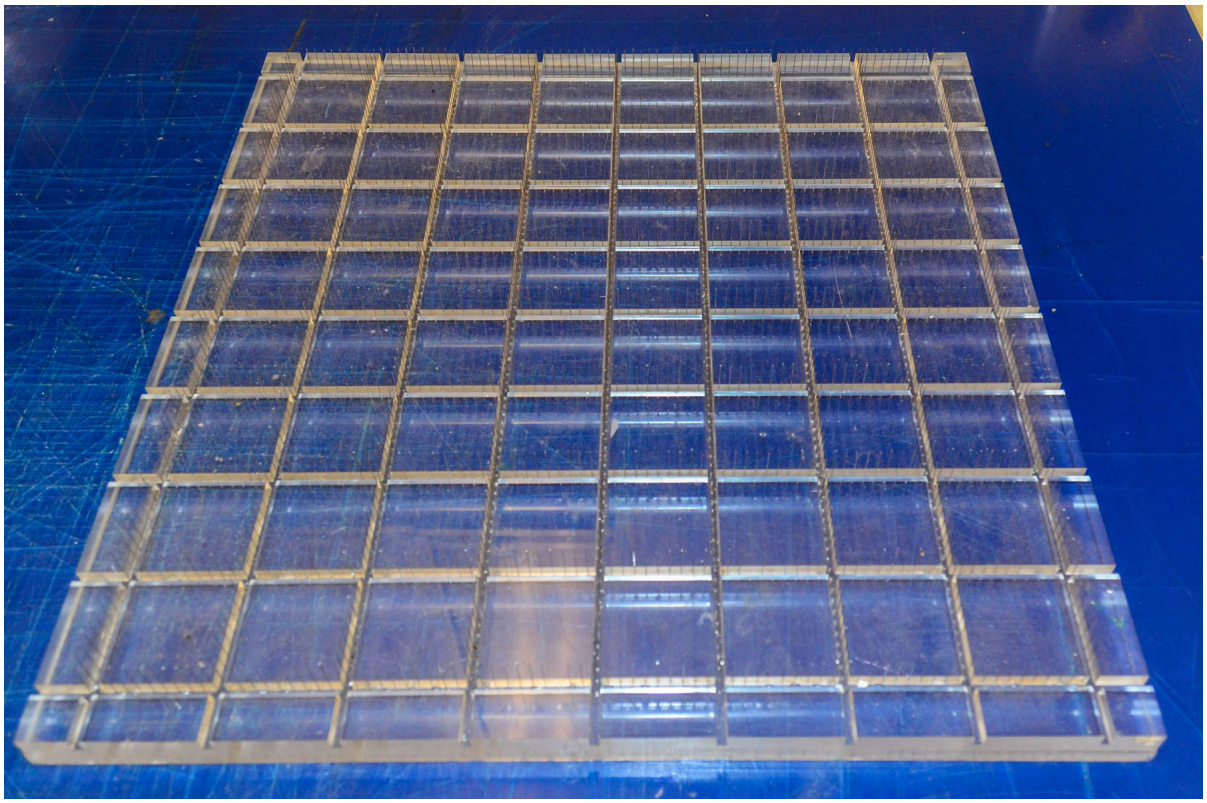

Figure 4.27: First prototype of a laydown machine manufacturing substrate, for production of $0^o/90^o$ preforms.

The original pin-board design is incompatible with the final version of the LM. Firstly, stiff pins were spaced at intervals nominally equal to the width of a 12K tows, 4.0 mm. As such it was not possible to design a feed nozzle capable of passing between the stiff pins while guiding the tow, which requires some thickness of material to be present along each side of the nozzle.

A new type of a pin-board was designed; the prototype was geared toward production of constant spacing $0^o/90^o$ bidirectional reinforcements with straight tows, Figure 4.28. This was designed to allow pins to spread apart when in contact with the nozzle, allowing it to pass though. After the nozzle ends contact with a pair of pins they immediately return to their neutral position, Figure 4.29a. In their neutral position, the pins are in contact with the recently deposited tow on both sides, generating frictional forces which hold the tow in place, Figure 4.29b.

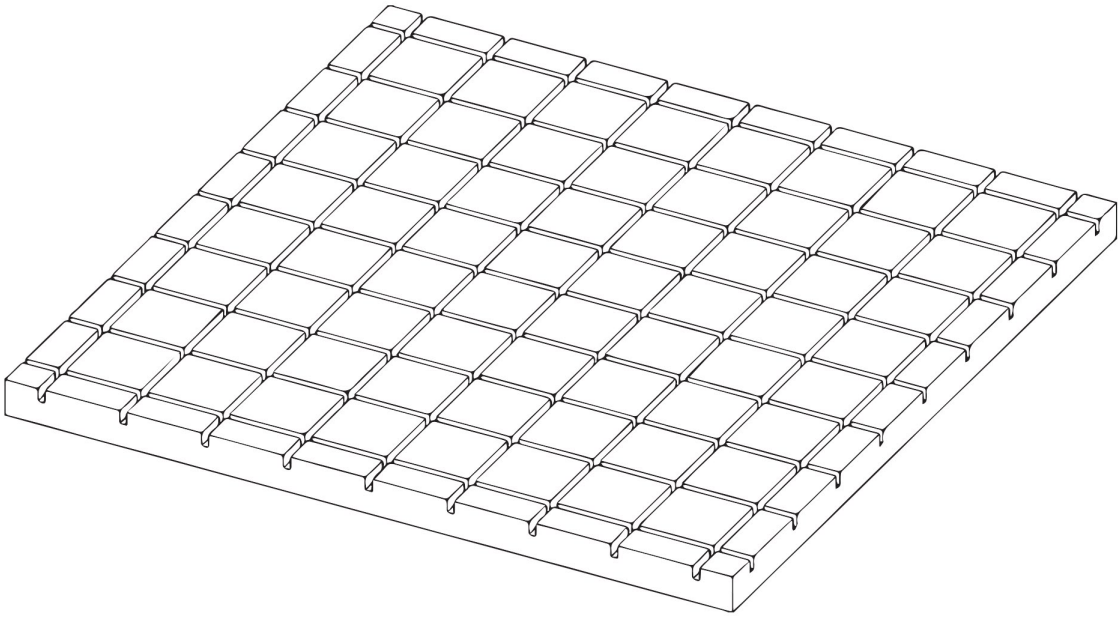

Figure 4.28: Final substrate base design; shown without pins inserted.

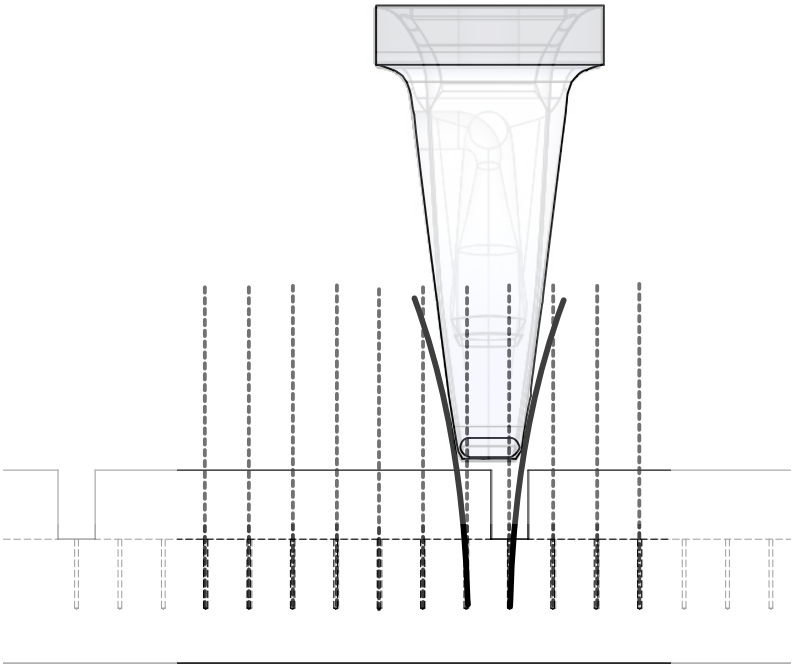

(a) Front view, pins' neutral positions show in dotted line; solid lines show pin's deformed positions.

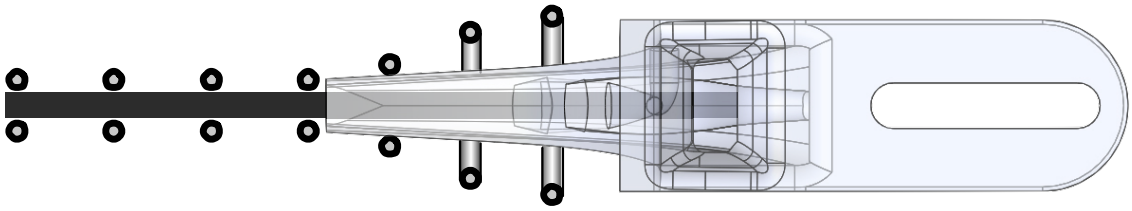

(b) Top view, interaction of feed nozzle and substrate pins.

Figure 4.29: Interaction of feed nozzle and substrate pins.

Pins were cut from 0.305 mm diameter spring steel wire and glued into sockets, holes drilled at 0.343 mm in diameter and 6.35 mm in depth. The socket holes were drilled at the bottom of 6.35 mm deep by 3.43 mm wide recessed groves, providing clearance for the pins to bend gradually in purely elastic deformation that allowed the pins to return to their neutral positions, Figure 4.29a. Implementation of these recessed groves prohibited pins from being placed around each tow intersection point; as such, pins were arranged in a courser grid made of single spaced pin rows in ten tow-width intervals.

In testing the substrate prototype functioned as intended, allowing the feed nozzle to progress through the pins easily and smoothly while holding the tows in position. Pins were removed in an effort to determine a minimum pin density required for successful operation; it was determined that the substrate functioned properly with as few as four pins per tow, two supporting each tow at each end, when depositing tows along straight paths, Figure 4.30. As such, and in effort to reduce substrate's manufacturing time, subsequent manufacturing substrates featured variable pin densities, where as few as four pins per tow were used for straight tows and higher pin density was used in areas exhibiting variable tow spacings and tow curvatures, Figure 4.31.

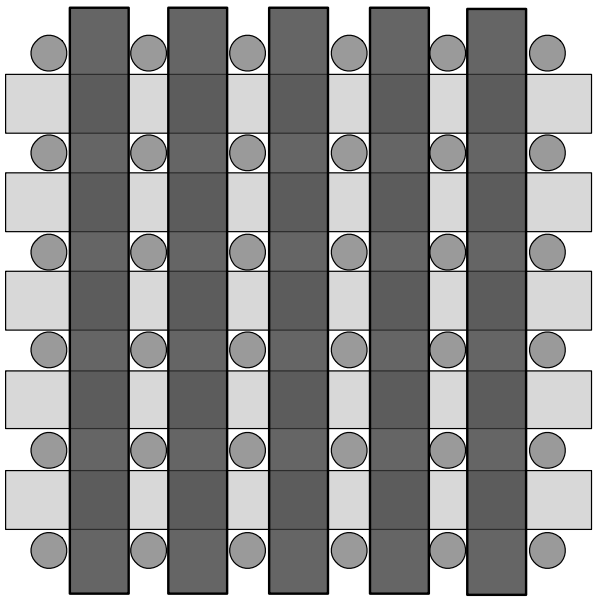

Figure 4.30: Pins within the substrate supporting $0^o/90^o$ preform, enlarged and not to scale.

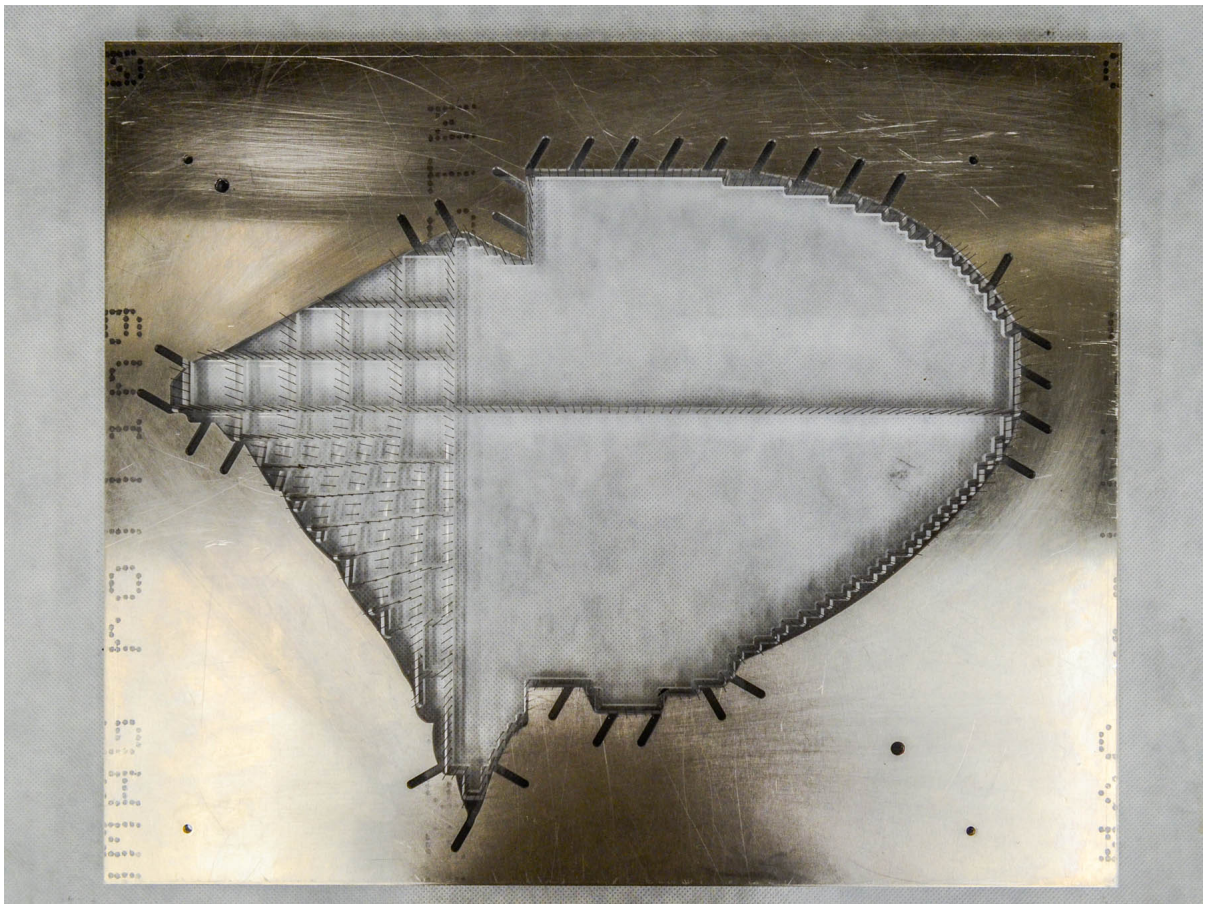

Figure 4.31: Manufacturing substrate and frame for producing preforms for manufacturing a automotive side-mirror; designed by MASc candidate L. West.

In complementary operations, a steel frame is positioned around the substrate pinboard, Figures 4.31 and 4.32. Double-sided adhesive tape is placed along the frame perimeter prior to beginning tow deposition, after each tow layer is deposited and after the final tow layer. A second, identical steel frame is then superimposed over the first and the two are clamped together, adhering to and compressing the tow ends. This frame is critical in aiding transfer of the unfinished preform from the LM to the CSM.

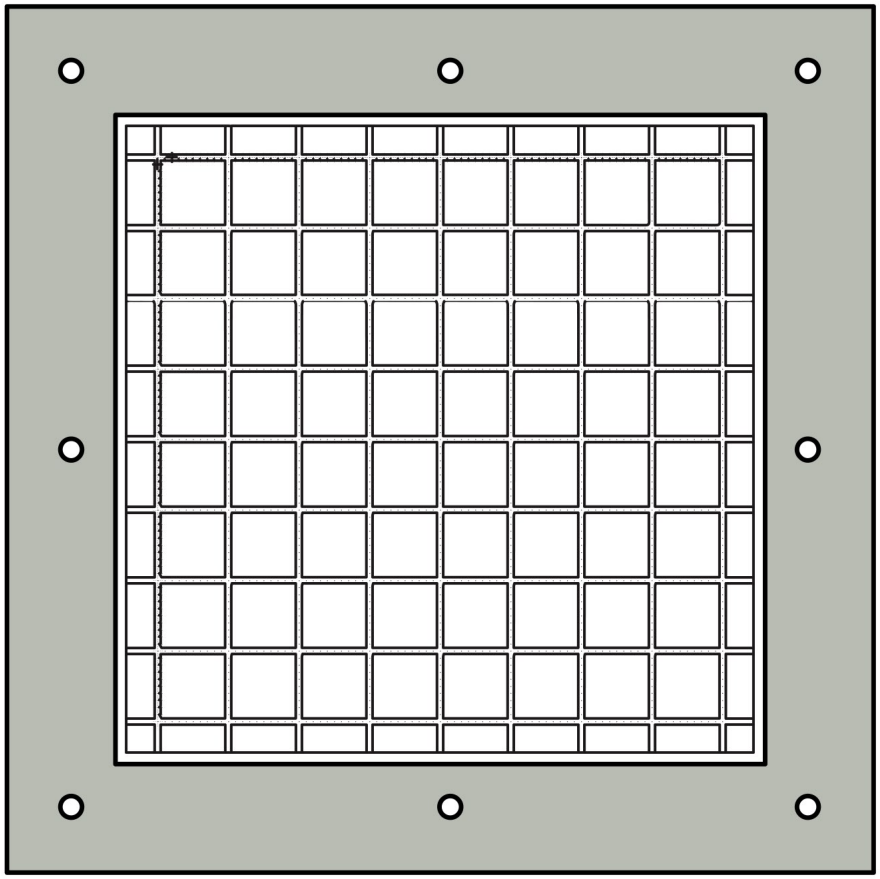

Figure 4.32: Manufacturing substrate frame

4.3.3.4.8 Registering substrate position

A limitation of the pin-board type substrate is that it must be placed in a known position relative to the LM; it must also be aligned with the X and Y coordinate axes of the machine. An error in position or orientation of the substrate will result in tows being deposited into the pins rather than between them, causing damage to the substrate and feed nozzle alike.

Prior to operating the LM, the pin-board's orientation is verified with a dial-indicator that is clamped onto the deposition head. Jogging the deposition head in the X or Y direction while the indicator's stylus is in contact with the substrate's edge confirms that the substrate is well aligned with the respective axis. If required, adjustments are made.

Once the substrate is aligned its position must be registered with the MCU. This is achieved by zeroing the X and Y axis positions as the feed nozzle's end is located directly above and centred on the first pin closest to the machine's origin, Figure 4.11. This is performed by jogging the deposition head in the Y direction at an orientation of 0^o to the point where side-contact is first made between the feed nozzle's end and the first pin. The head is then jogged in the reverse direction, one thousandth of an inch at a time until contact no longer exists, at which time the Y position of the deposition head is set equal to $-(\textit{nozzle width}/2)$. To register the substrate's X position the deposition head is brought up to the safe height, rotated to $\pm 90^o$, and side-contact is made with the same pin, followed by reversing the head position incrementally until contact ceases. The X position is then set to $-(\textit{nozzle width}/2)$.

4.4 Contour stitching machine (CSM)

4.4.1 Introduction to the contour stitching machine

The contour stitching machine (CSM) is an automated two-sided stitching machine, the second machine used within the uO-Tow manufacturing process, Figure 4.33. The CSM inserts lock stitch lines into the preform in the through-thickness direction. The stitch is primarily intended to hold tows within the position they were deposited in; transforming the output of the LM from an organized but loose stack of tows into a sturdy preform able to withstand handling and processing operations. Stitching may be performed with thermoplastic or semi-structural thread. When the latter is used, limited structural through-thickness reinforcement may be provided. A thread weight of 27-60 Tex [g/km] is typically compatible with the CSM stitching head.

One important feature of preforms manufactured using the uO-Tow process is that in order for them to be drapable, stitch lines must be implemented along paths that correspond to those of the tows. If tow paths are curved, stitch lines must be curved, requiring a device such as the CSM for creating them.

CO-OP student Hèlène Fortier compiled a tutorial video showing how this process is performed properly and efficiently.

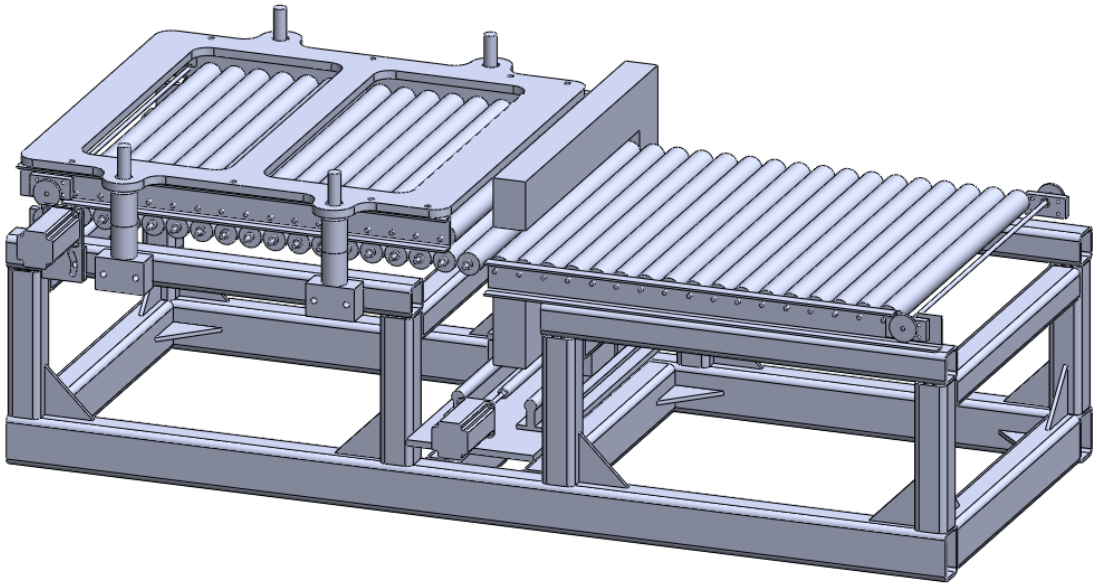

Figure 4.33: Trimetric view of CSM CAD assembly. Conveyor belts are hidden to show underlying rollers.

Stitch points may be inserted at variable density along a stitch line. However, generally a pitch of least one stitch per tow is inserted, holding each individual tow. The pattern most commonly used inserts a stitch over each tow, where the sewing needle inserts stitch at the points were substrate pins contacted tows during deposition, Figure 4.30. Preforms specifically manufactured to comply with a uO-Drape produced design must be stitched along the path of tows, Figure 4.34.

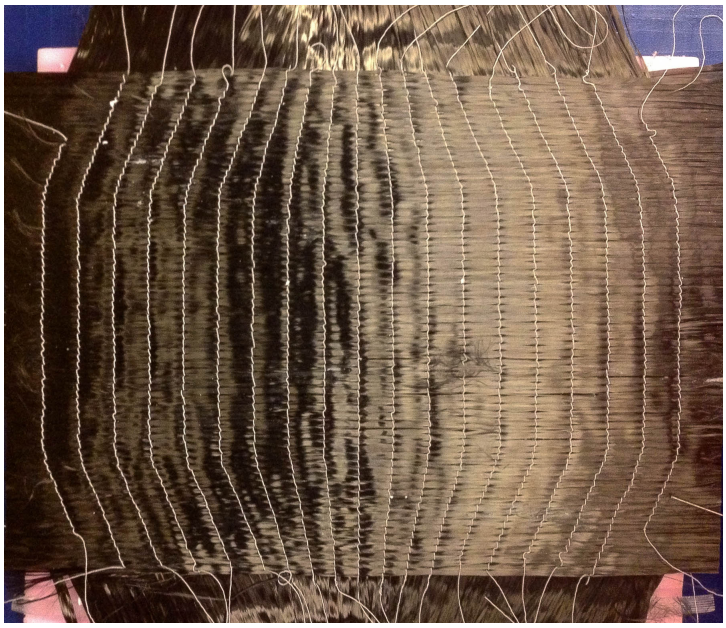

(a) Variable tow spacings reinforcement produced for a Bombardier Aéronautique aircraft fairing. Features steered yarns.

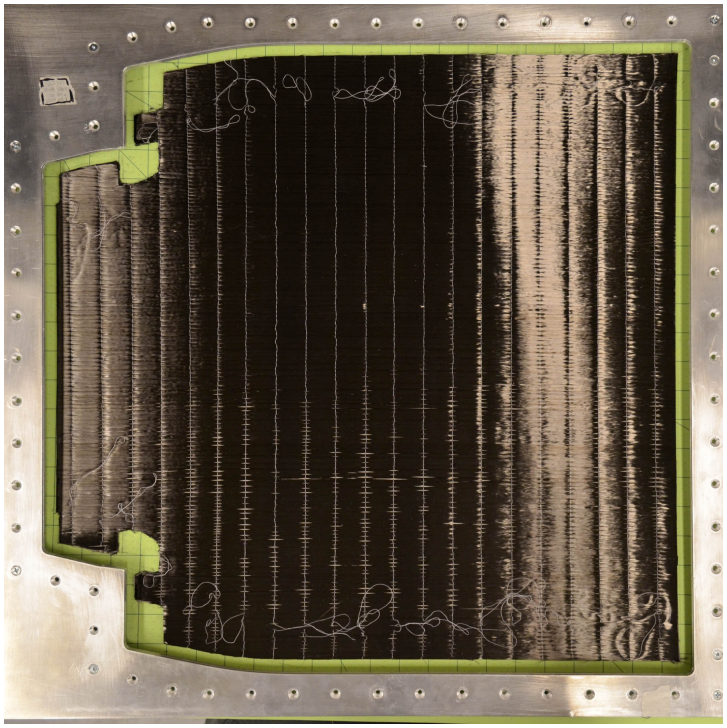

(b) Preform produced for a thermal bypass fairing for a turbofan engine.

Figure 4.34: Stitching path lines used in various aerospace demonstrator components.

4.4.2 CSM systems and components

4.4.2.1 Motors and tracking system

The CSM uses a system of conveyors belts to transport the preform along the X direction, through the opening of a robotic two-sided stitching head. The stitching head is mounted on a linear carriage, enabling it to move perpendicularly along the Y direction, Figure 4.36. Together, the motions provided by the conveyors and stitching carriage form the basis for motion of the stitching head relative to the preform, in the X – Y plane.

Four conveyors are used to translate the preform between the stitching head's opening, Figure 4.35. There are two conveyors on each side of the stitching head, where one conveyor is mounted to support the preform from below, and the other applies compressive pressure from above. This pressure maintains the position of tows which have yet to be stitched.

Each conveyor is driven by a single roller that is coupled directly to a dedicated stepper motor that operates at 3A per phase. The top two motors, hence conveyors rotate in the direction counter-to that of the bottom motors and all four motors are driven at identical feed rates to synchronize the speed of the four conveyors. This allows the preform to travel across the stitching gap without wrinkling or becoming distorting, Figure 4.35.

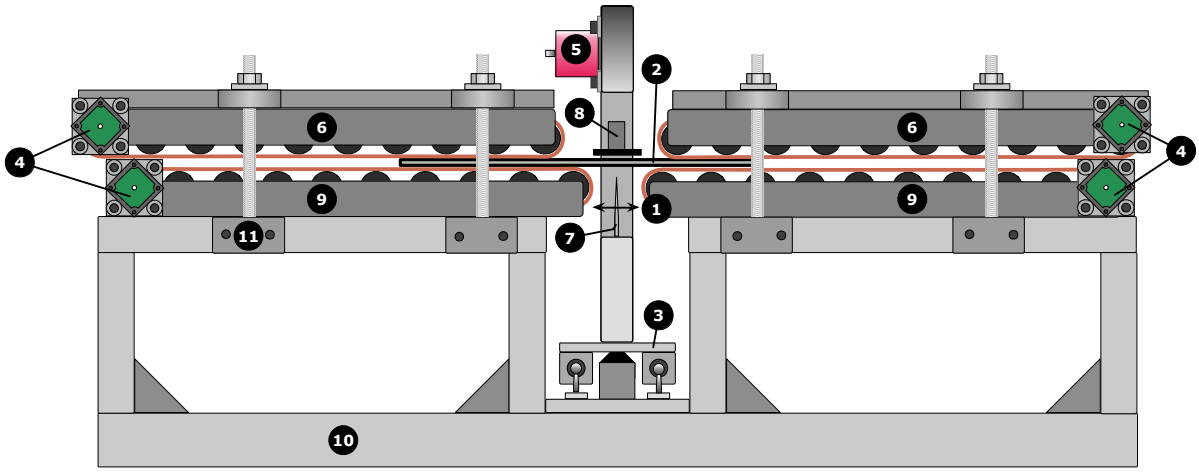

Figure 4.35: Side view of the CSM; ① stitching gap, ② preform and frame, ③ Y axis linear carriage, ④ X axis conveyor steppers, ⑤ stitching head and Z axis stitching head stepper, ⑥ X axis top conveyors, ⑦ sewing needle, ⑧ rotary hook bobbin, ⑨ X axis bottom conveyors, ⑩ base chassis, ⑪ top carriage alignment screws.

Each top-side conveyor is mounted on their its own one-piece laser cut aluminum chassis. This allows the two conveyors to be removed for loading/unloading a preform. After the top-side conveyors are removed, the preform in its support frame is placed over the stitching gap and the top conveyors are reinstalled over the preform. The top conveyor chassis are aligned and mounted to the remainder of the machine via four alignment screws, Figure 4.36. Wing-nuts are screwed onto the alignment screws and may be tightened over the chassis, applying additional compressive pressure to the preform.

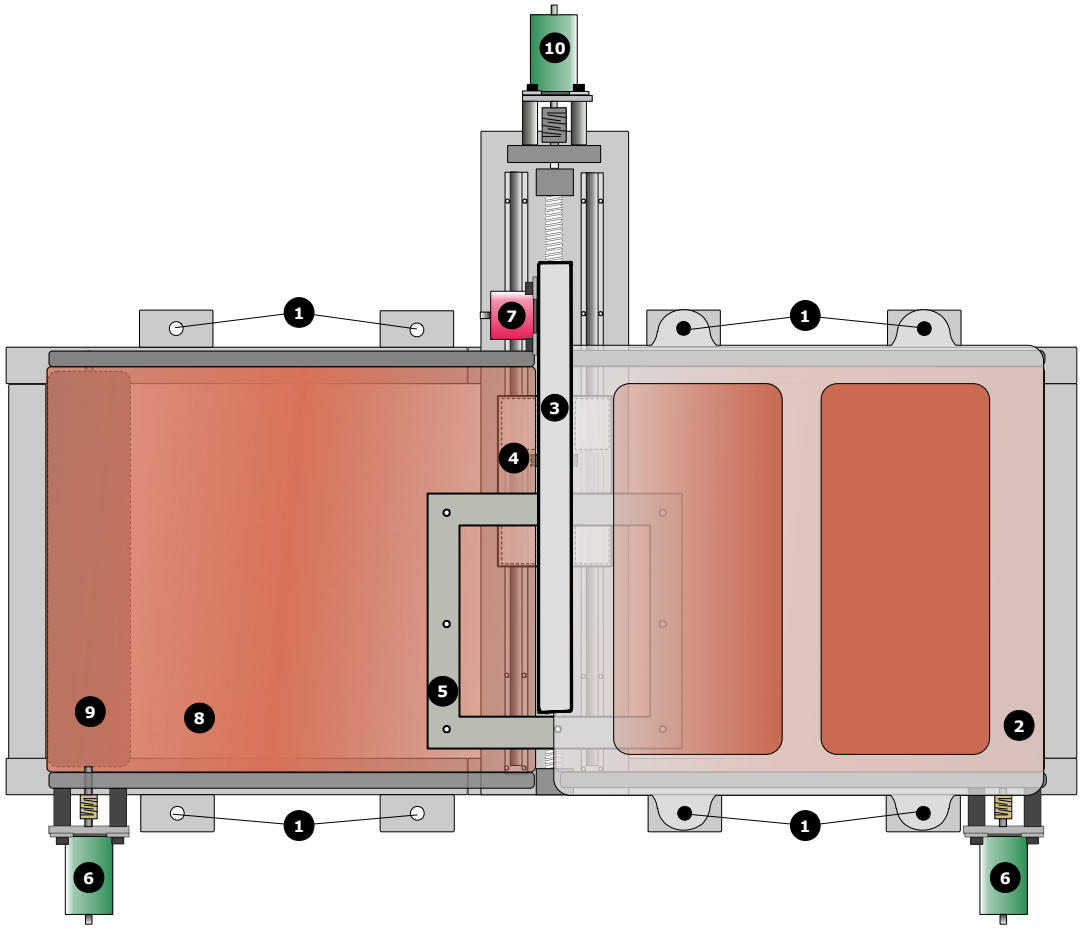

Figure 4.36: Top view of the CSM shown with top-left conveyor removed and top-right conveyor semi-transparent; ① alignment screws, ② X axis top-right conveyor chassis, ③ stitching head, ④ Y axis stitching head carriage, ⑤ preform/frame, ⑥ X axis conveyor steppers, ⑦ Z axis stitching head stepper, ⑧ X axis bottom-left conveyor, ⑨ X axis bottom-left conveyor drive roller, ⑩ Y axis carriage stepper.

The stitching head is mounted to a linear carriage that tracks in the Y direction. The stitching carriage is of identical design on that used in the LM, Section 4.3.2.1. Power is provided to the ball screw by a 2.82 N-m (400 oz-in) stepper motor operating at 3A per phase, Table 4.9.

Table 4.9: Summary of the stepper motors used in the CSM. All motors are operated in full-step microstepping mode F.

Axis	Current [A/Phase]	Actuation	Role	Model # HT23-×	Max torque [N-m (oz-in)]
X	3	Linear	Drive X conveyor (bottom-left)	400-8	2.82 (400)
U	3	Linear	Drive X conveyor (bottom-right)	400-8	2.82 (400)
V	3	Linear	Drive X conveyor (top-left)	400-8	2.82 (400)
W	3	Linear	Drive X conveyor (top-right)	400-8	2.82 (400)
Y	3	Linear	Drive Y carriage	400-8	2.82 (400)
Z	3	-	Drive stitching head	280-8	1.98 (280)

Conveyor width was set at 585 mm (23") which determines the maximum preform and stitching width. As a preform must remain within the conveyors to be supported properly, the CSM is limited to stitching an area of 4000 cm^2 (585 mm × 684 mm). Some geometries may be stitched in two stages, allowing preforms up to 8000 cm^2 to be stitched.

4.4.2.2 Stitching Head

The stitching head was manufactured using an existing design discussed by S. Audette in his MASc thesis titled *Mechanical Properties of Aerospace Composite Made from Multilayer 3D Carbon Fibre Preforms, 2014 [96].* The device was retrofitted with a stepper motor and mounted on the Y axis linear carriage. The stitching head chassis was manufactured from three CNC-machined aluminium sections and the chassis was outfitted with sewing assemblies and mechanisms harvested from a Brother® commercial sewing machine. Some mechanisms were not installed on the new head chassis as their functionalities were absorbed by other components or not needed. For example, the action carried out by the feed dogs was absorbed by X axis conveyors and the Y direction carriage. Similarly, the original machine's stitching pattern, width and length selector mechanisms were removed and their actions overridden.

The chassis was manufactured to accept a NEMA 23 frame-mounted stepper motor for replacing the OEM 120 VAC drive motor, allowing the MCU to control the stitching mechanism precisely. A Probotix® 1.98 N-m (280 oz-in) stepper motor was coupled to the stitching mechanism's input drive shaft via a timing-belt with 12.7 mm width and 0.508 mm pitch. Light-weight acetal timing-pulleys were used to produce a 22:7 reduction, multiplying the maximum torque available to 6.2 N-m at the stitching mechanism's input drive shaft.

4.4.2.2.9 Stitching cycle

A single stitching cycle produces a single stitch point, which is created by a single advance–retract motion of the needle and a single revolution of the rotary hook type bobbin. A stitching cycle is completed by advancing the stitching mechanism's drive shaft by one revolution. As a result, the Z axis which is allotted to control the motor that drives the stitching mechanism is calibrated so that it produces a single revolution of the stitching drive shaft when instructed to advance by one unit.

4.4.2.3 Contour stitching machine MCU

The MCU designed for controling the CSM is essentially identical to the MCU used in the LM, Section 4.3.1. As such, this section outlines the differences between the LM MCU and the CSM MCU. Components and quantities housed within the CSM MCU are identical to those of the LM's MCU, Section 4.10. The two exceptions are the low voltage PSU and the cooling fan which respectively provides and operates at 12VDC.

Table 4.10: Major components housed within the CSM machine control unit (MCU).

Function	Component	Quantity
Human interface device (HID)	PC	1
Main logic control board	Mk2	1
Breakout board	-	2
Motor driver	Unipolar stepper motor driver	6
PSU	40VDC - 10A linear PSU	1
PSU	12VDC - 1 A	1
Fuse	3A – 250V AGC slow blow fuse	7
Cooling/heat management	12VDC - 0.9A 60 mm x 60 mm fan	1
Peripheral connectors	5 pin DIN connector	6
Peripheral connectors	8 pin DIN connector	1

The layout of the CSM MCU is identical to the LM's MCU, Figure 4.37. All motor drivers were adjusted to provide steppers with 3A per phase and therefore, their order of arrangement differs from that used within the LM MCU. Hence, motor drivers were arranged according to their duty cycle, where the most frequently used circuits were positioned closest to the cooling fan, Table 4.11. The fan which services the motor driver circuits was upscaled to provide increased air flow and cooling.

Table 4.11: Table showing the sequence of the motor drivers as mounted within the MCU MCU housing.

Position from fan	1	2	3	4	5	6
Axis	X	U	V	W	Y	Z
Current (A)	3	3	3	3	3	3
Designation	linear	linear	linear	linear	linear	-

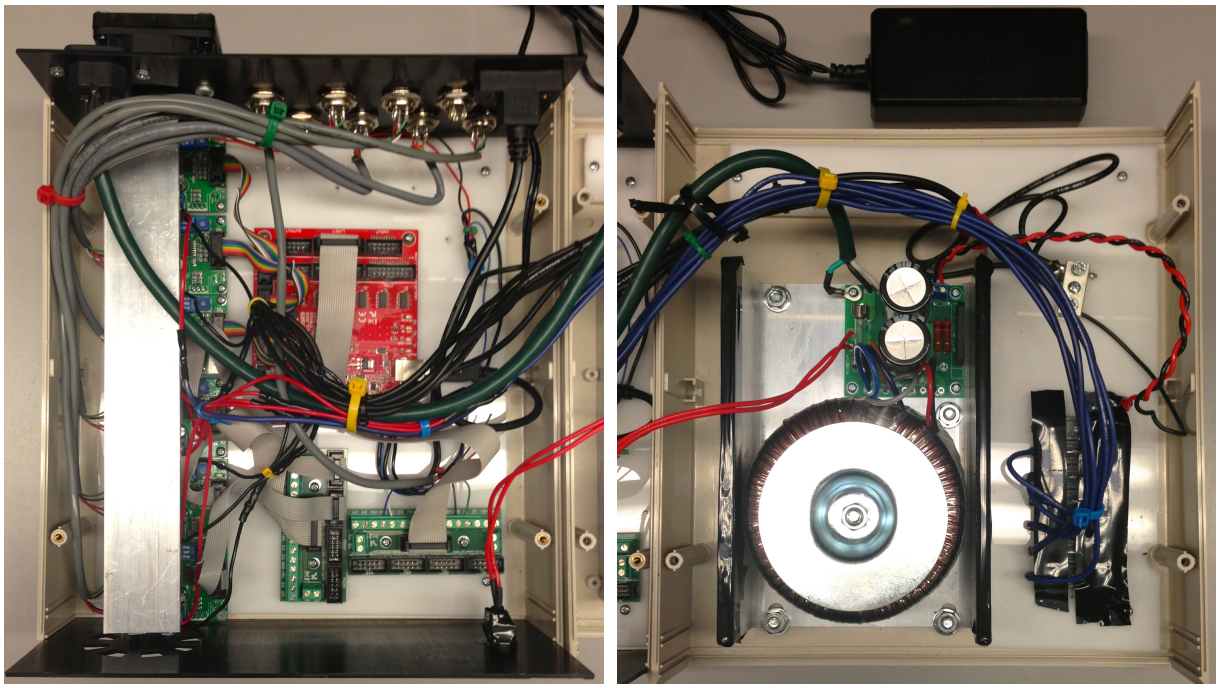

(a) Upper MCU housing-half. Mounted within: Mk2, breakout boards, motor drivers, peripheral connections, heat sink and cooling fan.

(b) Lower MCU housing-half. Mounted within: 40VDC PSU and fuses. External but pictured: 12VDC PSU.

Figure 4.37: Contour stitching machine MCU

Table 4.12: Warnings and cautions for CSM MCU operation.

Warnings and cautions
• Turn off box and wait for 1 minute before disconnecting any motor or inductive loads. Failure to do so will result in destruction of the motor driver.
• Ensure that cooling fan always provides substantial flow over the motor driver heat sinks when they are powered.
The cooling fan receives power from the 12VDC PSU. Ensure that the 12VDC PSU is receiving line power before attempting to power-on the MCU.

Chapter 5

Software Implementation

5.1 Laydown post-processor background

The software algorithms discussed within this chapter are the foundation of the post-processor. The post-processor, which is written in the MATLAB language, is used for translating the design outputs obtained from the uO-Drape software into G-code which is used to run the LM and CSM.

The post-processor can be broken into numerous elements: sub-operations and sub-routines. Each elements performs a distinct function that contributes to generating a G-code file. Many of these elements are required in multiple instances through a single run of the post-processor and hence, they appear repeatedly within this chapter. However, their algorithms do not change and so, are outlined at the point of their first appearance. This Chapter outlines how G-code is generated by the post-processor via progressing through the flow of the post-processors main algorithm, which shown by Figure 5.1.

Running of the post-processor starts by providing the two files obtained from a uO-Drape simulation, Section 5.2.1. Next, the post-processor is passed a number of parameters by the user. These parameters inform the post-processor about the aspects of LM and CSM operation which are independent of the manufacturing geometry; parameters include: tow laying rate, feed rate and how many time the tow cutting cycle should be repeated per tow. Section 5.2.2.1 provides details regarding these parameters. Next, an NC file is created and is initialized with headers that format the file for the LM and

CSM, Section 5.2.2.1. The position generator is summoned to calculate the coordinates for where tow intersections are located. This computation is described Section 5.3.1. After intersection coordinates are determined, the X and Y direction G-code generators can begin writing G-code instructions to the NC file, Section 5.3.2. The tow cutting and clearing G-code generator that is described in Section 5.3.3 is summoned after each laydown cycle to separate the tow from the deposition head.

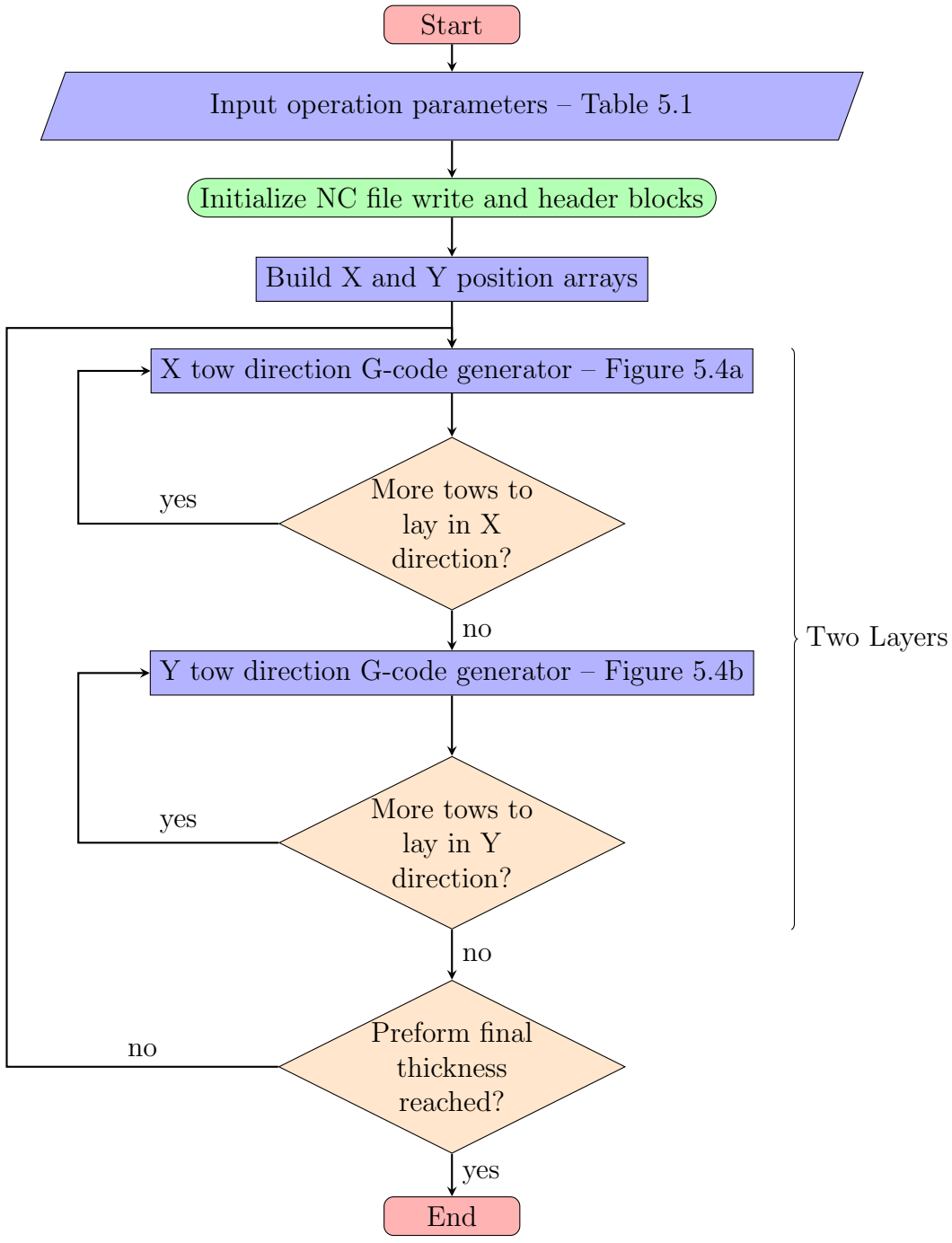

Figure 5.1: Post-processor for G-code generation (pointGenerator.m) flowchart.

5.2 Inputs and outputs

5.2.1 Input: uO-Drape tow spacings lengths

After a composite component's preform is designed in uO-Drape by the process discussed in Section 4.1, tow paths within the designed preform are mapped onto flat for manufacturing. uO-Drape outputs this flat design as a set of two CSV files, which contain the name of the design and an appendage: 'XLengths' or 'YLengths'. The XLengths file contains tow spacings along the X direction and the YLengths file contains spacings along the Y direction, where the spacings stored correspond to locations of tow intersections.

The XLengths and YLengths files each consist of a 501 row by 501 column array. Where the row and column indices map to the physical rows and columns of tows in the grid-like arrangement in which they appear within the preform. For example, the initial spacing in the X direction between the 14^{th} and 15^{th} tows running in the general X direction is given by the cell $XLengths[15, 1]$. uO-Drape always outputs Lengths files of size 501 by 501, limiting the maximum dimensions of a manufacturing geometry to approximately 501 tow-widths by 501 tow-widths. However, larger preforms may be manufactured by manually combining multiple uO-Drape outputs and inputting them into the post-processor.

When the lengths files are inputed to the post-processor they are mapped to two 501 by 501 arrays within the working memory of the post-processor respectively named xfile and yfile; these files are of identical format to the lengths files. As only non-zero and positive array indices are permitted within the MATLAB programming language, median tows in the centre of the preform are mapped to the median row and column within each array: row 251 and column 251. Following this notation, the tow intersection located in the top-right corner of the preform corresponds to indices $[1, 501]$.

5.2.2 User input: machine operation parameters

The post-processor requires the user to input machine operation parameters. These parameters control the machine's tracking speed as well as other aspects that ensure reliable and safe operation. The operation parameters and their default values are displayed in Table 5.1. As they are critical to safe machine operation, parameter values are

intentionally provided in imperial units.

Table 5.1: User provided machine running parameters; the unit presented for each parameter is critical to proper machine operation.

Parameter	Symbol	Default value	Unit
Geometric parameters			
Nozzle offset length	R	1.0	[in]
Forward cutting length - scissor advance	fcl	150.0	[1]
Backward cutting length - scissor return	bcl	3.0	[1]
Tow bleed length	yb	0.0	[in]
Tow height	yh	0.0079	[in]
Feed nozzle length	nl	3.5	[in]
Feed-from height (must have $fh > ch$ & $fh < sh$)	fh	0.25	[in]
Spool-out height ($ch < fh < sh$)	ch	0.0394	[in]
Safe (rapid) height ($sh > fh > ch$)	sh	0.875	[in]
Tow clearing length (distance traveled to allow the tow to eject from nozzle after each lay)	ycl	4.0	[in]
MCU position for deposition head at 90^o	noznine	233.3	[1]
MCU position for deposition head at -90^o	nozineneg	-233.3	[1]
Non-geometric parameters			
Compaction pause after each layer (1 for yes, 0 for no)	pau	1	[1]
Number of cutting cycles	cn	3	[1]
Rates			
Feed rate	fs	90.0	[in/min]
Plunge rate	ps	10.0	[in/min]
Nozzle preload rate	ns	36.0	[in/min]
Nozzle clearing rate	cs	35.0	[in/min]
Head rotation rate	hs	200.0	[1/min]
Cutting rate	cfs	200.0	[1/min]

5.2.2.1 Output: NC-file initialization

First a NC file is created and four initial code blocks are written to it. The code blocks are:

```
%
G20 (inch selection)
G17 (XY plane selection)
G90 (absolute coordinates)
```

These blocks format the file as G-code which will operate with the LM or CSM. The fist block informs the MCU where the code begins, and the following three insure that machines will run as intended[1].

Three more code blocks are appended to the file:

```
G40 (cancel tool radius compensation)
G49 (cancel tool length offset)
G80 (cancel canned cycles)
```

These blocks are used to cancel any programmed cycles or position offsets, which may remain within the MCU's memory from previous manufacturing operations.

5.3 Algorithms, sub-operations and subroutines

5.3.1 Position generator

The position generator is used for converting the xfile and yfile arrays into two new arrays, xpos and ypos, that store the cartesian coordinates of the tow intersection locations. Similarly to the xfile and yfile, the indices of the xpos and ypos correspond to the row–column address of tows forming an intersection point. For example the index $[1, 3]$ indicates the intersection of the first tow running along the X direction and the third tow running along the Y direction. Following this convention, the

[1]The MCU will not function properly unless imperial units are used. Hence, several variables and constants within this chapter are intentionally presented in imperial units.

cartesian coordinates corresponding to the intersection of the aforementioned tows are $(x, y) = (xpos[1, 3], ypos[1, 3])$ and the coordinates corresponding to the preforms origin are $(x, y) = (xpos[251, 251], ypos[251, 251]) = (0, 0)$

Coordinates of the tow intersection points are summing the spacing lengths. Summation starts at the xfile's or yfile's median column or row respectively, and ends at the index that corresponds with the coordinate being calculated, Figure 5.2. X positions are computed using an outward row-wise summation along solid lines within Figure 5.2a, where summations are additive in the $+a$ direction and subtractive in the $-a$ direction, Equation 5.1 and 5.2 respectively. Y positions are computed using an outward column-wise summation along solid lines within Figure 5.2b, where summations are additive in the $+b$ direction and subtractive in the $-b$ direction, Equation 5.3 and 5.4 respectively.

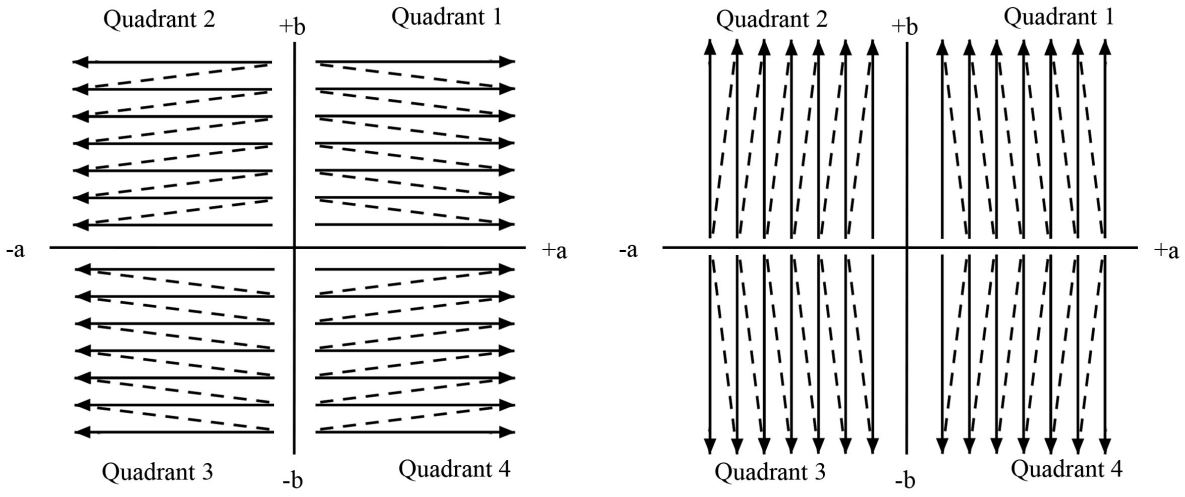

(a) X positions array generator sequence (b) Y positions array generator sequence

Figure 5.2: Post-processor position generator summation sequence, solid lines; dotted lines show the next summation performed after the previous is complete [91].

The X coordinates of tow intersection points within the first and fourth quadrants are calculated using Equation 5.1; where the X coordinate of an intersection located at index $[i, j]$ is given by:

$$xpos[i,j] = \sum_{n=252}^{j} xfile[i,n] \tag{5.1}$$
$$i \in \mathbb{Z} | 1 \leq i \leq 501 \quad and \quad j \in \mathbb{Z} | 252 \leq j \leq 501$$

In the second and third quadrants, the X coordinate of a tow intersection point at index $[i,j]$ is calculated using Equation 5.2:

$$xpos[i,j] = \sum_{n=j}^{250} -xfile[i,n] \tag{5.2}$$
$$i \in \mathbb{Z} | 1 \leq i \leq 501 \quad and \quad j \in \mathbb{Z} | 1 \leq j \leq 250$$

and the X coordinates of tow intersections along the b axis ($[i,j] = [i,251]$) are equal to zero.

The Y coordinates of tow intersection points within the first and second quadrants are calculated using Equation 5.3; where the Y coordinate of an intersection located at index $[i,j]$ is given by:

$$ypos[i,j] = \sum_{n=i}^{250} yfile[n,j] \tag{5.3}$$
$$i \in \mathbb{Z} | 1 \leq i \leq 250 \quad and \quad j \in \mathbb{Z} | 1 \leq j \leq 501$$

In the third and fourth quadrants, the Y coordinate of a tow intersection point at index $[i,j]$ is calculated using Equation 5.2:

$$ypos[i,j] = \sum_{n=252}^{i} -yfile[n,j] \tag{5.4}$$
$$i \in \mathbb{Z} | 252 \leq i \leq 501 \quad and \quad j \in \mathbb{Z} | 1 \leq j \leq 501$$

and the Y coordinates of tow intersections along the a axis ($[i,j] = [251,j]$) are equal to zero.

During the summation, if tow spacing values of zero are encountered in both $xfile[i,j]$ and $yfile[i,j]$ for a given intersection index $[i,j]$ other than the origin, the corresponding $xpos[i,j]$ and $ypos[i,j]$ variables are set to not a number (NaN). This places the value NaN within all position indices where no tow intersections are present; NaN values form an outline around the nonzero values stored within the position arrays, defining the boundaries of the preform that identify the end of a tow. Encountering a value of NaN instructs the path generator to end the current deposition cycle, Figure 5.3. Additionally, any subsequent calculation involving a NaN value results in a NaN answer, causing indices that are external to the preform to be exempt from subsequent computation.

						$+b$						
	NaN	NaN	NaN	NaN	NaN	NaN	NaN	NaN	NaN	NaN	NaN	
	NaN	NaN	NaN	NaN	NaN	8	NaN	NaN	NaN	NaN	NaN	
	NaN	NaN	NaN	NaN	9	6	7	NaN	NaN	NaN	NaN	
	NaN	NaN	NaN	6	5	5	7	7	NaN	NaN	NaN	
	NaN	NaN	5	4	4	4	6	6	8	NaN	NaN	
	NaN	NaN	4	2	3	2	6	6	8	9	NaN	
$-a$	NaN	0	0	0	0	0	0	0	0	0	NaN	$+a$
	NaN	NaN	-4	-2	-3	-1	-6	-6	-8	-9	NaN	
	NaN	NaN	-5	-6	-5	-4	-6	-6	-8	NaN	NaN	
	NaN	NaN	NaN	-6	-6	-5	-7	-7	NaN	NaN	NaN	
	NaN	NaN	NaN	NaN	-8	-8	-7	NaN	NaN	NaN	NaN	
	NaN	NaN	NaN	NaN	NaN	-9	NaN	NaN	NaN	NaN	NaN	
	NaN	NaN	NaN	NaN	NaN	NaN	NaN	NaN	NaN	NaN	NaN	
						$-b$						

Figure 5.3: Typical format of the *ypos* Y position array prior to coordinate system shift.

At this stage, the coordinates of X and Y tow intersections extend within positive and negative number domains, where each point is situated within one of the four cartesian quadrants, Figure 5.3. While negative coordinates are not prohibitive to NC-machine operation or prohibited in the G-code language, they are inconvenient during the machine setup procedure. Hence, all tow intersections are translated such that all points are situated in the first cartesian quadrant. The translation relocates the preforms first (bottom-left) tow intersection to the machine's spacial origin, Figure 4.11. This bottom-left tow intersection corresponds with the bottom-left substrate pin location, which is easily identifiable and a convenient location at which to register the machine's location

relative to the substrate[2]. The physical coordinate translation is performed by determining the coordinates of the bottom-left most located tow intersection and adding the magnitude of its respective X and Y coordinates to all values within the xpos and ypos arrays.

Tow paths are defined as a sequential sets of tow intersection points. Therefore, a tow path can be expressed as an incremental set of indices within the position arrays. For example, the path of a tow number i running along the X direction can be defined by all positions where said tow intersects tows running along the Y direction: $(x, y) = \{(xpos[i, j], ypos[i, j])\ , (xpos[i, j + 1], ypos[i, j + 1]), ..., (xpos[i, j + n], ypos[i, j + n])\}$. A tow running along the Y direction can be defined by a set of tow intersection points: $(x, y) = \{(xpos[i, j], ypos[i, j])\ , (xpos[i + 1, j], ypos[i + 1, j]), ..., (xpos[i + n, j], ypos[i + n, j])\}$.

5.3.2 X and Y direction generators

G-code is written by a series of path generators depending on the tow's directionality, Figure 5.4. Code generated to deposit tows running along the X direction is written by the X direction inbound, midsection, and outbound generators, Figure 5.4a; code generated to deposit tows running along the Y direction is written by the Y direction inbound, midsection, and outbound generators, Figure 5.4b.

[2]This startup procedure is found in Section 4.3.3.4.

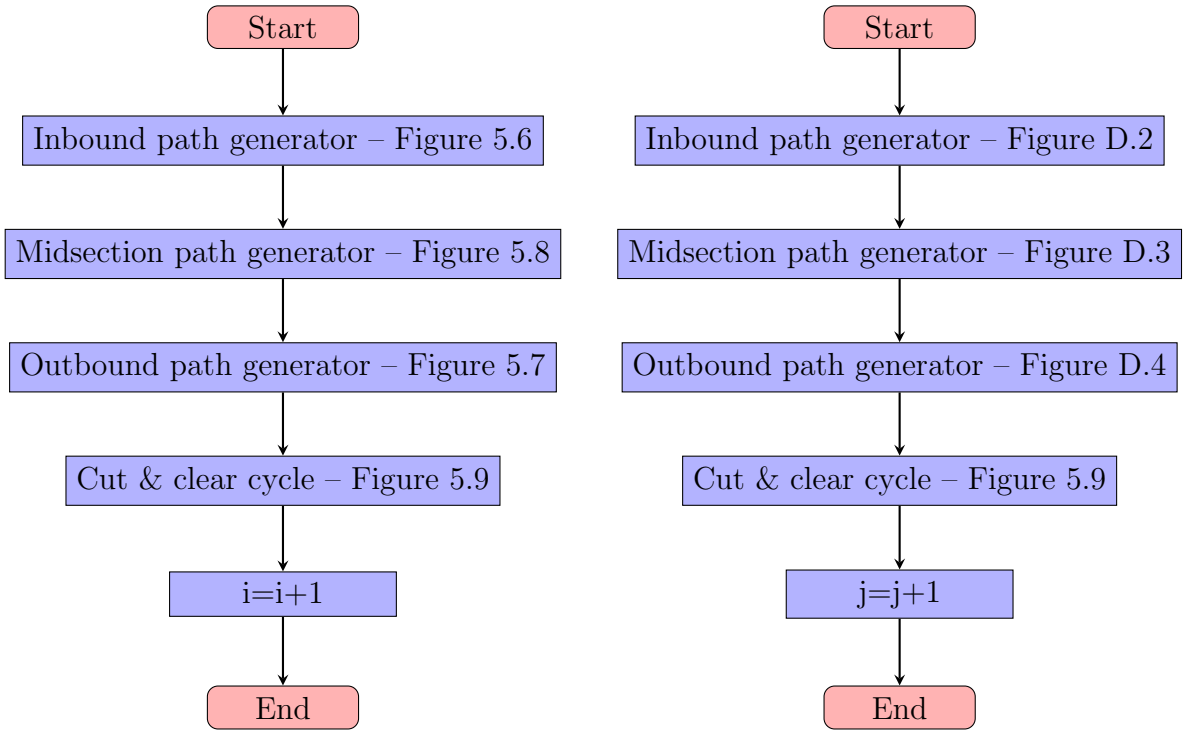

(a) X tow direction G-code generator (b) Y tow direction G-code generator

Figure 5.4: Flowchart for X and Y laydown G-code generation.

Figure 5.5 provides an example deposition path along tow intersection points ①, ②, ③ and ④. The tows path incorporates a inbound and an outbound bleed-length to points ⓘ and Ⓞ respectively. Deposition though the path in Figure 5.5 is broken into the following steps:

1. Inbound path generator:
   At position ⓘ:
   (a) Calculate inbound angle θ_{in} and extrapolate to obtain inbound bleed point, ⓘ at $P_{xib,yib}$.
   (b) Correct for nozzle offset induced by position shift in X–Y plane at deposition head angle θ_{in} and position point i'; orient deposition head accordingly.
   (c) Plunge from safe height to feed height, feed-from feed height to spool-out height.
   (d) Preload feed nozzle.

(e) Deposit while feeding through point ① to position 2^o.

At position 2^o:

(a) Calculate angle between intersection points ② and ③.

(b) Determine new position $2'$, at which deposition nozzle end is at point ② and angle $\theta_{2\to3}$ and correct for nozzle offset shift.

(c) Move to position $2'$

2. Midsection path generator:
At position $2'$:

(a) Deposit while feeding to position 3^o

(b) Determine new position $3'$, at which deposition nozzle end is at point ③ and angle $\theta_{3\to4}$ by correcting for nozzle offset shift.

(c) Move to position $3'$

(d) If point ③ is second last intersection point:

Exit from midsection generator and proceed using outbound generator.

(e) If point ③ is not second last intersection point:

Repeat midsection path generation for next point.

3. Outbound path generator:
At position $3'$:

(a) Calculate outbound angle, θ_{out}, between intersection points ③ and ④ and extrapolate to obtain outbound bleed point Ⓞ at $P_{xob,yob}$.

(b) Deposit while feeding through point ④ to position O^o.

4. Invoke cut and clear cycle.

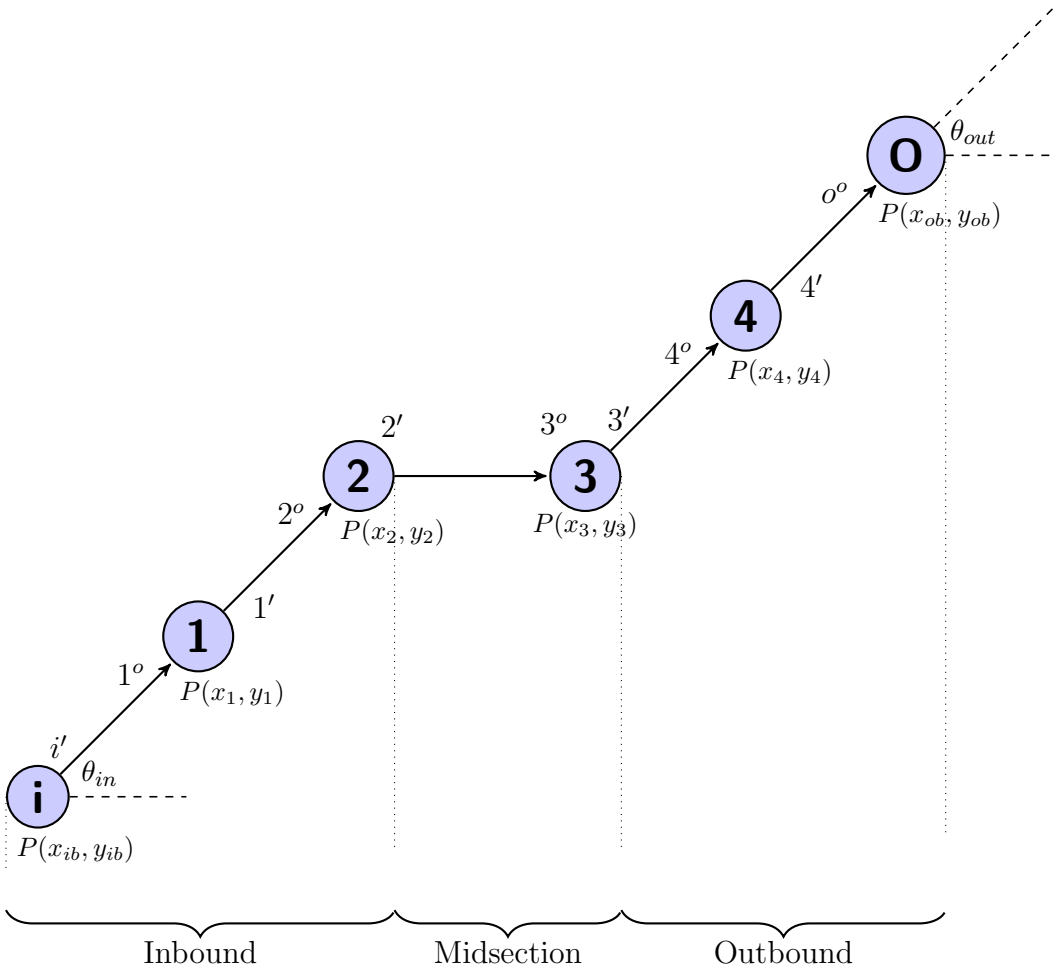

Figure 5.5: Beak-down of laydown pathline.

5.3.2.1 Inbound and outbound path and G-code generator

The inbound path generator is designed to guide tow deposition through the first two tow intersection points within a defined tow path. When the tow bleed-length variable *yb* is set to a non-zero value, the inbound path generator instructs deposition to begin at a point ⓘ, which is extrapolated at a distance *yb* from tow intersection point ① in the direction along the ①→② path, Figure 5.5. This allows a selectable length of excess material ('bleed-length') to be added to the inbound end of all tows. The slight bleed-length provides an area overhang by which the substrate frame can attach to the preform,

allowing it to be handled easily in subsequent stages of the process[3]. The flowchart in Figure 5.6 illustrates the inbound path and G-code generation algorithm. Figure D.2 shows the inbound and G-code generator algorithm for the Y direction.

[3]Since the time of writing this thesis, a new type of substrate frame was developed which does not require a tow bleed-length, allowing the manufacture of preforms that are truly net-shaped. Nonetheless, when this type of substrate frame is used, the post-processor operates using bleed-length of nil.

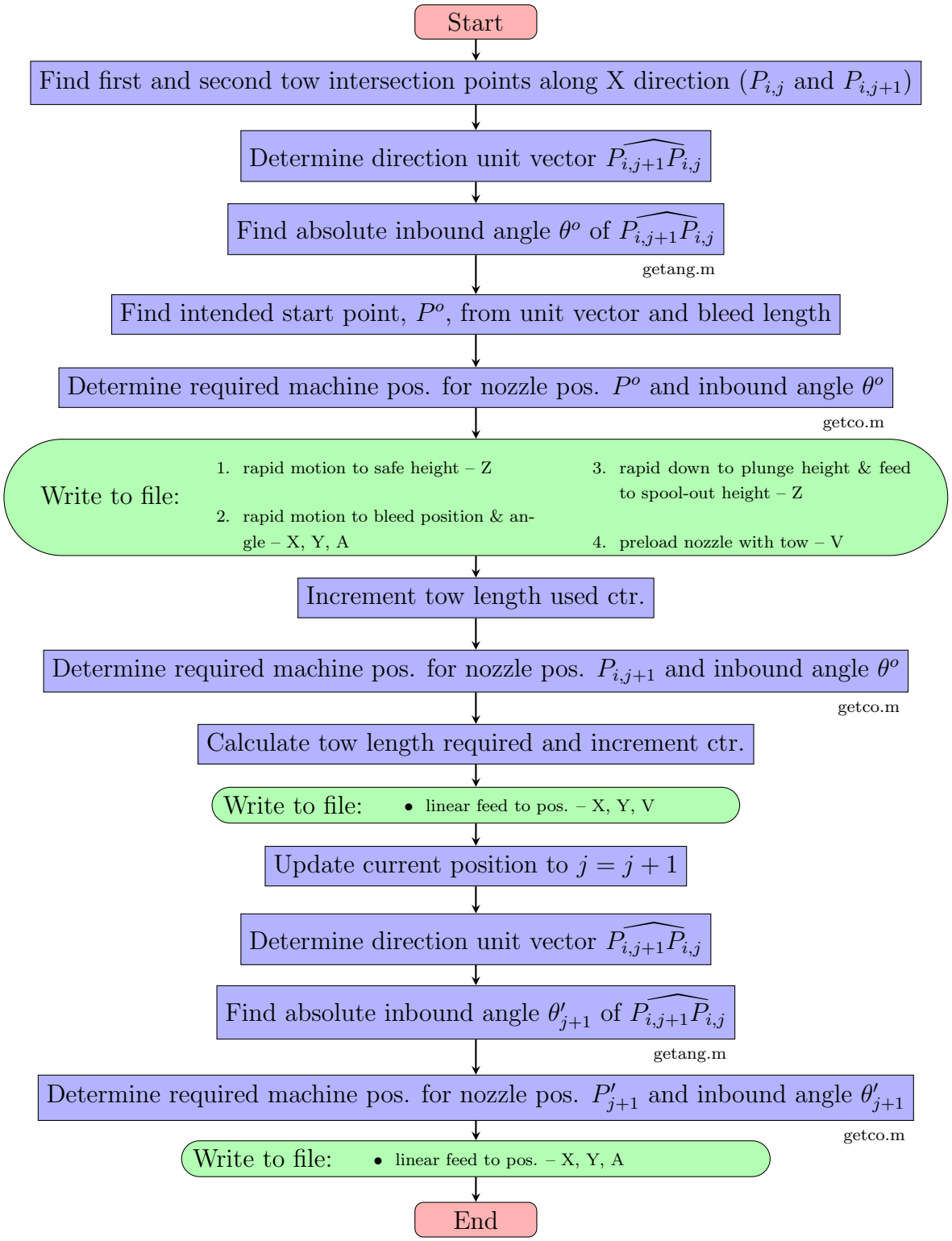

Figure 5.6: Inbound X direction path generator and code writer; this section of the post-processor code generates the instructions necessary to begin laying down each tow. Follows $P_{Row,Column}$ convention.

Similarly, a non-zero bleed-length variable *yb* will instruct the outbound path generator to extrapolate the path from the last two tow intersection points, adding an equivalent length of excess material to the tow end. The algorithm used in the X direction outbound path and G-code generator is displayed in Figure 5.7. Figure D.4 shows the outbound and G-code generator algorithm for the Y direction.

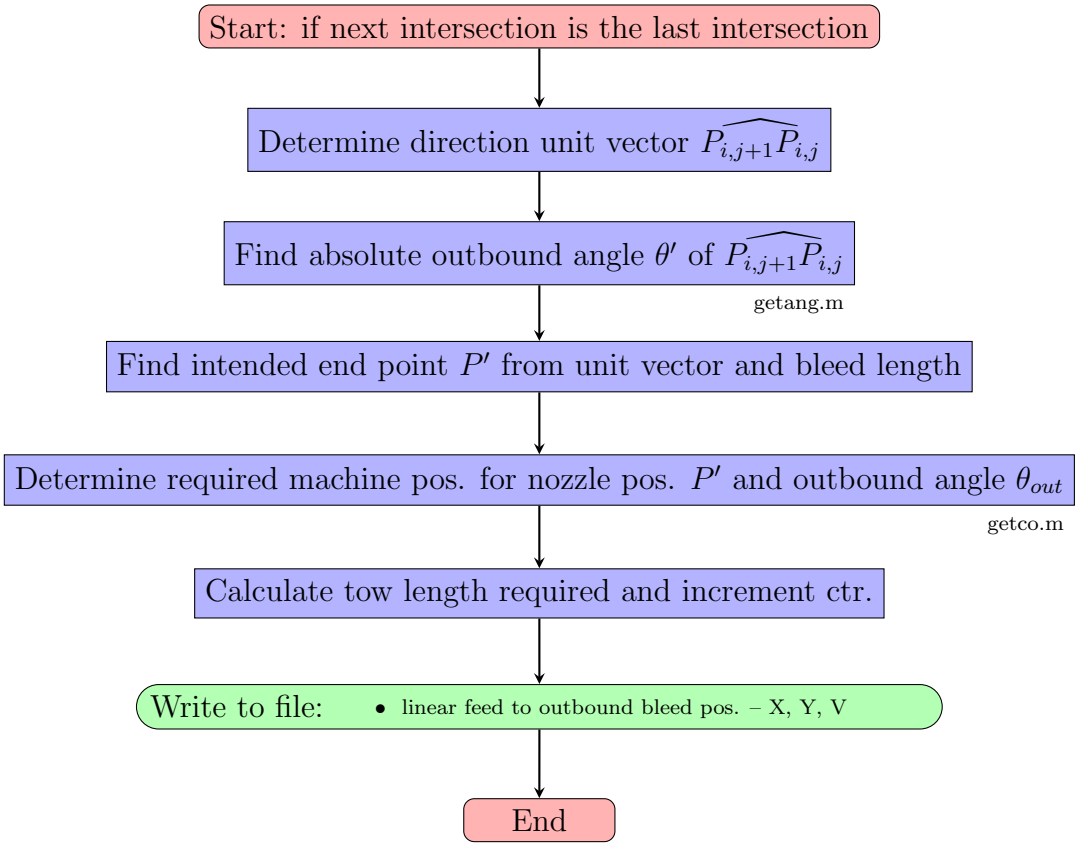

Figure 5.7: Outbound X direction path generator and code writer; this section of the post-processor computes the path from the second-last tow intersection position outward to the tow bleed-length. Then it writes the G-code which directs the LM to end deposition of a tow. Follows $P_{Row,Column}$ convention.

If the desired bleed-length variable *yb* is set to zero, deposition will begin at tow intersection point ① and end at intersection point ④, Figure 5.5. This enables manufacture of a fully net-shaped preform.

5.3.2.2 Midsection path and G-code generator

The midsection path generator writes G-code for directing tow deposition through all tow intersection points with an exception to the first two and last two intersections, which are written by the inbound and outbound path generators, The internal workings of the X and Y midsection path generators are explained in Figures 5.6 and D.2 respectively.

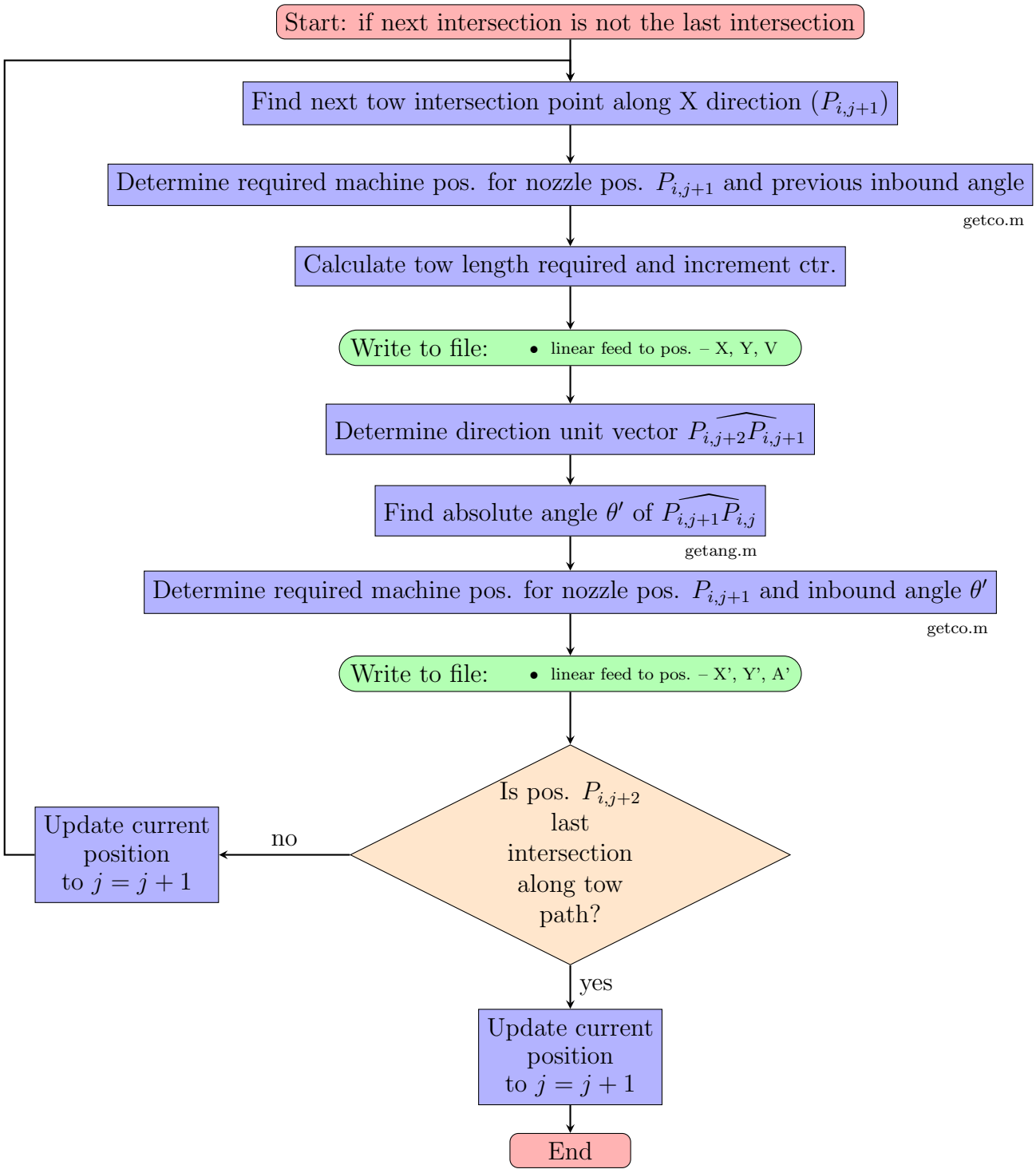

Figure 5.8: X direction midsection path generator and code writer; this section of the post-processor computes the paths between intermediate tow intersections (excludes first and last) and translates the paths to G-code instructions; directing the LM through this domain. Follows $P_{Row,Column}$ convention.

5.3.3 Cutting cycle and tow clearing G-code generator

The cutting and tow clearing cycle is invoked at the end of each laydown cycle to cut the tow and remove it from within the deposition head, Figure 5.9. The cutting and clearing G-code generator allows the cutting cycle to be repeated several times prior to clearing the tow. Repeating the cutting cycle increases the overall manufacturing cycle time. However, repeated cutting cycles increase the LM's reliability and reduces the frequency of machine breakdowns and restarts. The cutting cycle is discussed in Section 4.3.3.2.

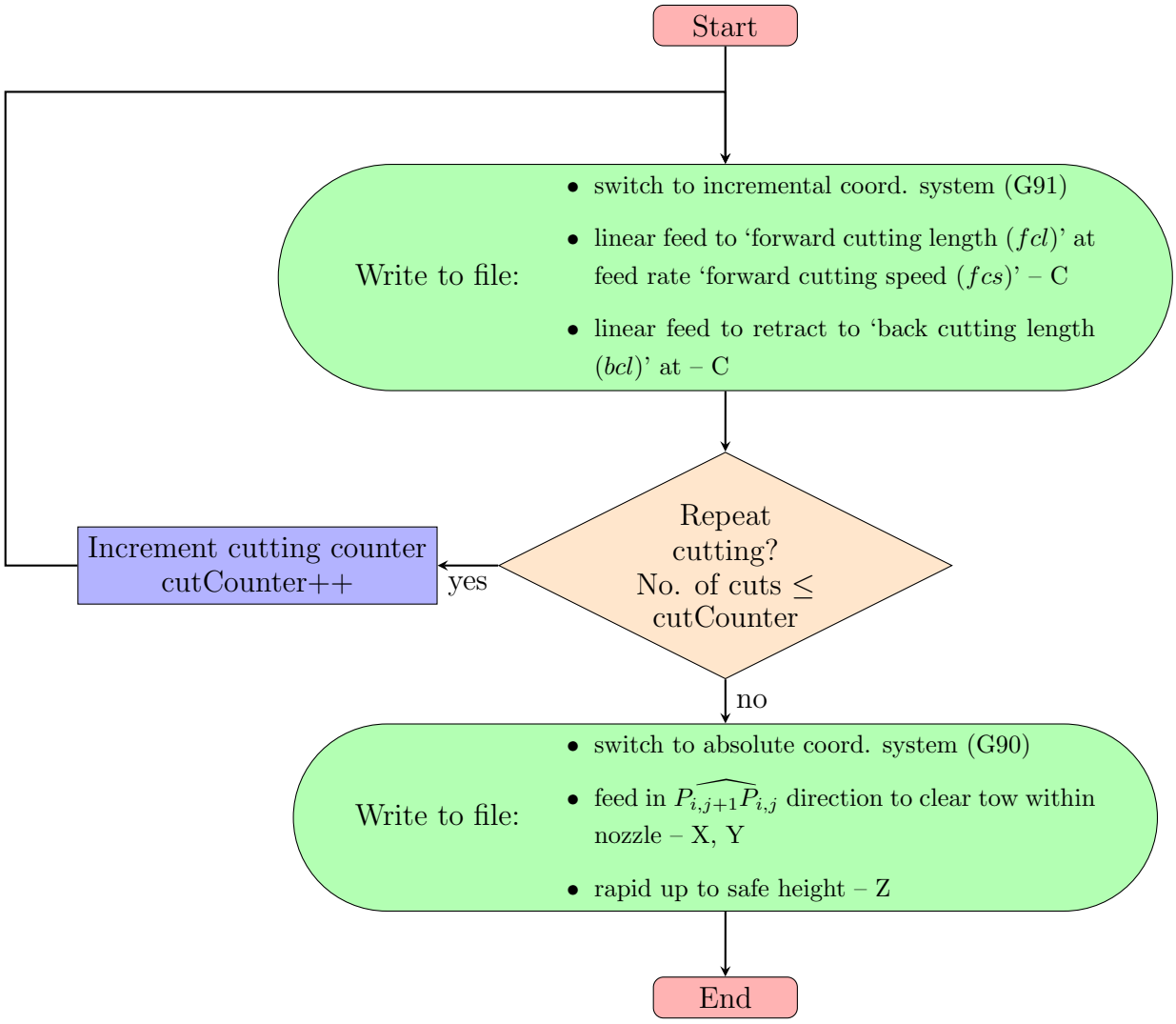

Figure 5.9: Cutting & clear cycle flowchart

5.3.4 Subroutines

5.3.4.1 getAng.m

The getAng.m subroutine is used for determining the absolute angle with respect to the X axis of an instantaneous tow orientation. The subroutine receives a unit vector $\widehat{ab}$ which defines the vector orientation of a tow and uses the vector product to determine its orientation, returning the result to the main program as an angle in degrees. The algorithm within the getAng.m subroutine is displayed in Figure 5.10.

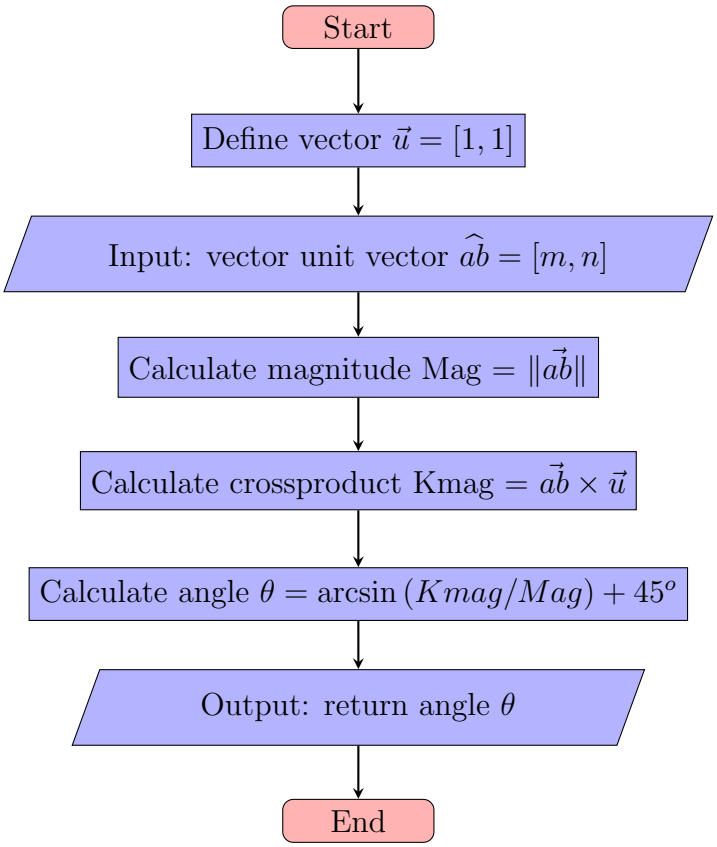

Figure 5.10: 'getAng.m' subroutine used for calculating the absolute angle of the inputed vector with the X axis.

5.3.4.2 getco.m

Due to the nozzle offset length, Figure D.1, the in-plane position of the nozzle end is shifted when the deposition head is rotated to an angle other than its native angle of 0^o.

When a tow is to be deposited at a non-zero angular orientation, the getco.m subroutine is invoked to calculate the correctional planar displacement required by the deposition head in order to place the feed nozzle end at the intended position, given its specified angular orientation. The getco.m subroutine receives the intended tow coordinates, nozzle offset radius and path angle (x_i, y_i, R, θ) and returns the resultant deposition head position and orientation ($resx$, $resy$, $resa$) required to correct the planar shift.

The X and Y correction factors are calculated using a 2-dimensional coordinate transform from polar to cartesian coordinates. The resulting corrected position is obtained by a summation of the intended position coordinates and the correction factors, Equations 5.5 and 5.6. The algorithm used in the getco.m subroutine is displayed in Figure 5.11.

$$resx = x_i - R\cos(\theta) \tag{5.5}$$

$$resy = y_i - R\sin(\theta) \tag{5.6}$$

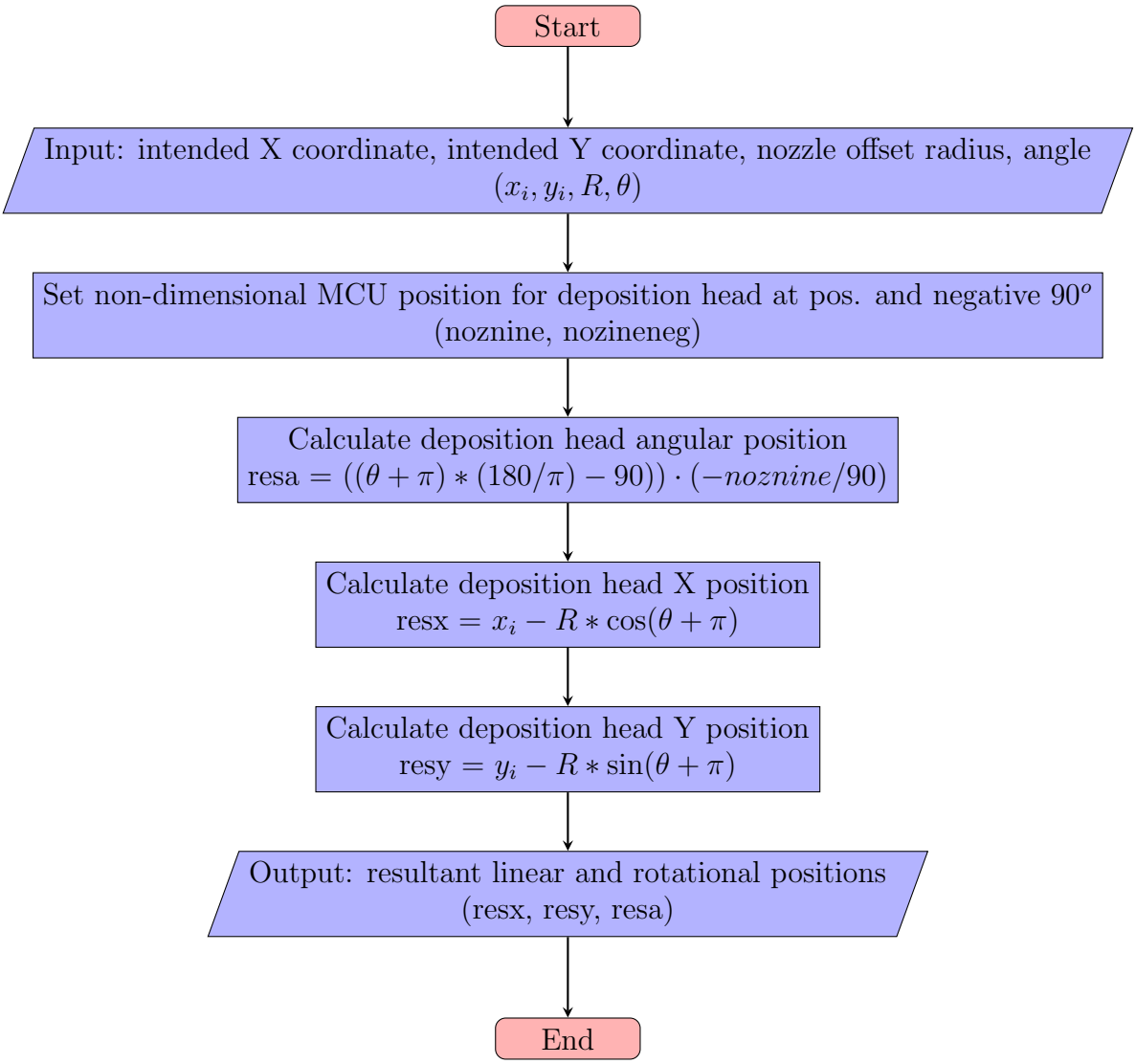

Figure 5.11: 'getco.m' subroutine used for calculating the positions and angle of the deposition head required to place a tow at a given point and orientation, by correcting for nozzle offset radius from the rotational axis of the deposition head.

5.4 CSM post-processor

The stitching post-processor is built on the same framework as the laydown post-processor, and as such, the CSM post-processor calculates stitch points from uO-Drape output files: XLengths, YLengths. X and Y position arrays are built using an identical method to that used in for the LM, Section 5.3.1. This results in X and Y position arrays that con-

tain the positions of tow intersection points rather than the positions in which substrate pins once were, where stitch will be inserted. However, this discrepancy is corrected during machine setup by shifting the point that is used to register the location of the preform within the CSM during machine setup. Incidentally, the CSM's origin is set to the location where the stitching needle is positioned on the first intended stitch point within the preform.

The NC file is initialized using the same format discussed in Section 5.2.2.1. Operational perimeters are inputed, allowing the operator to program the conveyor feed rate, stitching carriage feed rate, the stitching cycle time, and stitch-line direction. Stitch-lines are defined by a set of coordinates, which are obtained from an incremental set of position array indices. The general direction of the stitch-line is dictated by the index that is incremented. For instance stitch-line number i which runs in the general X direction is defined by the incremental set: $(x, y) = \{(xpos[i, j], ypos[i, j])\ , (xpos[i, j + 1], ypos[i, j + 1]), ..., (xpos[i, j + n], ypos[i, j + n])\}$. A stitch-line running in the general Y direction is defined by: $(x, y) = \{(xpos[i, j], ypos[i, j])\ , (xpos[i + 1, j], ypos[i + 1, j]), ..., (xpos[i + n, j], ypos[i + n, j])\}$.

A single stitching cycle is performed at each stitch point, thereby inserting a single stitch. During the stitching cycle, the needle penetrates the preform and remains embedded therein for a significant fraction of the cycle duration. Throughout that time, the stitching head must remain stationary with respect to the preform, as any relative motion between the two will result in tows becoming displaced by the sewing needle dragging through the preform. As a result, the Z axis that controls the stitching mechanism is always actuated as an independent process, and never in concurrence with a motion of the X direction conveyors or the Y direction carriage. Figure 5.12 displays the process used to build a stitching G-code file.

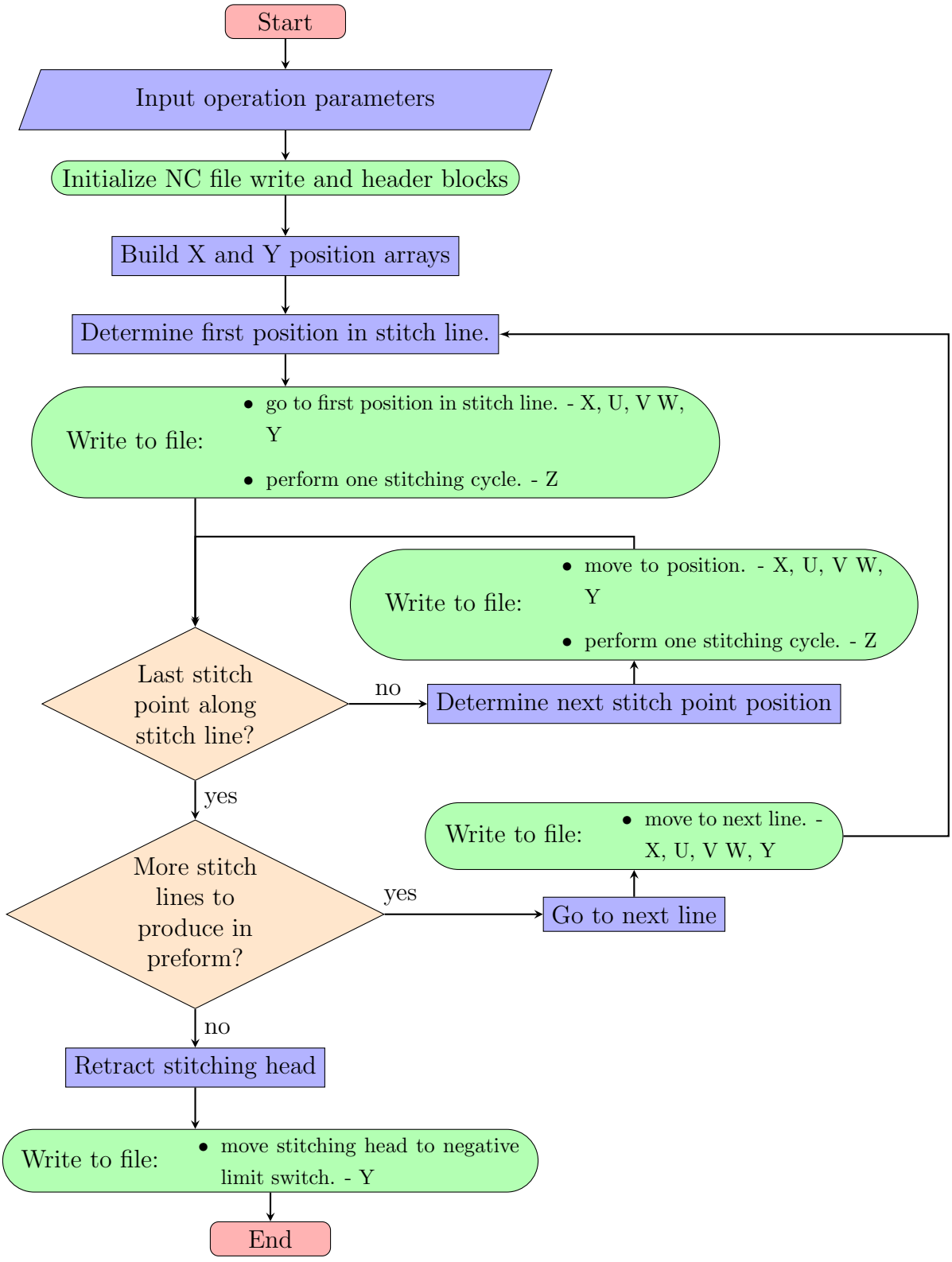

Figure 5.12: Post-processor for CSM G-code generation flowchart.

Chapter 6

Conclusions and Recommendations

This work brings a contribution to the CIRAQ COMP-501 project, which is ongoing at time of writing. The COMP-501 project focuses on investigating methods for cost-effective procurement of airframe components manufactured from carbon fibre reinforced polymer matrix composite materials. Efforts were made towards reducing the cost associated with layup operations that are typically used for producing preforms, which are required for manufacturing such components. This was approached by investigating the feasibility of using preforms that are manufactured to net-shape and final-thickness, using woven carbon fibre fabrics assembled using a structural carbon stitch. The effect of different stitching configurations on the forming behaviour of the assembled preform reinforcement was assessed in compaction, shear and bending.

Compaction tests were performed on areas with various stitching densities and patterns. Observation showed that an increase in stitch density lead to a loss in fibre volume fraction within the reinforcement. Additionally, stitching pattern was observed to have an effect on the fibre volume fraction, causing the fibre volume fraction to decrease in areas surrounding the intersections of discrete stitching lines. Further experimentation is required to confirm the mechanism of this phenomenon, specifically to confirm that the root cause thereof is yarn gathering that is caused by the stitch, rather than the presence of the stitch itself. This could be performed by an investigation into the fibre volume fraction in areas surrounding stitch line intersections with smaller diameter compaction platens that are positioned between individual stitches, thus assessing the fibre volume fraction of the fabric yarn without contact with and hence, the contribution of the stitching thread.

Data obtained through testing of the preforms in in-plane shear indicated that the force which is required to shear preforms is larger for preforms which have been stitched; however, the increase is limited. A specific locking angle could not be observed clearly for a number of preform samples. Instead, in said samples fibre locking occurred gradually and over a range of angles. Data gathered from samples in which a specific locking angle was observed displayed that fibre locking occurred at lower angles within the area confined by the stitch lines. In a number of samples it was very difficult to observe a specific angle corresponding to fibre lockup, even with the aid of high-resolution images which were captured during testing. It is recommended that subsequent testing employs a digital image correlation method.

Samples that were tested in bending displayed an increased resistance to the applied deformation when larger stitch densities were used to assemble them. Samples that were not stitched displayed the lowest resistance to bending. Bending was most problematic in the parallel bend configuration, bending along the stitch lines. In this configuration samples displayed the largest bending resistance, with stitch unravelling in one sample and yarn buckling observed visually in another. However, stitch unravelling and yarn buckling were not found to be highlighted by a significant event in the force–displacement quantitative data. Overall it was difficult to make any definitive conclusions as to events happening at a small scale in the inner bend radius due to the bending tight curvature, which significantly distorted the view.

Objectives for the uO-Tow manufacturing process were completed successfully. The process was developed through design, manufacturing and implementation of the equipment and support systems necessary to automate manufacturing of preforms with the characteristics sought.

As with any type of process, decisions both right and wrong appear more clearly with hindsight. This is no different for the work discussed in preceding chapters, and there are areas of the process that can still benefit from improvement. For example, large gains in overall process efficiency would have been realized if had the uO-tow post-processor been integrated into the uO-Drape software package. Such a pursuit was beyond of the scope of this study; however, the foundation and principles for its undertaking now exist.

The same principles governing design and operation of the laydown machine and contour stitching machine would apply to a scaled-up version of the machinery. However, in the event of such endeavour being undertaken, it is recommended that certain system within the LM be revised.

A revised cutting mechanism should be used; this mechanism should operate on similar principles as a guillotine, rather than the rotational type used in the prototype-scale deposition head. It is of the designer–authors' opinion that the reduced complexity in such a design would result with large improvements in tow cutting reliability. Additionally, a pneumatic linear piston is a far better suited actuator than the stepper motor drive used in the prototype, due to its ability to provide much greater force at a fraction of the size, weight and cost.

Improvements are still possible regarding the feed nozzle in terms of a reduction in the nozzle channel length. This would be beneficial to the process because the length ultimately limits the minimum tow length that can be deposited.

Bibliography

[1] A P Mouritz, M K Bannister, P J Falzon, and K H Leong. Review of applications for advanced three-dimensional fibre textile composites. *Compos. Part A Appl. Sci. Manuf.*, 30(12):1445–1461, 1999.

[2] J. Pridie (Airbus). Manufacture of a composite main landing gear rib by RTM. In *Compos. Struct. Dev. Centre. 8th Int. Conf. Text. Compos. (TEXCOMP- 8). Nottingham, UK, 16-18 Oct*, 2006.

[3] A. Mills. Development of an automated preforming technology for resin infusion processing of aircraft components. In *Proc. Inst. Mech. Eng. Part G J. Aerosp. Eng. 220*, pages 499–505, 2006.

[4] Suresh G. Advani. Jeffrey M. Lawrence, Scott T. Holmes, Michael Louderback, Addison Williams, Pavel Simacek. The use of flow simulations of large complex composite components using the VARTM process. In *FPCM-9 9th Int. Conf. Flow Process. Compos. Mater. Montreal (Quebec), Canada 8˜10 july*, 2008.

[5] K. Dambrine, B., Mahieu, J.-N., Goering, J., Ouellette. Development of 3D woven, resin transfer molded fan blades. In *Proc. 9th Int. Conf. Text. Compos. - TEXCOMP9 Recent Adv. Text. Compos.*, pages 19–24, 2008.

[6] A. Abusafieh (Cytec Engineered Materials). Recent Successes and Current Challenges in Implementing Resin Infusion Processes for Manufacturing of Aircraft Components. In *Proc. 9th Int. Conf. Text. Compos. - TEXCOMP9 Recent Adv. Text. Compos.*, 2008.

[7] Siqi Zhu. *An automated fabric layup machine for the manufacturing of fiber reinforced polymer composite*. PhD thesis, Iowa State University, 2013.

[8] Hilmar APMANN. Automatic Handling of Dry Carbon Fabrics and Prepregs. In *ICCM-17*. INTERNATIONAL COMMITTEE ON COMPOSITE MATERIALS, 2009.

[9] J. Wittig. Process automation for the production of large composite. *Reinf. Plast. -LONDON-*, 49(1):30–33, 2005.

[10] M. Tarsha Kordi, M. Husing, and B. Corves. Development of a multifunctional robot end- effector system for automated manufacture of textile preforms. In *2007 IEEE/ASME Int. Conf. Adv. Intell. mechatronics*, pages 30–33. IEEE, 2007.

[11] P Potluri T Sherif. Robotic Preforming of Thick Near-net Composites. In *Proc. TexComp 9*, Newark, Delaware, USA, October 2008. DEStech.

[12] Niklas Svensson. Development of textile structures for load carrying composites. In *World Conf. Text. Institute, Proc. 1*, pages 433–449, 1997.

[13] Ryuta Kamiya, Bryan A Cheeseman, Peter Popper, and Tsu-wei Chou. Some recent advances in the fabrication and design of three-dimensional textile preforms: a review. *Compos. Sci. Technol.*, 60:33–47, 2000.

[14] C Weimer, T Preller, P Mitschang, and K Drechsler. Approach to net-shape preforming using textile technologies. Part I: edges. *Compos. Part A Appl. Sci. Manuf.*, 31(11):1261–1268, November 2000.

[15] C Weimer, T Preller, P Mitschang, and K Drechsler. Approach to net-shape preforming using textile technologies. Part II: holes. *Compos. Part A Appl. Sci. Manuf.*, 31(11):1269–1277, November 2000.

[16] Christopher M. Pastore. Opportunities and challenges for textile reinforced composites. *Mech. Compos. Mater.*, 36(2):97–116, March 2000.

[17] Michael Bannister. Challenges for composites into the next millennium a reinforcement perspective. *Compos. Part A Appl. Sci. Manuf.*, 32(7):901–910, 2001.

[18] L. Tong, A.P. Mouritz, and M. Bannister. *3D Fibre Reinforced Polymer Composites*, volume 2002. Elsevier, 2002.

[19] C. Mitschang, P., Ogale, A., Schlimbach, J., Weyrauch, F., Weimer. Preform technology: A necessary requirement for quality controlled LCM-processes. *Polym. Polym. Compos.*, 11(8):605–622, 2003.

[20] M. K. Bannister. Development and application of advanced textile composites. *Proc. Inst. Mech. Eng. Part L J. Mater. Des. Appl.*, 218(3):253–260, July 2004.

[21] R. Ogale, V., Alagirusamy. Textile preforms for advanced composites. *Indian J. Fibre Text. Res.*, 29(3):366–375, 2004.

[22] T. Shelley. Maximum material performance. *Eureka*, 26(9):15–16, 2006.

[23] Jacques Lamon, Werner Hufenbach, Maik Gude, and Christoph Ebert. Hybrid 3D-textile reinforced composites with tailored property profiles for crash and impact applications. *Compos. Sci. Technol.*, 69(9):1422–1426, 2009.

[24] F. Greb, C., Schnabel, A., Gries, T., Kruse. Development of new preforming processes for high performance fibre-reinforced plastic (FRP) components. *SAMPE J.*, 46(5):42–51, 2010.

[25] MJ Shuart, NJ Johnston, and HB Dexter. *Automated fabrication technologies for high performance polymer composites*. Number May. Paper presented at the RTO AVT Workshop on Intelligent Processing of High Performance Materials, held in Brussels, Belgium, 13-14 May 1998, and published in RTO MP-9. -05_05X-, 1998.

[26] A Dewing, M Sarhadi, T A Mitchell, R I Davis, and J Eastham. Robotic tacking of high-quality composite preforms. *Proc. Inst. Mech. Eng. Part G J. Aerosp. Eng.*, 213(3):173–185, January 1999.

[27] A. Omar, S.; Goel. 3-Dimensional Fabrics. *Man-Made Text. India*, 52(4):120–123, 2009.

[28] M.H. Bogdanovich, A.E., Mohamed. Three-dimensional reinforcements for composites. *SAMPE J.*, 45(6):8–28, 2009.

[29] H Talvensaari, E Ladstatter, and W Billinger. Permeability of stitched preform packages. *Compos. Struct.*, 71:371–377, 2005.

[30] R. Fangueiro and M. De Araujo. Mechanical Properties of Composite Materials Made of 3D Stitched Woven-knitted Preforms. *J. Compos. Mater.*, 44(14):1753–1767, January 2010.

[31] L. Zhao, I. Porat, and K. Greenwood. The Computerised Weaving of Preforms for Composites Part I: The Flattening of 3-dimensional Preforms. *J. Text. Inst.*, 87(1):183–194, January 1996.

[32] K. Greenwood, L. Zhao, and I. Porat. The Computerised Weaving of Preforms for Composites Part II: Feature Analysis of the Flattened Structures. *J. Text. Inst.*, 87(1):195–202, January 1996.

[33] D. Dawson. Yarns and fibres learn the x, y and z of three dimensions. *Tech. Text. Int.*, 11(3):29–31, 2002.

[34] C.-H. Chiu and C.-C. Cheng. Weaving Method of 3D Woven Preforms for Advanced Composite Materials. *Text. Res. J.*, 73(1):37–41, January 2003.

[35] J Quinn, R McIlhagger, and A.T McIlhagger. A modified system for design and analysis of 3D woven preforms. *Compos. Part A Appl. Sci. Manuf.*, 34(6):503–509, 2003.

[36] B K Behera and Rajesh Mishra. 3-Dimensional weaving. 33(3):274–287, 2008.

[37] F. Oussu, X. Legrand, and C. Binetruy. General definition of warp interlock structures. In *Proc. 9th Int. Conf. Text. Compos. - TEXCOMP9 Recent Adv. Text. Compos.*, pages 399–407. DEStech Publications, Inc, 2008.

[38] P Potluri D Jetavat. Extension of 3D Weaving Concepts for Near-net Preforming. April 2008.

[39] Taylor, D., A.-F.M. Seyam, and N.B. Powell. Three-dimensional woven composites for automotive applications. In *Proc. 9th Int. Conf. Text. Compos. - TEXCOMP9 Recent Adv. Text. Compos.*, pages 208–287, 2008.

[40] S. Buchanan, A. Grigorash, J. P. Quinn, A. T. McIlhagger, and C. Young. Modelling the geometry of the repeat unit cell of three-dimensional weave architectures. *J. Text. Inst.*, 101(7):679–685, June 2010.

[41] J.A. Soden, G. Weissenbach, and B.J. Hill. The design and fabrication of 3D multilayer woven T-section reinforcements. *Compos. Part A Appl. Sci. Manuf.*, 30(3):213–220, 1999.

[42] A. Ebru Tayyar. Engineering, Manufacturing, and Measuring 3D Domed Woven Fabrics. *Text. Res. J.*, 73(5):375–380, May 2003.

[43] Mansour H. MOHAMED and Kvle K. WETZEL. 3D woven carbon/glass hybrid spar cap for wind turbine rotor blade. *J. Sol. energy Eng.*, 128(4):562–573.

[44] C. McHugh (Sigmatex). The Manufacture of One Piece Woven Three Dimensional Carbon Fiber Nodal Structures. In *Text. - SAMPE Seattle May 2010*.

[45] R. Heider, D., Deffor, H., Reuter, M., Gillespie Jr., J.W., Mohamed, M., Crane. Large-scale joint fabrication using 3-D fabric preforms, sandwich core structure and VARTM processing. *SAMPE J.*, 2008.

[46] D E Bates, S Kiko, and T R H Society. *Goodyear*. Images of America. Arcadia Pub., illustrate edition, 2010.

[47] Hasan Alhashmy. *Fabrication of Aluminium Matrix Composites (AMCs) by Squeeze Casting Technique Using Carbon Fiber as Reinforcement*. PhD thesis, University of Ottawa, 2012.

[48] P. W. Manders and M. G. Bader. The strength of hybrid glass/carbon fibre composites. *J. Mater. Sci.*, 16(8):2233–2245, August 1981.

[49] Francois Robitaille. MCG 2361 - Lecture Nine, 2009.

[50] C E Ford and C V Mitchell. Fibrous graphite US 3107152 A, 1963.

[51] American Chemical Society. High Performance Carbon Fibers - National Historic Chemical Landmark. American Chemical Society, September 2003.

[52] Schalamon W Bacon R. Process for producing carbon fibers having a high young's modulus of elasticity US 3716331 A, 1973.

[53] T. Centea and P. Hubert. Measuring the impregnation of an out-of-autoclave prepreg by micro-CT. *Compos. Sci. Technol.*, 71(5):593–599, March 2011.

[54] L.K. Grunenfelder and S.R. Nutt. Void formation in composite prepregs Effect of dissolved moisture. *Compos. Sci. Technol.*, 70(16):2304–2309, December 2010.

[55] Editor Elsevier. Technology update: prepregs. *Reinf. Plast.*, 47(6):20–21, June 2003.

[56] George Marsh. Prepregs raw material for high-performance composites. *Reinf. Plast.*, 46(10):24–28, October 2002.

[57] F C Campbell. *Structural Composite Materials*. A S M International, 2010.

[58] M Eldiwany, J M Powers, and L A George. Mechanical properties of direct and post-cured composites. *Am. J. Dent.*, 6(5):222–4, October 1993.

[59] B.R. Gebart. Permeability of Unidirectional Reinforcements for RTM. *J. Compos. Mater.*, 26(8):1100–1133, January 1992.

[60] D J Michaud, A N Beris, and P S Dhurjati. Thick-sectioned RTM composite manufacturing, part II. Robust cure cycle optimization and control. *J. Compos. Mater.*, 36(10):1201–1231, 2002.

[61] Brian W Grimsley. *Characterization of the Vacuum Assisted Resin Transfer Molding Process for Fabrication of Aerospace Composites*. PhD thesis, Virginia Polytechnic Institute and State University, 2005.

[62] J. G. Williams and Jr. Mikulas, M. M. Analytical and experimental study of structurally efficient composite hat-stiffened panels loaded in axial compression. May 1975.

[63] Masaki Aono, Paolo Denti, David E Breen, and Michael J Wozny. Fitting a woven cloth model to a curved surface: dart insertion. *IEEE Comput. Graph. Appl.*, 16(5):60–70, 1996.

[64] Jeff Sloan. Auto composites quest: One-minute cycle time? In *Compos. Technol. - August 2012*, chapter Features. August 2012.

[65] P Boisse. *Composite Reinforcements for Optimum Performance*. Woodhead Publishing Series in Composites Science and Engineering. Elsevier Science, 2011.

[66] R. McIlhagger, J.P. Quinn, A.T. McIlhagger, S. Wilson, D. Simpson, and W. Wenger. The influence of binder tow density on the mechanical properties of spatially reinforced composites. Part 2 Mechanical properties. *Compos. Part A Appl. Sci. Manuf.*, 39(2):334–341, 2008.

[67] S Rudov-Clark. Experimental investigation of the tensile properties and failure mechanisms of three-dimensional woven composites. 2007.

[68] QinetiQ Inc. Stitched Dry Fibre Preforms Data Sheet. 2011.

[69] B.R.K. Blackman, Denis D.R. Cartié, Giuseppe DellAnno, Emilie Poulin, and Ivana K. Partridge. 3D reinforcement of stiffener-to-skin T-joints by Z-pinning and tufting. *Eng. Fract. Mech.*, 73(16):2532–2540, 2006.

[70] M.N. Grimshaw, C.G. Grant, J.M.L., and Diaz. Advanced Technology Tape Laying for Affordable Manufacturing of Large Com- posite Structures. In *46th Int. SAMPE Symp.*, pages 2484–2494.

[71] V.K. Srivastava, M. Singh, G. Kostorz, and C. Soutis. Carbon fiber reinforced plastics in aircraft construction. *Mater. Sci. Eng. A*, 412(1):171–176, 2005.

[72] D.O. Evans. Fiber Placement. *ASM Handb.*, 21(Composites):477–479, 2001.

[73] C.D Rudd, M.R Turner, A.C Long, and V Middleton. Tow placement studies for liquid composite moulding. *Compos. Part A Appl. Sci. Manuf.*, 30(9):1105–1121, September 1999.

[74] R.A. Saunders, C. Lekakou, and M.G. Bader. Compression and microstructure of fibre plain woven cloths in the processing of polymer composites. *Compos. Part A Appl. Sci. Manuf.*, 29(4):443–454, January 1998.

[75] Francois Robitaille and Raymond Gauvin. Compaction of textile reinforcements for composites manufacturing. III: Reorganization of the fiber network. *Polym. Compos.*, 20(1):48–61, February 1999.

[76] Andrew Lawrence Stewart. *Measurement and analysis of flow in 3D preforms for aerospace composites*. PhD thesis, Ottawa-Carlton Institue for Mechanical and Aerospace Engineering, 2012.

[77] C M Van Wyk. Note on the Compressibility of Wool. *J. Text. Inst. Trans.*, 37(12):T285—-T292, 1946.

[78] B Chen. Compaction of woven-fabric preforms: nesting and multi-layer deformation. *Compos. Sci. Technol.*, 60(12-13):2223–2231, September 2000.

[79] B Chen, A.H.-D Cheng, and T.-W Chou. A nonlinear compaction model for fibrous preforms. *Compos. Part A Appl. Sci. Manuf.*, 32(5):701–707, May 2001.

[80] Francois Robitaille and Raymond Gauvin. Compaction of textile reinforcements for composites manufacturing. I: Review of experimental results. *Polym. Compos.*, 19(2):198–216, April 1998.

[81] U. Mohammed, C. Lekakou, L. Dong, and M.G. Bader. Shear deformation and micromechanics of woven fabrics. *Compos. Part A Appl. Sci. Manuf.*, 31(4):299–308, April 2000.

[82] Woong Ryeol Yu, Michael Zampaloni, Farhang Pourboghrat, Kwansoo Chung, and Tae Jin Kang. Analysis of flexible bending behavior of woven preform using non-orthogonal constitutive equation. *Compos. Part A Appl. Sci. Manuf.*, 36(6):839–850, June 2005.

[83] E. Bilbao, D. Soulat, G. Hivet, and A. Gasser. Experimental Study of Bending Behaviour of Reinforcements. *Exp. Mech.*, 50(3):333–351, March 2009.

[84] Marco Chilo. *Techniques of Meso-scale Measurement of Fibre Assemblies*. Phd, The University of Manchester, January 2013.

[85] Andrej Lippai. CNC USB Controller - User Manual. Technical report, 2013.

[86] Farshad Khorrami, Prashanth Krishnamurthy, and Hemant Melkote. *Modeling and Adaptive Nonlinear Control of Electric Motors (Google eBook)*. Springer, 2003.

[87] Instron Industrial Products. Instron 2525-800 Series Load Cells. Technical report, 2005.

[88] C Leduc. Description des parametres de couture.

[89] J. Cao, R. Akkerman, P. Boisse, J. Chen, H.S. Cheng, J. Wiggers, T.X. Yu, and B. Zhu. Characterization of mechanical behavior of woven fabrics: Experimental methods and benchmark results. *Compos. Part A Appl. Sci. Manuf.*, 39(6):1037–1053, June 2008.

[90] J Wittig. Recent development in the robotic stitching technology for textile structural composites. *J. Text. Apparel, Technol. Manag.*, 2(1):1–8, 2001.

[91] Nicholas Burnford. *Development of Drape Simulation Software and the Optimisation of Variable-Length Textiles*. PhD thesis, University of Ottawa, 2011.

[92] Probotix. ProboStepVX - Data sheet. Technical report, 2007.

[93] Zhengwen Zhang and Associate Member. Modeling and Analysis of Electrostatic Force for Robot Handling of Fabric Materials. *IEEE/ASME Trans. Mechatronics*, 4(March):39–49, 1999.

[94] X. Q. SARHAD and CHEN M. Investigation of Electrostatic Force for Robotic Lay-up of Composite Fabrics. *Mechanics*, 2(4):363–373, 1992.

[95] G.J. Monkman. Robot Grippers for Use With Fibrous Materials. *Int. J. Rob. Res.*, 14(2):144–151, April 1995.

[96] Scott. Audette. *Mechanical Properties of Aerospace Composite Made from Multi-layer 3D Carbon Fibre Preforms*. PhD thesis, Ottawa-Carlton Institue for Mechanical and Aerospace Engineering, 2014.

Acronyms

A

AFP
: advanced fibre placement

B

BA
: Bombardier Aéronautique

BH
: Bell Helicopter

C

CAD
: computer-aided design

CAM
: computer-aided manufacturing

CF
: carbon fibre

CRIAQ
: consortium for research and innovation in aerospace in Quebec

CS
: contour stitching

CSM
: contour stitching machine

CTLM
: contour tape-laying machine

CTLMs
: contour tape-laying machines

CTT
: Centre des Technologies Textiles

D

DIN
: Deutsches Institut für Normung

DOF
: degrees of freedom

E

EMF
: electromotive force

ETS
: École de Technologie Supérieure

F

FDM
: fused deposition modelling

FTLM
: flat tape-laying machine

FTLMs
: flat tape-laying machines

H

HA
: Hutchinson Aerospace

HID
: human interface device

I

ICE
: International Electrotechnical Commission

ILSS
: inter-laminar shear strength

J

JB
: JB Martin

L

LCM
: liquid composite moulding

LM
: laydown machine

M

MCU
: machine control unit

N

NaN
: not a number

NC
: numerical control

O

OEM
: original equipment manufacturer

P

PAN
: polyacrylonitrile

PMC
: polymer matrix composite

PMIC
: power management integrated circuit

PMMA
: polymethyl methacrylate – a transparent thermoplastic

PSU
: power supply unit

R

RFI
: resin film infusion

RTM
: resin transfer moulding

U

UL
: Université Laval

UO
: University of Ottawa

USB
: universal serial bus

V

VARTM
: vacuum assisted resin transfer moulding.

vf
: fibre volume fraction

Appendix A

Mechanical Testing

A.1 Compaction testing

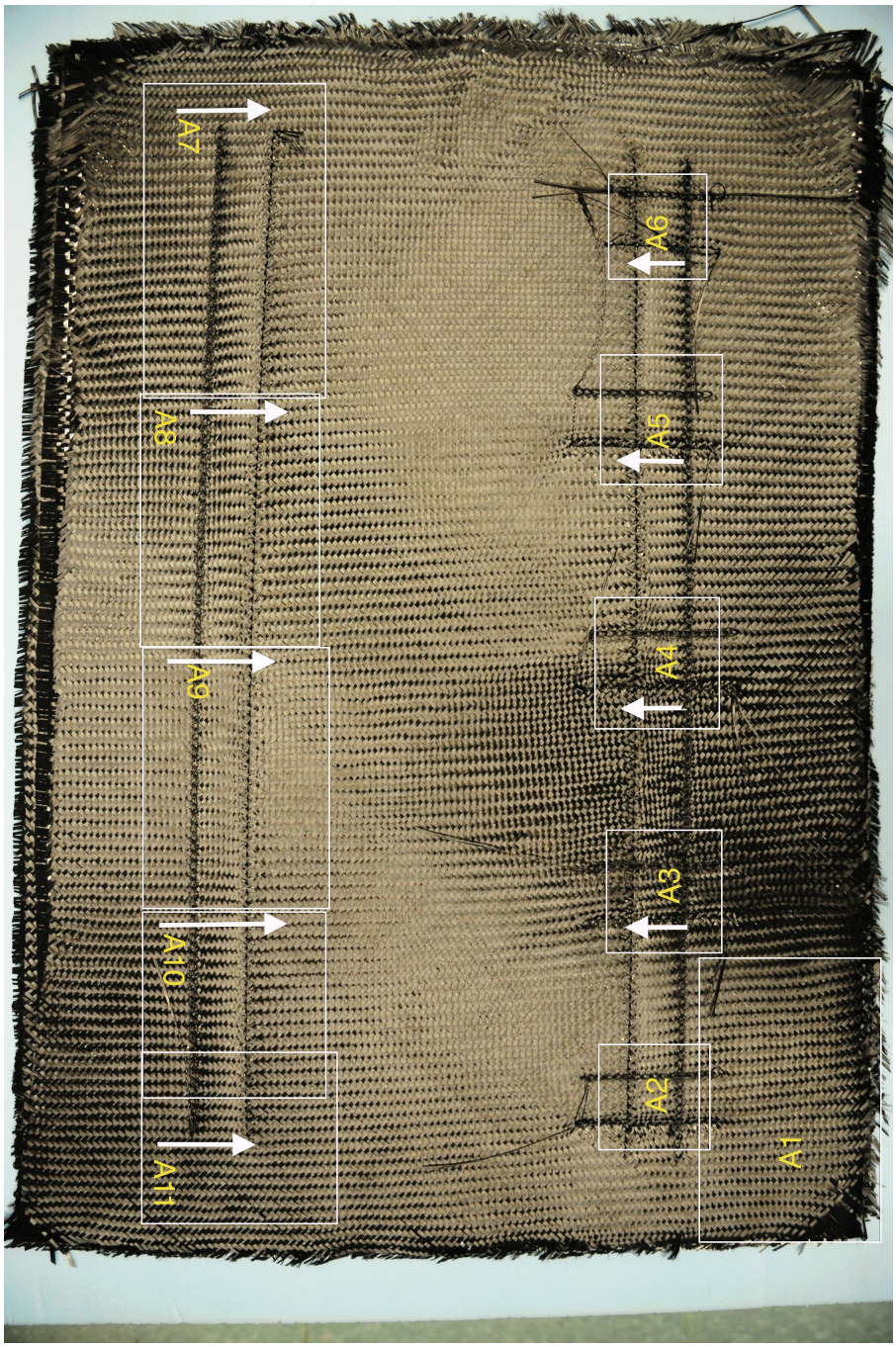

Figure A.1: Frontside overview of the '700-0005-p4' (4mm stitch) test preform, showing frontside test sample designations and photo frame area.

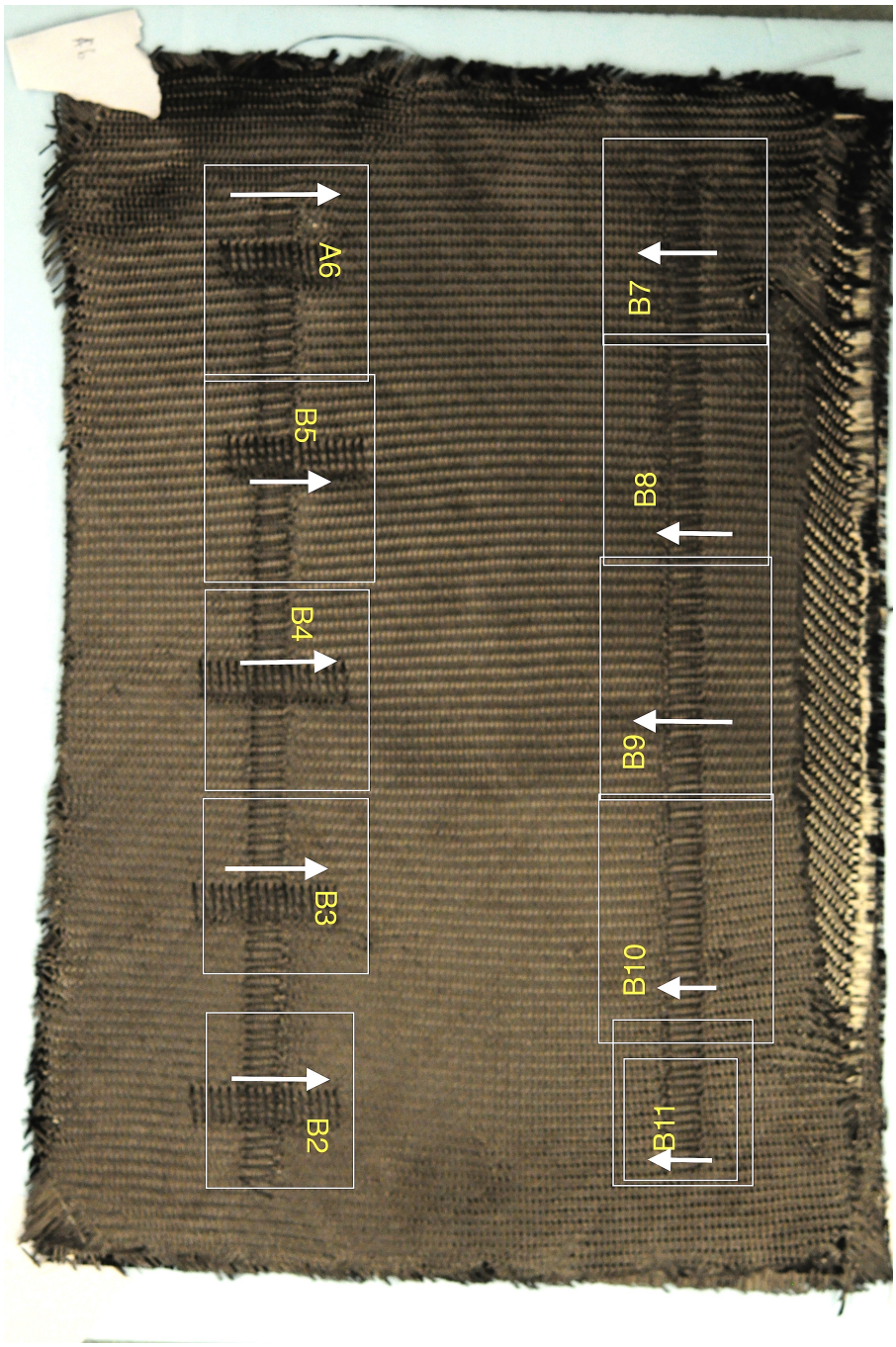

Figure A.2: Backside overview of the '700-0005-p4' (4mm stitch) test preform, showing backside test sample designations and photo frame area.

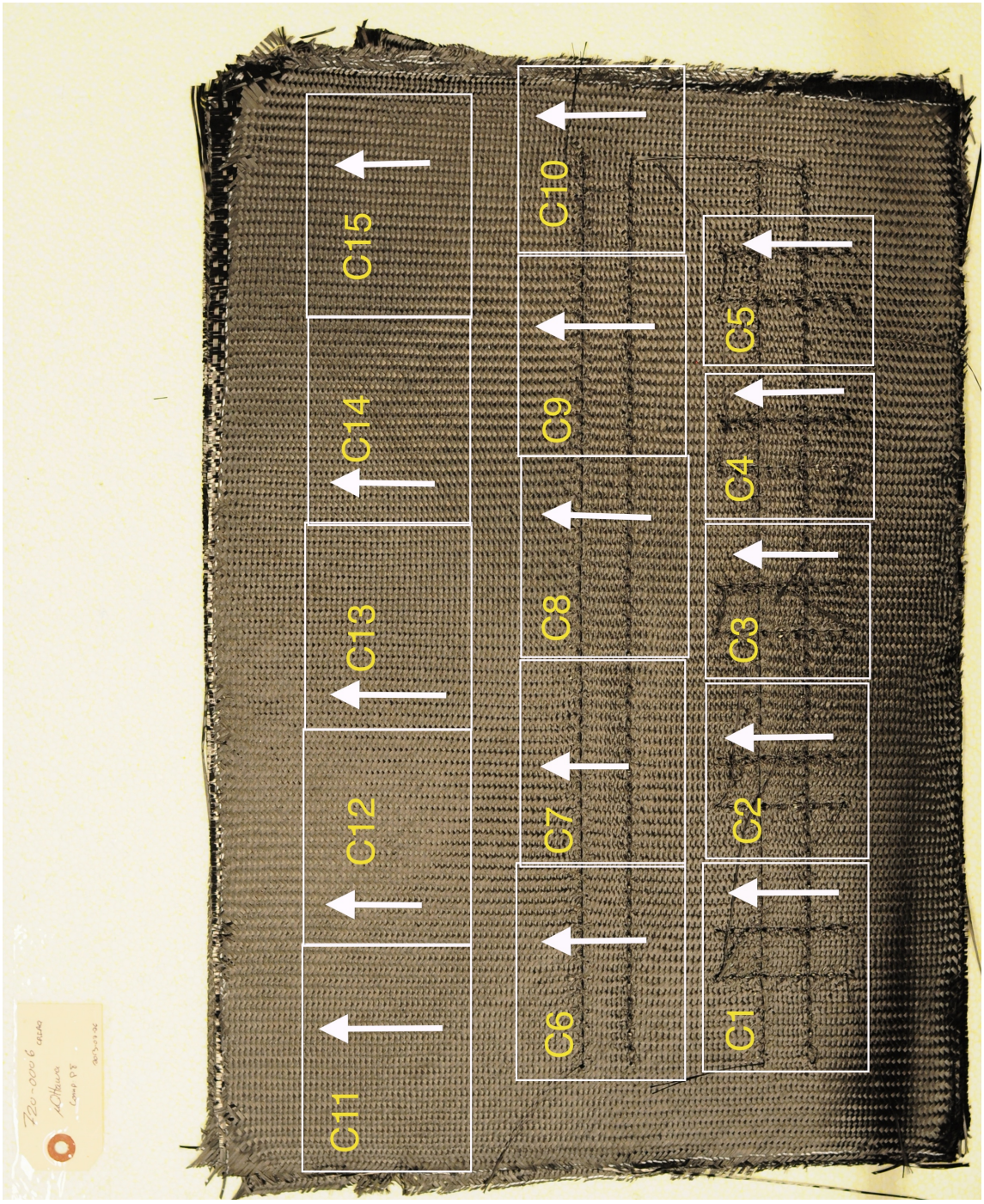

Figure A.3: Frontside overview of the '720-0006-p8' (8mm and 'sans' stitch) test preform, showing frontside test sample designations and photo frame area.

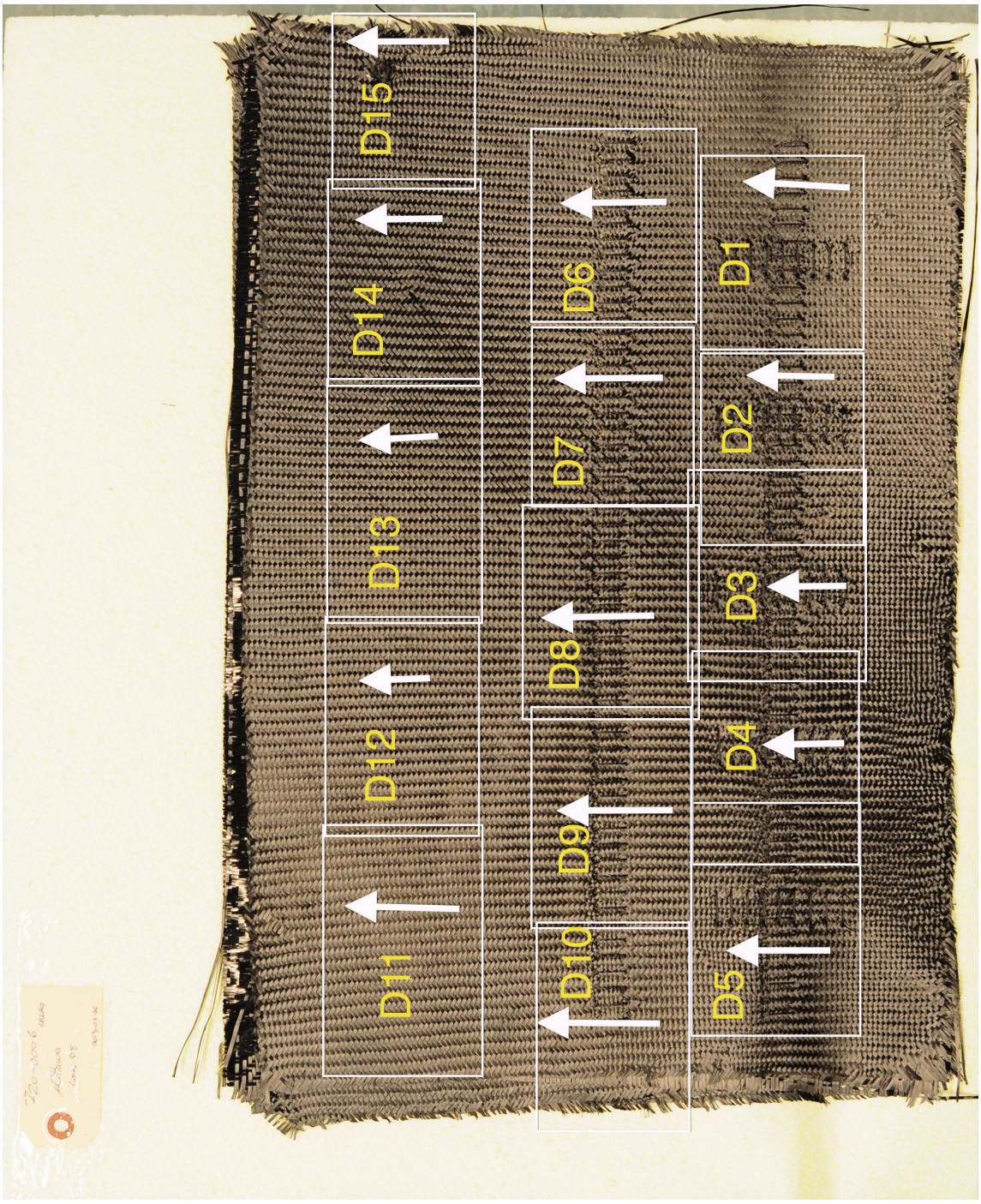

Figure A.4: Backside overview of the '720-0006-p8' (8mm and 'sans' stitch) test preform, showing backside test sample designations and photo frame area.

A.1.1 'E' Samples - sans-stitch

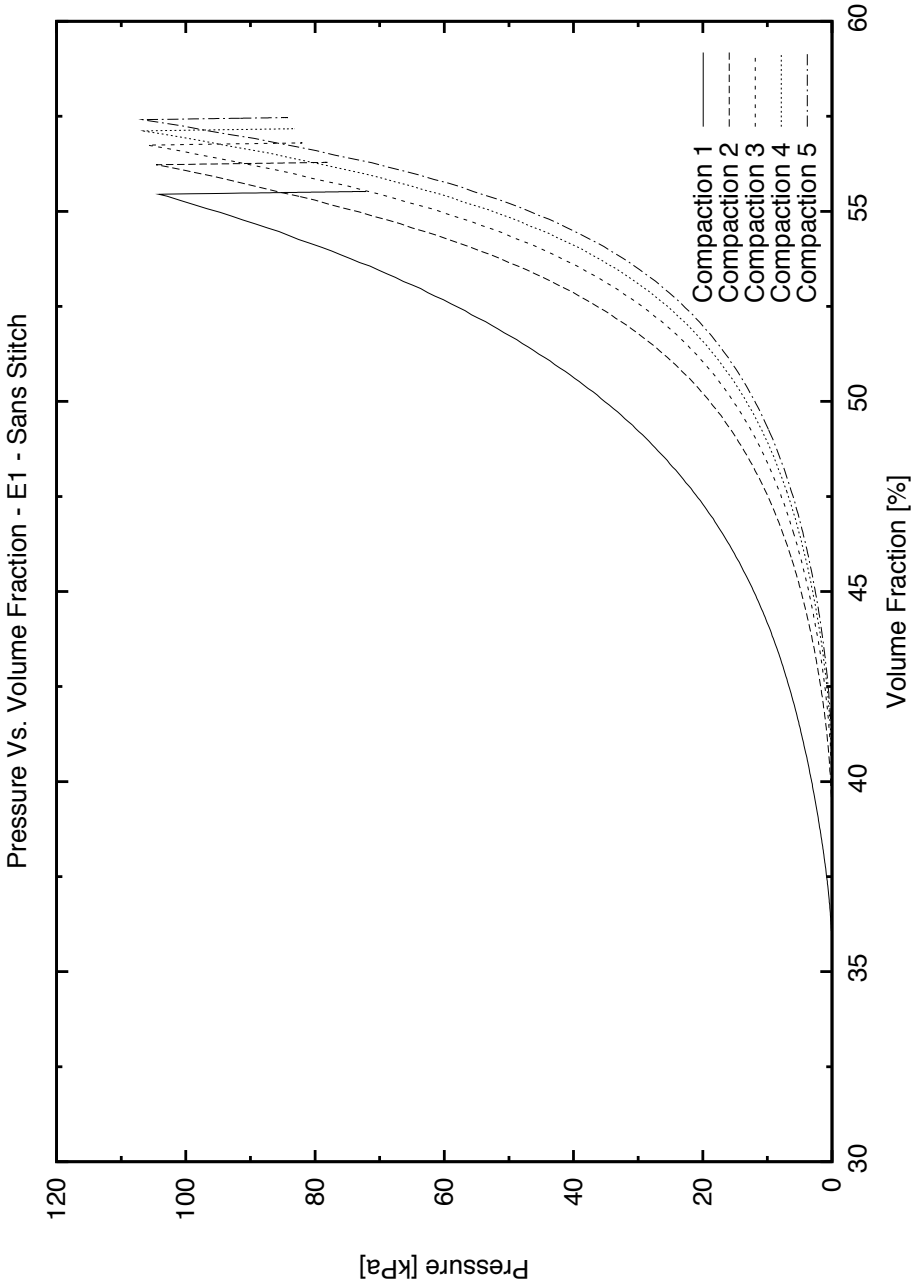
Pressure Vs. Volume Fraction - E1 - Sans Stitch
Pressure [kPa]
Volume Fraction [%]
Compaction 1
Compaction 2
Compaction 3
Compaction 4
Compaction 5
120
100
80
60
40
20
0
30
35
40
45
50
55
60

Figure A.5

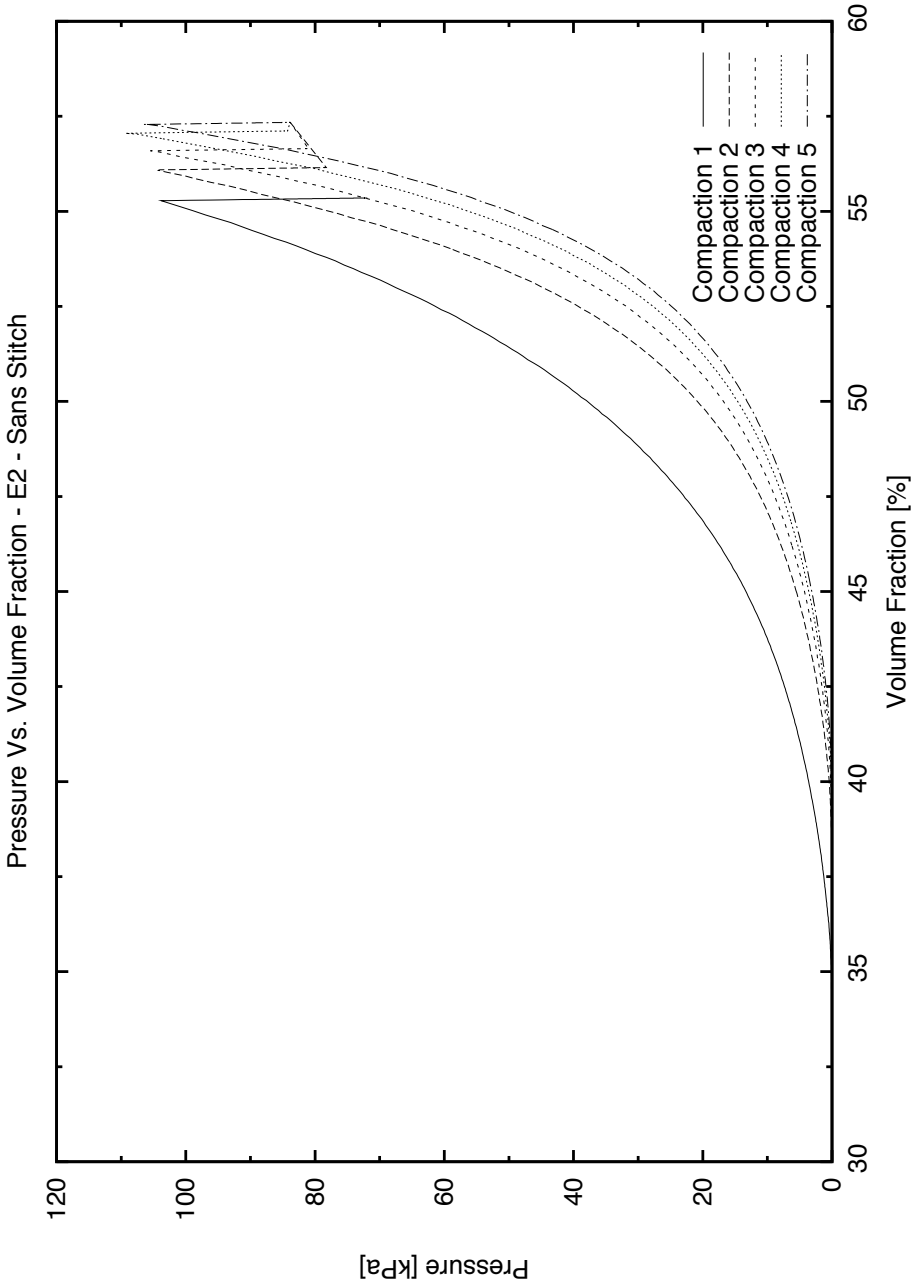
Pressure Vs. Volume Fraction - E2 - Sans Stitch
Pressure [kPa]
Volume Fraction [%]
Compaction 1
Compaction 2
Compaction 3
Compaction 4
Compaction 5
120
100
80
60
40
20
0
30
35
40
45
50
55
60

Figure A.6

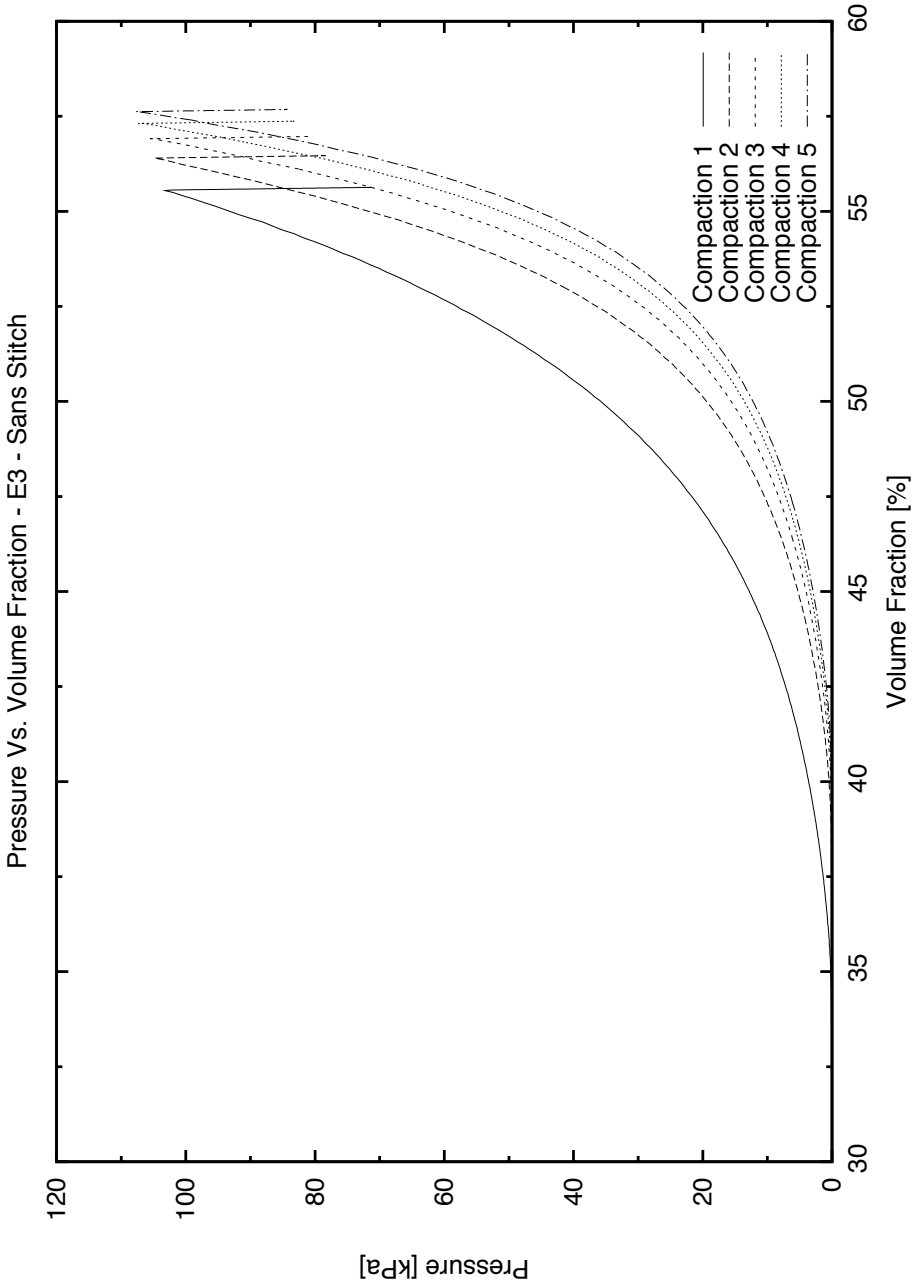
Pressure Vs. Volume Fraction - E3 - Sans Stitch
Pressure [kPa]
Volume Fraction [%]
Compaction 1
Compaction 2
Compaction 3
Compaction 4
Compaction 5
120
100
80
60
40
20
0
30
35
40
45
50
55
60

Figure A.7

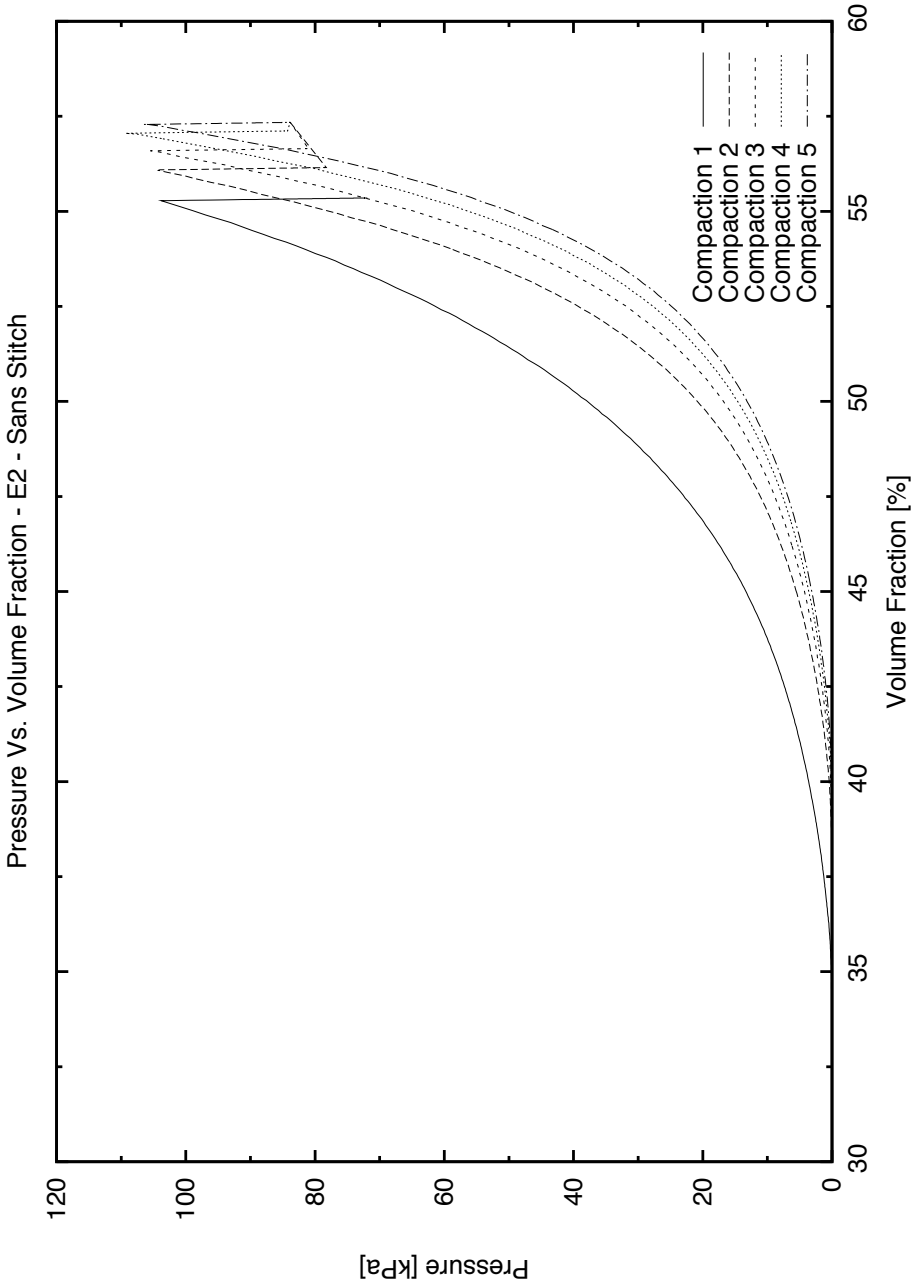
Pressure Vs. Volume Fraction - E2 - Sans Stitch
Pressure [kPa]
Volume Fraction [%]
Compaction 1
Compaction 2
Compaction 3
Compaction 4
Compaction 5
120
100
80
60
40
20
0
30
35
40
45
50
55
60

Figure A.8

A.1.2 'B' Samples - 4mm single stitch

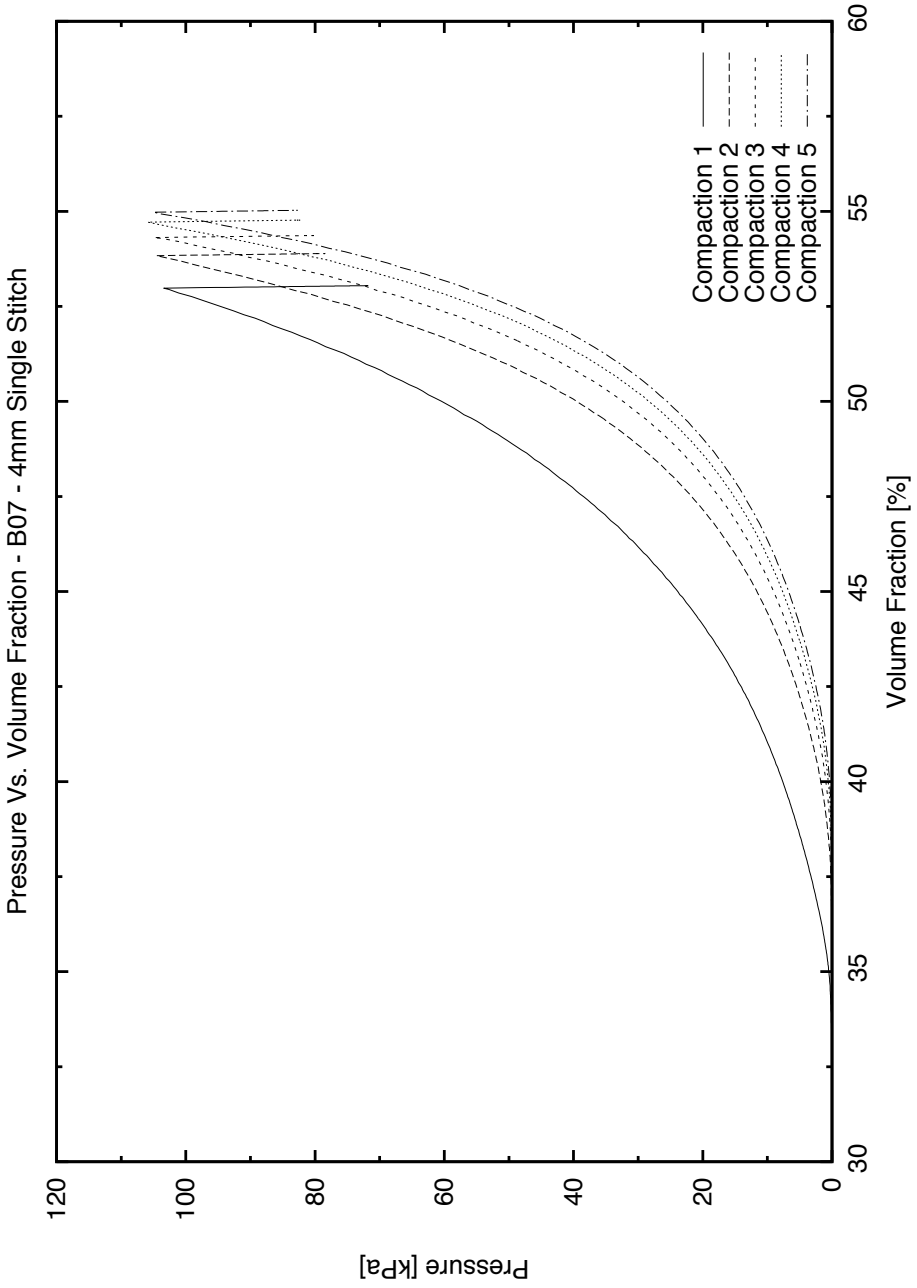
Pressure Vs. Volume Fraction - B07 - 4mm Single Stitch
Compaction 1
Compaction 2
Compaction 3
Compaction 4
Compaction 5
Pressure [kPa]
Volume Fraction [%]
120
100
80
60
40
20
0
30
35
40
45
50
55
60

Figure A.9

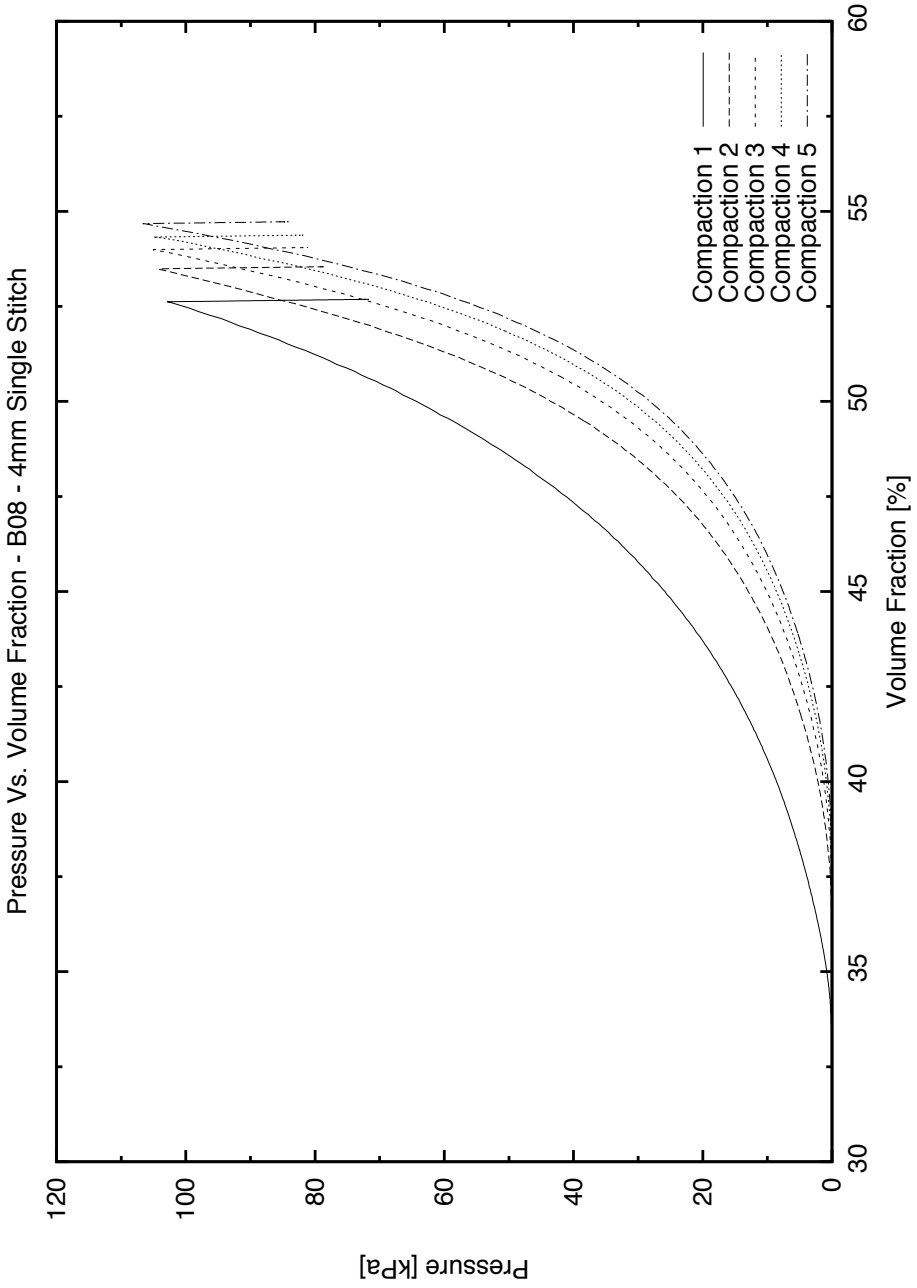
Pressure Vs. Volume Fraction - B08 - 4mm Single Stitch
Compaction 1
Compaction 2
Compaction 3
Compaction 4
Compaction 5
Pressure [kPa]
Volume Fraction [%]
120
100
80
60
40
20
0
30
35
40
45
50
55
60

Figure A.10

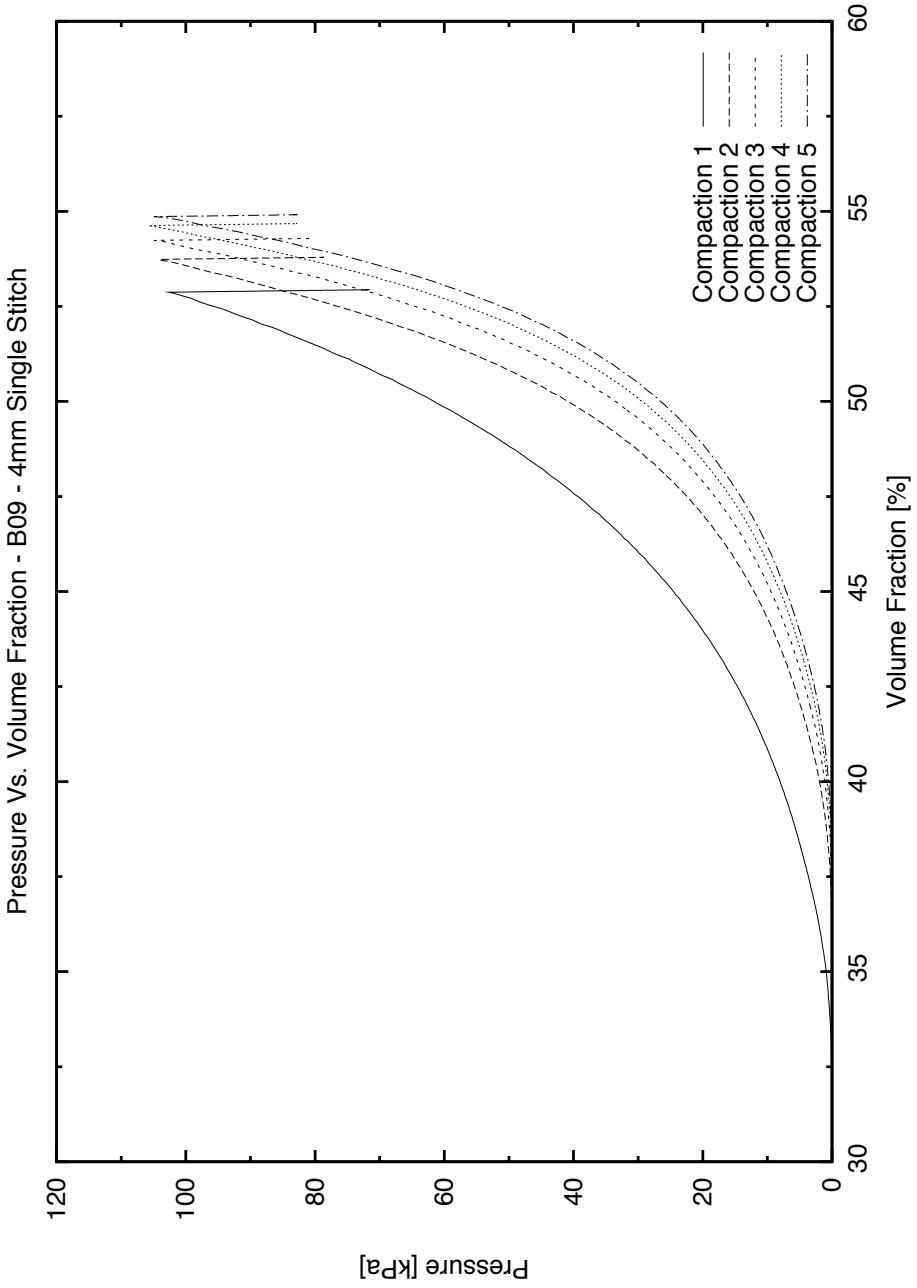
Pressure Vs. Volume Fraction - B09 - 4mm Single Stitch
Compaction 1
Compaction 2
Compaction 3
Compaction 4
Compaction 5
Pressure [kPa]
Volume Fraction [%]
120
100
80
60
40
20
0
30
35
40
45
50
55
60

Figure A.11

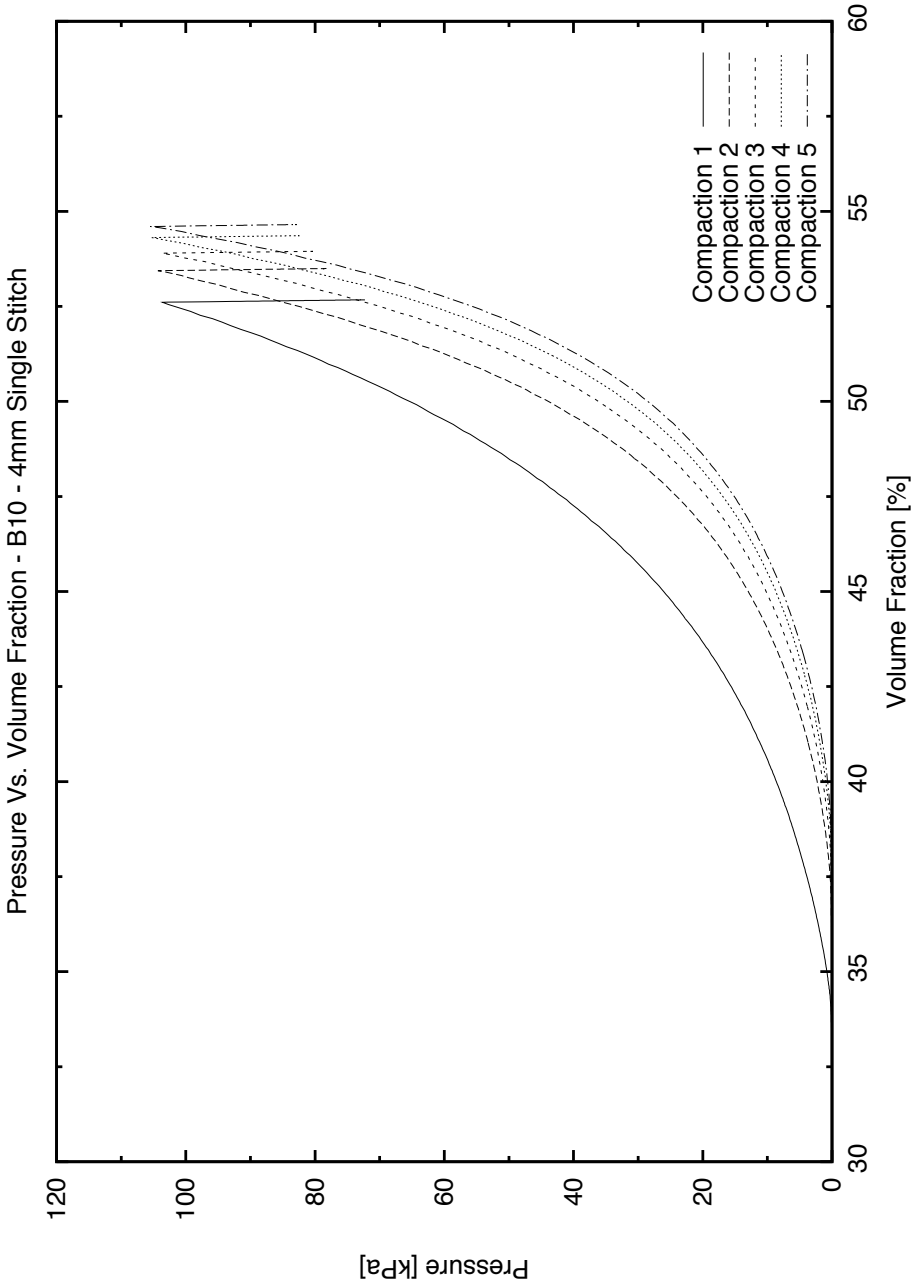
Pressure Vs. Volume Fraction - B10 - 4mm Single Stitch
Compaction 1
Compaction 2
Compaction 3
Compaction 4
Compaction 5
Pressure [kPa]
Volume Fraction [%]
120
100
80
60
40
20
0
30
35
40
45
50
55
60

Figure A.12

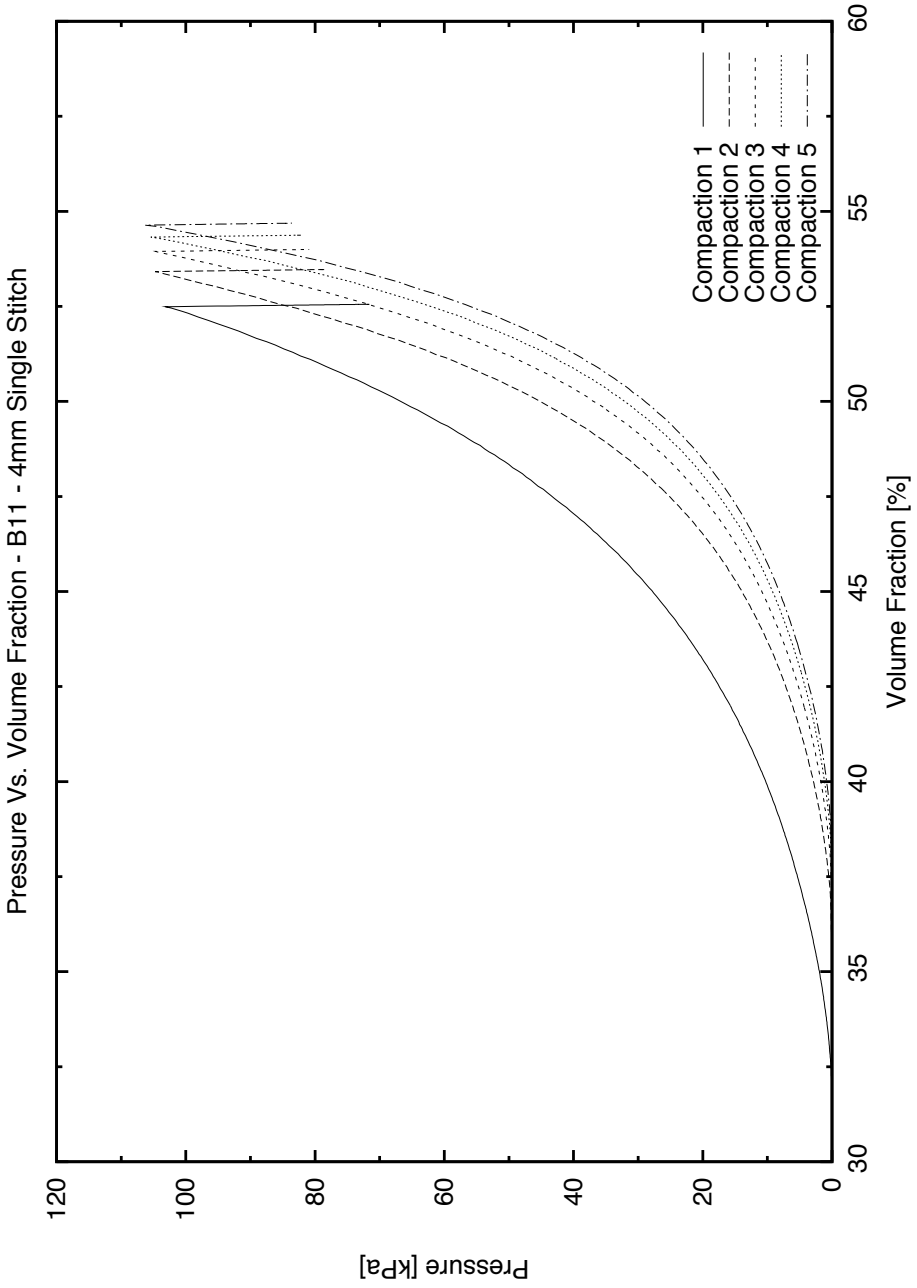
Pressure Vs. Volume Fraction - B11 - 4mm Single Stitch
Compaction 1
Compaction 2
Compaction 3
Compaction 4
Compaction 5
Pressure [kPa]
Volume Fraction [%]
120
100
80
60
40
20
0
30
35
40
45
50
55
60

Figure A.13

A.1.3 'B' Samples - 4mm superimposed stitch

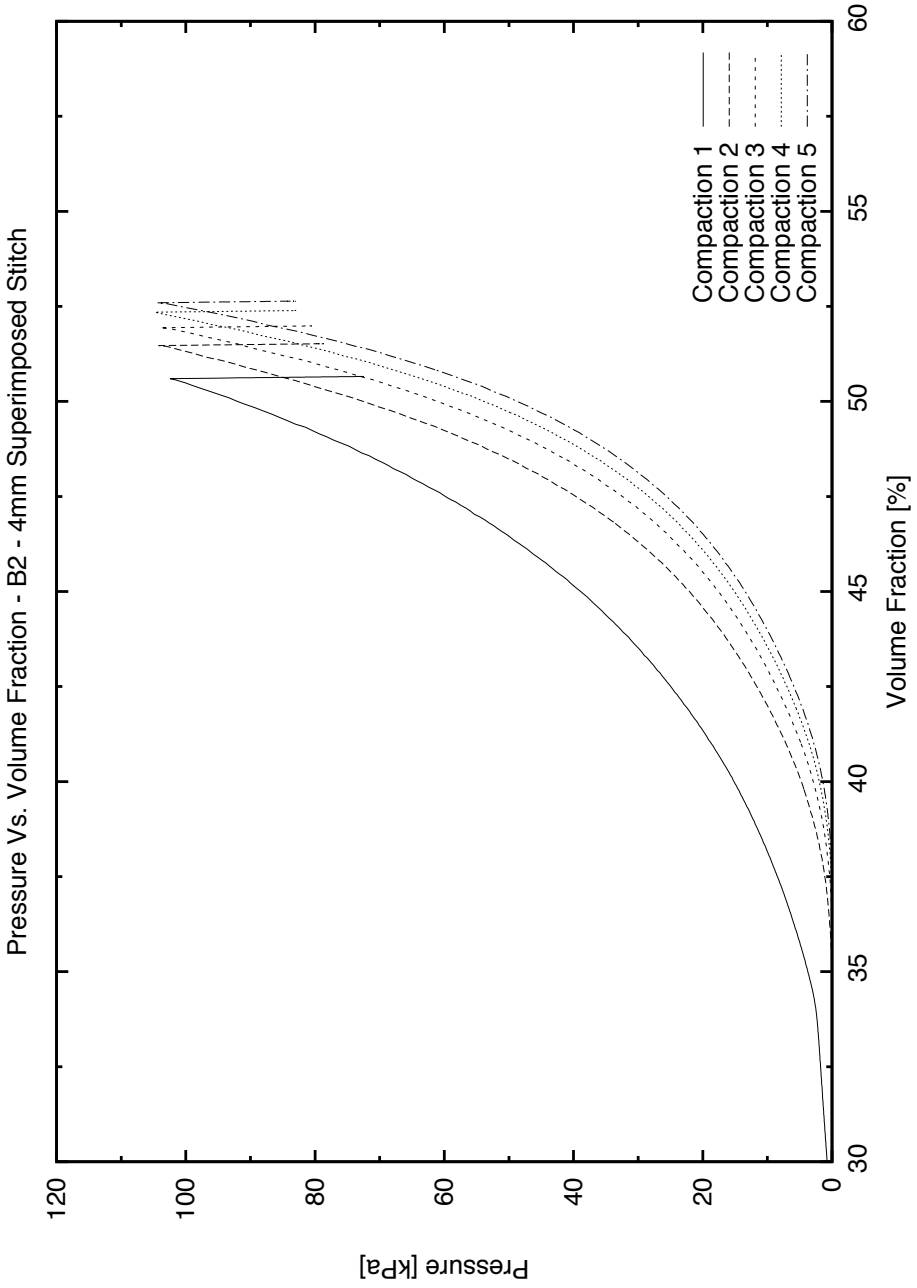
Pressure Vs. Volume Fraction - B2 - 4mm Superimposed Stitch
Compaction 1
Compaction 2
Compaction 3
Compaction 4
Compaction 5
Pressure [kPa]
Volume Fraction [%]
120
100
80
60
40
20
0
30
35
40
45
50
55
60

Figure A.14

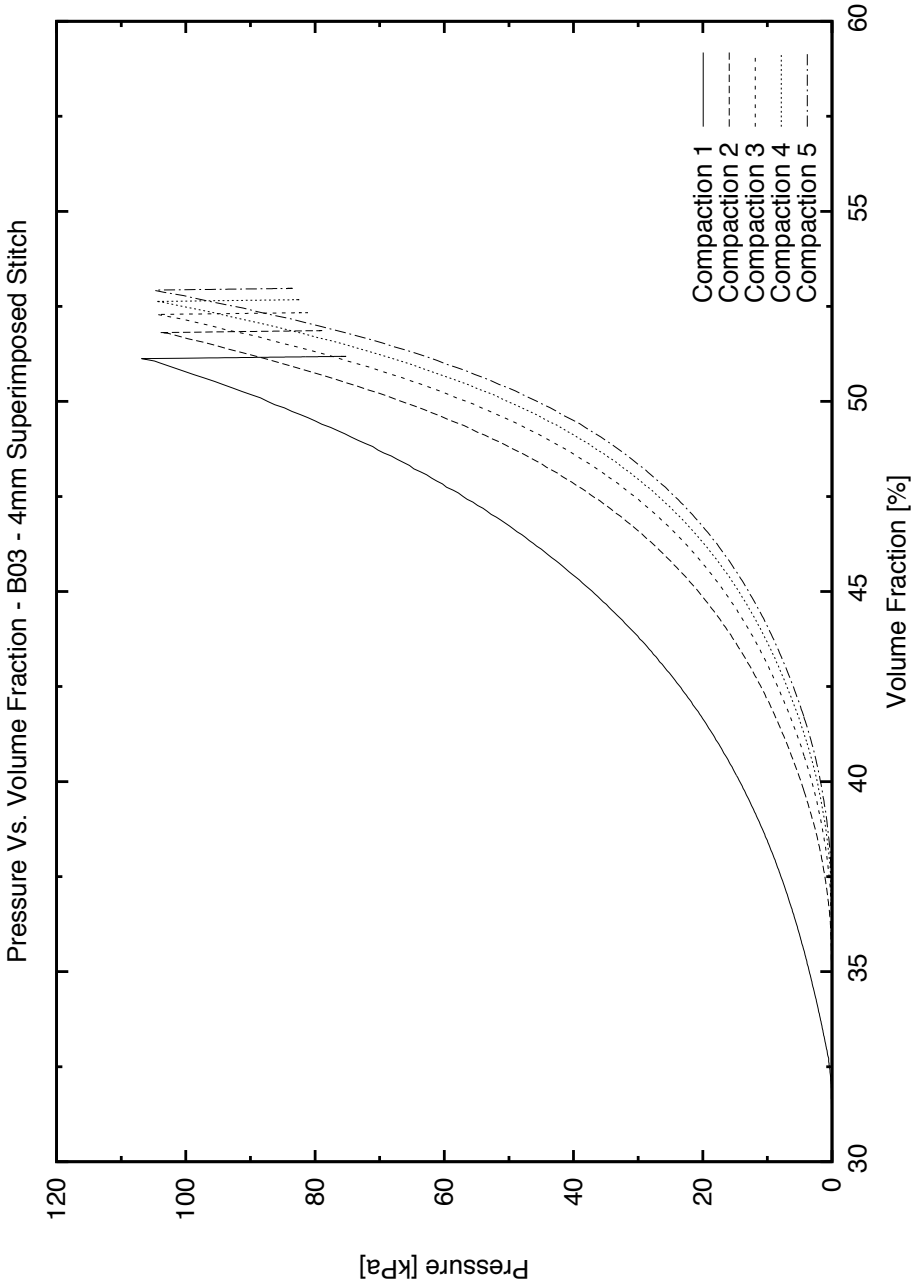
Pressure Vs. Volume Fraction - B03 - 4mm Superimposed Stitch
Compaction 1
Compaction 2
Compaction 3
Compaction 4
Compaction 5
Pressure [kPa]
Volume Fraction [%]
120
100
80
60
40
20
0
30
35
40
45
50
55
60

Figure A.15

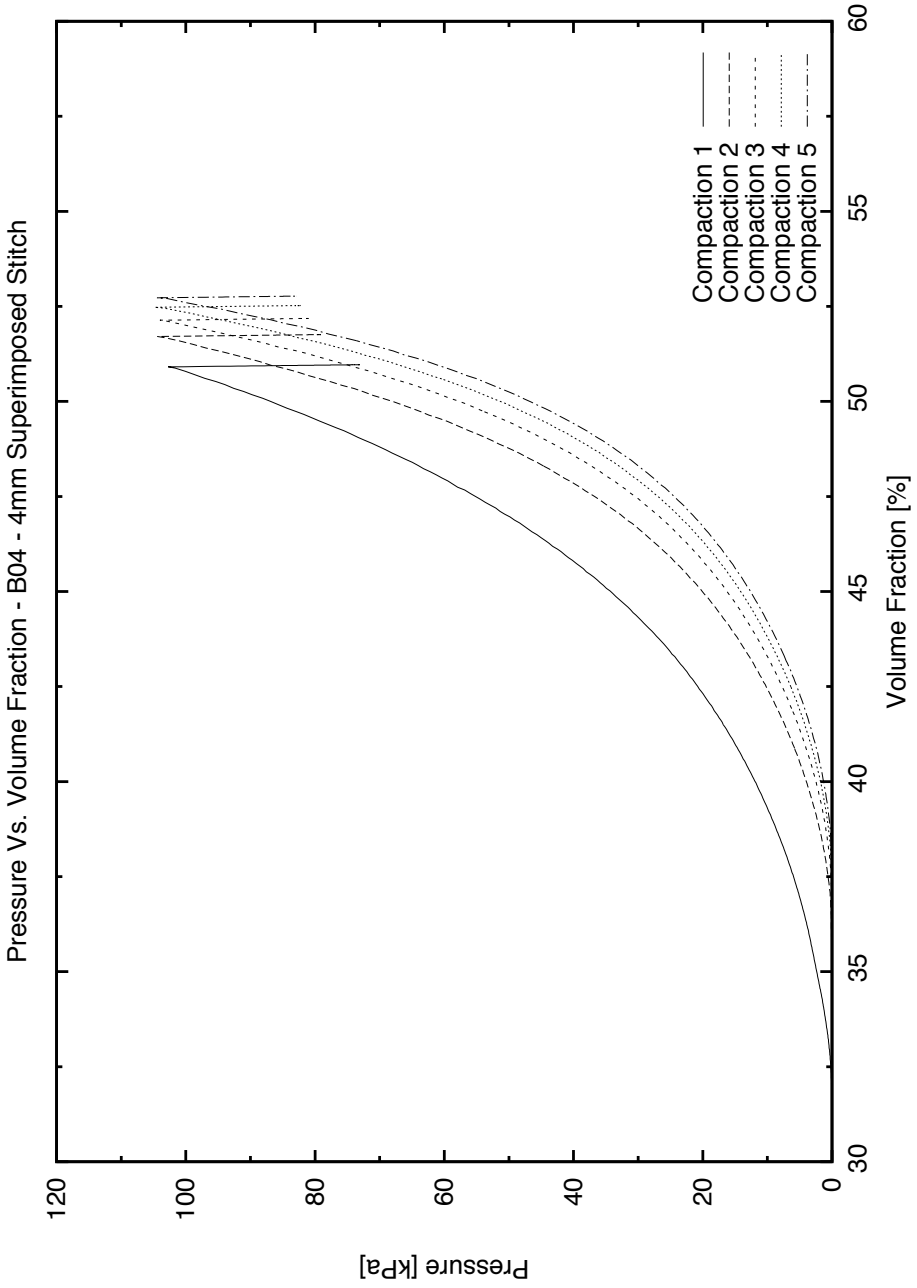
Pressure Vs. Volume Fraction - B04 - 4mm Superimposed Stitch
Compaction 1
Compaction 2
Compaction 3
Compaction 4
Compaction 5
Pressure [kPa]
Volume Fraction [%]
120
100
80
60
40
20
0
30
35
40
45
50
55
60

Figure A.16

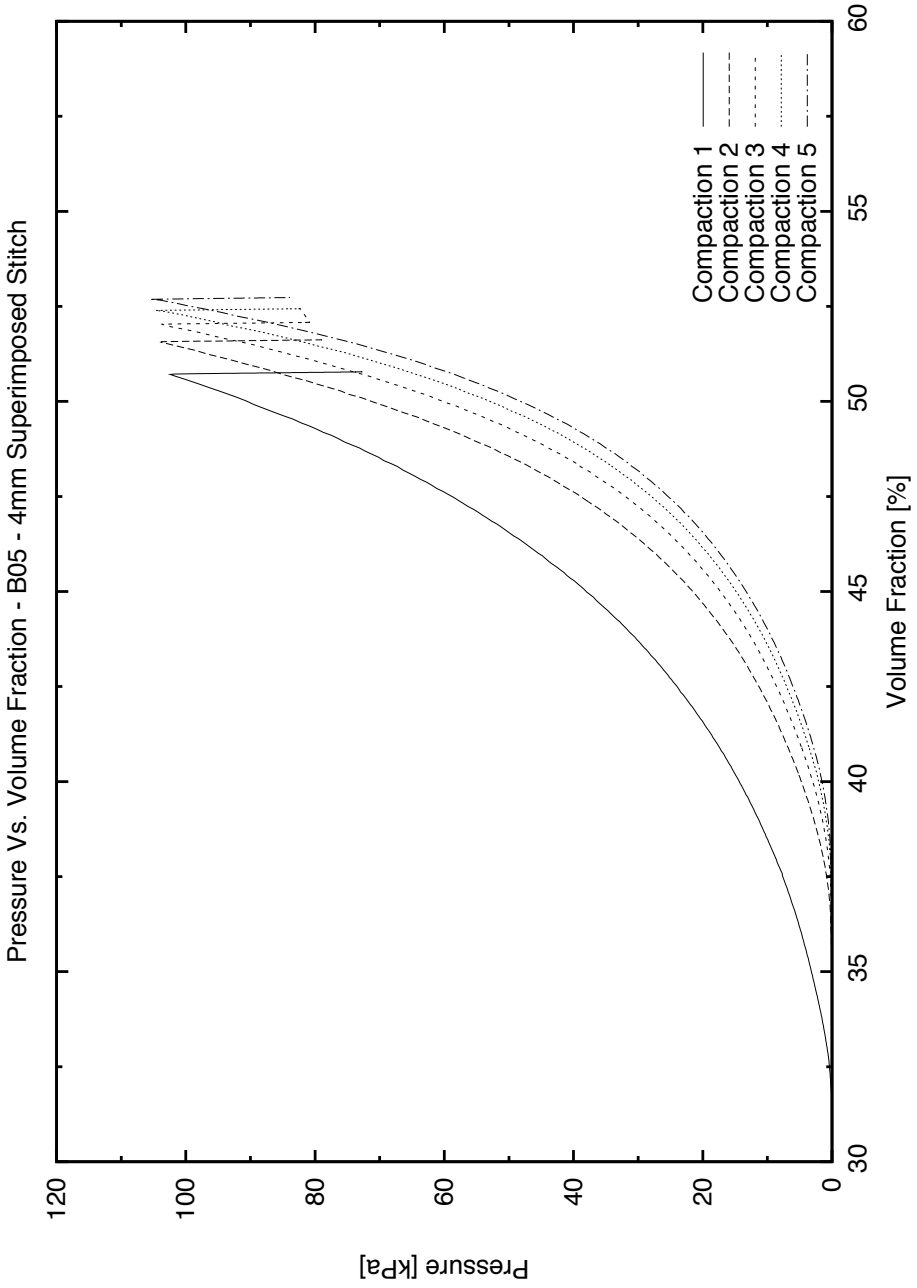
Pressure Vs. Volume Fraction - B05 - 4mm Superimposed Stitch
Compaction 1
Compaction 2
Compaction 3
Compaction 4
Compaction 5
Pressure [kPa]
Volume Fraction [%]
120
100
80
60
40
20
0
30
35
40
45
50
55
60

Figure A.17

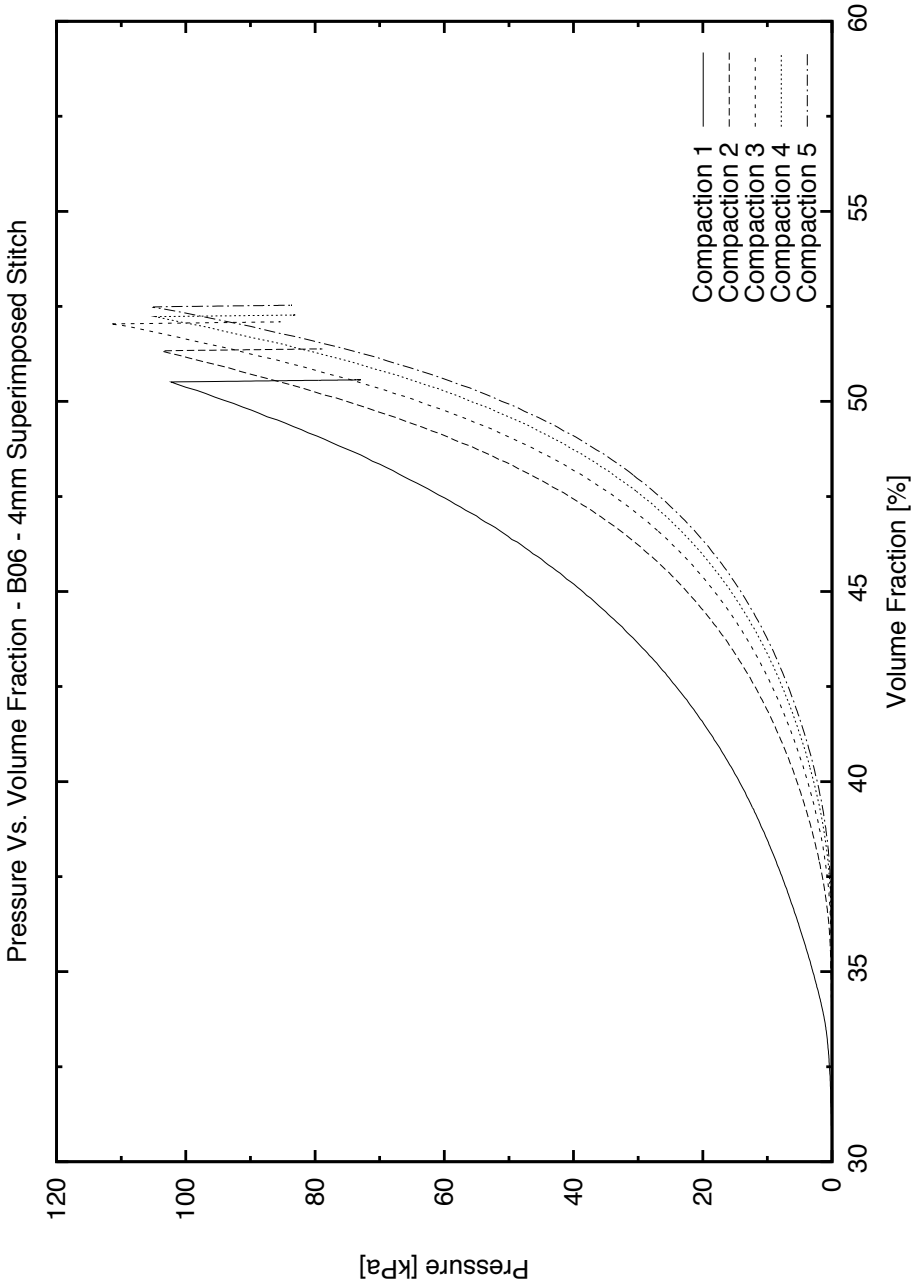
Pressure Vs. Volume Fraction - B06 - 4mm Superimposed Stitch
Compaction 1
Compaction 2
Compaction 3
Compaction 4
Compaction 5
Pressure [kPa]
Volume Fraction [%]
120
100
80
60
40
20
0
30
35
40
45
50
55
60

Figure A.18

A.1.4 'D' Samples - 8mm single stitch

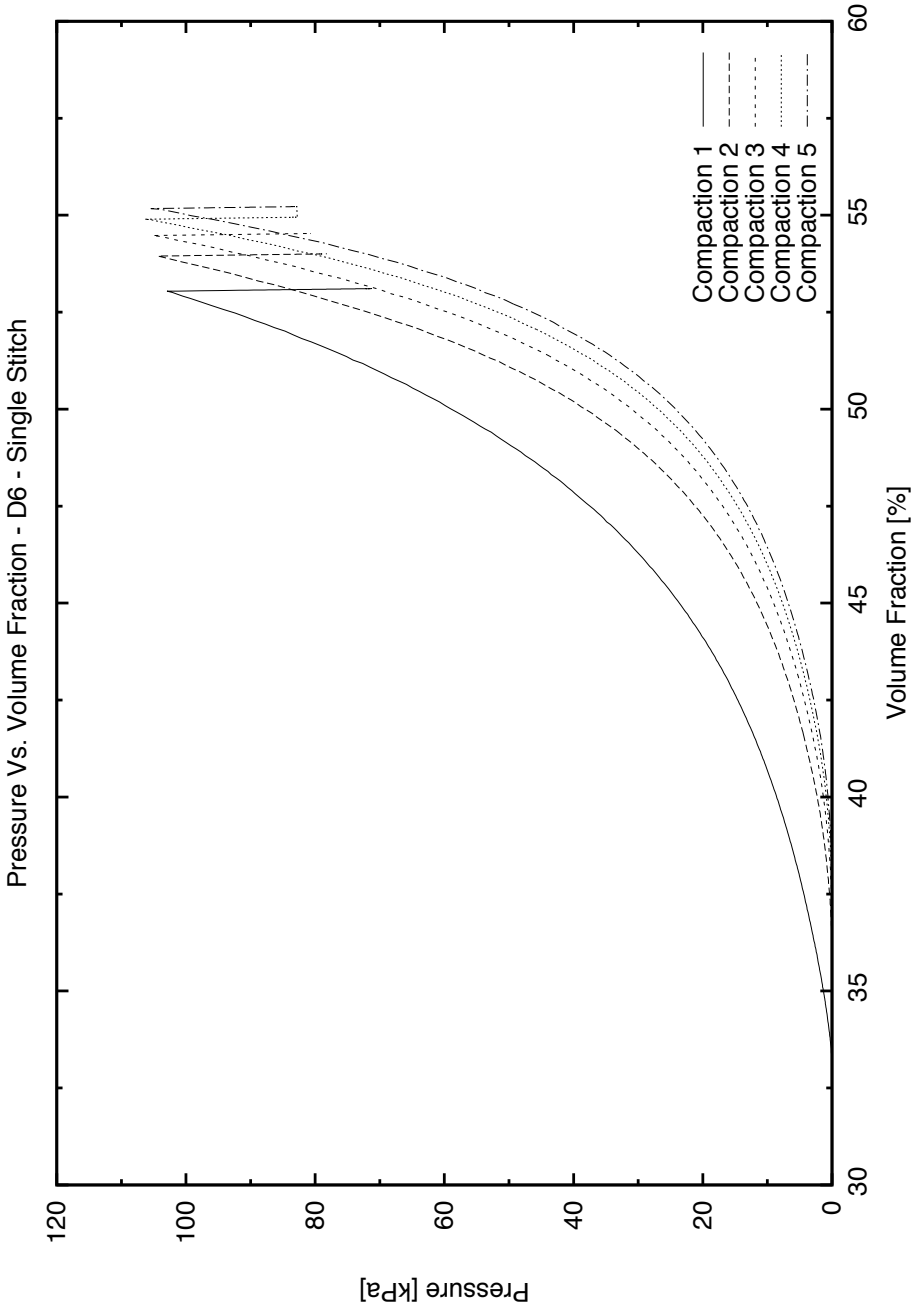
Pressure Vs. Volume Fraction - D6 - Single Stitch
Pressure [kPa]
Volume Fraction [%]
Compaction 1
Compaction 2
Compaction 3
Compaction 4
Compaction 5
120
100
80
60
40
20
0
30
35
40
45
50
55
60

Figure A.19

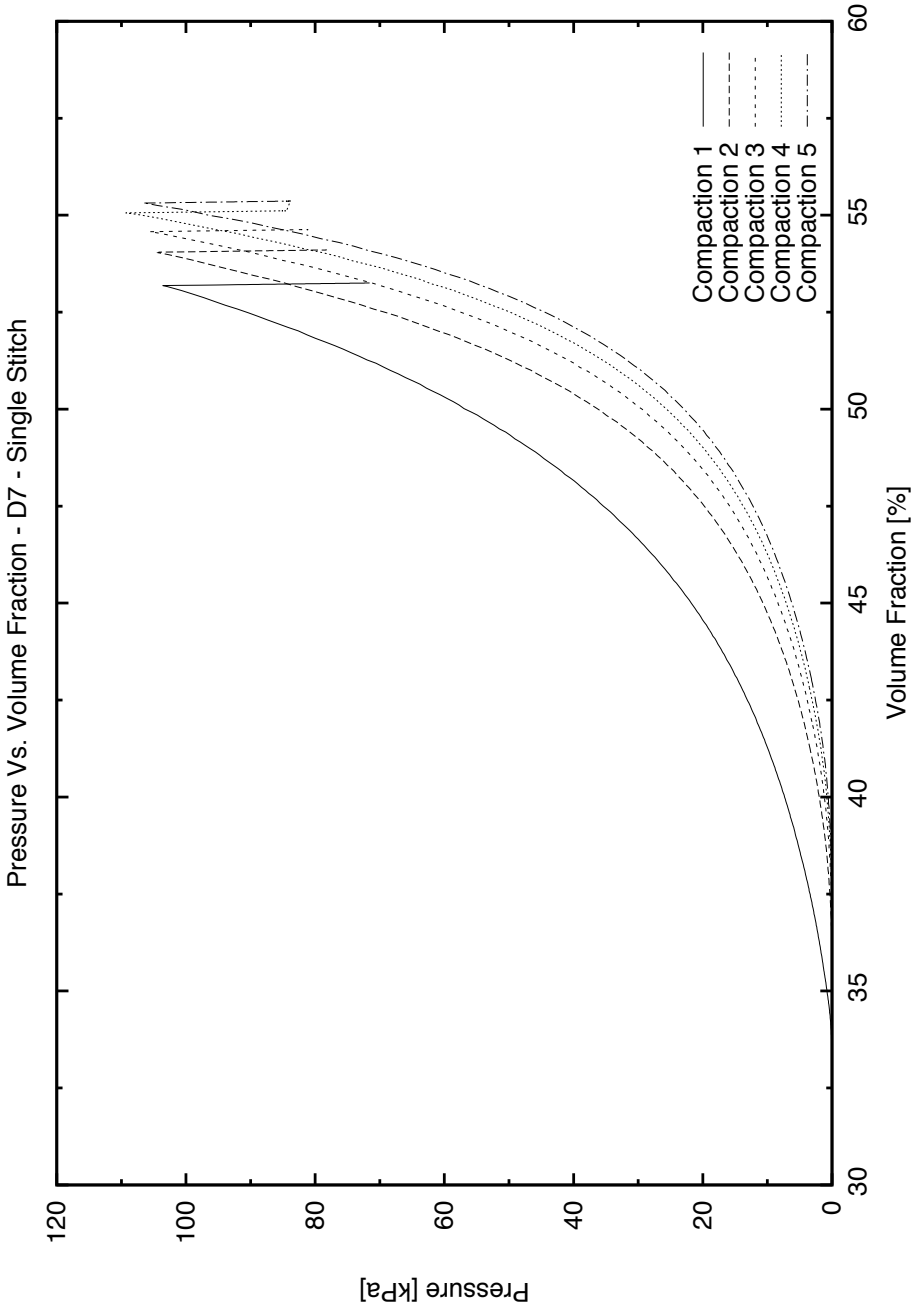
Pressure Vs. Volume Fraction - D7 - Single Stitch
Pressure [kPa]
Volume Fraction [%]
Compaction 1
Compaction 2
Compaction 3
Compaction 4
Compaction 5
120
100
80
60
40
20
0
30
35
40
45
50
55
60

Figure A.20

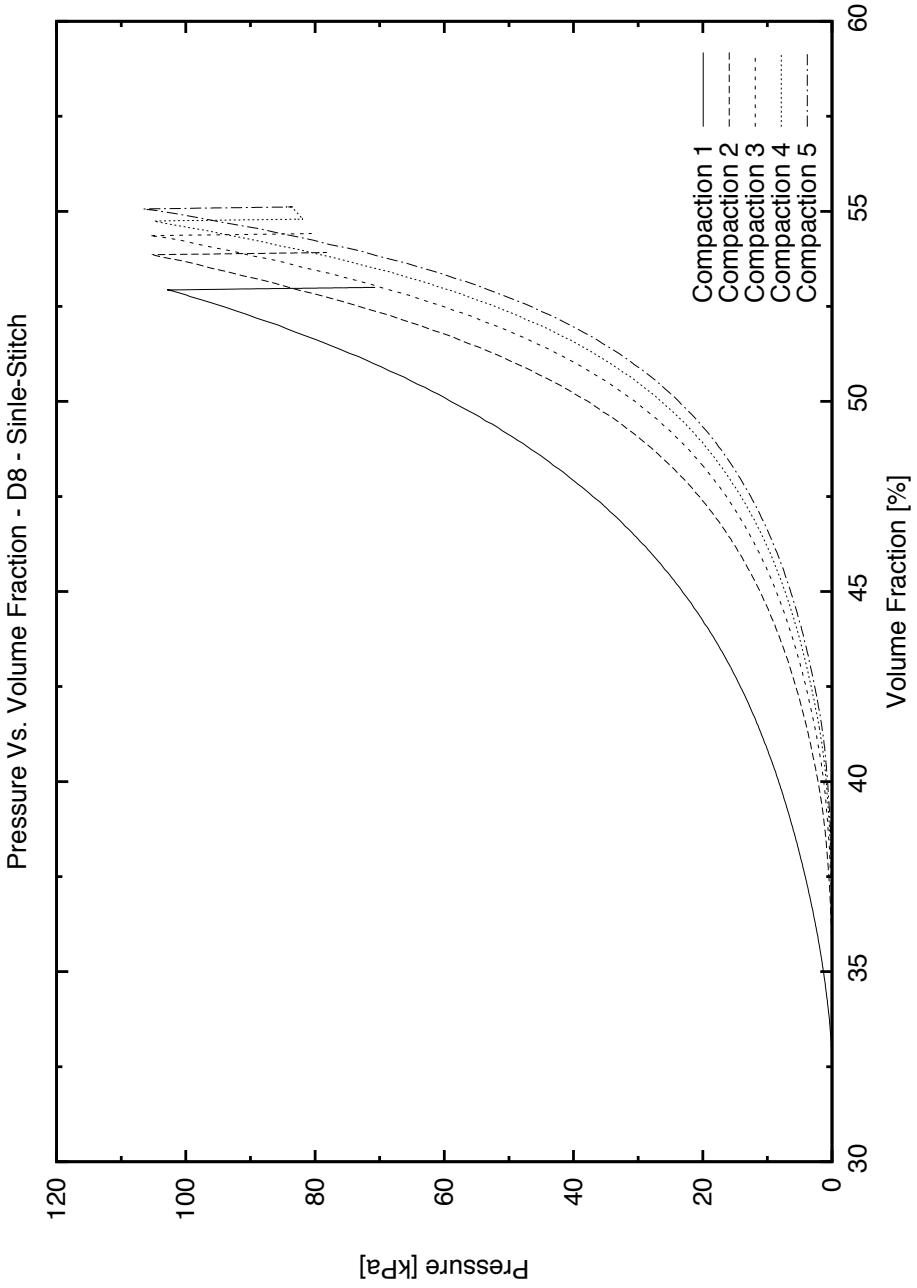
Pressure Vs. Volume Fraction - D8 - Sinle-Stitch
Pressure [kPa]
Volume Fraction [%]
Compaction 1
Compaction 2
Compaction 3
Compaction 4
Compaction 5
120
100
80
60
40
20
0
30
35
40
45
50
55
60

Figure A.21

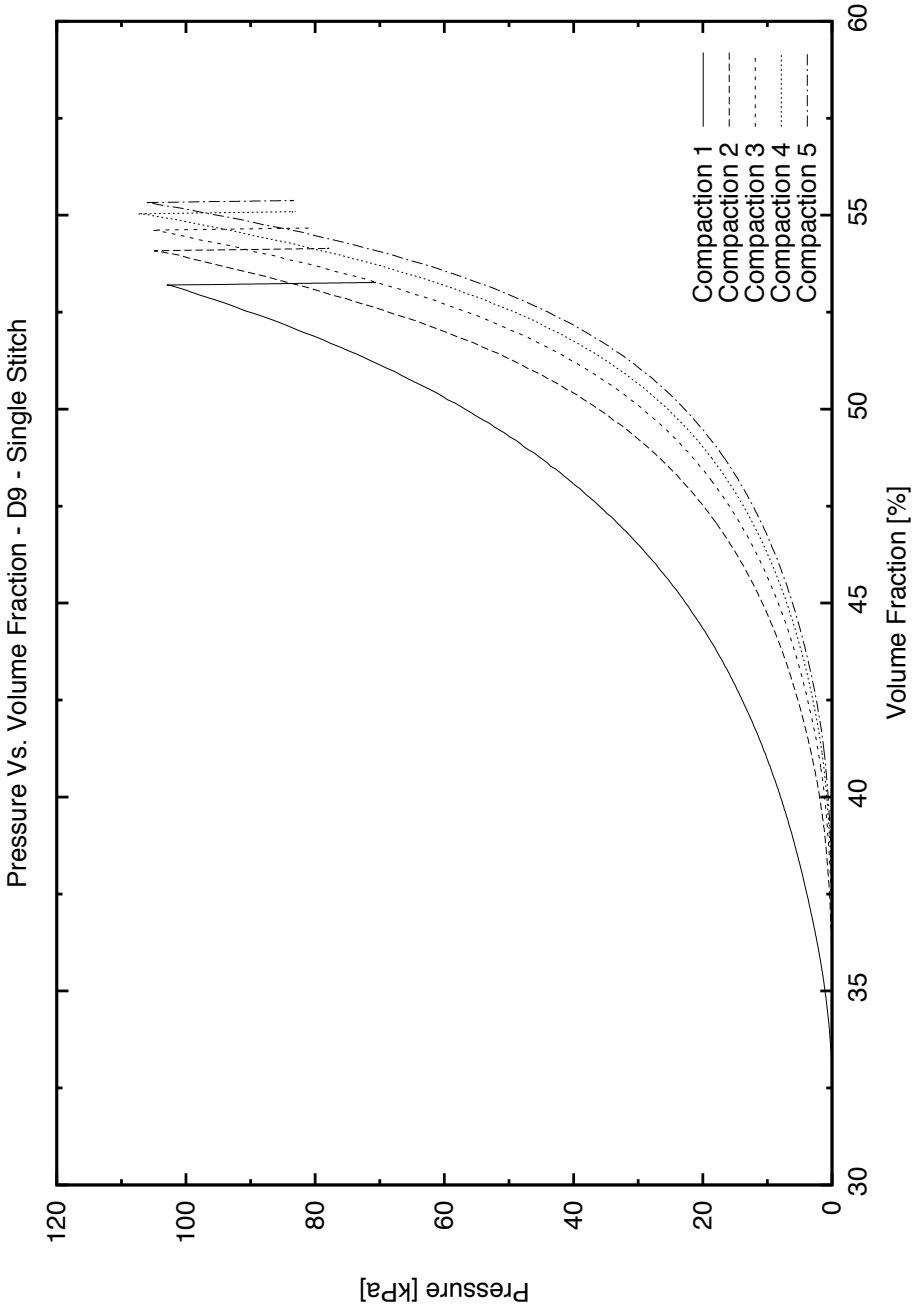
Pressure Vs. Volume Fraction - D9 - Single Stitch
Pressure [kPa]
Volume Fraction [%]
Compaction 1
Compaction 2
Compaction 3
Compaction 4
Compaction 5
120
100
80
60
40
20
0
30
35
40
45
50
55
60

Figure A.22

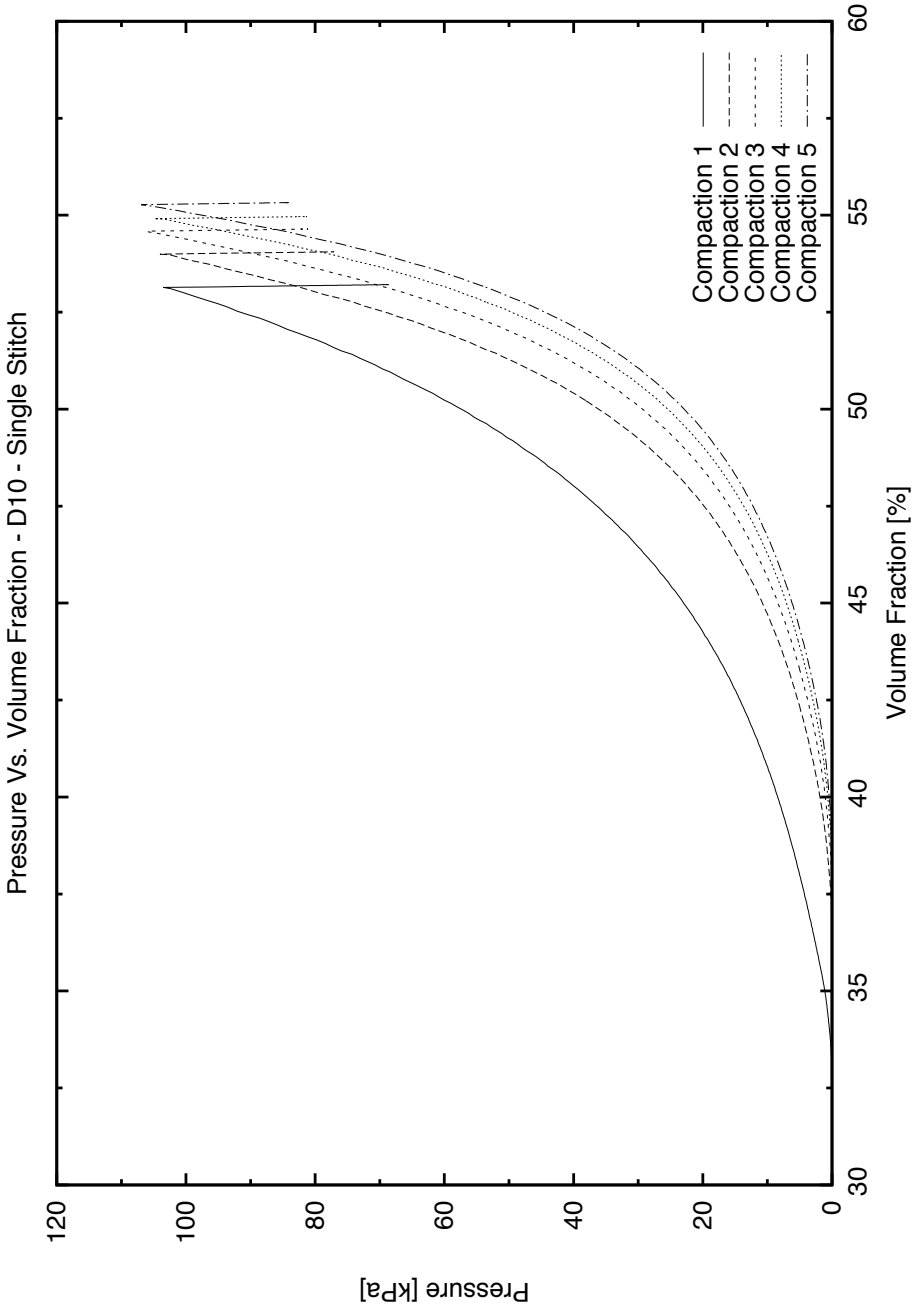
Pressure Vs. Volume Fraction - D10 - Single Stitch
Pressure [kPa]
Volume Fraction [%]
Compaction 1
Compaction 2
Compaction 3
Compaction 4
Compaction 5
120
100
80
60
40
20
0
30
35
40
45
50
55
60

Figure A.23

A.1.5 'D' Samples - 8mm superimposed stitch

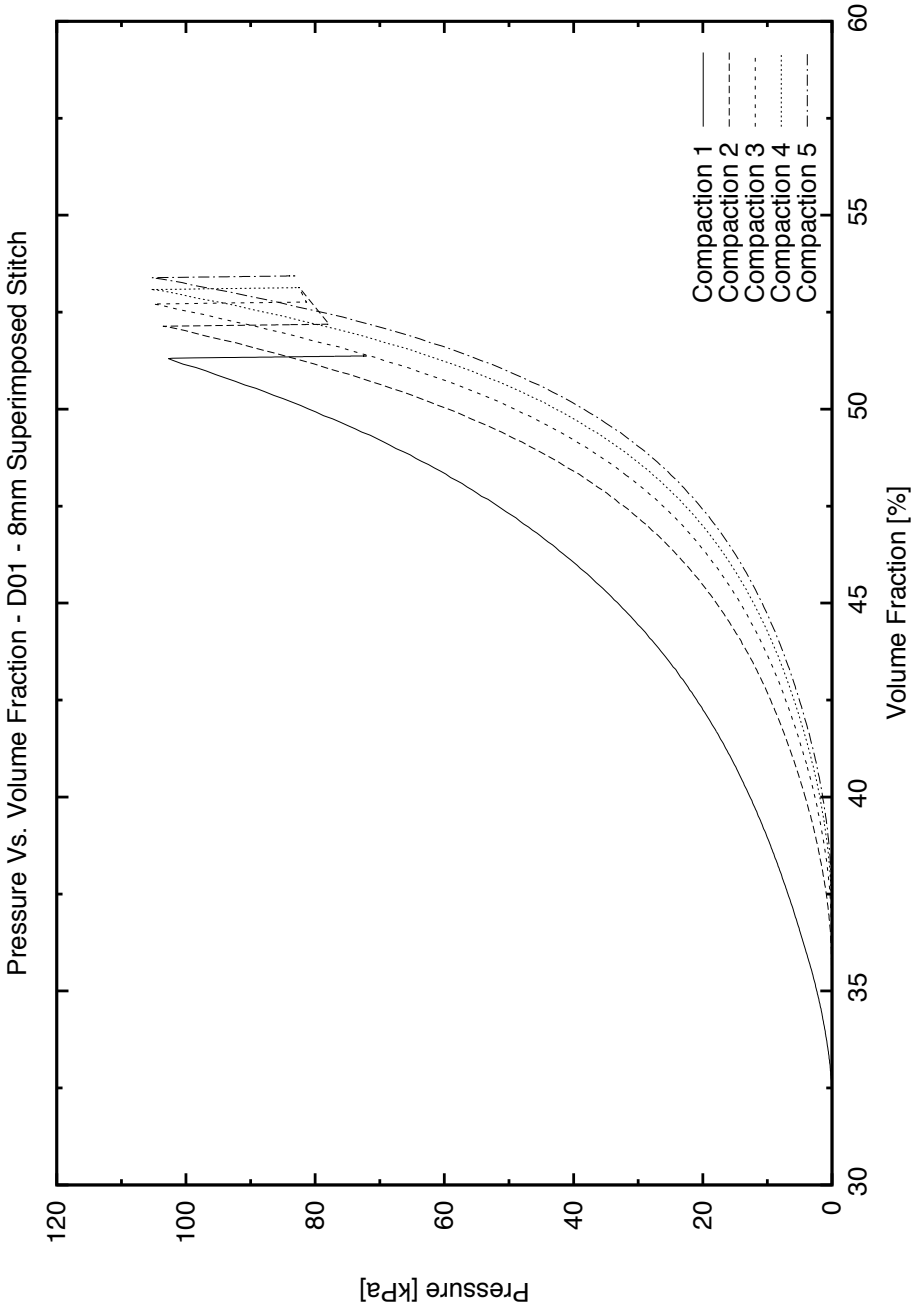
Pressure Vs. Volume Fraction - D01 - 8mm Superimposed Stitch
Compaction 1
Compaction 2
Compaction 3
Compaction 4
Compaction 5
Pressure [kPa]
Volume Fraction [%]
120
100
80
60
40
20
0
30
35
40
45
50
55
60

Figure A.24

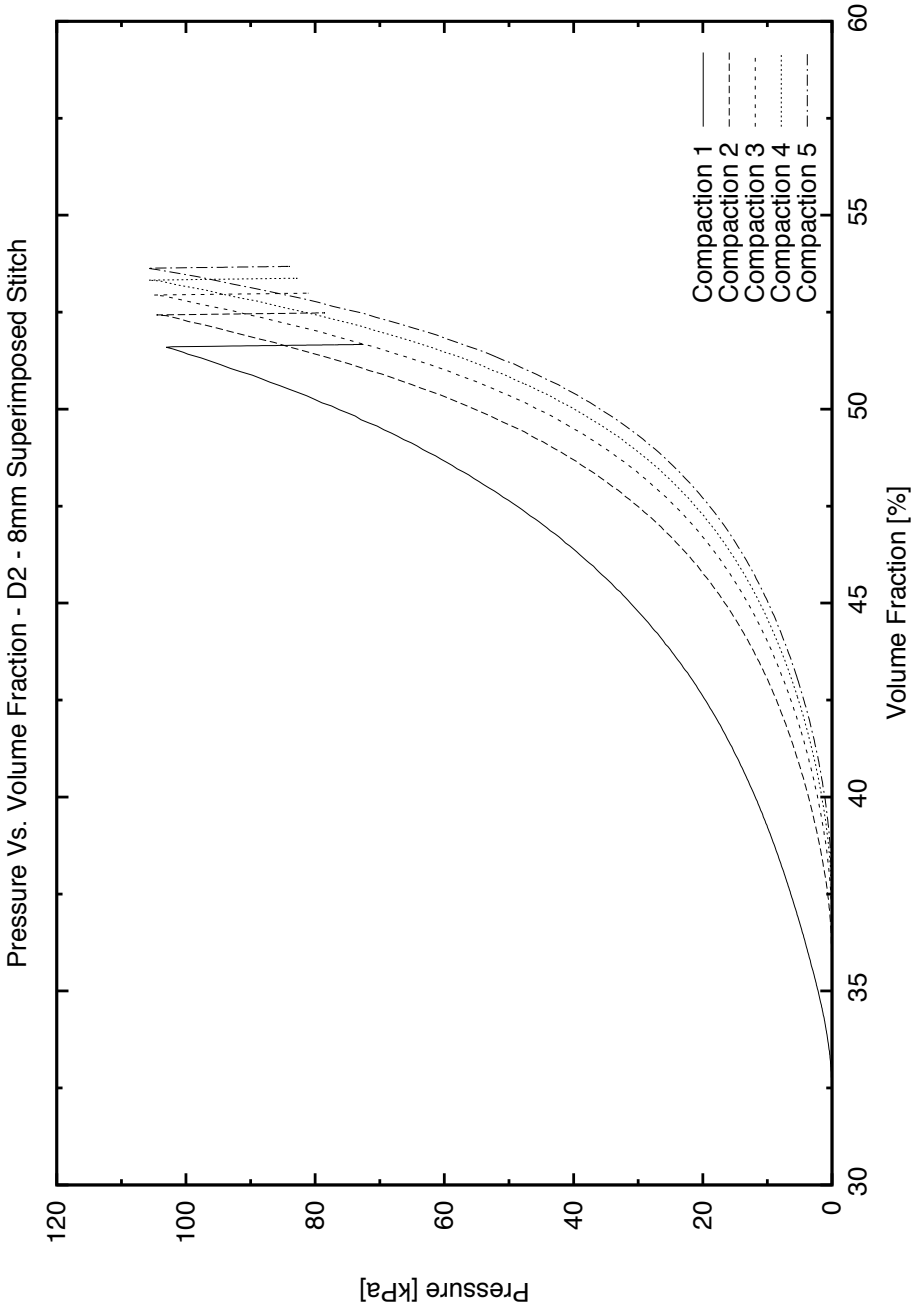
Pressure Vs. Volume Fraction - D2 - 8mm Superimposed Stitch
Pressure [kPa]
Volume Fraction [%]
Compaction 1
Compaction 2
Compaction 3
Compaction 4
Compaction 5
120
100
80
60
40
20
0
30
35
40
45
50
55
60

Figure A.25

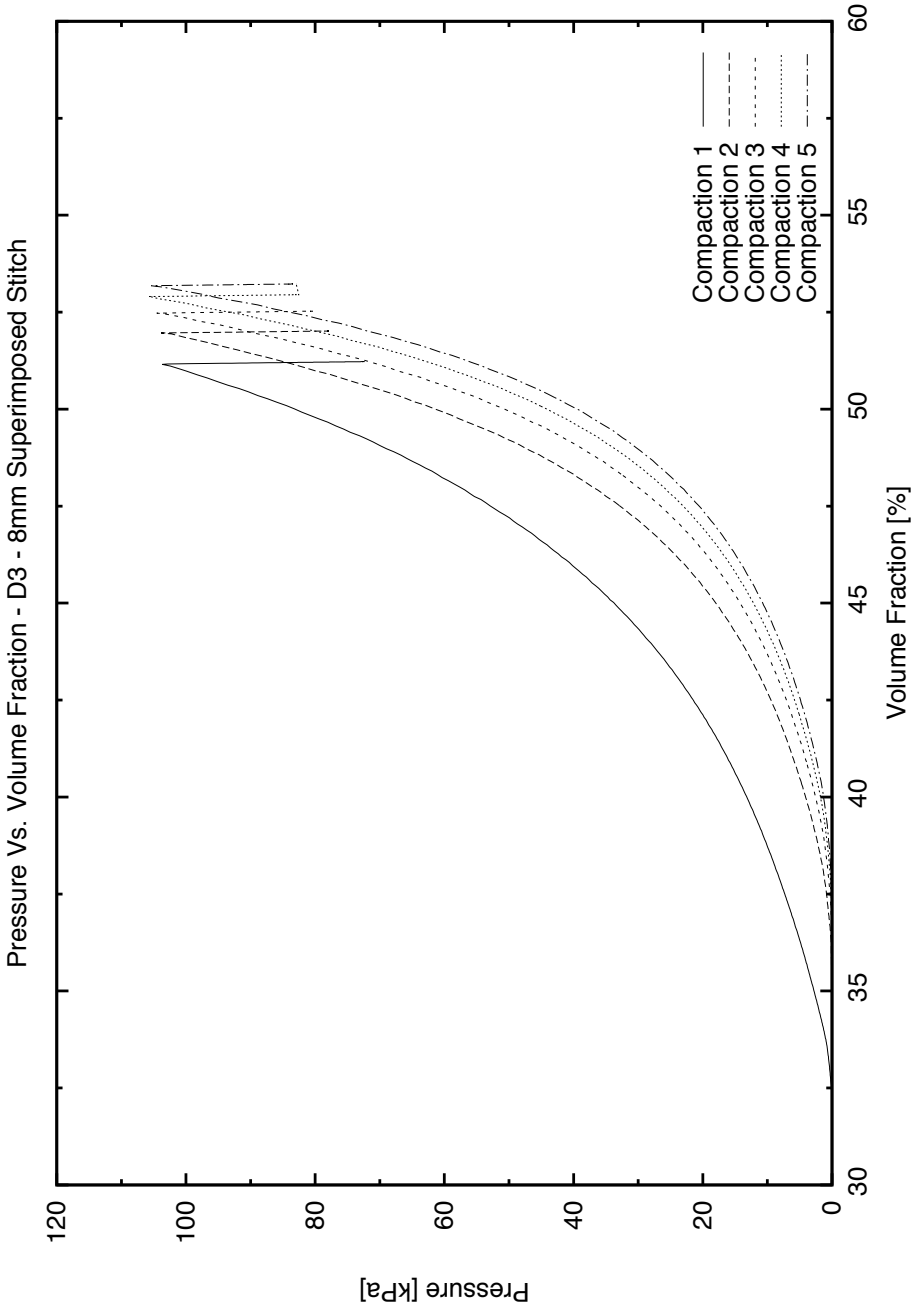
Pressure Vs. Volume Fraction - D3 - 8mm Superimposed Stitch
Compaction 1
Compaction 2
Compaction 3
Compaction 4
Compaction 5
Pressure [kPa]
Volume Fraction [%]
120
100
80
60
40
20
0
30
35
40
45
50
55
60

Figure A.26

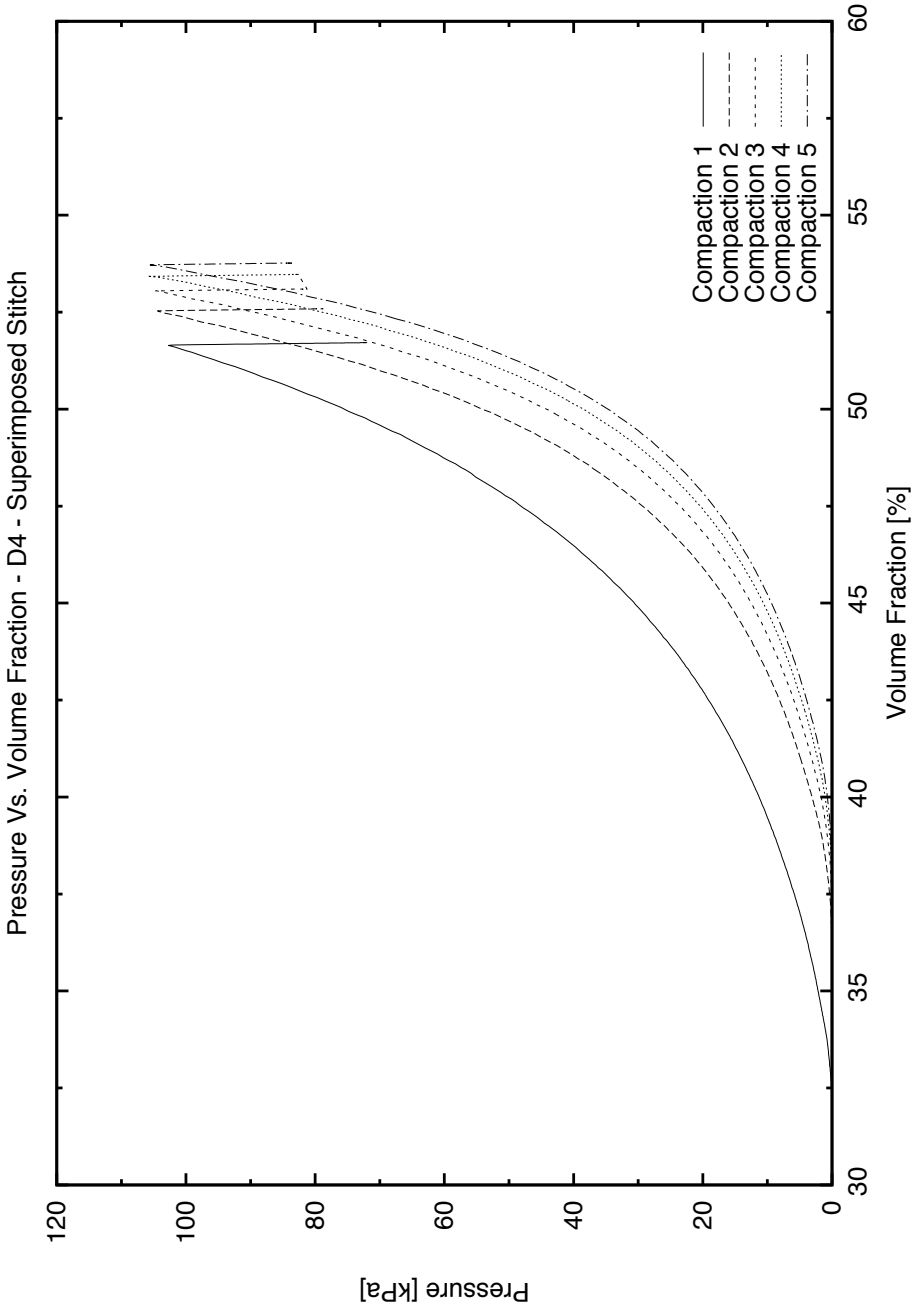
Pressure Vs. Volume Fraction - D4 - Superimposed Stitch
Pressure [kPa]
Volume Fraction [%]
Compaction 1
Compaction 2
Compaction 3
Compaction 4
Compaction 5
120
100
80
60
40
20
0
30
35
40
45
50
55
60

Figure A.27

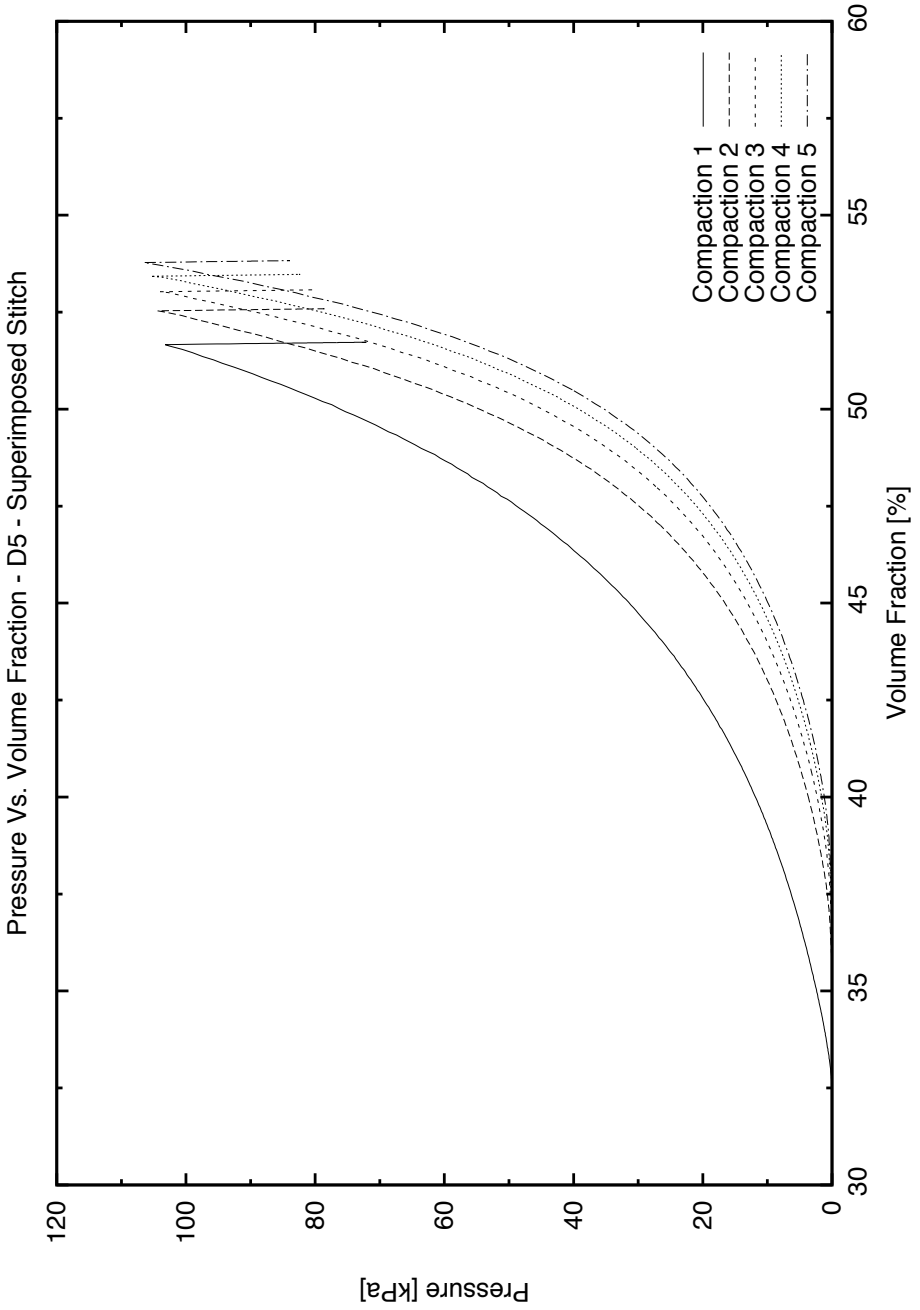
Pressure Vs. Volume Fraction - D5 - Superimposed Stitch
Compaction 1
Compaction 2
Compaction 3
Compaction 4
Compaction 5
Pressure [kPa]
Volume Fraction [%]
120
100
80
60
40
20
0
30
35
40
45
50
55
60

Figure A.28

A.1.6 Compaction platens

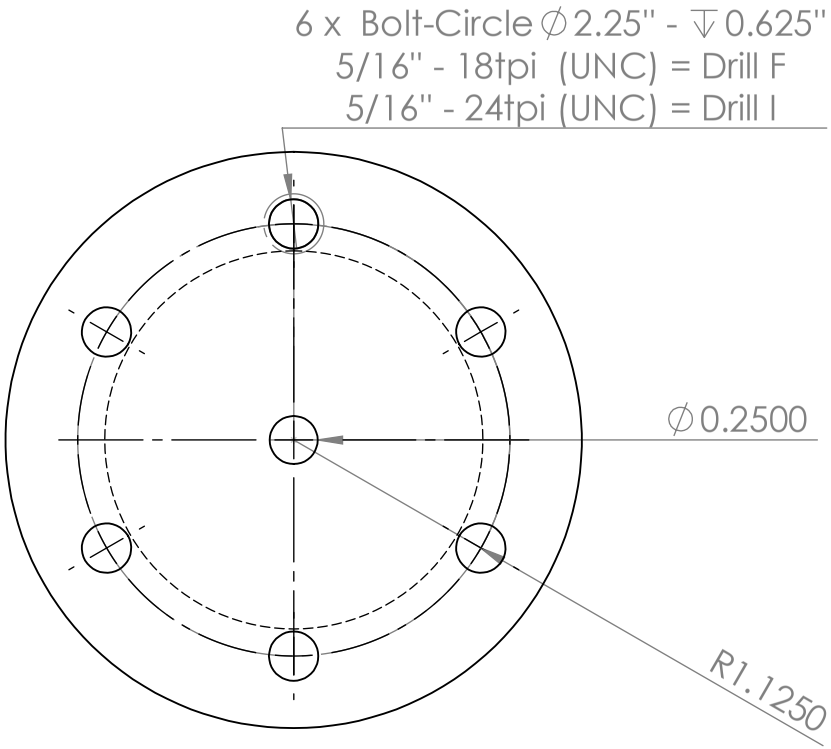
6 x Bolt-Circle ∅2.25" - ↧0.625"
5/16" - 18tpi (UNC) = Drill F
5/16" - 24tpi (UNC) = Drill I
∅0.2500
R1.1250

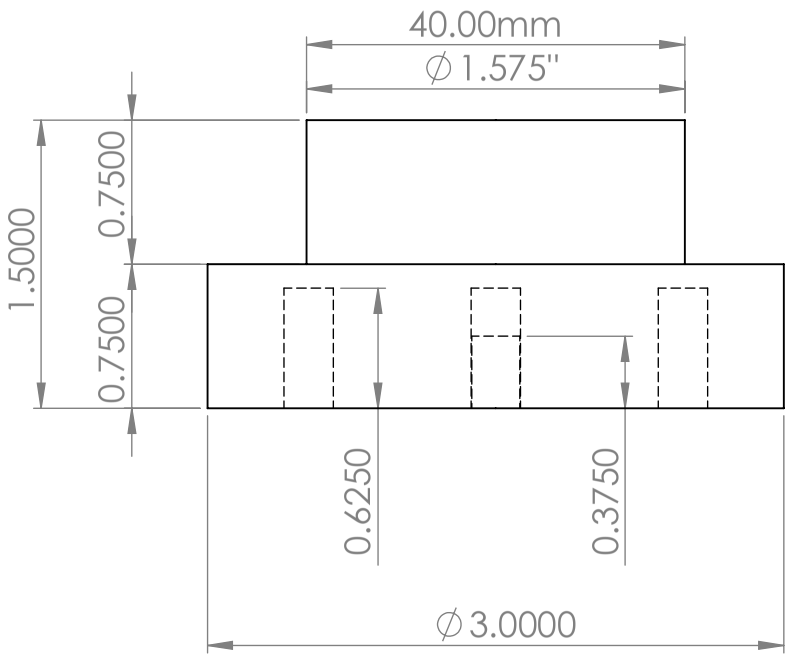
40.00mm
∅1.575"
1.5000
0.7500
0.7500
0.6250
0.3750
∅3.0000

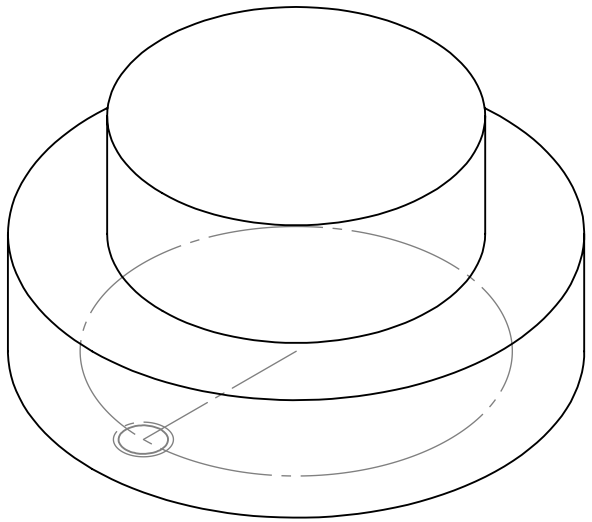

6 X Bolt Circle Dameter 4" - Through hole
5/16 Counterbore - 3/8 Depth

40mm Drawing

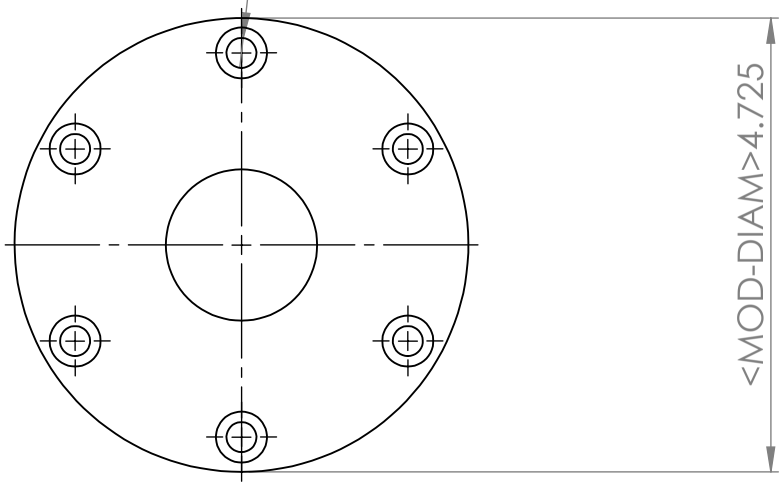

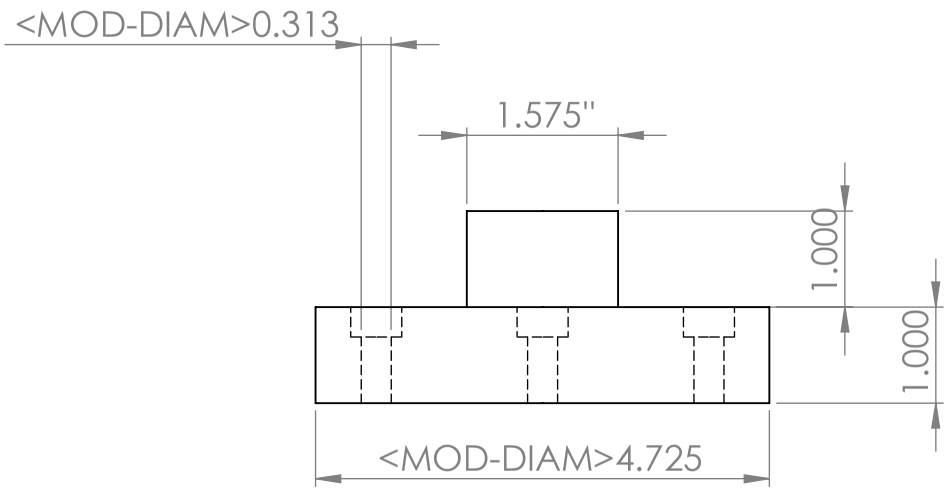

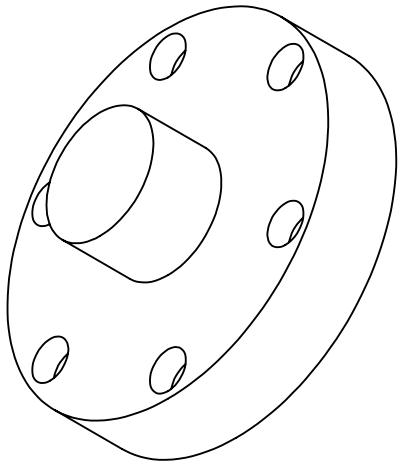

A.4 Shear testing

All shear testing results are listed within the corresponding section; see Section 3.4.5

A.5 Bending tests

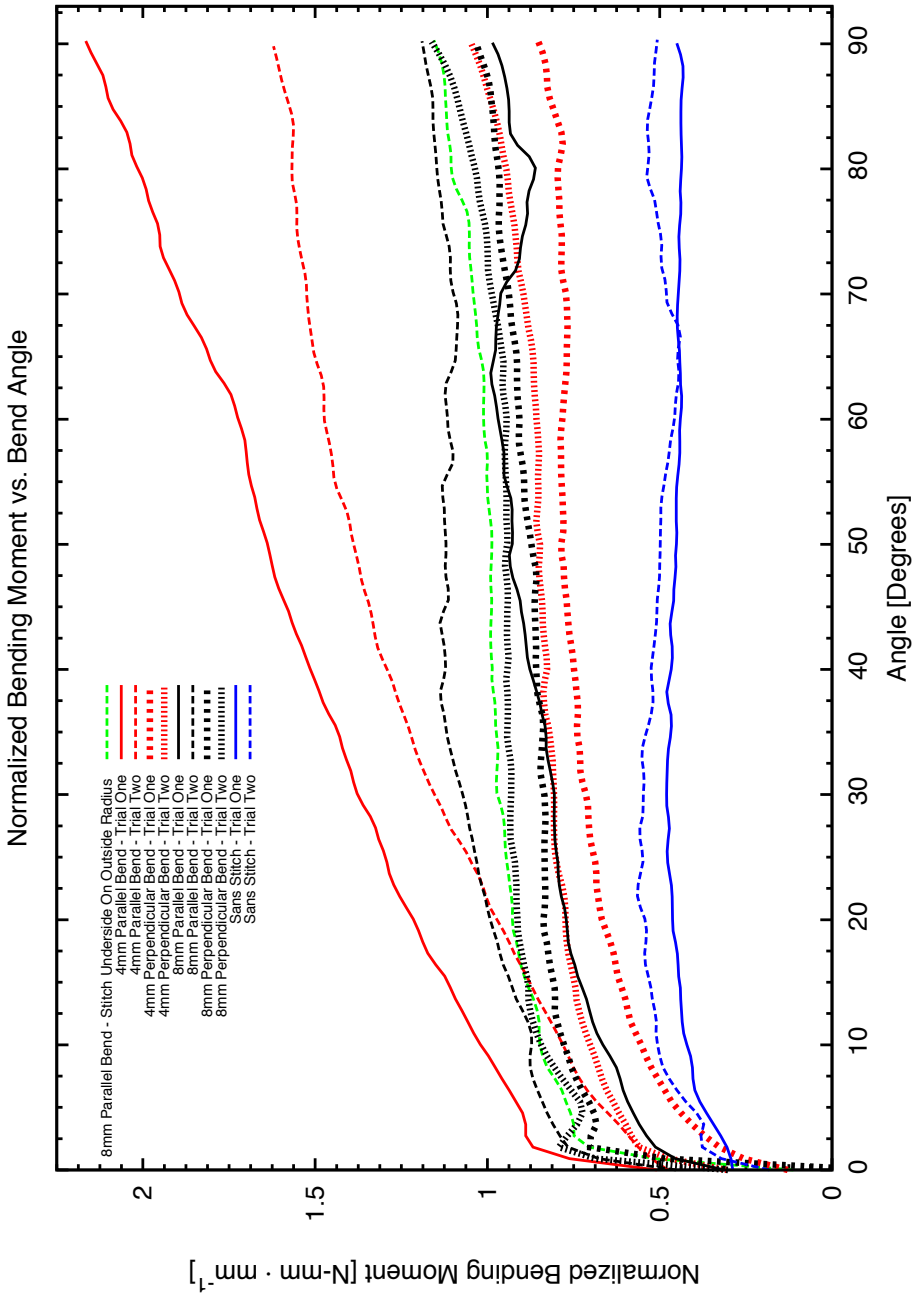
Normalized Bending Moment vs. Bend Angle
Normalized Bending Moment [N-mm · mm-1]
Angle [Degrees]
0
0.5
1
1.5
2
0
10
20
30
40
50
60
70
80
90
8mm Parallel Bend - Stitch Underside On Outside Radius
4mm Parallel Bend - Trial One
4mm Parallel Bend - Trial Two
4mm Perpendicular Bend - Trial One
4mm Perpendicular Bend - Trial Two
8mm Parallel Bend - Trial One
8mm Parallel Bend - Trial Two
8mm Perpendicular Bend - Trial One
8mm Perpendicular Bend - Trial Two
Sans Stitch - Trial One
Sans Stitch - Trial Two

Figure A.29

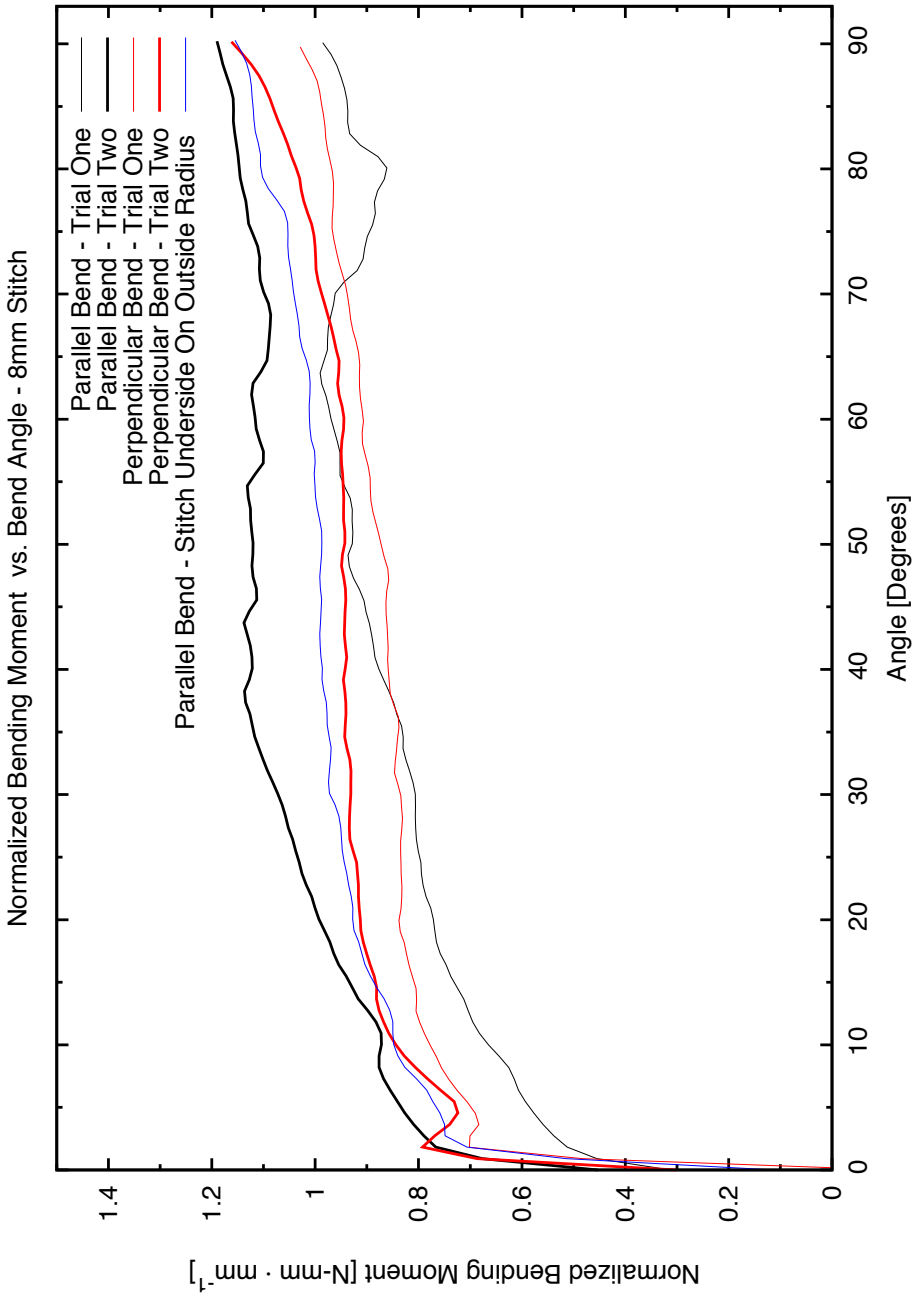
Normalized Bending Moment vs. Bend Angle - 8mm Stitch
Parallel Bend - Trial One
Parallel Bend - Trial Two
Perpendicular Bend - Trial One
Perpendicular Bend - Trial Two
Parallel Bend - Stitch Underside On Outside Radius
Normalized Bending Moment [N-mm · mm-1]
Angle [Degrees]
0
0.2
0.4
0.6
0.8
1
1.2
1.4
0
10
20
30
40
50
60
70
80
90

Figure A.30

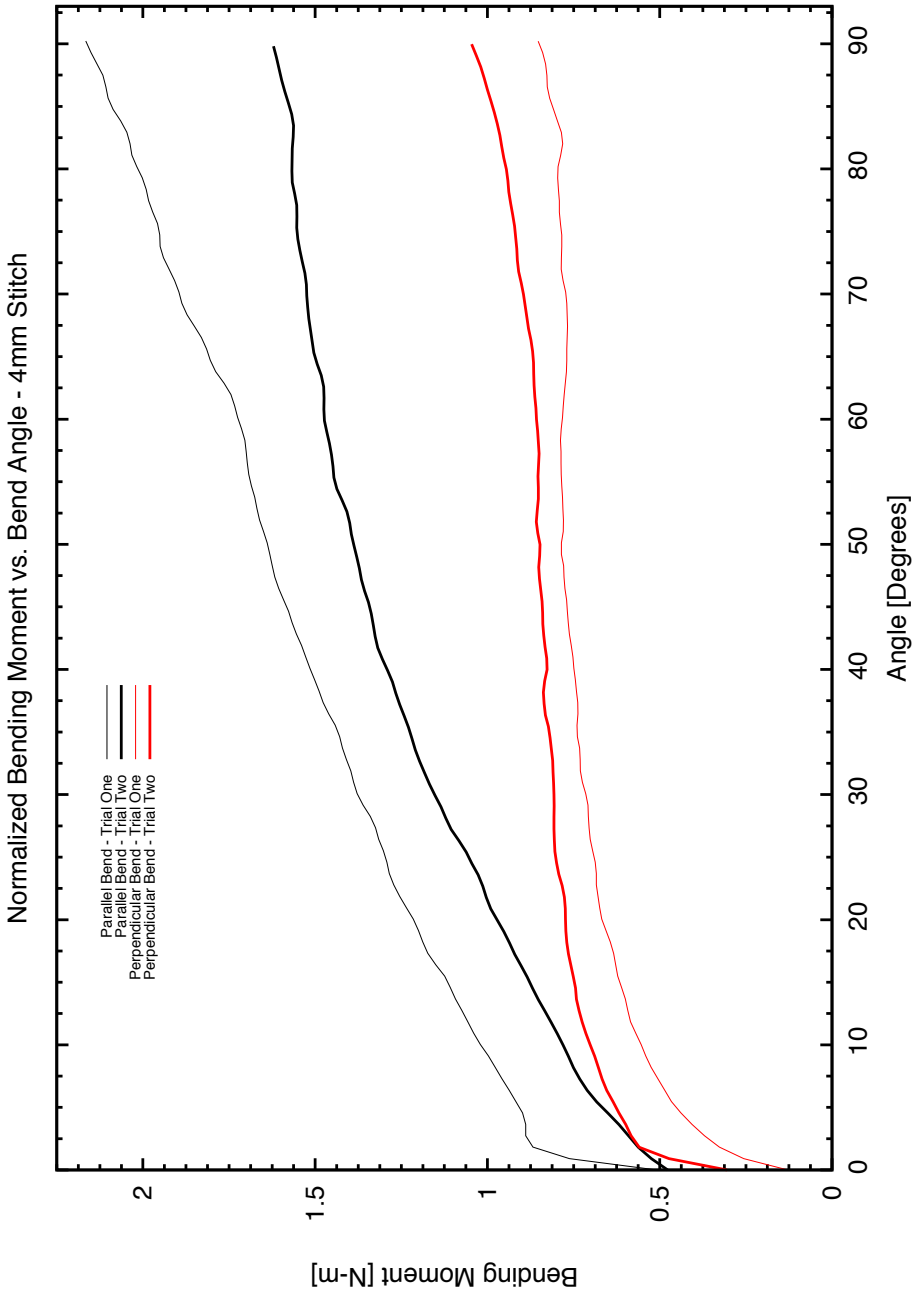
Normalized Bending Moment vs. Bend Angle - 4mm Stitch
Parallel Bend - Trial One
Parallel Bend - Trial Two
Perpendicular Bend - Trial One
Perpendicular Bend - Trial Two
Bending Moment [N-m]
0
0.5
1
1.5
2
Angle [Degrees]
0
10
20
30
40
50
60
70
80
90

Figure A.31

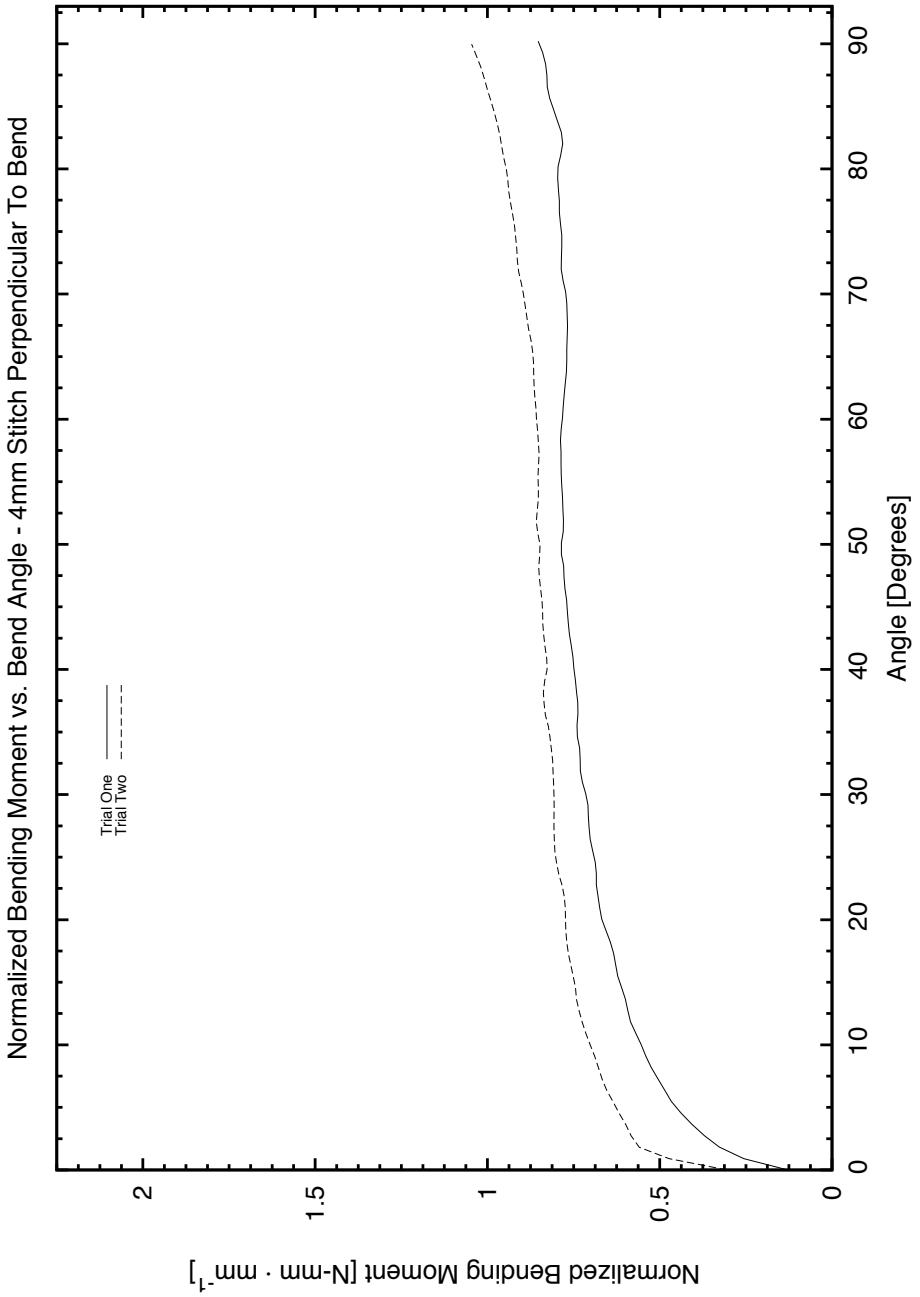
Normalized Bending Moment vs. Bend Angle - 4mm Stitch Perpendicular To Bend
Trial One
Trial Two
Normalized Bending Moment [N-mm · mm-1]
Angle [Degrees]
0
0.5
1
1.5
2
0
10
20
30
40
50
60
70
80
90

Figure A.32

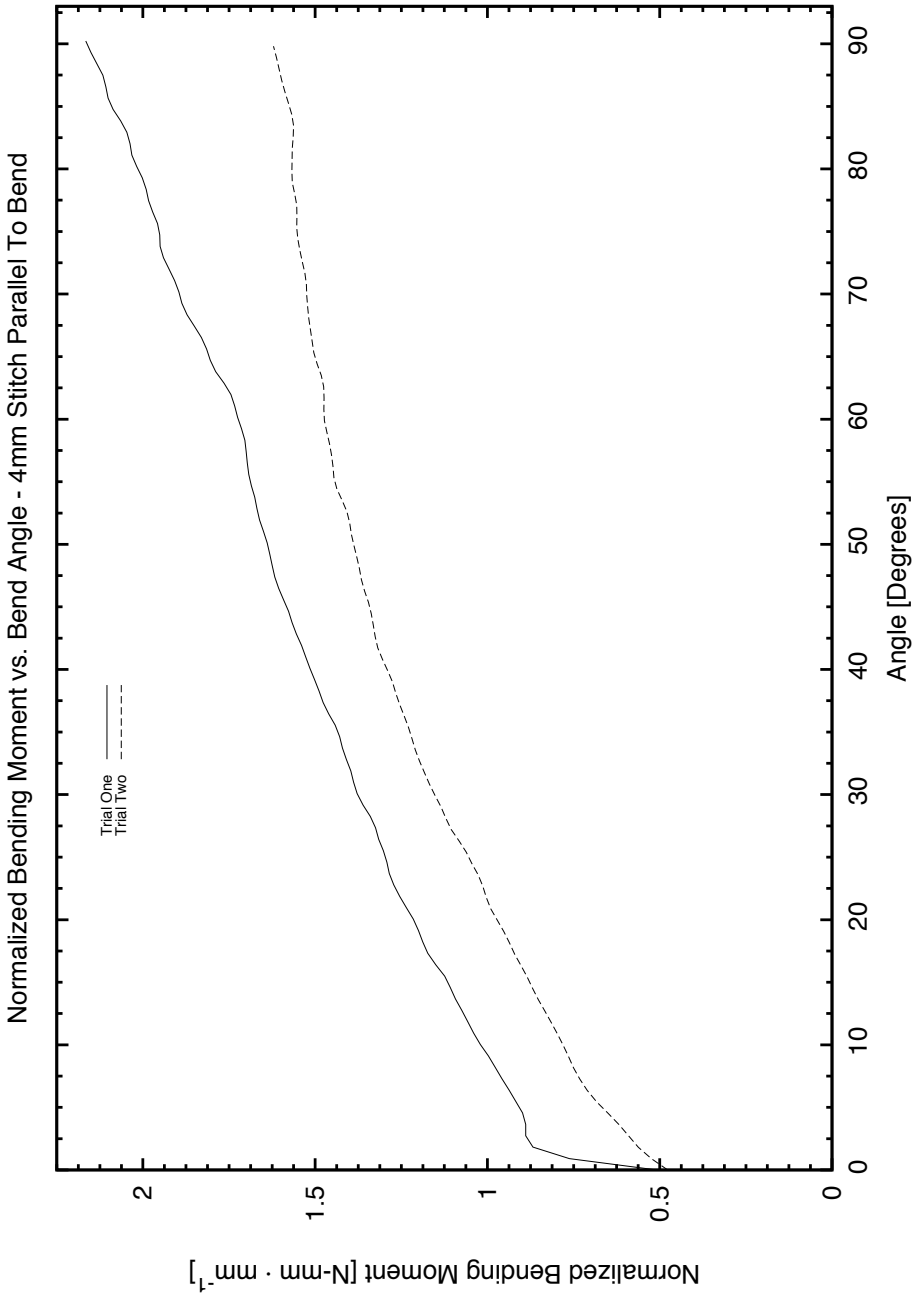
Normalized Bending Moment vs. Bend Angle - 4mm Stitch Parallel To Bend
Trial One
Trial Two
Normalized Bending Moment [N-mm · mm-1]
Angle [Degrees]
0
0.5
1
1.5
2
0
10
20
30
40
50
60
70
80
90

Figure A.33

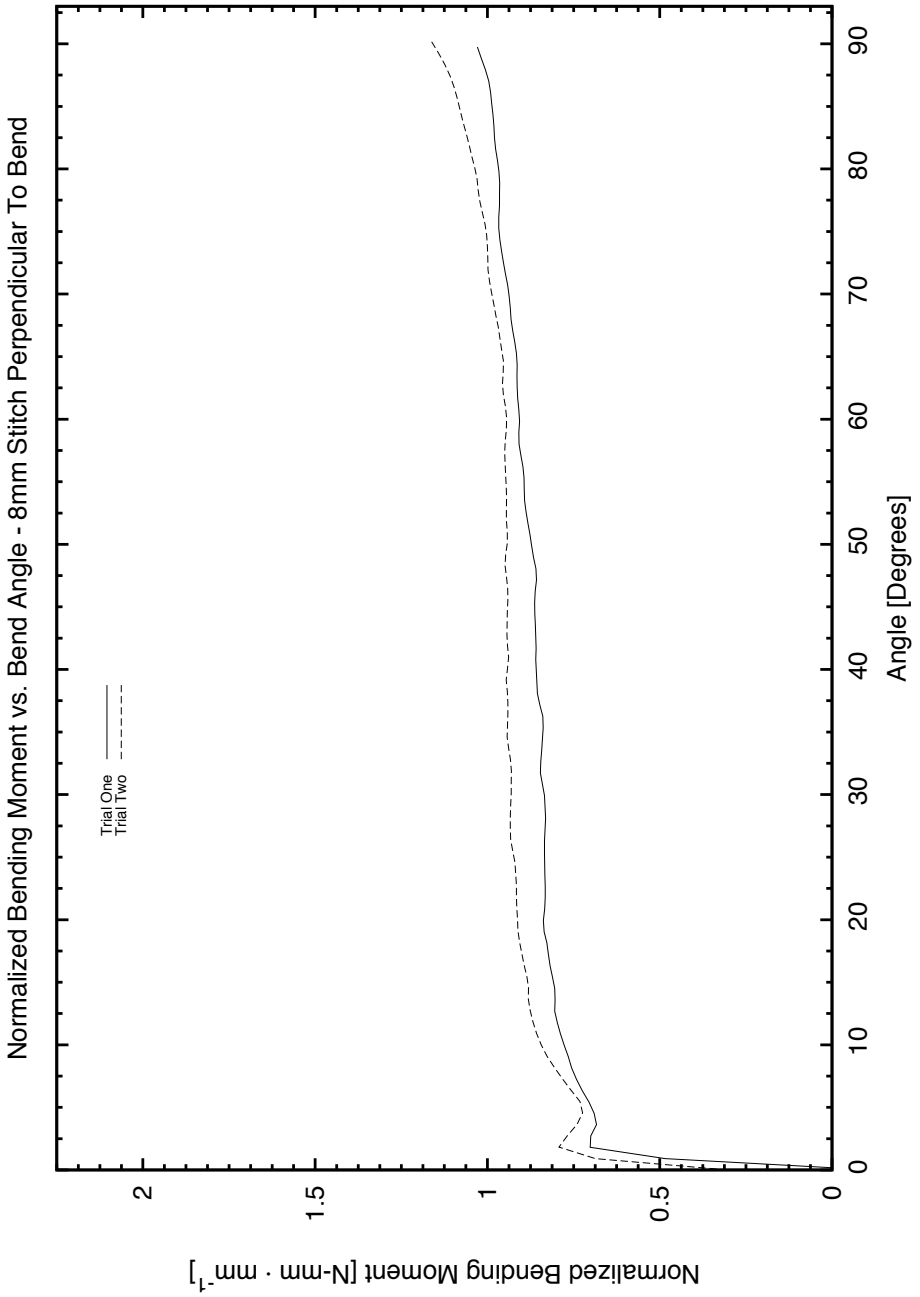
Normalized Bending Moment vs. Bend Angle - 8mm Stitch Perpendicular To Bend
Trial One
Trial Two
Normalized Bending Moment [N-mm · mm-1]
Angle [Degrees]
0
0.5
1
1.5
2
0
10
20
30
40
50
60
70
80
90

Figure A.34

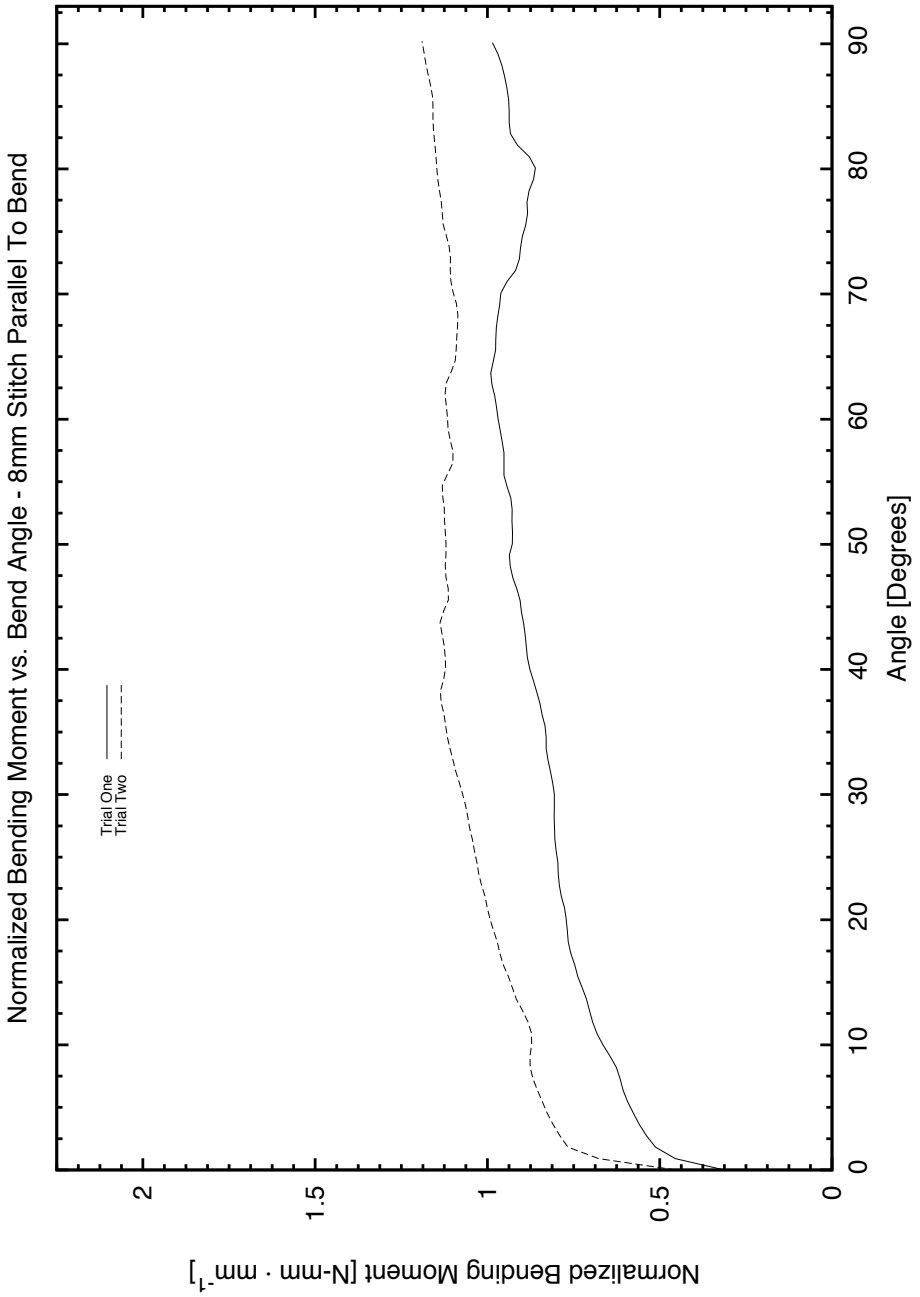
Normalized Bending Moment vs. Bend Angle - 8mm Stitch Parallel To Bend
Trial One
Trial Two
Normalized Bending Moment [N-mm · mm-1]
Angle [Degrees]
0
0.5
1
1.5
2
0
10
20
30
40
50
60
70
80
90

Figure A.35

Appendix B

Manufacturing Process

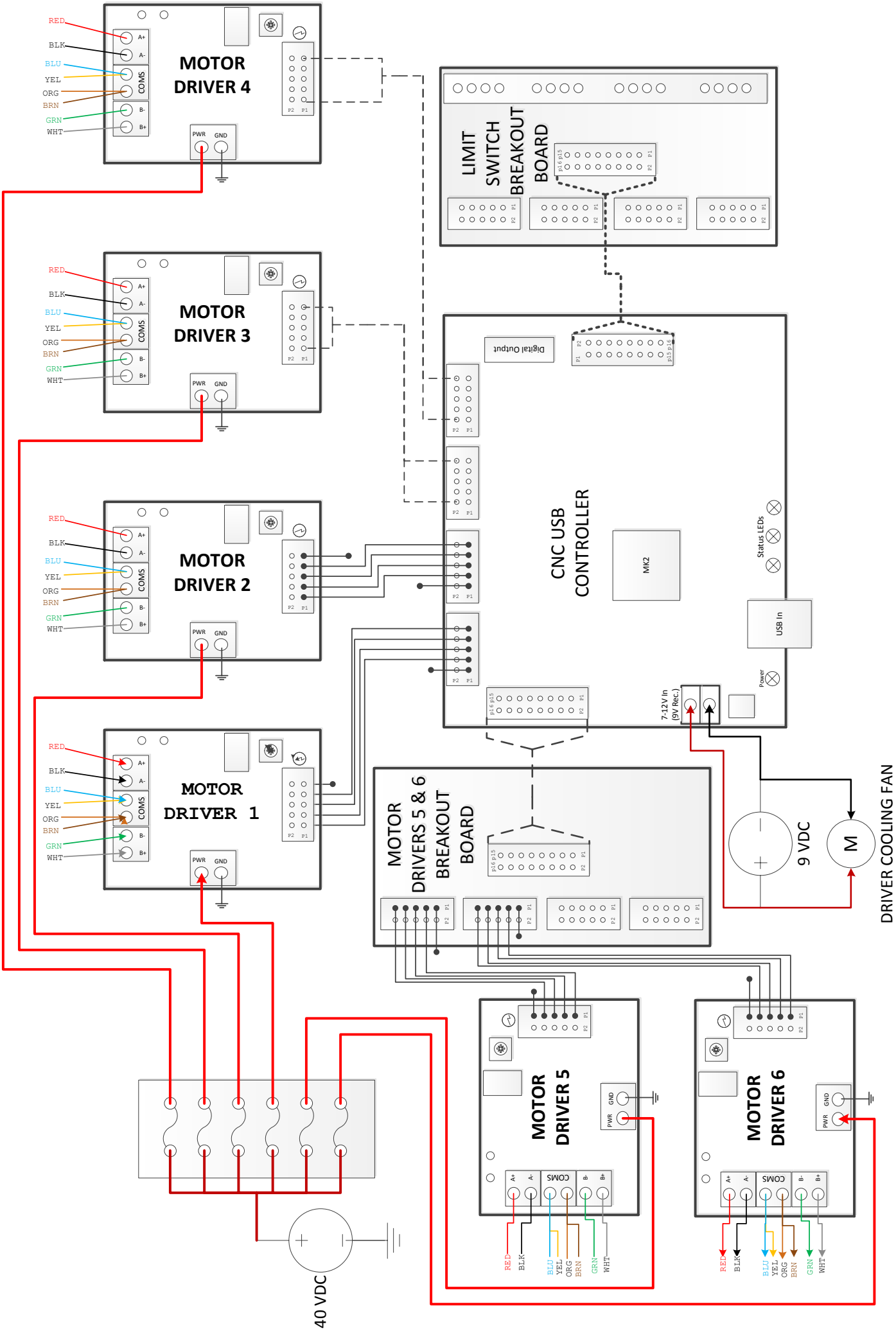
MOTOR DRIVER 4
MOTOR DRIVER 3
MOTOR DRIVER 2
MOTOR DRIVER 1
RED
BLK
BLU
YEL
ORG
BRN
GRN
WHT
A+
A-
COMS
B-
B+
PWR
GND
LIMIT SWITCH BREAKOUT BOARD
CNC USB CONTROLLER
MK2
Digital Output
Status LEDs
USB In
Power
7-12V In (9V Rec.)
MOTOR DRIVERS 5 & 6 BREAKOUT BOARD
9 VDC
M
DRIVER COOLING FAN
MOTOR DRIVER 5
MOTOR DRIVER 6
40 VDC

Material Specs for Frosted Detail & Frosted Ultra Detail

Properties	Frosted Detail & Frosted Ultra Detail
Composition	UV Curable Acrylic Plastic
Color	
Density @ 80 degree C (linquid), g/cm3	1.02
Tensile Strength, MPa	26.2
Tensile Modulus, MPa	1108
Elongation at Break, %	8.98
Flexural Strength, MPa	26.6
Heat Distortion Temp @ 66psi, Celsius	46
Heat Softening Temp, Celsius	80
Ash Content, %	.01

Appendix C

Datasheets and Manuals

Description des stratifiés

Préparé par C. Leduc
20 nov. 2012

Stratifié	**Quasi** (AML_0 = 25)	**Soft** (AML_0 = 70)	**Hard 1** (AML_0 = -20)	**Hard 2** (AML_0 = -29)
Séquence	$[\,(\mathbf{(\pm 45)} / \mathbf{(0/90)})_5\,]_S$	$[\,(\mathbf{(\pm 45)_2} / \mathbf{(0/90)} / \mathbf{(\pm 45)_2})_2\,]_S$	$[\,(\mathbf{(0/90)_2} / \mathbf{(\pm 45)} / \mathbf{(0/90)})_2\,]_S$	$[\,(\mathbf{(\pm 45)} / 0 / \mathbf{(0/90)})_3\,]_S$
Description	0° 90° ±45° Total 25% 25% 50% 20 plis	0° 90° ±45° Total 10% 10% 80% 20 plis	0° 90° ±45° Total 40% 40% 20% 20 plis	0° 90° ±45° Total 58% 14% 28% 18 plis
Schéma	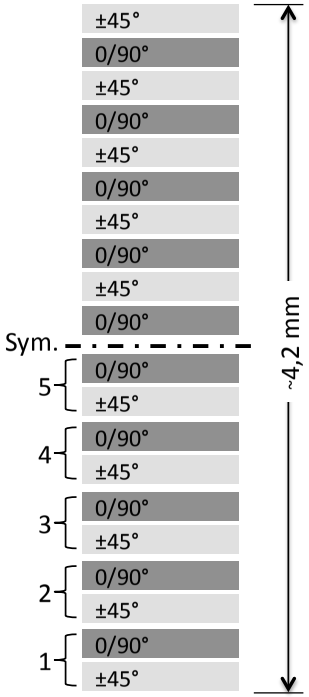	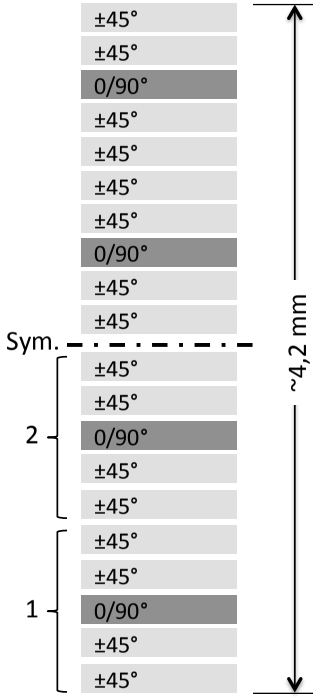	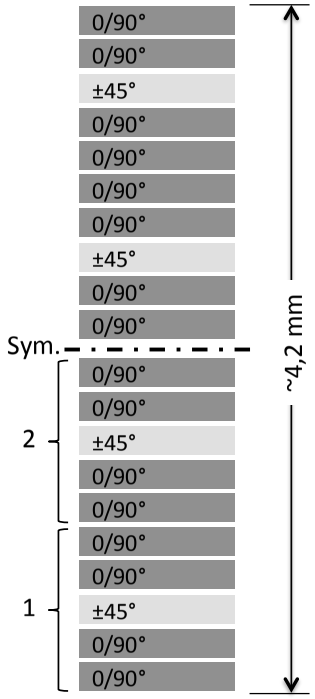	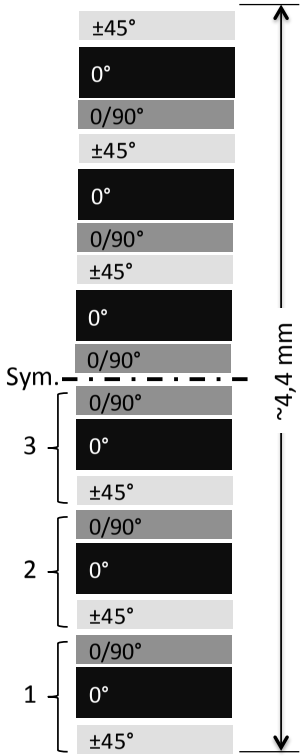

Légende

±45° Plis de sergé JB Martin TC-06-T (197 g/m^2 balancé)

0/90° Plis de sergé JB Martin TC-06-T (197 g/m^2 balancé)

0° Plis d'unidirectionnel JB Martin TC-09-U (315 g/m^2)

jb martin

MATERIAL SAFETY DATA SHEET

SECTION I: PRODUCT IDENTIFICATION

Product Name:	6.2 oz/yd² carbon fabric, TC-06-T
Weaver:	***jb martin ltée*** 445 St-Jacques Québec, Canada J3B 2M1 Tel.: (450) 346-6853
Raw material:	**Grafil, Inc.** **5900, 88th Street** **Sacramento, CA 95828** **USA**
Emergency Telephone:	(916) 386-1733
General Telephone:	(916) 386-1733
Facsimile Number:	(916) 383-7668

SECTION II: COMPOSITION/INFORMATION ON INGREDIENTS

Component	CAS RN	Exposure limits[1]	% by Weight
Carbon Fiber	7440-44-0	not established[2]	≥ 99%
Epoxy resin	not applicable	not established	0,4%

[1] There are no established OSHA PELs or ACGIH TLVs for these ingredients in the form in which they are present.

[2] At this time neither OSHA nor ACGIH has established any air contaminant limits specific to carbon fibers. OSHA has an established standard for particulate not otherwise regulated (nuisance dust) set at 5 mg/m³ (respirable fraction) and 15 mg/m³ (total dust). ACGIH has established an exposure value of 10 mg/m³ (total dust) for particules not other wise classified.

ProboStepVX

Uni-polar Microstepping Chopper Driver

Model: ProboStepVX

Stepper Motor Microstepping Driver Specs:

- Chopper Current Driver
- 0.5 - 3 Amp Current Limiting
- Short-circuit & Open-circuit Protection
- Full, Half, Quarter, Eighth & Sixteenth Microstepping
- Buffered Step & Direction Lines
- 10V - 44V Supply
- For 5-, 6-, and 8-wire Stepper Motors

Description:

The ProboStep is a complete microstepping motor driver and control system with a built-in translator. It is designed to operate uni-polar stepper motors in full-, half-, quarter-, eighth-, and sixteenth-step modes with output drive capability of 44V and 3.0 A. This driver utilizes the Sanken SLA7078MPR chip which includes built-in sense current detection and load circuit short or open protection provide lower loss and lower thermal resistance.

Features:

- Hardware or software selectable step and direction signals
- Current limit adjustable by potentiometer
- Wide range of motor power (10-42V)
- Power (for logic) indicator LED
- 3 A, 44 V Output Rating
- Fixed-offtime PWM blanking circuit reduces ringing
- 3.0-5.5 V Logic Supply Voltage Range
- Synchronous Rectification for Low Power Dissipation
- Internal UVLO and Short & Open Circuit Protection
- Crossover Current Protection

Flexible Design:

The ProboStep was designed with flexibility in mind with features including:

- Internal synchronous-rectification control circuitry is provided to improve power dissipation during PWM operation.
- Internal circuit protection includes short-circuit and open-circuit protection. Special power-up sequencing is not required.
- The logic signals are brought out to a .1" pin header on one side, allowing for use of an IDC cable to connect your boards. Every other pin on the IDC header is connected to ground, which acts to shield the control signals from noise. Noise in a stepper control system can cause miss stepping, which can damage your equipment, cause injury, and ruin your work piece.
- A schmitt trigger IC buffers the high voltage driver from your sensitive parallel port, and filters noise.
- Unlike the SideStep, the driver chip, the ProboStep does not have thermal protection, so a heatsink must be used when driving motors at greater than 1 amps.
- An under-voltage lockout circuit protects the A3977 from potential shoot-through currents when the motor supply voltage is applied before the logic supply voltage. All outputs are disabled until the logic supply voltage is above 2.7V; the control logic is then able to correctly control the state of the outputs.
- Patented short and open circuit protection.

Unipolar Chopper Drivers:

Unipolar chopper drivers are the simplest form of stepper motor control. A set of four sink drivers control the current to each of the four half-phases of a stepper motor. The circuit includes recirculating diodes and a sense resistor that maintains a feedback voltage proportional to the motor current. The high side of the supply is split out to one side of each half-coil, and the other end of each half-coil is routed to the low-side transistor switches. Motor windings, using a chopper driver, are energized to the full supply level by turning on one set the switching transistors. The sense resistor monitors the linear rise in current until the required level is reached. At this point the switch opens and the current decays until a preset position is reached and the process starts over. This "chopping" effect of the supply is what maintains the correct current voltage to the motor at all times.

probotix™

ProboStep

Uni-polar Microstepping Chopper Driver

VREF = .145 x amps

VREF (Volts)	Current (amps)
0.07	0.5
0.15	1
0.22	1.5
0.29	2
0.36	2.5
0.44	3

WARNING: Use a heatsink and fan when running higher than 1 amp.

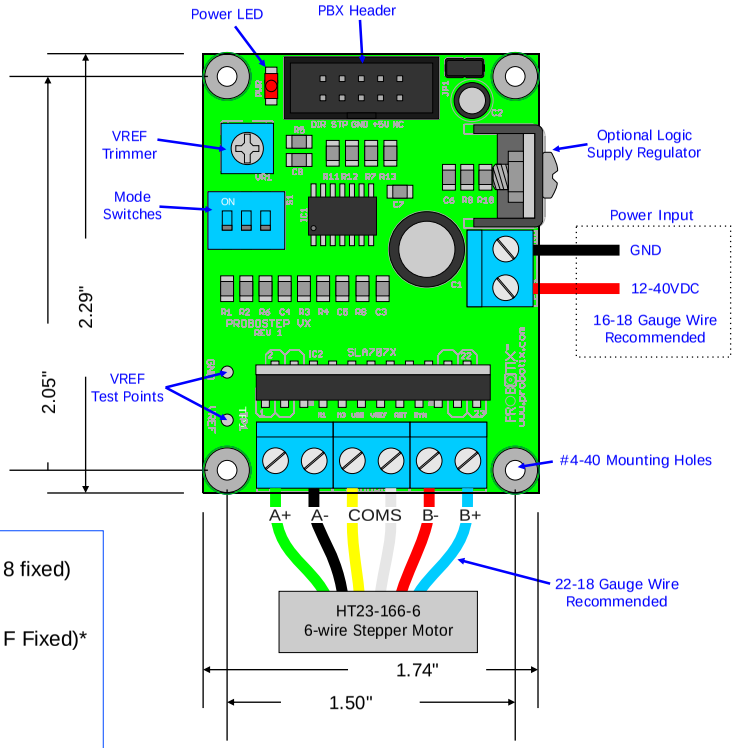

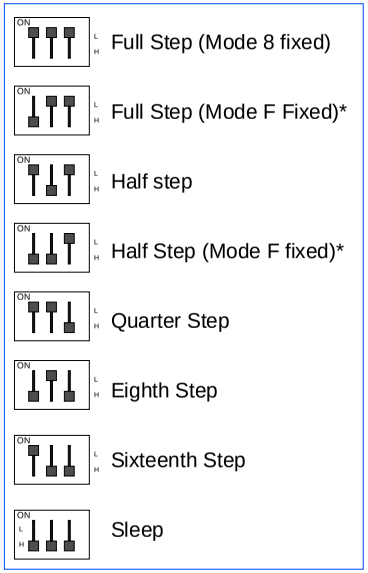

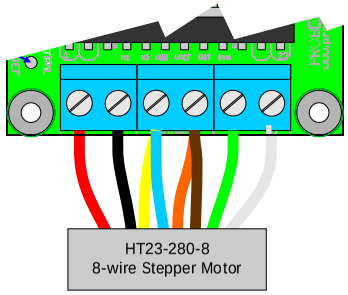

* Mode 8 uses 70% current ratio between phases, Mode F uses 100% current ratio between phases. Mode F should provide slightly more torque while Mode 8 should give smoother motion.

Setting Current Limit

Measure the DC voltage between the Ref Pin and GND, and adjust the trimmer as follows: Vref = .145 * desired motor current.

3 A = Vref .44 V
2 A = Vref .29 V
1 A = Vref .15 V
0.5 A = Vref .07 V

1. Determine the step resolution you wish to use, and set the dip switches according to Figure 2.

2. If driving your motors at more than 1 Amp, install a heat sink over the driver chip. A fan blowing over the heatsink will extend the life of your drivers. See the thermal warning on page three.

3. Apply power.

4. Connect a voltmeter between the VREF signal and GND and adjust the current trimmer to the desired voltage determined above.

WARNING: If the motor is connected during this adjustment, excessive heating may occur. Most motors can NOT experience temperatures above 100°C. At these temperatures internal melting and seizure may occur. Short-term current overdrive will, in general, not harm most motors.

WARNING: Never remove a connection to the stepper motor with power applied. There is a possibility the SLA7078 IC will be damaged. TheSLA7078 is rated for 46V DC max. The power supply voltage should be limited to ~42V DC to allow for back EMF generated by the stepper.

Control Software Setup

The ProboStep is negative logic. The STEP lines should be inverted in your software. Please contact us if you need help configuring your software.

Minimum pulse width for the step pulse is 5 uS. Maximum step frequency is 40 kHz. Most steppers torque really drop above 1 kHz at full step, or 8 kHz if you're using the eighth-step mode.

Figure 1: PBX Header Pin Diagram

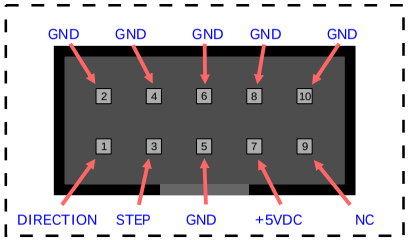

Thermal Warning

The ProboStepVX driver chip is not protected from temperature. Inadequate heatsinking will destroy the chip. Do not ever power the driver without a heatsink and cooling fan for even a few seconds - doing so will void your warranty.

A piece of 1/8” x 1” x 1” Aluminum angle makes a great heat sink if you bolt a 60mm fan to the top to help circulate air away from the heat sink. Use 4-40 Screws to attach the heat sink. Do not ever drill out the mounting holes to accomodate larger screws. Doing so will void your warranty.

Use thermal paste between the heatsink and driver to increase the efficiency. Make sure the heatsink covers the entire metal back plate of the chip. The hottest part of the chip is just above the center pin. The heat sink needs to touch the entire surface in order to properly wick away the heat.

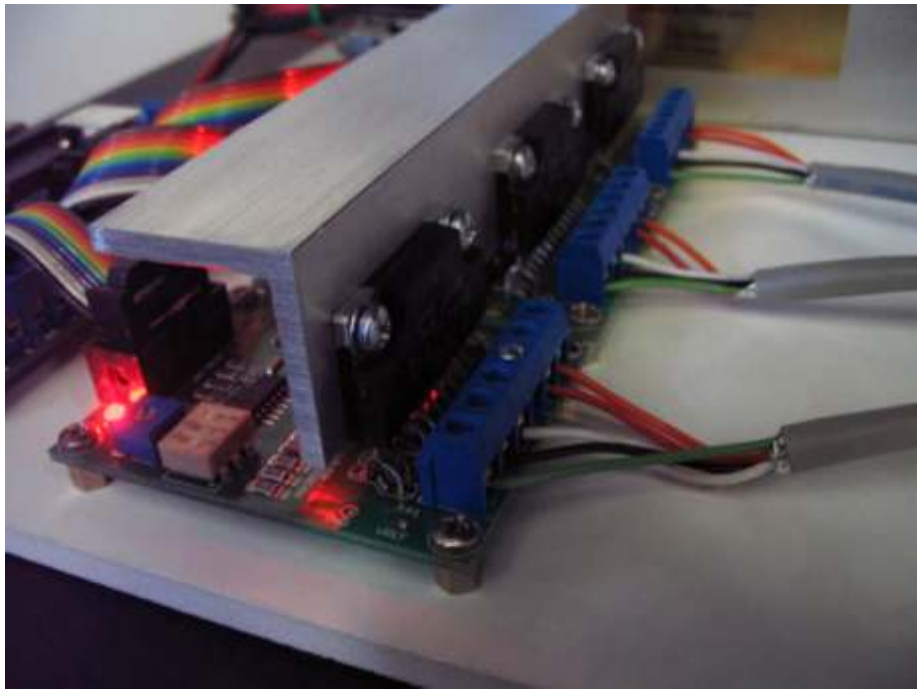

Appendix D

Code Appendix

D.1 Machine operation parameters

Nozzle offset length R is a property of nozzle geometry, defined as the length from the end of the tow feed nozzle to the rotational axis of the deposition head, Figure D.1. These values are used within the getco.m subroutine for correcting the in-plane position shift caused by the nozzle's end rotating at a distance from the rotational axis. More information is provided in Section 5.3.4.2.

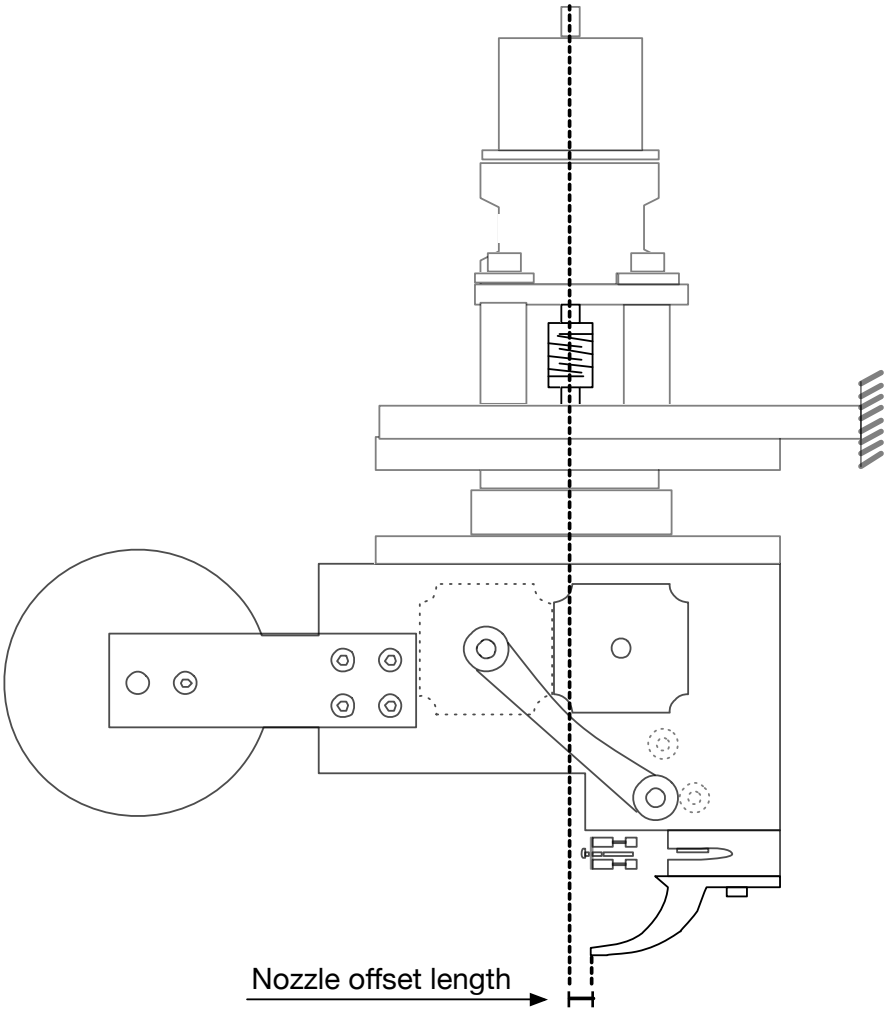

Figure D.1: Feed nozzle offset length

Feed nozzle length nl is the distance traveled by the tow from where it is cut by the cutting mechanism for the feeding nozzle end. This length is used to pre-feed tows into

the nozzle after each cutting cycle so that the tow is ejected from the nozzle and meets the substrate surface in syncronicity with the onset of a tow laydown cycle.

Spool-out height *ch* is the distance at which the feed nozzle moves above the substrate while depositing tows. After a layer is deposited, the spool-out height is increased by the tow height *yh* in order to account for the growing thickness of preform building below the feed nozzle.

The safe height *sh* is the distance above the deposition substrate's surface, at which rapid motions can safely be made by the machine's axes. This allows the deposition head to be quickly repositioned after each laydown cycle, reducing manufacturing cycle time. The safe height should be set sufficiently large so that the deposition system's components are undoubtedly clear of obstruction while in motion. Collisions at the speed of rapid motion will likely result in catastrophic destruction of the LM's components and systems.

After the deposition head is repositioned using rapid motion it must be lowered from the safe height to the spool-out height before beginning a tow deposition cycle. This is performed in two stages. Initially there is a rapid plunge which is followed by a slower prescribed-feed plunge. The deposition head is first lowered using rapid motion from the safe height to the feed-from height. From the feed-from height the deposition head is lowered at a prescribed slower feed rate *ps* until it reaches the spool-out height. By lowering the deposition in two stages, the manoeuvre can be performed in a timely, yet safe fashion. A high-speed machine crash during a plunge motion will likely result in severe damage to the machine's components as well as to the preform being manufactured at the time.

Tow clearing length *ycl* is the distance by which the deposition head must be moved after a cutting cycle in order to clear the section of tow that remains within the deposition head and nozzle. The tow clearing length is generally equivalent to the feed nozzle length plus a reliability length ($\approx 0.5''$).

D.2 Flowcharts

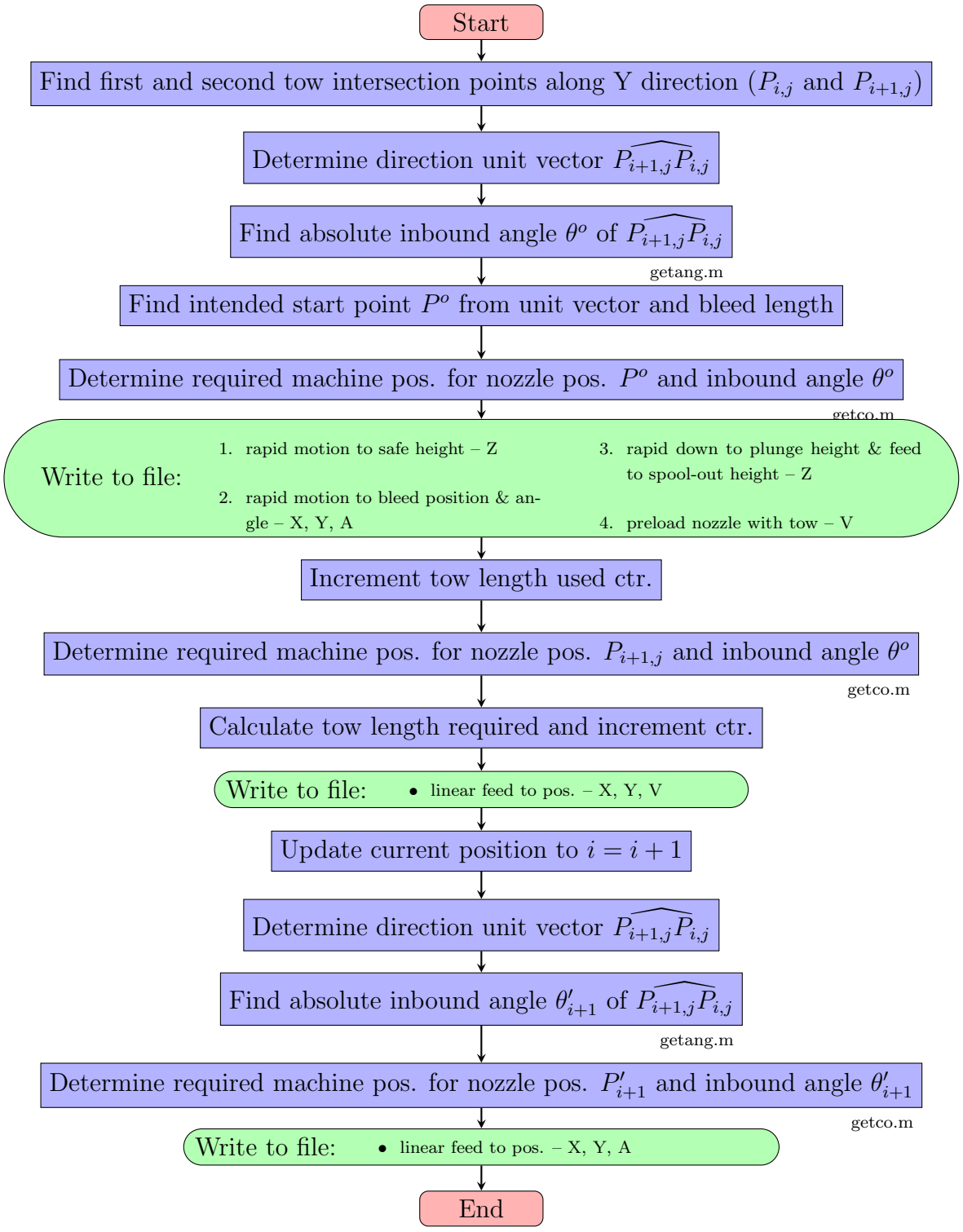

Figure D.2: Inbound Y direction path generator and code writer; this section of the post-processor code generates the instructions necessary to begin laying down each tow. Follows $P_{Row,Column}$ convention.

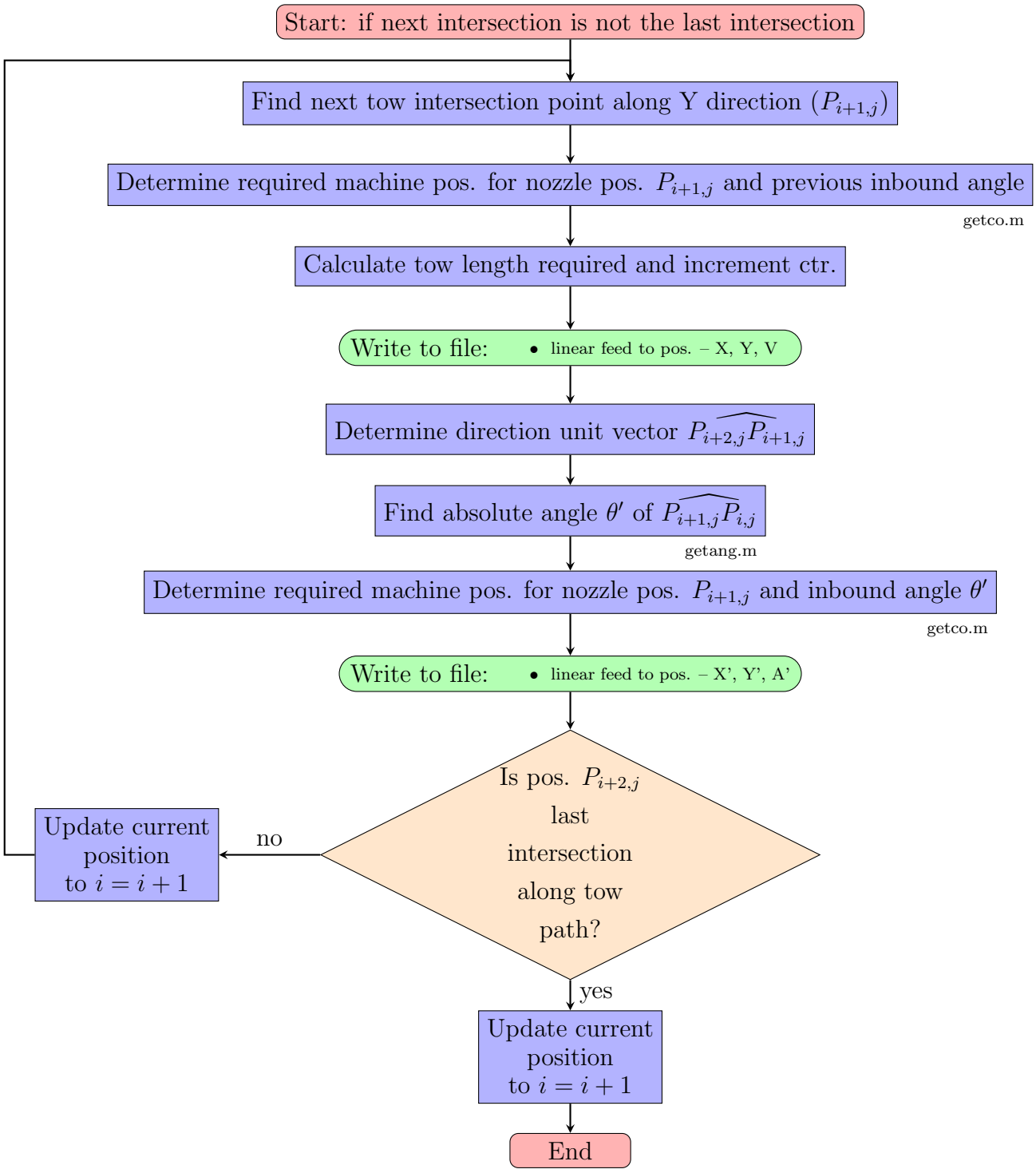

Figure D.3: Y direction midsection path generator and code writer; this section of the post-processor computes the paths between intermediate tow intersections (excludes first and last) and translates the paths to G-code instructions; directing the laydown machine through this domain. Follows $P_{Row,Column}$ convention.

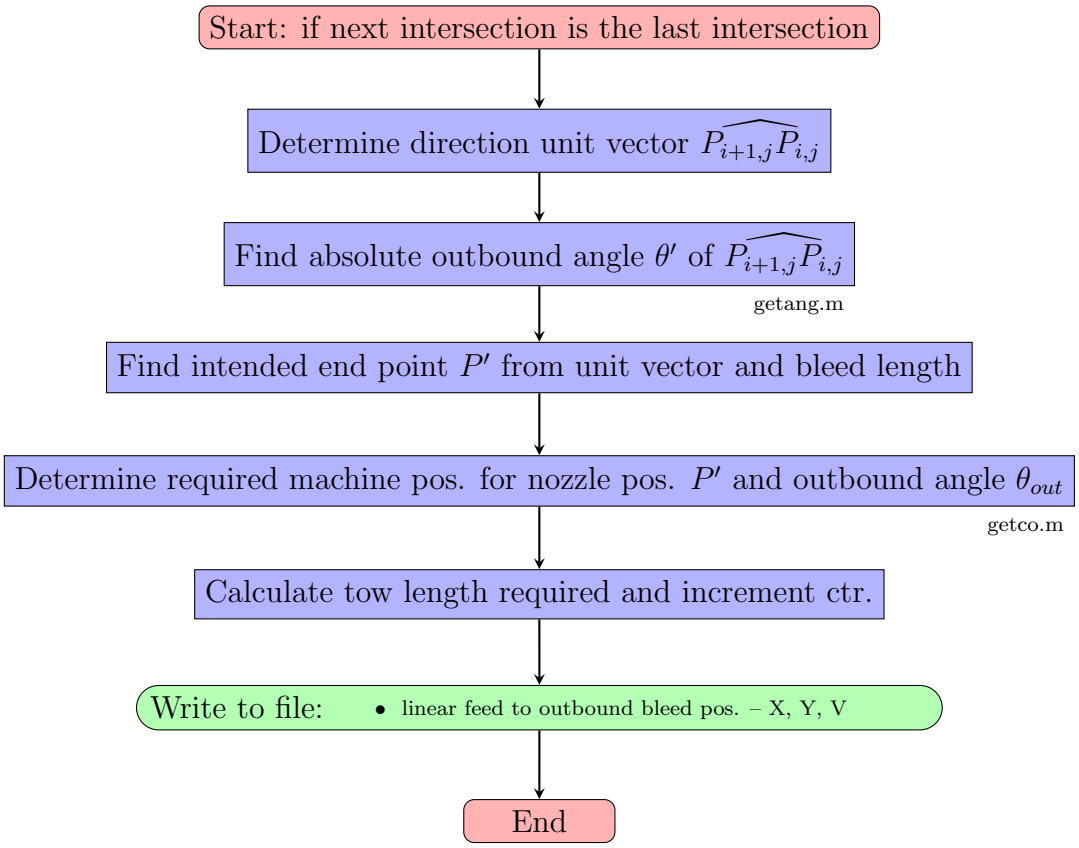

Figure D.4: Outbound Y direction path generator and code writer. This section of the post-processor computes the path from the second-last tow intersection position outward to the tow bleed-length. It then writes the G-code to direct the laydown machine to end deposition of a tow. Follows $P_{Row,Column}$ convention.

D.3 getAng.m

```
1  %Returns the angle of vector 'ab' with respect to the x axis.
2
3
4  function angle =  getAng(ab)
5                  xhat(1) = 1; %45 Degree unit vector
6                  xhat(2) = 1; % 45Degree vector
7
8                  %Calculate Theta using Cross-product (use 45deg ...
                       vector
9                  %because it handles all quadrents and directions
10                 Kmag = (xhat(1)*ab(2))-(xhat(2)*ab(1));
11                 Mag = (ab(1)^2 + ab(2)^2 )^0.5 * (xhat(1)^2+xhat(2)...
                       ^2)^0.5;
12                 angle = 0; %Clear Theta Vairable
13                 angle = (asin(  Kmag  / Mag ) * (180/ pi)) + 45 ; %...
                       Calculate Theta Compensate for 45deg vector
14                 angle = angle / (180/ pi);
15 end
```

D.4 getco.m

```
function [resx, resy, resa] = getco(xi, yi,r,theta)
noznine = 233.3 ;   % "Distance" to make nozzle turn 90 degrees
nozineneg = -233.3 ;   %negative deg value (indpendent of + or - Sign...
    )

theta = theta + pi;
resa = (theta*(180/pi)-90)* (-noznine/90) ;


resx = xi - r*cos(theta); %Calculate resultant X Cordinate
resy = yi - r*sin(theta); %Calculate resultant y Cordinate
end
```